XVIII CONGRESSO NAZIONALE DI SCIENZE PLANETARIE

6-10 Febbraio 2023
Sala dei Notari, Palazzo dei Priori Perugia

ABSTRACTS Book
Poster Presentations

PROGRAMMA

6 Febbraio, Lunedì

14:00 – 15:00	**Interventi Istituzionali**
	Prof. Alceo Macchioni Direttore Dip. di Chimica e Biologia
	Prof. Diego Perugini Direttore Dip Fisica e Geologia
	Prof. Ermanno Cardelli Direttore Ingegneria
	Prof. Giovanni Gigliotti Dipartimento di Ingegneria Civile ed Ambientale
	Prof. Fausto Elisei Prorettore
	Helios Vocca Rappresentanza del Rettore
	Marco Tavani Presidente INAF
	Leonardo Varasano Assessore alla Cultura Comune di Perugia

15:00 – 15:30	Prospettive delle scienze planetarie in Italia	Barbara Negri ASI
15:30 – 15:55	Il Programma di Esplorazione dell'ESA	Raffaele Mugnuolo ASI
15:55 – 16:10	Paving the way for the Italian community towards Mars Sample Return (MSR), the next step in Martian exploration	Francesca Altieri

16:10 – 16:45   Coffee Break

16:45 – 18:30 Sessione 1: Astrochimica - Astrobiologia 1

Chair: Maria Teresa Muscari Tomajoli

16:45 – 17:15	**INVITED TALK: From Interstellar Clouds to Planetary Systems: the Astrochemical Thread**	Cecilia Ceccarelli IPAG
17:15 – 17:30	Theoretical investigation of formation routes leading to S-bearing species in space via the reactions of electronically excited atoms	Andrea Giustini
17:30 – 17:45	Rotational spectroscopy of pyrrole: a model for astrophysical searches	Assimo Maris
17:45 – 18:00	A laboratory investigation of the reactions N(2D) + benzene and N(2D) + toluene and implications for the atmospheric chemistry of Titan	Gianmarco Vanuzzo
18:00 – 18:15	Detectability of aromatic organics in Sulfates by the Mars 2020 Perseverance rover	Teresa Fornaro
18:15 – 18:30	Survivability of Xhantoria Parietina in simulated Mars conditions for 30days	Christian Lorenz

7 Febbraio, Martedì

9:00 – 10:30 Sessione 1: Astrochimica - Astrobiologia 2

Chair: Teresa Fornaro

09:00 – 09:30	**INVITED TALK: Open questions about the origin of life: where to go in Solar System studies**	Giovanni Vladilo INAF - OaTs
09:30 – 09:45	Desert cyanobacteria: Lesson learned from astrobiology experiments in low Earth orbit and implications for future missions	Daniela Billi
09:45 – 10:00	Worldwide distribution of acidophilic extremophiles provides insight into future space biology applications	Luca Tonietti
10:00 – 10:15	Eukaryotic organisms exposed to space environment: a focus on the physiological adaptions of the brine shrimps A. Salina to astrobiological studies	M. Teresa Muscari Tomajoli
10:15 – 10:30	Evolution of climate and observational properties of a habitable rocky planet: Earth.	Laura Silva

10:30 – 11:00   Coffee Break

11:00 – 12:00 Sessione 2: Pianeti e Satelliti: Analisi Dati e Modellistica

Chair: Giovanni Munaretto

11:00 – 11:15	Microwave thermal emission from Solar System Planets and CMB calibration	Michele Maris
11:15 – 11:30	Mineralogical mapping of Ceres as revealed by the 1 µm absorption	Giacomo Carrozzo
11:30– 11:45	Volatile emission from a fracture on a planetary surface: a Smoothed-Particle-Hydrodynamics approach	Matteo Teodori
11:45– 12:00	Roughness of planetary surfaces: Hapke theory and statistical multi-facet algorithm. preliminary analysis	Andrea Raponi

12:00 – 14:00   Pausa Pranzo

14:00 – 15:30 Sessione 3: Esopianeti

Chair: Aldo Bonomo / Riccardo Claudi

14:00 – 14:15	Search for and occurrence rate of Jupiter analogues in planetary systems with short period sub-Neptunes	Aldo Bonomo
14:15 – 14:30	Cold Jupiter shaping the formation of Super-Earths	Matteo Pinamonti

	around M dwarfs	
14:30 – 14:45	Responses of Eukaryotic photosynthetic organisms from different systematic groups to a simulated M dwarf starlight	Mariano Battistuzzi
14:45 – 15:00	The GAPS Program at TNG: That strange case of the young planetary system V1298 Tau	Riccardo Claudi
15:00 – 15:15	An Exoplanet Atmosphere as Never Seen Before.	Luigi Mancini
15:15 – 15:30	The HADES Program with HARPS-N@TNG. HADES: THE HArps-n red Dwarf Exoplanet Survey	Laura Affer

15:30 – 16:00   Coffee Break

16:00 – 17:30 Sessione 4: Mercurio

Chair: Cristina Re

16:00 – 16:30	**INVITED TALK: BepiColombo first results of the Cruise phase and Fly-Byes**	Anna Milillo INAF-IAPS
16:30 – 16:45	Ca and CaO Mercury exosphere as product of micro-meteoroids and comet stream particles impact	Martina Moroni
16:45 – 17:00	Remote sensing of Mercury Sodium emission and relationship with magnetospheric activity	Stefano Orsini
17:00 – 17:15	Permanent Shadowed regions of Mercury: new hypothesis about water ice origin	Silvia Bertoli
17:15 – 17:30	Spectral detection of Water ice, S-bearing ad organic species in Mercury's PSR by SIMBIO-SYS-VIHI on the BepiColombo Mission	Gianrico Filacchione

17:45 – 18:45   Assemblea Generale della Società Italiana di Scienze Planetarie

19:30 Cena Sociale Ristorante del Sole – Via della Rupe 1

8 Febbraio, Mercoledì

9:00 – 10:30 Sessione 5: Piccoli Corpi – Results of the DART/LICIACube Mission 1

Chair: Davide Perna

09:00 – 09:30	**INVITED TALK: The Light Italian Cubesat for Imaging of Asteroids in support to the NASA mission DART**	Elisabetta Dotto and the LICIACube Team
09:30 – 09:45	Modelling the ejecta plume after the DART impact	Alessandro Rossi
09:45 – 10:00	Color analysis of Dimorphos plume produced by DART impact using Liciacube-Luke data	Giovanni Poggiali
10:00 – 10:15	Towards reconstructing the Dimorphos ejecta plume by means of non-spherical dust simulations and DART-Liciacube data	Stavro Ivanovski
10:15 – 10:30	The shape of Dimorphos as seen by Liciacube-Luke images	Angelo Zinzi

10:30 – 11:00   Coffee Break

11:00 – 12:00 Sessione 5: Piccoli Corpi – Results of the DART/LICIACube Mission 2

Chair: Angelo Zinzi

11:00 – 11:15	Bouncing Boulders: A "secondary plume" from Didymos surface observed by Liciacube-Luke camera after DART impact on Dimorphos's surface	Elena Mazzotta Epifani
11:15 – 11:30	After DART: The Didymos system in the aftermath of the DART event	Simone Ieva
11:30– 11:45	A first assessment on the origin of Didymos and Dimorphos, NASA's DART mission targets	Fabio Ferrari
11:45– 12:00	The boulder size-frequency distribution derived from DART/DRACO images of Dimorphos: Preliminary results	Maurizio Pajola

12:00 – 14:00   Pausa Pranzo

14:00 – 15:30 Sessione 6: Piccoli Corpi – Artificiali e Naturali 1

Chair: Alessandro Rossi

14:00 – 14:30	**INVITED TALK: On the synergy between Planetary Science and Space engineering in the study and exploitation of natural routes**	Elisa Maria Alessi CNR - IMATI
14:30 – 14:45	The LICIACube extended mission as an imminent	Ettore Perozzi

	impactor sentinel	
14:45 – 15:00	The NEOROCKS "Rapid-Response Experiment"	Davide Perna
15:00 – 15:15	NEOROCKS: Investigating the physical nature of the small asteroid population	Vasiliki Petropoulou
15:15 – 15:30	Analysis of spectral variability of asteroid 3200 Phaethon in preparation to DESTINY+ space mission.	Marianna Angrisani

15:30 – 16:00   Coffee Break

16:00 – 16:45 Sessione 6: Piccoli Corpi – Artificiali e Naturali 2

Chair: Simone Ieva

16:00 – 16:15	VIS-IR imaging spectroscopy of Martian Meteorites	Simone De Angelis
16:15 – 16:30	Spectroscopic and nanoscale mineralogical investigation of Ryugu returned samples	Marco Ferrari
16:30 – 16:45	ProDisCo: A Systematic Comparison Between Measured Molecular Abundances in Comets and Protoplanetary Disks	Manuela Lippi

16:45 – 18:00 Sessione 7: Meteore e Meteoriti 1

Chair: Anna Barbaro

17:00 – 17:15	Water reactivity on Schreibersite: from Phosphites to Posphates	Stefano Pantaleone
17:15 – 17:30	Multi-collector ^{40}Ar-^{39}Ar dating in planetary geosciences: dating terrestrial impact structures	Gianfranco Di Vincenzo
17:30 – 17:45	Early differentiation of planetesimals: insights from melting experiments of an L6 ordinary chondrite	Matteo Masotta
17:45 – 18:00	Glass of possible impact origin from Pica (Chile)	Gabriele Giuli

9 Febbraio, Giovedì

9:00 – 9:45 Sessione 7: Meteore e meteoriti 2

Chair: Matteo Masotta

09:00 – 09:15	Cavezzo: fall, recovery and analysis of the first Italian meteorite found by PRISMA	Daniele Gardiol
09:15 – 09:30	Carbon phases in Ureilites with increasing the degree of shock: the example of five frontier mountain Ureilites.	Anna Barbaro
09:30 – 09:45	The chondritic impactor origin of the Ni-rich component in australasian tektites/microtektites	Luigi Folco
9:45 – 10:00	The Brachinites and Brachinite-like ungrouped achondrites connection: insights from Spinels mineral-chemistry	Tiberio Cuppone

10:00 – 10:30 Sessione 8: Dischi Protoplanetari e fasi primordiali

Chair: Manuela Lippi

10:00 – 10:15	Protoplanetary disks around solar-analogues: factories of pre-biotic molecules?	Claudio Codella
10:15 – 10:30	Kinematics perturbation in the protoplanetary disk of AS 209:signature of a giant protoplanets at 100 au	Davide Fedele

10:30 – 11:00   Coffee Break

11:00 – 12:00 Sessione 9: Marte 1

Chair: Ilaria Di Pietro

11:00 – 11:15	Buried faults, Sedimentary sequences and Playa environments	Gene Walter Schmidt
11:15 – 11:30	Methane on Mars: possible geomorphic indicators of Methane emission in three impact craters	Elettra Mariani
11:30– 11:45	Application of the Minimum Noise Fraction technique to Exomars/TGO-NOMAD LNO channel nadir data: SNR enhancement evaluation	Fabrizio Oliva
11:45– 12:00	Water cycle and aerosols at Mars with the NOMAD spectrometer onboard ExoMars TGO	Giuliano Liuzzi

12:00 – 14:00   Pausa Pranzo

14:00 – 15:15 Sessione 9: Marte 2

Chair: Simone Silvestro

14:00 – 14:15	Structural mapping and stress analysis to unravel the polyphasic tectonic history of the Claritas Fossae, Mars	Evandro Balbi
14:15 – 14:30	Did MARSIS find liquid water beneath the Martian south polar layered deposits?	Roberto Orosei
14:30 – 14:45	High-resolution compositional map and subsurface investigation of a martian valley close to Olympia Planum	Nicole Costa
14:45 – 15:00	debate of the large martian ripples	Hezy Yizhaq
15:00 – 15:15	Study of the dust lifting and electrification physics by means of martian analogues	Gabriele Franzese

15:15 – 15:45   Coffee Break

15:45 – 17:00   Sessione 10: Il Sistema Gioviano

Chair: Mauro Ciarniello

15:45 – 16:00	A preliminary study of Ganymede's energetic ion environment to be investigated with JUICE	Christina Plainaki
16:00 – 16:15	Observability of Callisto's exosphere with MAJIS/JUICE	Emiliano D'Aversa
16:15 – 16:30	Combining remote sensing and laboratory analysis to search for organics on the surface of Europa	Silvia Pagnoscin
16:30 – 16:45	The Jupiter's hot spots as observed by Juno-JIRAM: limb-darkening in thermal infrared	Davide Grassi

16:45 – 17:45 Sessione Europlanet a cura di Stavro Ivanovski e Federica Duras

18:00 – 20:30 Sessione Poster – Apericena e Premiazione Poster

10 Febbraio, Venerdì

9:00 – 10:30 Sessione 11: Planetologia Sperimentale 1

Chair: Alessandro Pisello

09:00 – 09:15	Water desorption from lunar sample analogues to support the ESA PROSPECT instrument development	John Brucato
09:15 – 09:30	Dielectric spectroscopy analyses of lunar regolith simulants for the radar detection of water ice on the Moon	Chloe Helena Martella
09:30 – 09:45	Alteration of organic matter on Ceres: results from laboratory studies on the complex geo-chemical history of the innermost dwarf planet	Maria Cristina De Sanctis
09:45 – 10:00	Preliminary results on the infrared H2-H2 and H2-He experimental collision induced absorption coefficients	Stefania Stefani
10:00 – 10:15	Hypervelocity impacts on Comet Interceptor dust impact sensor and counter for dust shield and detection system assessment	Stefano Ferretti
10:15 _ 10:30	The spectral and chemical changes of atmosphere-less surfaces induced by ion bombardment	Riccardo Urso

10:30 – 11:00   Coffee Break

11:00 – 11:45 Sessione 11: Planetologia Sperimentale 2

Chair: Eliana La Francesca

11:00 – 11:15	Low temperature reflectance spectra of NH4+ minerals in the VNIR: effect of phase trasitions for planetary investigation	Maximiliano Fastelli
11:15 – 11:30	UV irradiation experiments of organo-sulfate martian analog samples to support detection of organics on Mars by the NASA MARS2020 and ESA ExoMars rovers	Andrew Alberini
11:30– 11:45	Simulating icy-world surfaces in the laboratory: NIR spectra of natron, mirabilite and epsomite dissolved in water	Daniele Fulvio

11:45 – 12:30 Candidature Consiglio Direttivo SISP; Candidature Sede Edizione 2024; Premiazione della migliore presentazione

12:30 Fine Congresso

Poster Session
Giovedì 9 Febbraio ore 18:30 – 20:30

1	The key role of silicon in astrochemistry	Matteo Michielan
2	Photo-processing and thermal desorption of acetaldehyde, acetonitrile, and water ice mixtures on olivine grains: TPD and mass spectra analyses	Maria Angela Corazzi
3	Thermal desorption of PA(N)Hs-water ice mixtures from dust grains	Valeria Lino
4	The use of the correlation matrix for Martian life detection	Andrea Meneghin
5	Combined crossed-beams and theoretical investigation of the O(3p,1d) + acrylonitrile reactions and implications for Extraterrestrial environments	Giacomo Pannacci
6	Computed binding energies distribution of relevant S-bearing species at interstellar icy grains	Vittorio Bariosco
7	Testing alternative theories of gravity with the Bepicolombo mission: the case of Brans-Dicke theory	Miriam Falletta
8	Discovery of the TOI-411 system: a super-Earth and two sub-Neptunes orbiting a bright, nearby, sun-like star	Laura Inno
9	SETI within 30 parsecs from Earth	Graziano Chiaro
10	Dart-vetter: a deep learning tool for automatic vetting of TESS candidates.	Stefano Fiscale
11	Petro-mineralogical and geochemical study of lunar meteorite NWA 13859	Riccardo Avanzinelli
12	Early differentiation of planetesimals: insights from melting experiments of an L6 ordinary chondrite	Matteo Masotta
13	The NWA12800: an extremely interesting CV3 carbonaceous chondrite	Andrea Vitrano
14	The LUMIO cubesat: detecting meteoroid impacts on the lunar farside	Fabio Ferrari
15	Meteorite-dropping bolides observation with the PRISMA fireball network	Dario Barghini
16	MIDIR spectral characterization of Ol-bearing ungrouped achondrites	Cristian Carli
17	Microscopic impactor debris at Kamil crater, Egypt: the origin of the Fe-Ni oxide spherules	Luigi Folco
18	Mineralogical characterization of the fusion crust of the Cavezzo L5 chondrite	Marianglona Rondinelli
19	Mineralogical characterization and microchemical analysis of the Alfianello, Monte Milone, and Siena ordinary chondrites.	Valeria De Santis
20	First find of ringwoodite in the Alfianello L6 ordinary chondrite	Laura Carone
21	Preliminary characterization of two Rantila fall fragments.	Anna-Irene Landi
22	Alteration fronts in reckling peak 17085 CM carbonaceous chondrite: an investigation of the aqueous alteration process in the CMs parent asteroid.	Anna Musolino
23	Geochemical characterisation and Cr isotope composition of libyan desert glasses and ordinary chondrites: preliminary data	Martina Casalini

24	VIS–MIR spectral characterization of the NWA 12184 meteorite and modifications induced by solar wind irradiation experiment	Anna Galiano
25	New impact crater catalogue of the moon based on the deep learning approach	Riccardo La Grassa
26	Martian surface photometry with TGO/Cassis: current results and future perspectives	Giovanni Munaretto
27	Dielectric properties of sodium chloride doped ice for the characterization of Europa's ice shell	Alessandro Brin
28	Unvealing the chemistry of nitriles in titan's atmosphere: the reaction of excited atomic nitrogen, N(2d), with cyanoacetylene (HC3N), acrylonitrile (C2H3CN) and acetonitrile (CH3CN)	Luca Mancini
29	Aeolian landforms in the exomars landing site, a regional perspective	Simone Silvestro
30	Ubiquity of landslides in the solar system	Maria Teresa Brunetti
31	Geological mapping and preliminary spectral analysis of mare Ingenii basin.	Gloria Tognon
32	Possible volcanic origin for "mounds" of the Hypanis fan system, Mars: magmatic vs sedimentary.	Agnese Caramanico
33	On the nature of the dark resistant unit (DRU) in the oxia planum area, Mars	Michelangelo Formisano
34	Terrestrial and martian paleo-hydrologic environments: systematic comparison by means of prisma and crism hyperspectral data	Angelo Zinzi
35	A grid of climate models for the Noachian Mars using EOS-ESTM	Paolo Simonetti
36	MESSENGER grand finale at Mercury: surface age and property characterization	Elena Martellato
37	Geological and structural mapping of the Michelangelo (H-12) quadrangle of Mercury: preliminary results	Salvatore Buoninfante
38	Geological studies with MATISSE: a Mercury surface study case	Veronica Camplone
39	Landing site characterization of Marius Hills pit (Moon): a feasibility evaluation for the ESA lunar caves CDF study.	Riccardo Pozzobon
40	The planetary mapping and GIS laboratory at INAF-IAPS.	Alessandro Frigeri
41	Geological mapping of sedimentary sequences of impact craters in Arabia Terra: a test site for standardized planetary maps.	Lucia Marinangeli
42	Clay-rich deposits in Oxia Planum and north Xanthe terra: an updated overview of the infrared data in context with ExoMars rover mission	Jeremy Brossier
43	Improvement of the MARSIS on-board SW, on the Mars Express mission. Preliminary scientific results on Phobos and Mars.	Andrea Cicchetti
44	Eolo megaripple archive: mapping the recent aeolian deposits to support the luminescence investigation on Mars	Lucia Marinangeli
45	The surface of mercury investigated by means of principal component analysis on MASCS/MESSENGER data.	Anna Galiano
46	Structural analysis of the Discovery quadrangle (H-11), Mercury.	Antonio Sepe
47	Segmentation analysis of selected lobate scarps on Mercury	Luigi Ferranti

48	LICIACube activities at ASI-SSDC: processing, calibration, archiving and analysis of images	Angelo Zinzi
49	Visible spectroscopic survey of near earth objects from the Asiago observatory in the framework of the NEOROCKS project	Monica Lazzarin
50	A database for the thermal analysis of the comet 67p	Edoardo Rognini
51	NEOROCKS: the EU H2020 programme for NEO rapid observation, characterization, and key simulations.	Elisabetta Dotto
52	Future perspectives of the NEO physical properties database by the NEOROCKS EU project	Ilaria Di Pietro
53	Search and study for meteorites analogues to Didymos in preparation to the Milani/HERA investigation.	Giuseppe Massa
54	Laboratory investigation of icy surface analogs of some solar system objects	Alessandra Migliorini
55	Visible and near-infrared spectroscopy of Mars analogues in support of the ESA's ExoMars rover mission.	Simone Filomeno
56	Reflectance spectra of mascagnite and salammoniac minerals by varying viewing geometry.	Maximiliano Fastelli
57	Using the DAVIS laboratory setup to simulate and test MA_MISS surveys on rock samples.	Lorenzo Rossi
58	Stereo validation activities for the new stereo hyperspectral pushbroom camera: HYPSOS	Cristina Re
59	Dust detector on-board Milani cubesat: VISTA FM calibration and instrument main goals in the framework of HERA mission.	Chiara Gisellu
60	The PVRG spectral database of lab-made volcanic products on the SSDC infrastucure: a new catalog of reference spectra to characterize volcanic terrains on planetary bodies.	Alessandro Pisello
61	DAEDALUS Cam: an immersive stereoscopic camera to explore lunar caves	Claudio Pernechele
62	Astroinformatic and digital planetology laboratory in INAF	Romolo Politi
63	Making Janus ready to launch: on ground calibration campaign	Livio Agostini
64	TRIS: transmission and illumination system.	Eliana La Francesca
65	Ma_Miss and scientific activities in support of the exploration of the martian surface and subsurface in the next decade	Cristina De Sanctis
66	SHRK the high-contrast imager and spectrograph for LBT	Dino Mesa
67	Contamination-free manipulation of extraterrestrial dust particles using acoustic tweezers	Stefano Ferretti
68	Comparison of infrared spectral features from planetary surfaces and laboratory rock samples	Matteo Bisolfati
69	Finding long-period solar system or interstellar objects with machine learning in LSST.	Antonio Vanzanella
70	The age of Saturn's Rings: Clues from Ring-Moon composition	Mauro Ciarniello

THE KEY ROLE OF SILICON IN ASTROCHEMISTRY

M. Michielan[1], D. Ascenzi[1], N. Balucani[2,3,4], G. di Genova[2], L. Tinacci[3,5], C. Ceccarelli[3]

[1] Dipartimento di Fisica, Università degli Studi di Trento, 38123, Povo, Italy; matteo.michielan@unitn.it; daniela.ascenzi@unitn.it.
[2] Dipartimento di Chimica, Biologia e Biotecnologie, Università di Perugia, 06123 Perugia, Italy; nadia.balucani@unipg.it
[3] Université Grenoble Alpes, CNRS, IPAG, 38000 Grenoble, France; cecilia.ceccarelli@univ-grenoble-alpes.fr; lorenzo.tinacci@univ-grenoble-alpes.fr
[4] Osservatorio Astronomico di Arcetri, Largo E. Fermi 5, 50125 Firenze, Italy
[5] Dipartimento di Chimica and Nanostructured Interfaces and Surfaces (NIS) Centre, Università degli Studi di Torino, via P. Giuria 7, 10125 Torino, Italy

Abstract:
The chemistry in space is prolific and ubiquitous despite the harsh nature of the environments involved. Understanding how molecules are formed and destroyed is paramount to give an insight on the history, the properties, and the evolution of astronomical objects in which such species have been detected. To reach this goal, the theoretical and experimental knowledge of the mechanistic aspects of these formation/destruction processes, involving neutral and ionic species, is fundamental.

Silicon is the 8th element in the universe by abundance, and it is mostly present in the core of dust grains, in meteoroids, and meteorites as silicates, and it is mainly released in the gas phase as Si and SiO after intense shocks.[1],[2] For this reason, SiO is typically considered as a good probe for shocked regions in space (*i.e.* young-forming stars).[2] Once released in the interstellar medium (ISM), Si atoms are generated and the reconverted into gaseous SiO and its isotopologues.[3] Moreover, silicon has also been detected in space as carbides with variable geometry and stoichiometry such as SiC, c-SiC$_2$, c-SiC$_3$, and SiC$_4$.[1] These species allow to explain the presence of molecules like phenylsilane, methyldilane or cyanosilane formed *via* neutral-neutral reactions in the circumstellar envelope of the carbon star IRC+10216.[4] Furthermore, silicon carbide can contribute to the synthesis of fullerenes and other species like polycyclic aromatic hydrocarbons.

In different astronomical environments like Sgr B2, Orion KL, and the interstellar shock L1157-B1, SiS has also been detected.[3],[5] Differently from the well-studied SiO and SiC species, the reactivity of SiS is not yet fully understood. In fact, despite many conversion channels of Si ions could bring to the formation of SiS, only one reaction pathway (HSiS$^+$ + e$^-$ → H + SiS), is currently reported in the existing chemical networks (*e.g.* KIDA[1]). The reagent HSiS$^+$ could be formed starting from Si$^+$ either through the reaction with OCS or H$_2$. However, the reaction SiS$^+$ + H$_2$ → H + HSiS$^+$ seems to be unlikely.[6] H$_2$S, which has already been detected toward the dark clouds TMC 1 and L134N, could also react with Si$^+$ producing HSiS$^+$ (e.g., H$_2$S + Si$^+$ → HSiS$^+$ + H). However this formation pathway is not yet reported.[7]

Another key aspect of silicon chemistry is given by the reactivity of Si$^+$ with hydrocarbons and of Si with atomic and molecular hydrogen.[8] Regarding the first type of reactions, the information listed in the available networks is either incomplete (*e.g.* the reaction data are available only at room temperature or related to photoassociative products, as for the reaction Si$^+$ + CH$_4$ → CH$_3$Si$^+$ + H, KIDA) or incorrect (*e.g.* the destruction of SiO by H$_3$O$^+$ and HCO$^+$, as reported in the databases, indicates HSiO$^+$ as ionic product instead of SiOH$^+$, which is the most stable isomer, thus making the process endothermic, as pointed out in GRETOBAPE[2]).[9]

A correct and comprehensive modelling of the silicon chemistry in the various phases of star formation and evolution from protostellar to protoplanetary disk is pivotal to understand how Si containing species, *e.g.* silicates [10], are assembled into structures of increasing complexity from clusters to nanoparticles and primordial dust particles that provide the main building blocks of planets and planetesimals during the process of planet formation. [11]

However, the variety and complexity of silicon chemistry in space is not yet fully understood and the data reported so far in the literature are uncertain. Hence, herein we will critically reappraise and present the state of the art of the silicon chemistry, by taking into account information and data from different networks

---

[1] https://kida.astrochem-tools.org
[2] https://github.com/TinacciL/GreToBaPe Cleaning.

like KIDA, UMIST[3], and the more recent GRETOBAPE, with the aim of defining a new landmark for the investigation of the reactivity of silicon and Si-bearing molecules.

References:

[1]   He, C. *et al.*, (2022), "Formation of the Elusive Silylenemethyl Radical (HCSiH$_2$; X^{2}B2) via the Unimolecular Decomposition of Triplet Silaethylene (H$_2$CSiH$_2$; a^{3}A″)" *J. Phys. Chem. A*, vol. 126, no. 21, pp. 3347–3357

[2]   Codella, C. *et al.*(2012), "The CHESS spectral survey of star forming regions: Peering into the protostellar shock L1157-B - I. Shock chemical complexity" *A&A*, vol. 518, p. L112

[3]   Podio, L. *et al.* (2017), "Silicon-bearing molecules in the shock L1157-B1: first detection of SiS around a Sun-like protostar" *Mon. Not. R. Astron. Soc. Lett.*, vol. 470, no. 1, pp. L16–L20

[4]   Lucas, M. *et al.* (2018), "Bimolecular Reaction Dynamics in the Phenyl-Silane System: Exploring the Prototype of a Radical Substitution Mechanism" *J. Phys. Chem. Lett.*, vol. 9, no. 17, pp. 5135–5142

[5]   Zanchet, A. *et al.* (2018), "Formation and Destruction of SiS in Space" *Astrophys. J.*, vol. 862, no. 1, p. 38

[6]   Wlodek, S. (1989) "Gas-phase oxidation and sulphidation of Si$^+$(^{2}P), SiO$^+$ and SiS+" *J. Chem. Soc., Faraday Trans. 2*, vol. 85, no. 10, pp. 1643–1654

[7]   Minh, Y. C. et al. (1989) "Detection of Interstellar Hydrogen Sulfide in Cold, Dark Clouds", *Astrophys J.*, 345 (1), L63-L6

[8]   Accolla, M. *et al.* (2021), "Silicon and Hydrogen Chemistry under Laboratory Conditions Mimicking the Atmosphere of Evolved Stars," *Astrophys. J.*, vol. 906, no. 1, p. 44

[9]   Tinacci, L. *et al.* (2022) "The GRETOBAPE gas-phase reaction network: the importance of being exothermic," *Submitt. to ApJS*

[10]   He, C. *et al.*, (2022), "Gas-phase formation of silicon monoxide via non-adiabatic reaction dynamics and its role as a building block of interstellar silicates" *Phys. Chem. Chem. Phys.*, vol. 24, pp. 19761-19772

[11]   Villeneuve, J. *et al.* (2020), " Silicon isotopic compositions of chondrule silicates in carbonaceous chondrites and the formation of primordial solids in the accretion disk", *Earth &Planet. Sci. Lett.* vol. 542, 116318

---

³ http://udfa.ajmarkwick.net

PHOTO-PROCESSING AND THERMAL DESORPTION OF ACETALDEHYDE, ACETONITRILE, AND WATER ICE MIXTURES ON OLIVINE GRAINS: TPD AND MASS SPECTRA ANALYSES

M. A. Corazzi[1], S. Biancalani[2,1] V. Lino[3], P. Manini[4], G.Poggiali[5], and J. R. Brucato[1]

[1]INAF - Astrophysical Observatory of Arcetri, Largo E. Fermi 5, 50125 Florence, Italy, [2]Department of Physics and Astronomy, University of Florence, Via G. Sansone 1 Sesto Fiorentino (Firenze), I-50019, Italy, [3]Scuola Normale Superiore, Piazza dei Cavalieri 7,56126 Pisa, Italy, [4]Department of Chemical Sciences, University of Naples Federico II, Via Cintia 4, 80126 Naples, Italy, [5]LESIA-Observatoire de Paris, Université PSL, CNRS, Sorbonne Université, Université de Paris, 5 place Jules Janssen, 92190 Meudon, France

Introduction: Over 200 different molecular species have been detected in the interstellar and circumstellar medium to date. Of these, about 50 contain 6 or more atoms including carbon and have been defined by astronomers as interstellar complex organic molecules (iCOMs). Specifically, iCOMs are observed in different star-forming sites, from the earliest stages of star formation [1] to protoplanetary disks [2, 3, 4, 5], the place where planets form. Studying the interactions between complex organic molecules and interstellar dust is fundamental to understanding the physico-chemical mechanisms that lead to the synthesis of complex molecules observed in the gas phase in space.

By pursuing this approach, in laboratory, we succeeded in identifying a set of products formed in ice mixtures of acetaldehyde, acetonitrile, and water deposited on top of a hundred-micron thick olivine layer, and irradiated with UV photons of 4-6 eV energy. The product identification was possible thanks to the combination of Temperature Programmed Desorption (TPD) experiments and Electron Ionization (EI) mass spectrometry analyses.

Through the deep inspection of the products formed from pure ices and binary and ternary ice mixtures, we defined four main reaction pathways occurring due to the combined action of UV irradiation and olivine grains: photodissociation, recombination, isomerization, and hydrogen addition [6]. Overall, these processes account for the formation of molecules already identified in the interstellar medium (i.e., hydroxylamine, hydrogen cyanide, formamide) and also for the formation of key intermediates in the organic content available on Earth for the development of prebiotic chemistry: formamide, acetamide, and urea.

Experimental method: We assembled an ultra-high vacuum (UHV) chamber ($P\sim 6.68 \cdot 10^{-10}$ mbar) with feedthroughs for gas-phase deposition from a prechamber ($P \sim 10^{-7}$ mbar), where the mixtures of molecules were prepared controlling their partial pressure. The UHV chamber interfaces with a Quadrupole Mass Spectrometer for mass spectrometry, with an ARS closed-cycle helium cryocooler able to get a temperature of 11 K, and with a 300 W UV-enhanced Newport Xenon lamp for UV irradiation.

Results: The experiments carried out both for pure ices and for mixtures showed that the mere presence of olivine did not modify the mass spectra. Olivine performed its catalytic action only in the presence of UV radiation. The water dissociation was the main process observed with high levels of hydroxyl radical detected. In the case of UV irradiation and olivine grains, we found peaks relative to methanol (CH_3OH, m/z 32), hydroxylamine (NH_2OH, m/z 33) and acetic acid (CH_3COOH, m/z 60) deriving from recombination processes involving the hydroxyl radical. We can argue that these latter molecules could be detected in star-forming regions where acetaldehyde, acetonitrile, UV radiation and silicates are present and where water is by far the most abundant molecule. Hydroxylamine is of particular interest, amino acid precursor and not yet observed in hot corinos and low mass protostar [7].

Interestingly, despite the presence of water in our ice mixtures, cross- recombination processes involving only the radicals generated by the photodissociation of acetaldehyde and acetonitrile occurred, leading to the formation in the solid phase of iCOMs responsible for the development of prebiotic chemistry, such as formamide ($HCONH_2$ m/z 45), acetamide (CH_3CONH_2 m/z 59) and urea ($NH_2 CONH_2$ m/z 60). A complete picture of the photodissociation, recombination, isomerization, and hydrogen addition reactions is showed in Figure 1 [6], which could represent the possible pathway to assign the peaks revealed by the mass analysis of the UV irradiated ice mixtures on olivine grains. Complex organic molecules such as those detected in our mass spectra are expected to form in the solid phase and then released in the gas phase of different interstellar environments through the combined action of the grain surface which acts as a catalyst for recombination. These types of studies are increasingly important in view of the new discoveries of organic molecules that we expect from the James Webb Space Telescope (JWST), which will be able to observe disks around young stars and to study the presence of organic molecules.
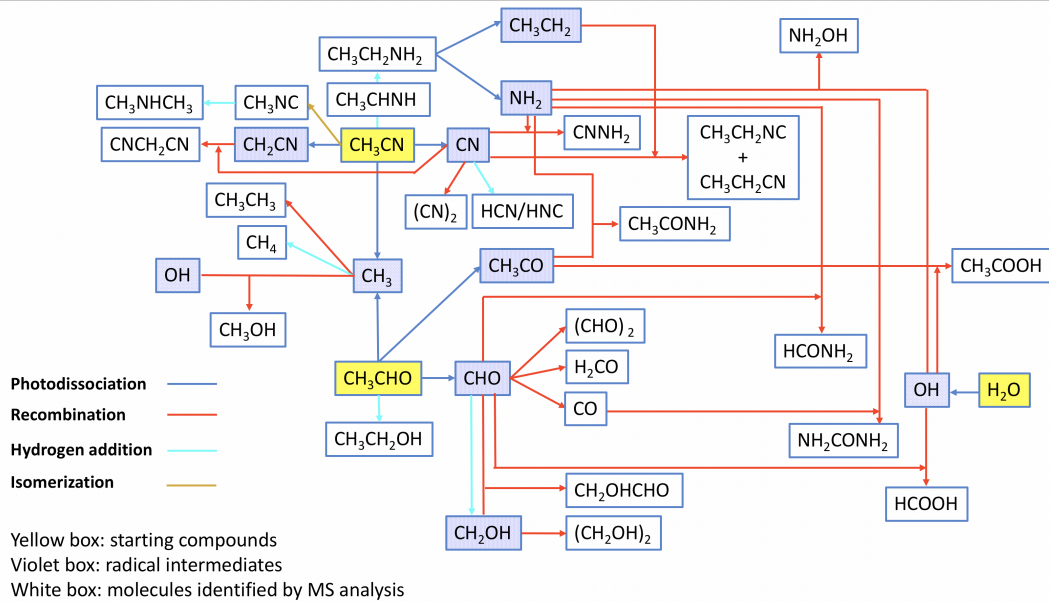
Figura 1 Photodissociation, recombination, isomerization, and hydrogen addition reactions involved in the formation of the peaks revealed by the mass analysis of the UV irradiated ice mixture on olivine grains [6].

References:

[1] Caselli P. and Ceccarelli C. (2012) *The Astronomy and Astrophysics Review, 20,* 56

[2] Walsh C. et al. (2016) *ApJ, 823,* L10

[3]Öberg K. I. et al. (2015) *Nature, 520,* 198

[4] Favre C. et al. (2018) *ApJ, 862,* L2

[5] Brunken N. G. C. et al. (2022) *A&A, 659,* A29

[6] Corazzi M. A. et al. (2022) *MNRAS under review*

[7] Ligterink N. F. W. Et al. (2018) *A&A, 619,* A28

THERMAL DESORPTION OF PA(N)Hs-WATER ICE MIXTURES FROM DUST GRAINS

V. Lino[1,2], Maria A. Corazzi[3], J. R. Brucato[3], G. Davide Fedele[3] and P. Manini[2]

[1]Scuola Normale Superiore, Piazza dei Cavalieri 7,56126 Pisa, Italy
[2]Department of Chemical Sciences, University of Naples Federico II, Via Cintia 4, 80126 Naples, Italy
[3]INAF - Astrophysical Observatory of Arcetri, Largo E. Fermi 5, 50125 Florence, Italy

Introduction: For a long time the interstellar medium (ISM) has been considered an ''inhospitable'' environment where low temperature and density together with intense ionizing radiations may prevent any kind of chemical reactivity. Actually, we know now that the space between the stars hosts a rich palette of molecular species, with the identification of more than 250 compounds, excluding isotopologues.

Polycyclic aromatic hydrocarbons (PAHs) and related aromatic molecules are among the most diffuse interstellar polyatomic molecules known in the gas phase and are thought to account for up 30 % of the universe's molecular carbon.
Their widespread presence is witnessed by the strong and ubiquitous mid-infrared (mid-IR) emission features set at 3.3, 6.2, 7.7, 8.6, 11.3, 12.7 and 17 μm, commonly known as unidentified infrared (UIR) bands.[1-5]

Polycyclic aromatic nitrogen heterocycles (PANHs) which can be formally derived from PAHs by replacing a methylidyne (CH) moiety with an isoelectronic nitrogen atom (N), are also supposed to be present in the ISM, being nitrogen the fourth most abundant element in space. Indeed, they are considered possible carriers of the UIR band at 6.2 μm[6-8] and a reservoir of at least 1–2 % of all cosmic nitrogen. In particular, the detection of purines, pyrimidines, quinolines, isoquinolines and pyridines in carbonaceous meteorites[9] highlighted their likely extraterrestrial formation and survival.
Surprisingly, even though these molecules exhibit a permanent electric dipole moment, which makes them easily detectable by rotational spectroscopy, such heterocyclic molecules have never had any successful detection. To date, only PAH nitriles, such as benzonitrile (C_6H_5CN), 1-cyano-1,3-cyclopentadiene (C_5H_6CN), and 1- and 2-cyanonaphthalene ($C_{11}H_7CN$) have been detected in a cold molecular cloud.[10-12]

Herein, we report for the first time the results of TPD experiments carried out on water ice mixtures of naphthalene ($C_{10}H_8$) or quinoline (C_9H_7N), chosen as representative molecules of the PAHs and PANHs family (structures in Figure 1), condensed on micrometric grains of olivine (($Mg,Fe)_2SiO_4$) at 11K.
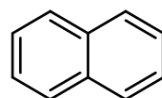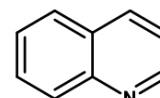
Figure 1. Chemical structures of naphthalene and quinoline.

The main focus of the present work is: a) to shed more light on the mechanisms responsible for the release of PAHs in the gas phase during the protostar formation process; b) to verify if different mechanisms may be envisaged in the desorption process when comparing a PAH *vs* a PANH water ice; c) to delineate the influence of olivine grains on the thermal desorption process. To this aim, temperature-programmed desorption (TPD) analyses were performed allowing for the definition of the thermal desorption temperatures and energies.

References:
[1] Smith J.D.T. et al. (2007) *ApJ,* 656, 770.
[2] Draine et al. (2007) *ApJ,* 663(2) 866-894.
[3] Draine B. T. and Li A. (2007) *ApJ,* 657, 810.
[4] Tielens (2008) *Annu. Rev. Astron. Astrophys*. 46, 289–337.
[5] Allamandola L. J. et al. (1999) *ApJ,* 511, L115.
[6] Hudgins D.G. et al. (2005) *ApJ* 632, 316.
[7] Ricca A. et al. (2021) *ApJ* 923, 202.
[8] Vats et al. (2022), *MNRAS*, 517(4), 5780–5790.
[9] Sephton M.A. (2002) *Nat. Prod. Rep.,* 19, 292-311.
[10] McGuire et al. *Science (*2018) 359(6372), 202-205.
[11] McCarthy et al. *Science* (2021), 371(6535), 1265-1269.
[12] McGuire et al. *Science* (2021), 371(6535), 1265-1269.

THE USE OF THE CORRELATION MATRIX FOR MARTIAN LIFE DETECTION A. Meneghin[1], J.R. Brucato[1], T. Fornaro1 and G. Poggiali[1] and C. D. Author[2], [1]INAF-OAA, andrea.meneghin@gmail.com

Introduction: Samples brought back to Earth from Mars will be placed inside a receiving facility to check for the presence of life. Properly setting up receiving facilities is of extremely interest to the Mars exploration community [1].

Many studies identified the life-correlated biosignatures. The most detailed one is probably the international MSR Objectives and Samples Team (iMOST) study [2], which assessed the expected value of the samples to be collected by the Mars 2020 rover mission. A number of techniques and approaches have been proposed to investigate biosignatures. Wilson et al. [3] proposed a set of instruments to investigate the presence of life and biological risk in samples. Kminek et al. [4] suggested how to organize the analysis sequence. NRC [5] proposed a list of techniques starting from samples general characteristics. Nevertheless, there is the need of an approach able to weighten the importance of the techniques, such as the correlation matrix. Our major driver was to find which techniques are important and which can be optional.

The correlation matrix: The correlation matrix translates the customer needs into plans able to meet those needs. The tool was originally developed in Japan [6] in the 60s of the last century and considerably evolved since then. To build the matrix, the first step is to gather the characteristics and the quality attributes of a product desired by the customer (the VOCs, voice of costumer), then to identify the engineering characteristics (the CTQs, critical to quality) which may be relevant to those desires.

Method application: The correlation matrix we build (Figure 1) correlate the Martian biosignatures with the life detection techniques, by means of a quantitative approach [9]. An earlier step of our correlation matrix, not Martian-centred, was published [7] as a result of the EURO-CARES project [8]. Since then, the iMOST study assessed the most promising Martian biosignatures. This gave us the opportunity to build a new matrix, focused on Mars samples. According to iMOST, the biosignatures were organized into five main categories: morphological, chemical, organic, isotope, mineralogical. Each category was then given an importance rate in order to disentangle how much each biosignature is able to provide us with a greater or lesser proof of the presence of life: the highly diagnostic biosignatures were given a 33% higher importance value with respect to others.

A number of techniques were then identified and the correlation matrix was built.

Figure 1. The correlation matrix between biosignatures and detection techniques

The correlation values between biosignatures and techniques were given in a exponential range: value 0 if no correlation exists (absence of correlation), 1 if the technique is no specific but still gives some information at low resolution (low correlation), 3 if the technique is suitable, although not specific, with medium resolution (medium correlation) and 9 if the technique is very specific technique, with high resolution (high correlation).

It was then possible to start evaluating the techniques. Three indexes were calculated: the Biosignatures Occurrence (the number of biosignatures that can be detected by a single technique), the Techniques Mean Value (the mean correlation of each technique

with the detected biosignatures) and the Techniques Importance (the degree of correlation of a single technique with all the listed biosignatures, as the sum of products of the biosignature importance and the correlation value).

To emphasize the technique importance, a destructive/non-destructive coefficient was introduced: value 1 if destructive, 1.1 if partially, 1.33 if non-destructive.

It was possible to calculate the Techniques Overall Importance, the final degree of correlation of a technique with all the biosignature, as the product of the technique importance and the latter coefficient.

All the input data of the matrix were chosen and quantified through a discussion process that involved a broad number of expert participants.

Main Results: We identified 19 biosignatures, grouped into five categories, 11 of these are highly diagnostic for Martian life.

There are 18 techniques able to detect the biosignatures, with at least one or more high correlation with the biosignatures. The occurrences are in the range between 3 and 12.

The techniques mean values are in the range between 3.6 and 9.0. The mean value of techniques mean values is 6.5. This means that the set of techniques was properly chosen.

The minimum number of techniques able to detect all the biosignatures is 3 (e.g. a combination should be optical microscopy, FTIR and SIMS) but the minimum number of techniques able to detect all the biosignatures, with a high correlation, is 5 (e.g. SEM, MALDI-TOF, GC-MS, TEM XRF). The minimum number of techniques able to detect the highly diagnostic biosignatures, with any level of correlation, is 2 (e.g. a combination should be SEM and LDI-MS).

Table 1. Techniques ranking according to the importance and the overall importance.

Techniques	Importance	Overall importance
LDI-MS	114.8	126.3
MALDI-TOF	114.8	114.8
SIMS	114.8	114.8
FTIR	71.9	95.7
Isotope ratio mass spectrometry (IRMS)	77.9	77.9
GC-MS	75.9	75.9
Optical microscopy	56.9	75.7
XRF	52.3	69.5
Fluorescence microscopy	51.9	69.0
X-Ray CT	51.9	69.0
LC-MS	66.9	66.9
SEM	56.9	62.6
MC-ICP-MS	61.9	61.9
TEM	43.9	58.4
Raman spectroscopy	49.3	54.2
Immuno/enzymatic assay	47.9	47.9
SEM-EDX	40.6	44.7
XRD	11.0	14.6

In terms of importance and overall importance the techniques are ranked as shown in Table 1. The ranking according to the overall importance is different from the one according to the importance, because the destructivity of the techniques is not negligible.

Conclusions: To find a good method to help scientists and designers to build a receiving facility, the major questions we tried to give an answer were: Among the available detecting technologies, how is it possible to choose the ones that are really important? How can this help to organize the activities inside the curation? How is it possible to provide a support for the evaluation of the design choices of the curation?

The correlation matrix is a powerful, adaptable tool: it allows to convert a subjective approach to an objective one, helping to rationalize a problem from the boundaries conditions to the final solution, giving numbers, ranking the information, helping to orientate the decisional process and facilitating the design choices.The matrix can be easily modified and adapted to include new techniques or biosignatures or other valuation idexes, such as the sizing and the layout of the facility, the nature of samples, etc.

References:

[1] Meneghin A. and Brucato J.R. (2021) Preservation of Samples, Sample Return Missions, the Last Frontier of Solar System Exploration. Elsevier, Chapter 17.

[2] Beaty D.W. at al. (2018) The potential scientific value of returned Martian samples: the 2018 iMOST study, 42nd COSPAR Scientific Assembly.

[3] Wilson A, (1999) Exobiology in the Solar System & the search for life on Mars, ESA, ISBN 9290925205

[4] Kminek G. at al. (2014) Report of the workshop for life detection in samples from Mars. Life Sciences and Space Research 2, 1–5..

[5] NRC (2009) Assessment of planetary protection requirements for Mars sample return missions. The National Academies Press.

[6] Akao Y. (1994) Development History of Quality Function Deployment. In QFD The Customer Driven Approach to Quality Planning and Deployment, Asian Productivity Organization, 1st edn, Tokyo, Japan: Asian Productivity Organization, pp. 339–351.

[7] Longobardo a. (2021) Sample return missions, the last frontier of Solar System exploration, Elsevier, ISBN 9780128183311.

[8] Smith C.L. et al. (2021) A Roadmap for a European Extraterrestrial Sample Curation Facility – the EURO-CARES Project, In. Sample Return Missions, the Last Frontier of Solar System Exploration. Elsevier, Chapter 13.

[9] Meneghin A. et al. (2022) Life detection in Martian returned samples: correlation between analytical techniques and biological signatures, International Journal of Astrobiology, 21(5), 287-295.

COMBINED CROSSED-BEAMS AND THEORETICAL INVESTIGATION OF THE O(^{3}P,^{1}D) + ACRYLONITRILE REACTIONS AND IMPLICATIONS FOR EXTRATERRESTRIAL ENVIRONMENTS

G. Pannacci[1*], L. Mancini[1], G.Vanuzzo[1], P. Liang[1], D. Marchione[1], P. Recio[1], Y. Tan[1], M. Rosi[2], D. Skouteris[3], P. Casavecchia[1], and N. Balucani[1]

[1]Dept. of Chemistry, Biology and Biotechnology, University of Perugia, Via Elce di Sotto 8, 06123 Perugia, IT
[2]Dept. of Civil and Environmental Engineering, University of Perugia, Via G. Duranti 93, 06125 Perugia, IT
[3]Master-Tec srl, Via Sicilia 41, 06128 Perugia, IT
[*]e-mail: giacomo.pannacci@studenti.unipg.it

Introduction: Atomic oxygen, both in its ground electronic state (^{3}P) and in its first electronically excited state (^{1}D), triggers numerous reactions in various extraterrestrial environments, such as interstellar medium (ISM), molecular clouds,[1,2] and cometary comas.[3] In particular, the reactions between O(^{3}P,^{1}D) and unsaturated aliphatic[4,5] and aromatic[6,7] hydrocarbons clearly show the dual ability of oxygen atoms to decrease the chemical complexity of the system, by breaking C-C bonds and leading to CO or CO precursors, and to increase the complexity of the species, with the formation of oxygenated organic compounds, also with biological potential. The possibility to know the identity of the primary products of elementary reactions involving atomic oxygen and their relative yields (Branching Fractions, BFs) is of utmost importance for better understanding the rich chemistry of the Universe and for improving astrochemical models.

In this context, we have exploited a well-established combined experimental and theoretical strategy, based on the combination of crossed molecular beams experiments with mass spectrometric detection and time-of-flight (TOF) analysis and theoretical computations of the relevant triplet/singlet potential energy surfaces (PESs) with statistical RRKM/ME (Rice-Ramsperger-Kassel-Marcus/Master Equation) estimates of product BFs, to shed light on the dynamics of the O(^{3}P,^{1}D) + acrylonitrile (CH$_2$CHCN) reactions, being acrylonitrile an important species observed in several interstellar and circumstellar environments.

In particular, from an experimental point of view, the schematic view of the apparatus is shown in Fig. 1 and its characteristics were extensively described elsewhere.[8,9] Briefly, two supersonic beams were crossed at 90° inside a scattering chamber where single collision conditions are achieved thanks to a vacuum system which keeps the chamber at 7×10^{-7} hPa in operating conditions. The very large mean free path of the species simulates the very rarefied conditions of many extraterrestrial environments.

The supersonic beam of oxygen atoms was generated by a radio-frequency (RF) discharge of a O$_2$(5%)/He gas mixture inside a water-cooled quartz nozzle. This source produces oxygen atoms mainly in their ground state ^{3}P ($\geq$90%), but a small percentage ($\leq$10%) of O(^{1}D) is also present,[10] and this allows us to investigate the reaction dynamics of both electronic states of atomic oxygen. The supersonic beam of CH$_2$CHCN was produced by keeping liquid acrylonitrile at a fixed temperature (293 K) and expanding 115 hPa of neat acrylonitrile through a stainless steel (S.S.) nozzle, followed by a S.S. skimmer and a further collimating aperture.

The primary products of the O(^{3}P,^{1}D) + CH$_2$CHCN reactions were ionized by an electron impact ionizer, contained in the third region of a triply differentially pumped, ultra high-vacuum chamber, selected by a quadrupole mass filter, and collected in a Daly-type detector.[11] By rotating the detection unit, the intensity of the products as a function of the scattering angle, namely the angular distribution, was recorded. The product velocity distributions were also measured by inserting a disk with four pseudo statistic sequences of peripheral open-closed slits in front of the detector.
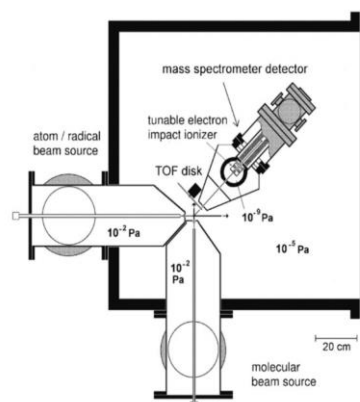
Figure 1. Schematic top-view of the Perugia crossed molecular beam apparatus (reproduced from Ref. 9 with permission from the PCCP Owner Societies).

Information on the micro-mechanism of the O(^{3}P,^{1}D) + CH$_2$CHCN reactions and the partitioning

of the energy of the products between translational and internal degrees of freedom is obtained by moving from the laboratory (LAB) reference frame to the center-of-mass (CM) one by using a forward convolution routine. After the derivation of the CM best-fit angular and translational energy distributions for the various reactive channels, the experimental BF of each primary product was determined by using the procedure outlined by Schmoltner et al.[12]

The experiments were supported by theoretical calculations of the underlying triplet and singlet C_3H_3NO PESs. The geometries of the stationary points were optimized using density functional theory (DFT), with the Becke 3-parameter exchange and the Lee-Yang-Parr correlation (B3LYP) functional,[13,14] and the energies of the optimized geometries were computed at the coupled-cluster level, including single and double excitations and a perturbative estimate of connected triples (CCSD(T)).[15-17] Both methods were used in conjunction with the correlation consistent valence polarized basis set aug-cc-pVTZ.[18-20] The energies were corrected to 0 K by adding the zero-point energy correction computed using the scaled harmonic vibrational frequencies evaluated at the B3LYP/aug-cc-pVTZ level. Furthermore, more accurate calculations for the stationary points involved in the main reactive pathways were performed at the CCSD(T) level corrected with a Density Fitted (DF) MP2 extrapolation (by using Martin's two parameter scheme[21]) to the complete basis set (CBS) and with corrections for core electron excitations. A kinetic investigation (RRKM/ME) was also carried out on the two individual PESs to derive the product BFs at the collision energy of the experiment (E_c = 31.4 kJ/mol) and at the temperatures of various extraterrestrial environments.

For signal/noise (S/N) reasons, we have been able to register angular and TOF distributions only at m/z = 67 (C_3HNO^+), 40 ($C_2H_2N^+$), and 39 (C_2HN^+). The synergistic analysis of the experimental results, the preliminary best-fit functions, the topology of the PESs, and the statistical product BFs allowed us to infer that, among the various energetically allowed reactive channels, the O(^3P) + CH_2CHCN reaction mainly leads to the formation of ketenimine (CH_2CNH) + CO after a nonadiabatic transition (intersystem crossing, ISC) from the entrance triplet to the underlying singlet PES. The same reaction pathway is also reached adiabatically on the singlet PES after the barrierless addition of O(^1D) to the C=C bond of acrylonitrile. A minor contribution of the HCOCHCN + H reactive channel is also observed in the O(^3P) + CH_2CHCN reaction, when it evolves adiabatically on the triplet PES.

Due to the presence of an entrance potential energy barrier of ~7 kJ/mol in the O(^3P) + CH_2CHCN reac-

tion, the present study can enrich our knowledge of the O(^3P) reactivity in warm extraterrestrial environments where acrylonitrile has also been detected, such as the hot molecular core Sgr B2(N),[22,23] the circumstellar envelope of the C-rich star IRC+10216,[24] and, possibly, the upper atmosphere of Titan,[25] where some oxygen is present.[26] Furthermore, the elucidation of the O(^1D) + CH_2CHCN reaction dynamics can contribute to improve the models related to interstellar ices[27] and cometary comas.[3]

References: [1] Occhiogrosso A. et al. (2013) *MNRAS, 432,* 3423–3430. [2] Skouteris D. et al. (2018) *Astrophys. J., 854,* 135 (10 pp). [3] Cordiner M. A. and Charnley S. B. (2021) *MNRAS, 504,* 5401–5408. [4] Fu B. et al. (2012) *J. Chem. Phys., 137,* 22A532–1-22. [5] Leonori F. et al. (2015) *J. Phys. Chem. C, 119,* 14632-14652. [6] Vanuzzo G. et al. (2021) *J. Phys. Chem. A, 125,* 8434–8453. [7] Recio P. et al. (2022) *Nat. Chem., 14,* 1405–1412. [8] Casavecchia P. et al. (2015) *Int. Rev. Phys. Chem., 34,* 161-204. [9] Casavecchia P. et al. (2009) *Phys. Chem. Chem. Phys., 11,* 46–65. [10] Alagia M. et al. (1997) *Isr. J. Chem., 37,* 329–342. [11] Daly N. R. (1960) *Rev. Sci. Instum., 31,* 264–268. [12] Schmoltner A. M. et al. (1989) *J. Chem. Phys., 91,* 6926–6936. [13] Becke A. D. (1993) *J. Chem. Phys., 98,* 1372-1377. [14] Stephens P. J. et al. (1994) *J. Phys. Chem., 98,* 11623-11627. [15] Barlett R. J. (1981) *Annu. Rev. Phys. Chem., 32,* 359-401. [16] Olsen J. et al. (1996) *J. Chem. Phys., 104,* 8007-8015. [17] Raghavachari K. et al. (1989) *Chem. Phys. Lett., 157,* 479-483. [18] Dunning T. H. Jr. (1989) *J. Chem. Phys., 90,* 1007-1023. [19] Woon D. E. and Dunning T. H. Jr. (1993) *J. Chem. Phys., 98,* 1358-1371. [20] Kendall R. A. et al. (1992) *J. Chem. Phys., 96,* 6796-6806. [21] Martin J. M. L. (1996) *Chem. Phys. Lett., 259,* 669-678. [22] Nummelin A. and Bergman P. (1999) *Astron. Astrophys., 341,* L59-L62. [23] Müller H. S. et al. (2008) *J. Mol. Spectrosc., 251,* 319-325. [24] Agúndez M. et al. (2008) *Astron. Astrophys., 479,* 493-501. [25] Palmer M. Y. et al. (2017) *Sci. Adv., 3,* 1700022. [26] Martens H. R. et al. (2008) *Geophys. Res. Lett., 35,* L20103 (4 pp). [27] Bergner J. B. et al. (2019) *Astrophys. J., 874,* 115 (16 pp).

COMPUTED BINDING ENERGIES DISTRIBUTION OF RELEVANT S-BEARING SPECIES AT INTERSTELLAR ICY GRAINS

V. Bariosco,[1] S. Pantaleone,[1,] A. Germain,[1] L. Tinacci,[1,2] M. Corno[1] and Piero Ugliengo[1], [1]Dipartimento di Chimica and Nanostructured Interfaces and Surfaces (NIS) Centre, Università degli Studi di Torino, via P. Giuria 7, I-10125, Torino, Italy (vittorio.bariosco@unito.it), [2]Université Grenoble Alpes, CNRS, Institut de Planétologie et d'Astrophysique de Grenoble (IPAG), F-38000 Grenoble, France.

The formation steps of a Sun like planetary system, which occur starting from dense clouds, are always accompanied by an enrichment of the chemical complexity of the interstellar medium (ISM). This complexity, once star and planets are created, could be inherited onto meteorites, asteroids and finally planets, perhaps triggering the emergence of life [1]. ISM is unevenly scattered with gaseous species and submicron-sized grains.

In the dense clouds due to the low temperatures (T=5-10K) dust grains are covered by freeze out/adsorbed molecules, which can react with other species thus leading to an increase in the chemical complexity of the ISM. Binding energies (BEs) are crucial parameters to understand the evolution of the chemical species in the ISM, determing wheter or not a species is frozen onto the grain surfaces or free to desorb to the gas phase. Nowadays, both experimental and theoretical procedures usually provide point values of the BE associated to each molecule. This is a critical constrain considering the predominant amorphous nature of the ices enveloping the interstellar grains [2]. Clearly, the amorphicity gives rise to a great ensemble of possible adsorption sites, each with distinct values that generate a BE distribution. Until now, no open access grain models are available to astrochemical community; several models have appeared in the literature, however, lacking a correct physical and systematical description. Recently, ACO-FROST, an automatic procedure to simulate realistic grains has been released [3]. This code allows to build models of amorphous water up to 1000 molecules apt to mimic interstellar icy grains. On top of this grain, the program generates a grid, as dense as the user desires, whose points can be substituted with selected molecules in order to compute the BE distribution of the species of interest, see Figure 1. Tinacci et al [4], used this procedure to computed the BE distribution of ammonia with more than 160 different adsorption sites and obtained unprecedent results thanks to the variety of chemical interactions taken into account.

In the present work, the aforementioned combined procedure was slightly modified and extended to S-bearing species, i.e., CS, CH_3SH, H_2CS, H_2S and OCS. S-species were selected in order to contribute to a long standing issue in the field: the sulphur depletion problem [5]. Indeed, with this work, we want to provide high quality results of S-species on amorphous icy surface, which can be used as input data in the astrochemical models aimed at rationalizing observations and laboratory experiments. Therefore, an icy water grain of 200 molecules was optimized using the program xTB, in the specific the GFN2 semiempirical tight-binding Hamiltonian [6]. After that, a grid of 162 point was generated around the grain, and each point was substituted by the S-species and projected nearer to the surface. In the end, the BEs distribution was computed with the ONIOM procedure [7], where the low level method is GFN2, used for almost all the icy grain, while the adsorbates plus a portion of the surface were studied with the high level composite method r^2SCAN-3c [8].
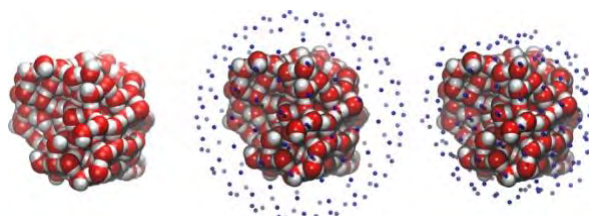
Figure 1: (left) Icy grain model of 200 molecules, (center) grain with overlapped 162 grid points shown in blue and (right) model with the points projected closer (2.5–3 Å) to the surface. Legend: oxygen in red, hydrogen in white.

References:
[1] Caselli P. and Ceccarelli C. (2012) *Astron Astrophys Rev, 56, 20, 1-68.* [2] Boogert A. et al. (2015) *Annu. Rev. Astron. Astrophys, 53,* 541-581. [3] Germain A., Tinacci L., Pantaleone S., Ceccarelli C. and Ugliengo P. (2022) *ACS Earth Space Chem, 6,* 1286-1298. [4] Tinacci L., Germain A., Pantaleone S., Ferrero S., Ceccarelli C. and Ugliengo P. (2022) *ACS Earth Space Chem, 6,* 1514-1526. [5] Wakelam V. et al. (2004) *Astron. Astrophys, 422,* 159-169. [6] Bannwarth C., Ehlert S. and Grimme S. (2019) *J. Chem. Theory Comput., 15,* 1652-1671. [7] Svensson M. et al. (1996), *J. Phys. Chem., 100,* 19357-19363. [8] Grimme S. et al. (2021) *J. Chem. Phys., 154, 064103,* 1-18.

TESTING ALTERNATIVE THEORIES OF GRAVITY WITH THE BEPICOLOMBO MISSION: THE CASE OF BRANS-DICKE THEORY.
M. Falletta[1], G. Schettino[1-2], G. Tommei[1]. [1] Dipartimento di Matematica, Università di Pisa, Largo Bruno Pontecorvo 5, 56127 Pisa, Italy; [2] IFAC – CNR, Via Madonna del Piano 10, 50019 Sesto Fiorentino (FI), Italy; miriam.falletta@phd.unipi.it (M.F.), g.schettino@ifac.cnr.it (G.S.), giacomo.tommei@unipi.it (G.T.).

The Mercury Orbiter Radio science Experiment (MORE) is one of the experiments on board the ESA/JAXA BepiColombo mission to Mercury. The experiment consists of an on-board transponder capable to provide very precise tracking measurements, by acquiring radio signals received from a number of on-ground antennas, thus allowing to determine with a very high accuracy the mercurycentric orbit of the spacecraft and the heliocentric orbit of Mercury and the Earth. This, in turn, will provide a better understanding of the geodesy and geophysics of Mercury, on one side, and of fundamental physics, on the other (see [1]).

One of the main scientific objectives of MORE is the so-called "relativity experiment", which consists in performing an accurate test of relativistic theories of gravitation. Indeed, the primary goal of the relativity experiment is to determine with improved accuracy the values of some of the post-Newtonian (PN) parameters and other related quantities, thus allowing to test the validity of theories of gravity that modify or extend Einstein's theory of General Relativity (see, e.g., [2], [3]).

We focus on the particular case of Brans-Dicke theory as a first modification of the standard General Relativity theory. Brans-Dicke theory was formulated by C. Brans and R. H. Dicke in 1961 in order to implement the idea that the Newtonian gravitational constant might actually not be a constant and therefore might vary with space and time [4]. In particular, the predictions of Brans-Dicke theory directly depend on the value of an adimensional parameter, the coupling constant ω. In the case of the Brans-Dicke theory, the Eddington PN parameter γ is a function of the coupling constant ω: as a consequence, in Brans-Dicke theory the parameter γ takes a different value with respect to the predictions of General Relativity, where γ is expected to be unity (see, e.g., [5]).

We tackle the problem of testing Brans-Dicke theory by means of the MORE relativity experiment. To this aim, we present the results of a set of simulations of the MORE relativity experiment. The simulations have been performed with the orbit determination software ORBIT14, developed by the Celestial Mechanics Group of the University of Pisa for the analysis of the data of the BepiColombo radio science experi-ment [6]. The purpose of the simulations is to determine the level of accuracy up to which the Brans-Dicke theory can be tested with the MORE relativity experiment. This can be done, in turn, by determining the expected accuracy in constraining the coupling constant ω. To this aim, we devised a sensitivity study consisting in varying the preliminary accuracy by which γ can be determined and studying the corresponding variation in the estimate of ω, as it can be determined by MORE. We therefore show that Brans-Dicke theory should be suitably constrained thanks to the MORE relativity experiment.

References: [1] Iess L. et al. (2021) *Space Sci. Rev., 217(1),* 21. [2] Schettino G. and Tommei G. (2016) *Universe, 2(3),* 21. [3] Schettino G. et al. (2020) *Universe, 6(10)*, 175. [4] Brans C. and Dicke R. H. (1961) *Phys. Rev., 124,* 925–935. [5] Will C. M. (2014) *Living Rev. Relativ., 17,* 4. [6] Lari G. et al. (2022) *Experimental Astronomy, 53(1),* 159-208.

DISCOVERY OF THE TOI-411 SYTEM: A SUPER-EARTH AND TWO SUB-NEPTUNES ORBITING A BRIGHT, NEARBY, SUN-LIKE STAR. Laura Inno[1,2], Luca Cacciapuoti[3,4], Giovanni Covone[4,5,2], Veselin B. Kostov[6], Thomas Barclay[7] et al. (for a complete author list see Cacciapuoti et al, 2022, A&A 668, A85). [1]Science and Technology Department, Parthenope University of Naples, CDN IC4, 80143 Napoli, Italy; [2]INAF-Osservatorio Astronomico di Capodimonte, Salita Moraliello, 16, 80131 Napoli, Italy; [3]European Southern Observatory, Karl-Schwarzschild-Strasse 2, 85748 Garching bei Munchen, Germany; [4]Department of Physics "Ettore Pancini", University of Naples, Fed- erico II, 80138 Napoli NA, Italy;[5]INFN, Sezione di Napoli, Strada Comunale Cinthia, 80126 Napoli NA, Italy; [6]NASA Goddard Space Flight Center, Exoplanets and Stellar Astro- physics Laboratory (Code 667), Greenbelt, MD 20771, USA and University of Maryland, Baltimore County, 1000 Hilltop Circle, Baltimore, MD 21250, USA

Introduction: Multi-planetary systems are ideal laboratories to test theories of planet formation and evolution, since they allow for comparative analysis of objects with a common origin and environment. The Transiting Exoplanet Survey Satellite (TESS [1]) has been particularly efficient in identifying similar opportune systems, contributing, together with its predecessor, Kepler, to discover over 800 of them.

Here, we present the discovery reported in [2] of a multi-planetary system consisting of a super-Earth and two sub-Neptune-sized planets orbiting the bright (V≈8.3 mag), nearby (63 pc), Sun-like star HD 22946, indicated also as TOI-411.

Host star proprieties: In the transit method, the proprieties of the planets are derived from observations relatively to the corrisponing ones of the host star. Therefore, characterizing the host star in termis of its mass, $M_\star$, radius, $R_\star$, and effective temperature, T_{eff}, is critical. We took advantage of all the available astrometric, photometric and spectroscopic observations of the system, and we constrained the physical parameters of HD 22946 by performing both SED fitting and spectrosynthesis. We found that the host star is a late-type F main sequence star, with T_{eff} = 6040 ± 48 K, $M_\star$ =1.104± 0.012 $M_\odot$, and $R_\star$ = 1.157 ± 0.025 $R_\odot$[2].

Detection and characterization of the planet candidates: TESS observed HD 22946 in sectors 3 and 4 during its primary mission (2018-2020), and in sectors 30 and 31, during the extended mission (2020-to date). In these data, two planet candidates of period 9.57 days (planet *c*) and 4.04 days (planet *b*) were already identifyied by the automated Science Processing Operation Center pipeline [3]. By applying the Transit Least Square method [4], to the extracted aperture photometry, we were able to confirm these two candidates and recover an additional single transit-like signal, likely related to a third planet with a longer period of about 46 days.

By modeling the transits with EXOPLANET[5], we determined the planet radii: 1.48 ± 0.06 $R_\oplus$ for planet *b*, 2.35 ± 0.08 $R_\oplus$ for planet *c*, and 2.78 ± 0.13 $R_\oplus$ for planet *d*.

Validation of the planet candidates: While the nature of the single event cannot be verified as follow-up data is not yet available, we vetted the two inner exoplanets. We used the pipelines DAVE[6], VESPA[7], and TRICERATOPS[8] to exclude false-positive scenarios or determine that the false-positive probability is negligible, whilst we used the TESS-Followup program [9] photometry and high-resolution imaging to rule out faint bound companions and foreground, background, or nearby eclipsing binaries that could contaminate the TESS light curve. Therefore, we validated the discovery of planets *b* (or ***TOI-411.02***) and *c* (or ***TOI-411.01***), while we plan to collect additional data (radial-velocity curve and photometric follow-up observations) in order to further confirm the nature of candidate planet *d* (or ***TOI-411.03***)

The planetary system proprieties: TOI-411 *b*, with an inferred mass of ~3.5 M is a hot super-Earth [10] populating the so-called Fulton gap [11], a transition region from rocky worlds with a high-molecular-weight atmosphere, to low-density worlds dominated by a H/He gaseous envelope.

With an equilibrium temperature of about 1000 K, TOI-411 *c* is a hot sub-Neptunian, capable of hosting a tick atmosphere potentially observable with JWST. Moreover, we used dynamical simulations to investigate the dynamics of this sytem and found that it could possibly host at least one more planet between *c* and *d* without compromising its dynamical stability.

Conclusions: We conclude that HD 22946 hosts one small planet stripped of its atmosphere (or with a secondary, accreted atmosphere), two larger planets at significantly different temperatures, and probably yet-to-be-discovered intermediate ones.

The study of this system offer fundamental insights to reach a better understanding of the formation pathways that can lead to similar multi-planetary systems. Moreover, by hosting such a bright star, it provides the perfect target for synergetic observations from space- (e.g. CHEOPS) and ground-based (e.g. ESPRESSO@VLT) facilities in order determine the planets' bulk density, and for JWST to investigate the possible presence of an atmosphere around TOI-411 *c*.

References: [1] Ricker, G. R., Winn, J. N., Vanderspek, R., et al. 2015, *JATIS*, 1, 014003; [2] Cacciapuoti, L., Inno, L., Covone, G., Kostov, V.B., Barclay, T., Quintana, E.V., et al. 2022, *A&A,* 668, A85; [3] Jenkins, J. M., Twicken, J. D., McCauliff, S., et al. 2016, *SPIE Conf. Ser.*, 9913,99133E; [4] Hippke, M., & Heller, R. 2019, *A&A*, 623, A39; [5] Foreman-Mackey, D., Luger, R., Agol, E., et al. 2021, *J. Open Source Softw.*, 6,3285; [6] Kostov, V. B., Mullally, S. E., Quintana, E. V., et al. 2019, *AJ*, 157, 124;[7] Morton, T. D. 2015, *Astrophysics Source Code Library;* [8] Giacalone, S., & Dressing, C. D. 2020, *Astrophysics Source Code Library;* [9] Fressin, F., Torres, G., Charbonneau, D., et al. 2013, *ApJ*, 766, 81; [10] Fulton, B. J., Petigura, E. A., Howard, A. W., et al. 2017, *AJ*, 154, 109

SETI within 30 parsecs from Earth

G.Chiaro   Chiaro⋆,1
Institute of Space Astrophysics and Cosmic Physics, Via A. Corti 12, 20133 Milano, Italy

Abstract:

What are we looking for in SETI? What gratifies us the most? Is it enough to know that we are not alone or, better, to seek a relationship with other civilizations? The answers to these questions lead to two different SETI strategies. The first aims to detect technological signals confirming the existence of other civilizations regardless of who they are and where they are. Therefore, the answer is: are we alone? Yes or no.
On the other hand, an alternative strategy assumes the possibility of a relationship. Will we ever be able to dialogue with another extraterrestrial civilization? This study considered the possibilities of success by analyzing solar-like exoplanetary systems within 30 parsecs from Earth. Considering the known physical parameters and the environmental conditions of in G – type and M – type star planetary systems, we hypothesized the reasons that could have prevented the formation of life and the consequent failure
of the SETI research.
The novelty in this study is the analysis of the required environment for an exoplanet able to host an intelligent civilization based on the Earth model. Attention to exoplanets within 30 parsecs of Earth is due to consider a two-way communication between transmitter and receiver in a reasonable time.

References:

Anglada-Escud´e G.et al., 2016, Nature, vol. 536, 7617, 437–440
Anglada-Escudel G. et al.,2013, A%A, 2013
Bains W., 2004, Astrobiology, 4,2,137
Bains w. et al., 2021, Life, 11,5
Burchell M.J., 2006, Astrobiology, 5 243
Basilevsky A.T. at al.,2003, Rep. Prog. Phys. 66 (10), 1699–1734.
Edgeworth K.E., 1946, Nature, 157 (3989), 48

Fauchez J et al., 2020, Geosci. Model Dev., 13, 707-716
Firsoff A.V., 1962, Discovery, 23, 36
Fujii J. et al., 2017, ApJ, 848, 100
Grimm S. et al., 2018, arxiv 1802.01377
Hand K.P. et al., 2020, Space Sci Rev., 216, 95
Hart M.H. et al, 1982, Pergamon Press, 182
Hendrix A.R. et al., 2019; Astrobiology, 19, 1-27
Kaltenegger L. et al., 2021, Nature, 594, 505–507
Kasting, J. F. et al. (1993), Icarus, 101, 108
Knutson H. et al., 2014, arxiv 1403.4602
Irwin L.N., 2018, Handbook of Exoplanets, Springer Ed., 3375
Jones E.M., 1985, Los Alamos Report663
Larson C.A. et al., 2013,JPR, 35, 1154
Manhesa G. et al., 1980, Earth and Planetary Science Letters 473, 370–382.
Mengel J.G. et al, 1979, ApJ Supplement Series,40, 733
Nagel T., 2012, Oxford Univ. Press, Mind and cosmos
Patterson C. et al. ,1955, Science. New Series, 121, 3134.
Ramirez R.M. et al., 2018, ApJ, 858,2
Sagan C. et al., 1997, Scientific American, 6,1
Schulze Makuch D. et al., Astrobiology, 20, 12
Schulze Makuch D. et al., Astrobiology,11, 1041
Schulze Makuch D. et al., 2004, Life in the Universe, Springer Ed.
Seager S. et al. , 2007, arxiv 0707.2895
Seager S. et al., 2010, A&A, 48,631
Seager S. et al., 2012, Astrobiology, 12, 1
Seager S. et al., 2013, Science, 340, 577
Seager S., 2018, Astrobiol. 17,
Wandel A., 2019, arxiv 1906.077046
Zechmeister M.et al.,2019, A%A, 627, A49
MNRAS 000, 000–000 (2022)

DART-VETTER: A DEEP LEARNING TOOL FOR AUTOMATIC VETTING OF TESS CANDIDATES.

S. Fiscale[1] , L. Inno[1,6], A. Rotundi[1,2,3], A. Ciaramella[2], G. Covone[4,6], L. Cacciapuoti[5], P. De Luca [1] , A. Galletti[1,2] , F. Gallo[4] , R. M. Ienco[4] , C. Magliano[4] , L. Marcellino[2], M.T. Muscari Tomajoli[1], L. Tonietti[1] , A. Vanzanella[2] .

[1] UNESCO Chair "Environment, Resources and Sustainable Development, Department of Science and Technology, Parthenope University of Naples, Italy. stefano.fiscale001@studenti.uniparthenope.it,
[2] Department of Science and Technologies, Parthenope University of Naples, Naples, Italy,
[3] INAF-Istituto di Astrofisica e Planetologia Spaziali, Rome, Italy,
[4] Department of Physics "Ettore Pancini", University of Naples Federico II, Naples, Italy,
[5] European Southern Observatory, Karl-Schwarzschild-Strasse 2 D-85748 Garching bei Munchen, Germany,
[6] INAF-Osservatorio Astronomico di Capodimonte, Salita Moraliello, Naples, Italy.

Topic*: Pianeti e sistemi planetari extrasolari: Esopianeti.*

Introduction: The detection of new planets outside the Solar System - or exoplanets - is one of the most active and exciting current research fields. In the last two decades, more than 5,000 exoplanets have been discovered. Modern exoplanet surveys are performed with efficient and effective telescopes thanks to the advancement of hardware and software technologies. In its nine years of mission, NASA's space mission Kepler continuously observed the luminosity emitted by ~200,000 stars in a portion of the Milky Way. Kepler was designed to detect exoplanets by means of the transit method, i.e. looking for periodic decreases, or events, in the observed flux of a star. The human-based visual analysis, or vetting, of these events resulted in the discovery of more than 2,600 exoplanets. NASA led off to the Transiting Exoplanet Survey Satellite (TESS) mission in 2018 thus replacing Kepler. TESS is looking for events in the luminosity emitted by a set of target stars distributed in the entire sky by means of the transit method [1]. TESS is collecting a huge amount of data with respect to its predecessor providing us ~1,000,000 new stars light curves each month from its Full Frame Images [2].

The visual detection of exoplanets: The vetting of the thousands of events detected in these light curves is unsustainable in time terms. A team of expert astronomers could take from a few hours up to several weeks to determine the nature of a single event due to: a planet candidate (PC), an eclipsing binaries (EB), an instrumental systematic (IS) or stellar variability (V). Such amount of involved time is mainly due to two reasons: (i) the high rate of false positives because of the similarity between events due to a PC and those related to an EB; (ii) the lack of objectivity in the vetting process, i.e. two or more astronomers might disagree on the nature of a given event.

Automatic vetting: Machine Learning (ML) approaches have become an attractive alternative to human vetting thanks to their effective and efficient data analysis. Here, we present a ML approach based on Deep Neural Networks to perform a binary classification of the events present in TESS data, in planet candidate and not-planet candidate (including EB, IS, V). More specifically, we deployed a Convolutional Neural Network (CNN) whose architecture is based on the work proposed by [3]. Our network features ~1,900,000 parameters that need to be optimized during the network training process in order to achieve an effective events classifier. For this reason, our network needs to learn from a large training set. We decided to use both Kepler data and TESS data. Our training set consists in a subset of events detected in Kepler [4] and TESS [2] light curves. The nature of each of these events is already known because it has been analyzed across the years by different research groups [5][6]. However, an a-priori application of a process, known as domain adaptation, is required when exploiting data collected by different surveys. To this aim, we deployed a distributed pre-processing pipeline in order to standardize the underlined events before feeding them to the network. To further expand the dimension of our training set we applied data augmentation techniques on the standardized input events. Like in [7], we used ML regularization techniques such as Dropout and Batch Normalization to minimize the generalization error (e.g. the error on test set).

Experimental results: Our CNN has a precision of 87% and a recall of 90% when applied on the thousands of events provided in the catalogs [8] and [2]. By processing these events in a few milliseconds our network is many orders of magnitude faster with respect to a team of astronomers. During the presentation I will show and provide details about: (i) the underlined

experimental results; (ii) the architecture of our neural network; (iii) the application of our network to the identification of potential Earth-like planets from the TESS events characterized in [9].

References: [1] Ricker, G., et al (2014). *Journal of Astronomical Telescopes, Instruments, and Systems*, *1*(1), 014003. [2] Yu, L., *et al.* (2019). *The Astrophysical Journal, 158(*25). [3] Simonyan K. *et al.* (2014). *arXiv preprint arXiv:* 1409.1556. [4] Coughlin, J., et al. (2016). *The Astrophysical Journal Supplement Series*, *224*(1), 12. [5] Morton, T. D., et al. (2016). *The Astrophysical Journal*, *822*(2), 86. [6] Mullally, F., et al. (2016). *Publications of the Astronomical Society of the Pacific*, *128*(965), 074502. [7] Olmschenk, G., et al. (2021). *The Astronomical Journal*, *161*(6), 273. [8] Akeson, R., et al. (2019). In *American Astronomical Society Meeting Abstracts# 233* (Vol. 233, pp. 140-09). [9] Kaltenegger, L., et al. (2019, ApJL, 874, L8).

PETRO-MINERALOGICAL AND GEOCHEMICAL STUDY OF LUNAR METEORITE NWA 13859 R.

Avanzinelli[1*], M. Casalini[1*], T. Cuppone[1], G. Pratesi[1], A. Langone[2], C. Carli[3] and F. Tosi[3], [1]Dipartimento di Scienze della Terra, Univeristà degli Studi di Firenze, Via G. La Pira 4, 50121 Firenze (*corresponding authors: riccardo.avanzinelli@unifi.it, martina.casalini@unifi.it), [2]CNR - Istituto di Geoscienze e Georisorse, U.O.S. di Pavia, Via Ferrata 1, 27100 Pavia, [2]INAF-IAPS Istituto Nazionale di AstroFisica - Istituto di Astrofisica e Planetologia Spaziali, Via del Fosso del Cavaliere 100, 00133 Roma.

The composition of the lunar crust provides key information on the petrological evolution of the Moon. Studies mostly based on analyses of Apollo samples revealed the presence of two main groups of rocks [1]: i) Ferroan Anorthosites (FAN), characterized by >90% high-An plagioclase and mafic minerals with Mg# = Mg/(Mg + Fe) < 75, and ii) Mg-suite, characterised by plagioclase with decreasing anorthite content (An$_{97-85}$), coupled with high, yet decreasing, Mg# (90-65). The presence of these two well defined groups represents one of the main evidence supporting the the Lunar Magma Ocean hypothesis [2]. Data from lunar meteorites, which may better represent the compositional and mineralogical variability of the lunar surface, have shown the presence of a more widespread compositional range leading to a reevaluation of the Lunar Magma Ocean model [3]. However, the "pristine" character of lunar meteorites has been questioned as they may represent impact-mixtures [4].

In the framework of the MELODY project, we investigated the lunar meteorite NWA 13859, a polymict feldspatic breccia made up by several lithic clasts of variable lithologies (anorthosites, gabbric anorthosites, troctolites, anorthositic norites, gabbric norites) surrounded by a fine grained and sometimes glassy matrix.

Major and trace elements of the mineral phases within the clasts and the matrix glass have been analysed by Electron Microprobe (EMPA) and Laser-Ablation ICPMS (LA-ICPMS). The major elements composition of plagioclase crystals of the different clasts shows a limited variability ranging from An$_{95}$ to An$_{98}$. The Mg# of mafic minerals displays a larger variability ranging from 53 to 88. Few clasts (mainly gabbroic anorthosites and anorthositic norites) fall within the field of FAN, whilst gabbroic norites have mafic minerals with high Mg#, sometimes reaching the composition typical of Mg-rich suites. However, most of the data (from all the lithologies) fall at intermediate Mg# values. Matrix glasses have major elements compositions broadly resembling the average of the mineral phases of the clasts.

Rare earth elements (REE) in plagioclase were present in abundances from ~0.1 to approximately 5× chondritic (CI) values, consistent with previous data on felspatic lunar meteorites [5]. Light REE (LREE) are slightly enriched with respect to Heavy ones (HREE) and every plagioclase exhibits a positive Eu-anomaly, with Eu abundances of up to approximately 20×CI. Pyroxene shows higher REE contents between ~1 and ~15×CI, with higher HREE and ubiquitous Eu negative anomalies.

Contents of compatible elements such as Ni, are higher in olivine than in plagioclase and pyroxene, with the lowest values generally found in FAN clasts.

Matrix glasses have REE abundancies from ~3 to ~7×CI and Eu positive anomalies, similar to those of plagioclase. In particular LREE are, on average, higher than those of all the other mineral phases hosted in the lithic clasts. Similarly, Ni contents of matrix glasses are high, similar to those of olivine. The trace element composition of matrix glasses is compatible with an origin as impact melts derived from the sum of the various mineral phases making up the clasts. However, their high Ni and REE contents indicate a contribution from extralunar material related to the impactor that blasted the meteorite off the Moon, or to micrometeorites associated with regolith gardening and maturation [6].

Overall, our data suggest that the contribution of exogenous material in the meteorite NWA 13859 is mainly concentrated in the matrix glass, whilst the single clasts (and the minerals within them) may preserve the composition of the original lunar crust.

References: [1] Warren, P. H. (1993) *Am. Mineral, 78(3-4)*, 360-376. [2] Wood, J. A. et al. (1970) *Proc. Lunar Sci. Conf. 1st*, 965-988. [3] Gross, J et al. (2014) *Earth Planet. Sci. Lett, 388*, 318-328.[4] Warren, P.H., (2012) *2nd Conf. Lunar Highlands Crust*, A9034. [5] Russel, S. S. et al., (2014) *Phil. Trans. R. Soc.* A372: 20130241. [6] Korotev, R. L. et al (2003) *Geochim. Cosmochim. Acta 67(24)*, 4895-4923.

EARLY DIFFERENTIATION OF PLANETESIMALS: INSIGHTS FROM MELTING EXPERIMENTS OF AN L6 ORDINARY CHONDRITE. M. Masotta[1], S. Iannini Lelarge[1], L. Folco[1], L. Pittarello[2], L. Mancini[3]

[1]Dipartimento di Scienze della Terra, Università di Pisa, Via Santa Maria 53, Pisa, Italy (matteo.masotta@unipi.it), [2]Natural History Museum Vienna, Mineralogisch-Petrographische Abteilung, Burgring 7, 1010 Vienna, Austria, [3]Elettra-Sincrotrone Trieste, S.S. 14 - km 163.5, Area Science Park, 34149 Basovizza, Trieste, Italy

Introduction: Planetary differentiation in small bodies is believed to be ruled by several partial end-states that were dominated by variable degrees of melting and fractionation of the metallic and silicate phases. Studying the melting behaviour of undifferentiated chondritic materials is pivotal for reconstructing differentiation processes occurring during the early evolution of planetesimals and, eventually, leading to the formation of rocky planets and partially differentiated asteroids. In this study, we present results from melting experiments performed at 1 GPa, using an L6 ordinary chondrite (DAV 01001).

Results: At the temperature of 1100 °C, the initial chondritic texture is preserved and melting of silicate minerals is not observed, while the opaque phases (kamacite, taenite and troilite) react forming two immiscible liquid phases, a FeNi metal phase and a S-rich phase. Melting of the silicate domain initiates at 1200 °C and slightly increases with temperature, yielding to a progressive obliteration of the chondrules and textural re-equilibration of the silicate assemblage (recrystallization at mineral-melt interfaces and within the melt). No substantial textural changes are observed for the FeNi metal and S-rich phase upon further temperature increase, with the FeNi metal phase typically forming spherical or cruciform blebs enveloped by the S-rich phase. The non-modal melting of the silicate mineral assemblage (in the order: plagioclase > high-Ca pyroxene > low-Ca pyroxene > olivine) and subsequent re-crystallisation determines the evolution of the silicate melt from a dominantly trachy-andesitic composition at 1200 °C, to basaltic trachy-andesitic at 1300 °C and andesitic at 1400 °C. The composition of the silicate melt produced in the experiments shows analogies with the trachy-andesitic and andesitic bulk compositions of some anomalous achondrites, whereas the compositional variation of the silicate minerals compares well with that of several achondrite groups, such as pallasites, acapulcoites, lodranites, ureilites, brachinites and IAB inclusions.

Discussion: At the experimental conditions, the FeNi metal and S-rich liquids are always immiscible and the surface tension-dominated regime causes the FeNi metal to be preferentially wet by the S-rich phase, remaining thus insulated from the silicate domain. Under such circumstances, the partitioning of siderophile elements into the metal phase is expected to be limited by the presence of the S-rich phase, which acts as a chemical barrier reducing the exchange of these elements between the silicate and FeNi metal phases. This is consistent with the "excess" of siderophile elements in the Earth's mantle, relative to the abundance expected from complete core-mantle equilibration. Overall, melting experiments suggest that small degrees of melting and re-crystallisation under magmatic conditions could have been dominant processes at the onset of planetesimal differentiation, explaining the formation of both differentiated (crustal-like) and undifferentiated (mantle-like) lithologies. The absence of evidence for silicate-metal fractionation suggests that, in the lack of differential stress or strain (possibly induced by impact processes or spin rotation) and particularly when silicate melt is present interstitially, the efficiency of metal-sulphide segregation into a core may be severely limited in small planetesimals.

XVIII Congresso Nazionale di Scienze Planetarie (2023). Meteore, meteoriti e polvere interplanetaria.

THE NWA12800: AN EXTREMELY INTERESTING CV3 CARBONACEOUS CHONDRITE

A. Vitrano[1,2]

[1]Università degli Studi di Siena, Italy (Strada Laterina, 8 53100 Siena. a.vitrano@student.unisi.it); [2]Università degli Studi di Palermo, Italy (Via Archirafi, 22. 90123. Palermo. andrea.vitrano@gmail.com);

NWA12800 is classified as CV3 chondrite in the Meteoritical Bulletin [1], but detailed information on this meteorite has not yet been disclosed. Some preliminary studies are presented here. CV chondrites represent one of the rocks that have best recorded and preserved the history of primordial dust aggregations in the protoplanetary disk.

Polished thin sections of NWA12800 were studied first by means optical microscopy. A high-resolution image of the meteorite was used for a preliminary estimate of the component abundance. The meteorite contains more abundant fine-grained matrix and microfragments than many other CV3, but less chondrules, chondrule fragments and refractory inclusions. NWA 12800 clearly shows a chondritic texture, with well-defined chondrules ranging in size between approximately 60 μm and 3 mm in diameter. Dark grey, fine-grained matrix and glass mesostasis inside chondrules show no mosaicism, indicative of near 3 petrologic type.

Figure 1 Thin section image of meteorite in transmitted light.

Compositions of chondrules, refractory inclusions and matrix were obtained by backscattered electron (BSE) imaging, X-ray elemental mapping and energy dispersive X-ray spectrometry (EDS) analysis by using a Zeiss Sigma 300 FE-SEM (Field-emission scanning electron microscope) equipped with a high-resolution backscattered electron detector and a QUANTAX $60x60$ mm^2 detector for EDS, at LIME (University of Roma Tre).

Textural characteristics of chondrules are evidence of their primary origin as melted droplets and crystallization of melts at different cooling rates and compositions [2-3]. The meteorite shows wide textural types of chondrules: barred olivine (BO), porphyritic olivine pyroxene (POP), granular olivine (GO), isolated olivine grain (IOG) and radial pyroxene (RP). Each chondrule, even belonging to the same textural typology, is different from the others. For example, a BO show two distinct bundles oriented along two different directions and displaying different optical properties, both related to different cooling rate of the two portions of the chondrule.

Some chondrules include fragments with angular shapes, suggesting previous impact processes that have broken chondrules into pieces. An enstatite rim was observed in one IOG. This rim's formation indicates that IOG was splashed out of chondrule when it was still partially molten and experienced gas–melt (or gas–solid) interaction as isolated object [4]. Igneous rims have been observed in some chondrules consisting of olivine rim, sometimes thick and continuous, otherwise occurring as thin and discontinuous grains. They are interpreted as the result of a heating event that occurred when the chondrules were still free-floating in space and had been coated in dust-accretionary rims, which are composed by the same material of the matrix.

A large area of matrix don't shows defined chondrules, which have experienced a high degree of aqueous alteration, more close to the C1 carbonaceous chondrites. Furthermore, taking into account the large difference in both the general apparence and the size distribution of the components, the collected data allow concluding that NWA12800 is a breccia, having a marked heterogeneity of the distribution of its components and carrying records of the complex history of its aggregation and evolution in different times and areas of the protoplanetary disk.

References: [1] Meteoritical Bulletin, no. 108 (2020) *Meteorit. Planet. Sci. 55,* 1146-1150. [2] Lofgren, G., & Russell, W. J. (1986) *Geoch. Cosm. Act., 50(8),* 1715–1726. [3] Gooding J. L. and Keil K. (1981) *Meteoritics 16,* 17-43. [4] Jacquet et al., (2020) *Meteoritics & Planet. Sci.* 1-21.

THE LUMIO CUBESAT: DETECTING METEOROID IMPACTS ON THE LUNAR FARSIDE.

F. Ferrari[1], F. Topputo[1], G. Merisio[1], V. Franzese[1], C. Buonagura[1], C. Giordano[1], A. Morselli[1], P. Panicucci[1], F. Piccolo[1], A. Rizza[1], S. Borgia[1], A. Cervone[2], D. Koschny[3,4], E. Ammannito[5], R. Moissl[3], D. Labate[6], M. Pancalli[6], G. Pilato[6], E. Lhome[3], R. Walker[3], and the LUMIO Team.

[1]Department of Aerospace Science and Technology, Politecnico di Milano, IT
[2]Department of Space Engineering, Delft University of Technology, NL
[3]ESA/ESTEC, Keplerlaan 1, NL-2200 AG Noordwijk, NL
[4]TU Munich, Chair of Astronautics, Boltzmannstr. 15, D-85748 Garching, DE
[5]Agenzia Spaziale Italiana, IT
[6]Leonardo, IT

Introduction: A large number of meteoroids and micrometeoroids enter the Earth–Moon system continuously, constituting a potential threat to our planet. Lunar meteoroid impacts have caused in the past substantial changes in the morphology of the lunar surface and its properties. The Moon has no atmospheric shield, and therefore is subject to a large number of impacts from meteoroids, typically ranging from a few tens of grams to a few kilograms every day. The high impact rate on the lunar surface has important implications for future human and robotic assets that will inhabit the Moon for significant periods of time. A better understanding of the meteoroid population in the cislunar environment is required for future exploration of the Moon. The refinemement of current meteoroid models is of paramount importance for many applications, including planetary science investigations. For instance, understanding meteoroids and associated phenomena is extremely important for the study of asteroids and comets and their dynamical paths, as meteoroids carry valuable information about their parent body and its evolution. Studying meteoroid impacts can help deepening the understanding of the spatial distribution of near-Earth objects in the Solar System.

The study of dust particles is also relevant to the topic of space weather in the Earth proximity. The ability to predict impacts is therefore critical to many applications, both related to engineering aspects of space exploration, and to more scientific investigations regarding evolutional processes in the Solar System. Also, accurate impact flux models would be crucial to support planetary defense actions, as large meteoroids can cause severe damage to our communities.

The LUMIO Mission: In this context, the Lunar Meteoroid Impacts Observer (LUMIO) is a CubeSat mission to observe, quantify, and characterise lunar meteoroid impacts, by detecting their impact flashes on the farside of the Moon. This complements the information available from Earth-based observatories, which are bounded to the lunar nearside, with the goal of synthesising a global recognition of the lunar meteoroid environment. LUMIO envisages a 12U CubeSat form-factor placed in a halo orbit at Earth-Moon L2. The detections are performed using the LUMIO-Cam, an optical instrument capable of detecting light flashes in the visible spectrum (450-950 nm). LUMIO is one of the two winners of ESA's LUCE (Lunar CubeSat for Exploration) SysNova competition and is currently in Phase B development.
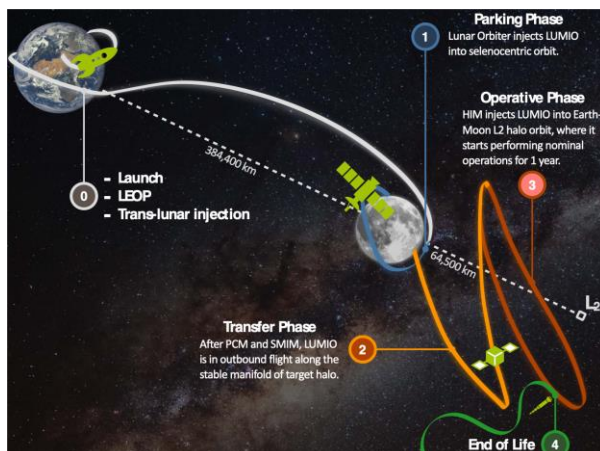
Fig.1: LUMIO Concept of Operations
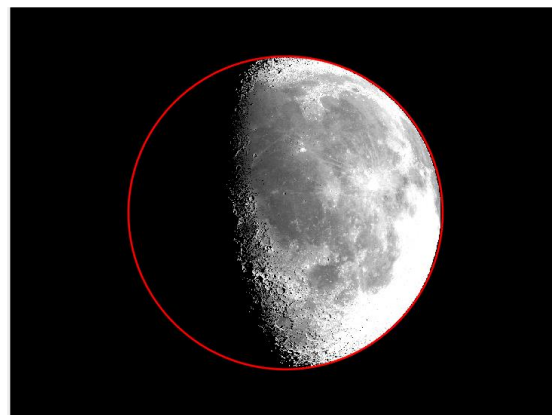
Fig.2: LUMIO-Cam Synthetic Image Generation

In this work, we present the latest results on the modelling of the meteoroid environment in the Earth-Moon system, including an estimate of LUMIO's potential impact on our existing knowledge of meteoroids. In particular, we present results of high-fidelity simulations [1,2], which reproduce datasets to be acquired from LUMIO, as well as their scientific exploitation. An overview of the present-day LUMIO CubeSat design is also given, with a focus on the latest developments involving both the ongoing/planned scientific activities and the development of the payload. In this context, we present opportunities to join the LUMIO Scientific Team and collaborate on LUMIO-related topics.

References: [1] Merisio et al., 2022, Icarus. [2] Topputo et al., 2022, Icarus.

Meteorite-dropping bolides observation with the PRISMA fireball network

D. Barghini[1,2], S. Bertocco[3], A. Carbognani[4], M. Di Carlo[5], M. Di Martino[1], C. Falco[1], D. Gardiol[1], G. Pratesi[6,7], W. Riva[1,8], G. M. Stirpe[4], C. Volpicelli[1], and the PRISMA team,　[1]INAF – Osservatorio Astrofisico di Torino, via Osservatorio 20, 10025 Pino Torinese (TO), dario.barghini@inaf.it, [2]Università di Torino – Dipartimento di Fisica, Torino, [3]INAF – Osservatorio Astronomico di Trieste, [4]INAF – Osservatorio di Astrofisica e Scienze dello Spazio, Bologna, [5]INAF – Osservatorio Astronomico d'Abruzzo, Teramo, [6]Università di Firenze, Dipartimento di Scienze della Terra, Firenze, [7]INAF – Istituto di Astrofisica e Planetologia Spaziali, Roma, [8]Osservatorio Astronomico del Righi, Genova.

Introduction: PRISMA is the Italian fireball network dedicated to the systematic observation of bright meteors and fireballs [1]. It started in 2016 and nowadays involves more than 70 institutes, coordinated by INAF, the Italian National Institute for Astrophysics. To date, the network counts 70 all-sky cameras deployed over the Italian territory. Figure 1 shows the location of PRISMA stations. The coverage of the northern and central part of Italy is already appropriate, while the southern portion of the country still need few cameras to achieve its optimal state. PRISMA is also a member of the European FRIPON collaboration [2].
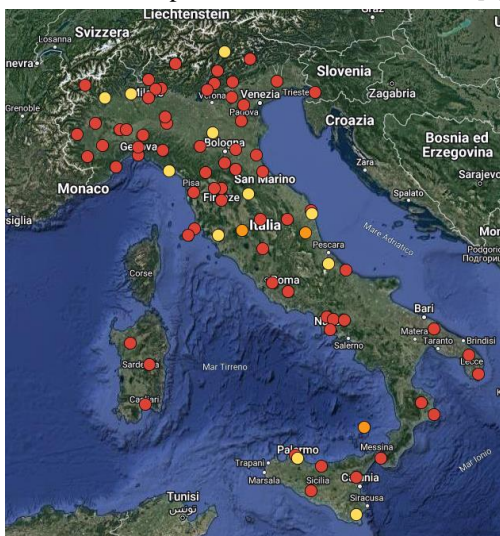
Figure 1: the map of PRISMA stations in Italy. Red points shows the position of deployed and operational cameras, while orange and yellow points are station in installation and purchasing phase, respectively (http://www.prisma.inaf.it/)

Observation strategy: Since the beginning of its activities, PRISMA has observed more than 2500 bright meteors. Alongside the observations of meteors, which are performed at 30 Hz frame rate, each camera acquires a set of long-exposure images (5 seconds exposure every 10 minutes) that are used for the astrometric and photometric calibration of the instruments [3]. These calibration images can be also used for secondary scientific objectives, *e.g.*, the monitoring of light pollution and cloud coverage.

Thanks to this observation strategy and to a precise calibration of our instruments, we are able to determine the 3D trajectory of the observed events with a typical precision of hundreds of meters at an average distance of 100 km. This allows to determine the radiant of the event with a typical precision of some to tens of arcminutes. From the evaluation of a dynamic model, we can therefore estimate the pre-atmospheric speed of the meteoroid, with an uncertainty of the order of 100 m/s, and its mass both at the beginning and at the end of its bright flight in the atmosphere, together with other physical properties, for example related to the mechanical strength of the meteoroid. Figure 2 shows the results of the dynamic model fitting over the data of speed and magnitude of the event recorderd by 10 PRISMA cameras on the evening of the 5th March 2022 (see Table 1).
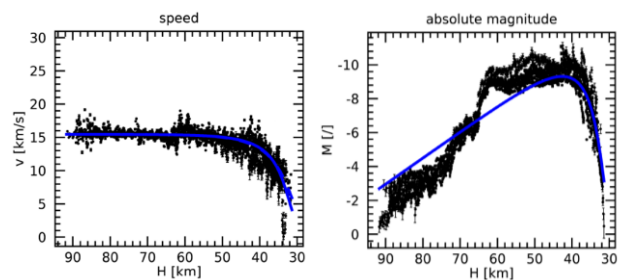
Figure 2: speed and absolute magnitude data of one event observed by 10 PRISMA cameras on the evening of the 5th March 2022.. The blue curves plot the results of the dynamic model fit (see Table 1).

Meteorite-dropping bolides: The analysis of these observations unveiled that at least six of the events observed by PRISMA since 2017 were meteorite-dropping fireballs, with a significantly non-zero residual mass and a predicted strewn-field over the Italian territory. The most noticeable led, on 4th January 2020, to the recovery of two meteorite fragments near Cavezzo (MO) in the area predicted thanks to PRISMA observations and just three days after the fall. This was the first recovery of this type in Italy [4,5]. In addition, five more meteorite-dropping fireballs were observed in 2017, 2018, 2021 and 2022, for which a reliable strewn-field is available. In Table 1 we give relevant results about these events and Figure 3 shows the approximate position of the fall.

Date	Time UTC	Region	Speed [km/s]	Incl. [deg]	Init. mass [kg]	Final mass [kg]
30/12/2017	21:09:26	Padova	15.5	29°	4 – 12	0.2 – 4
22/08/2018	21:37:28	Sondrio	17.9	72°	2 – 5	0.4 – 1.2
01/01/2020	18:26:54	Modena	12.2	68°	10 – 40	0.5 – 1.5
15/03/2021	19:57:32	Isernia	14.7	84°	~ 2	~ 1
01/10/2021	01:04:57	Pistoia	16.0	31°	3 – 8	0.01 – 0.1
05/03/2022	18:55:52	Ascoli P.	15.5	17°	10 – 90	0.3 – 1.5

Table 1: relevant data about the six meteorite-dropping bolides observed by PRISMA from 2017 to 2022 over Italy. In order: date and region of fall, pre- atmospheric speed, trajectory inclination, initial and final mass (68% confidence intervals).

Conclusions: In this paper we gave a short summary of the current status of the PRISMA network and its operation. PRISMA collected data about 2500 bright meteors in the skies over Italy since 2017. We developed a full data analysis pipeline for the reduction of both calibration and bolides data. A first data release of the PRISMA database will take place within 2023. The successful recovery of the Cavezzo meteorite in January 2020 demonstrates the effectiveness of accurate processing of fireball network data even on challenging events generated by small size meteoroids. The meteoroid of Cavezzo is one of the smallest among the current ~40 cases in which meteorites were recovered from precise strewn-field computation thanks to observational data.

Figure 3: the map of potential meteorite falls observed by the PRISMA network from 2017 to 2022 over the Italian territory. Details about each event are given in Table 1. The orange point near Modena (Emilia-Romagna) refers to the recovery of the two samples of the Cavezzo meteorite.

References: [1] Gardiol D. et al. (2019) *Proc. Of the 37th IMC*, 81-86. [2] Colas F. et al (2019) *Astron. Astrophys.*, 644, A53. [3] Barghini et al. (2019) *Astron. Astrophys.*, 626, A105. [4] Gardiol D. et al. (2021) *Mon. Notices Royal Astron. Soc.*, 501, 1215–1227. [5] Pratesi G. et al. (2021) *Meteorit. Planet. Sci.*, 56, 1125–1150.

MidIR Spectral Characterization Of Ol-Bearing Ungrouped Achondrites. C. Carli[1], E. Bruschini[1], T. Cuppone[2], S. Stefani[1], A. Migliorini[1], G. Pratesi[2], [1]INAF-IAPS Istituto di Astrofisica e Planetologia Spaziali, Via Fosso del Cavaliere 100, 00133, Roma, Italia (cristian.carli@inaf.it), [2]Dipartimento di Scienze della Terra, Università di Firenze, Via G.La Pira 4, 50121, Firenze, Italia.

Introduction: Sample return missions are at present one of the primary goals of the Solar System exploration. Different missions addressing that goal are ongoing. Nevertheless, meteorites are a natural sampling of our Solar System bodies and they provide important information about their parent bodies, spanning from the most primitive, associated with the origin of our Solar System, to the most evolved ones.

Among meteorites, those that have experienced a process of differentiation are achondrites, and they span from primitive to highly differentiated. They are mainly composed of mafic minerals and feldspars.

Among mafic minerals olivines are expected to be very abundant being the main component of differentiated bodies. However planetary bodies characterized by a clear olivine spectral signature are less than what expected.

These objects are often observed in the Visible Near Infrared (VNIR) from Earth or spacecraft, addressing the capability to detect the olivine to the crystal field absorption to be attributed mainly to Fe^{2+} in octahedral coordination. The capability to detect it depends on the abundance of olivine, the mineral association (so can change depending which minerals are combine with) and the abundance of iron within a given crystal structure (e.g. [1,2]).

Here we investigate the spectral properties of more than 20 ungrouped achondrites with variable mineral association, olivine abundance and olivine composition within the Middle Infrared (MidIR) to evidence how the spectral properties changes in a spectral range where spectroscopy allows recognition of the mineralogical structures of the shallow crystalline assemblages. This capability mainly relies upon the characteristic spectral features arising from cation–anion and lattice vibrations of crystalline structures in the middle portion of the electromagnetic spectrum [3].

Set-Up and Data set: The MidIR data were acquired at Planetary LABoratory at IAPS-INAF. Measurements were performed by using a Fourier transform interferometer (mod. Bruker Vertex 80) operating in the range from 2 to 15 μm range with the MCT detector. The sample was insert into a bidirectional compartment and measurements were done with observing conditions of i=30° and e=0°. We used an infragold as reference standard. We acquired "bulk" spectrum of the sample with about 3 mm in diameter, where possible we acquired more than one spectrum from the cut surface (slab here after) of each sample. For a selected number of samples, where material was more abundant, we produced also a 0.2 g of powder at <100 μm from a representative portion of the samples. For powdered samples we acquired three spectra which were finally merged into a single spectrum.

The meteorites have been then characterized from a mineralogical and petrographical point of view by SEM and EPMA at MEMA – Department of Earth Sciences of Florence.

Preliminary Results: In the VNIR spectral range these sample clearly show a systematic trend between the Band Center at 1μm and the Band Area Ratio that correlate with the olivine abundance with some exception. In fact meteorites with high olivine amount but a very low Fa content (i.e. low iron) have position of the absorption coherent with the associated pyroxene [1,2].

Powders vs slabs indicate how the spectral contrast is better defined in the slab sample with stronger peaks of the Reststrahler bands (RB) whereas the Christiansen Features (CF) is in general better defined in powdered samples. Moreover is interesting to see that transparency features are not present or weak in our data. This indicate that within the sieved range (0-100 μm) the distribution of sizes is not enriched in the very fine fraction (<20 μm). Often, the spectral shapes are very similar considering the correspondent powdered and slab samples (e.g. NWA 13446; NWA 5400). Whereas other cases show a larger variegation as indicated by NWA 6112. This shows that several samples are relatively homogenous at the investigated spot sizes, but not all.

The MidIR spectra show a clear variation from orthopyroxene rich samples (e.g. NWA 13995 Fig. 1 top) up to olivine rich samples (e.g. NWA 5400 Fig.1 bottom). In some samples, the volume fraction of olivine equates the fraction of orthopyroxenes. In these samples the spectral features are influenced by the olivine and pyroxenes (and maybe plagioclases). The peaks change in intensity and slightly in position, a systematic analysis of the relationship between specific peaks and their positions will be done to investigate if some trends can be defined and to understand if the detection limits are different with respect the VNIR analysis.

Conclusions: The MidIr spectrum is dominated by cation–anion and lattice vibrations of crystalline structures and the vibrational absorptions can be comple-

mentary to the crystal field absorption that we can investigate for the differentiated material in the VNIR. We clearly see a correspondence within the mafic mineralogy and MidIR spectra and in particular the extreme cases (or endmembers) show CF and RBs attributable to olivine or pyroxenes. Samples where these phases are more equal in abundance shows different relationship between the CF position and in particular RBs positions and intensity which could permit to create also for MidIR trends to extrapolate the main mineralogical composition at least for mafic phases.

References:
[1] Bruschini E., et al. 2022. SGI-SIMP conference abs. Pg. 777; [2] Bruschini E., et al. 2022 EPSC abs. EPSC2022-349; [3] Farmer V.C., et al. 1974, https://doi.org/10.1180/mono-4.
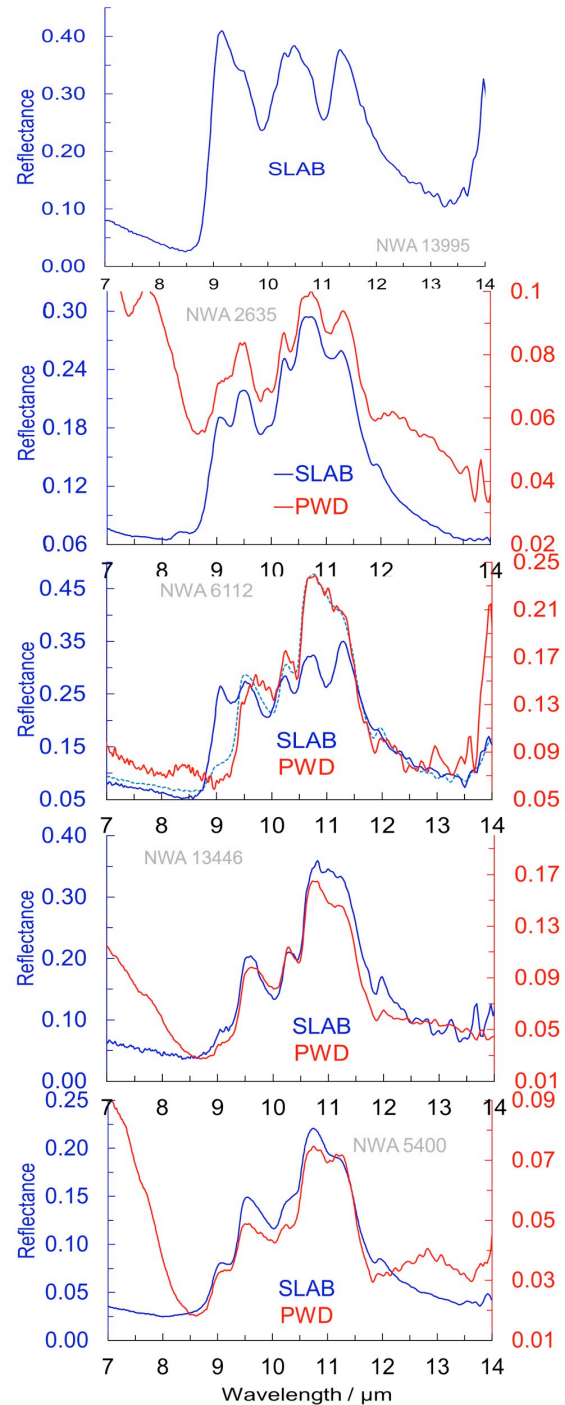
Fig.1. MidIr spectra from ol-rich up to pyroxene enriched ungrouped achondrites for powders (in red) and slabs (in blue).

MICROSCOPIC IMPACTOR DEBRIS AT KAMIL CRATER, EGYPT: THE ORIGIN OF THE Fe-Ni OXIDE SPHERULES.

L. Folco[1,2], L. Carone[3], M. D'Orazio[1,2], C. Cordier[4], M. D. Suttle[5,1], M. van Ginneken[6], M. Masotta[1,2], [1]Dipartimento di Scienze della Terra, Università di Pisa, Via S. Maria 53, Pisa, Italy, [2]CISUP, Centro per la Integrazione della Strumentazione dell'Università di Pisa, Lungarno Pacinotti, Pisa, Italy, [3]Università di Camerino, Scuola di Scienze e Tecnologie, Sezione di Geologia, Via Gentile III da Varano 7, 62032 Camerino, Italy, [4]Université Grenoble Alpes, Université Savoie Mont Blanc, CNRS, IRD, IFSTTAR, ISTerre, 38000 Grenoble, France, [5]School of Physical Sciences, The Open University, Walton Hall, Milton Keynes MK7 6AA, UK, [6]Centre for Astrophysics and Planetary Science, School of Physical Sciences, Ingram Building, University of Kent, Canterbury CT2 7NH, UK. (correspondence: luigi.folco@unipi.it).

Introduction: Kamil crater (Egypt, 22˚10'06"N, 26˚05'16" E; 45 m in diameter) is a natural laboratory for the study of processes and products associated with the impacts of small iron projectiles on the Earth's crust [1, 2]. In particular, because of the distinctive composition of the impactor (an ungrouped Ni-rich ataxite) and the target (Cretaceous sandstones and minor wackes) [3, 4, 5, 6] it offers a unique opportunity to study impactor–target physical–chemical interactions.

Continuing the study of impact melt ejecta [7], we investigated the mineralogy and geochemistry of 25 Fe-Ni oxide (n=24) and metal (n=1) spherules representative of a suite of 135 - recovered from the soil around the crater. Data reveal i) a variety of textures, compositions and oxidation states, ii) are consistent with an impact origin, and iii) provide the basis for discussing a general formation mechanism during hypervelocity impacts of iron projectiles.

Samples and methods: Samples were collected during our 2010 geophysical expedition [1] and investigated by combining scanning electron microscope imaging (SEM-FEG-EDS), electron probe microanalyzer (EPMA) and Raman spectroscopy analyses.

Results and discussion: Spherules range in size from 100 to 500 μm and show a variety of dendritic textures and mineral compositions dominated by Fe-Ni oxides of the wüstite – bunsenite and magnetite – trevorite series or Fe-Ni metal (Figure 1). All these features indicate quenching of high temperature (1600–1500 ˚C) oxide or metal liquid droplets under varying oxidizing conditions.

A geochemical affinity with the iron impactor recorded by the Fe, Co, Ni ratios in the constituent phases (average Ni/Co element ratio of 25.1 ± 7.6; average Ni/(Ni + Fe) molar ratio of 0.21 ± 0.13), combined with target contamination (i.e., the ubiquitous occurrence of Si and Al from trace to minor amounts), document their origin as impact melt spherules formed through the physical and chemical interaction between metal projectile and silicate target melts and air.
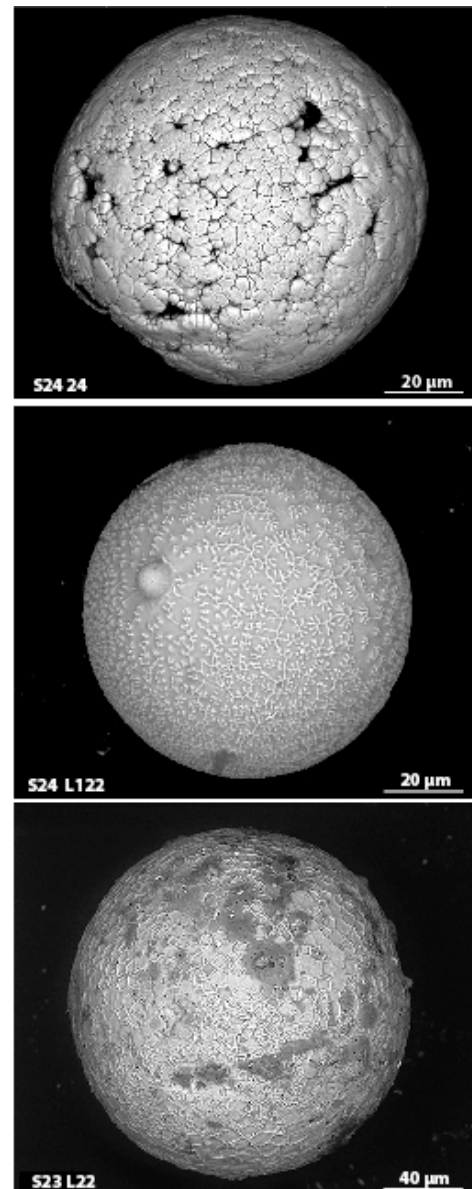
Figure 1. Back-scattered electron image of a selection of Fe-Ni oxide spherules from Kamil crater, Egypt.

We propose a petrogenetic model that envisions formation as liquid droplet residues of immiscible projectile in a mixed silicate melt and their subsequent separation as individual spherules by stripping during hypervelocity ejection. We also argue that this model applies to all impact events produced by small iron projectiles and that such individual Fe-Ni oxide and metal spherules should be common impact products, despite little documentation in the literature.

Our detailed mineralogical and geochemical characterization will facilitate their distinction from other, similar spherules of different origin (cosmic spherules, ablation spherules) often encountered in the geologic record.

This work has been recently published in [8].

References: [1] Folco L. et al. (2010) *Science* 329, 804. [2] Folco L. et al. (2011) *Geology* 39, 179–182. [3] D'Orazio M. et al. (2011) *Meteorit. Planet. Sci.* 46, 1179–1196. [4] Fazio A. et al. (2014) *Meteorit. Planet. Sci.* 49, 2175–2200. [5] Fazio A. et al. (2016) *Geochim. Cosmochim. Acta* 18, 33–50. [6] Hamann C. et al. (20180 *Meteorit. Planet. Sci.* 53, 1594–1632. [7] Folco L. et al. (2015) *Meteorit. Planet. Sci.* 50, 382–400. [8] Folco L. et al. (2022) *Geochim. Cosmochim. Acta* 335, 297–322.

MINERALOGICAL CHARACTERIZATION OF THE FUSION CRUST OF THE CAVEZZO l5 CHONDRITE.

M. Rondinelli[1], D. Gardiol[2], G. Pratesi[3], A. Di Michele[4], M. Bellesi[1], G. Giuli[1], [1]Università di Camerino, sez. Geologia, Via Gentile III da Varano 7, 62032 Camerino (MC), I marianglo.rondinelli@studenti.unicam.it; [2]OATO, Via dell'osservatorio 20, 10025 Pino Torinese (TO), I; [3]Università di Firenze, MEMA, Via G. Capponi 3R, 50121 Firenze, I; [6]Dipartimento di Fisica e Geologia, Università di Perugia, Via Pascoli, 06123 Perugia, I.

Introduction: On January 1st at 18:26:53 UT, eight stations of the PRISMA network detected a brilliant fireball, named IT20200101, in the skies of northern Italy[1]. Thanks to the involvement of local people by an effective media campaign, two fragments were recovered, weighing 3.12 g (specimen 1) and 52.19 g (specimen 2), three days after the bolide was observed. In this contribution we describe the mineralogical characterization of the fusion crust of specimen 2.

Experimental: A thin section of specimen 2, and a polished mount with several chips from the fusion crust have been studied by both optical microscopy and by FE-Scanning electron Microscopy.

Results: Both Optical observations and microchemical analyses of the meteorite interior were consistent with published classification as a L5 ordinary chondrite [2]. The fusion crust display a complex texture of scheletal and acicular olivine, often zoned with a rim richer in Fe than the core. The small size of most olivine crystal prevented to obtain an accurate composition for most of them. Magnetite dendrites are commonly associated to the olivines in the outermost portions of the fusion crust. Minor minerals found in the crust include euhedral crhomites, ilmenites, plagioclases in aggregates with chromites (Pl-chr assemblages) and a nichel sulphide whose composition is close to Ni_2S. One of the two Ni sulphides found display submicroscopic inclusions of metallic Ni.

The chromite grains analysed in the crust generally display a much higher Mg# than the chromites in the bulk, compatibly with previous results from a Phd thesis by Bellesi [3]

To our knowledge, Ni_2S has never been reported before in chondritic material; thus, in order to confirm the composition and in order to determine the structure of this phase, we are planning to cut a slice of one of these grains by FIB and to study this phase by Transmission Electron Microscopy

References:

[1] Gardiol D. et al., Cavezzo, The first Italian meteorite recovered by the PRISMA fireball network. Orbit, trajectory and strewn-field., (2020), Monthly Notices of the Royal Astronomical Society, 501(1), 1215-1227.

[2] Pratesi G., Moggi Cecchi V., Greenwood C. R., Franchi I.A., Hammond S.J., Di Martino M., Barghini D., Taricco C., Carbognani A., Gardiol D., Cavezzo-The double face of a meteorite: Mineralogy, petrography., (2021), Meteoritics & Planetary Science, 56(6), 1-26

[3] Bellesi M., Chromites in ordinary chondrite fusion crusts, PhD thesis, 2021

MINERALOGICAL CHARACTERIZATION AND MICROCHEMICAL ANALYSIS OF THE ALFIANELLO, MONTE MILONE, AND SIENA ORDINARY CHONDRITES.

V. De Santis[1], L. Pittarello[2], L. Carone[1], G. Pratesi[3], A. Di Michele[4], G. Giuli[1], [1]Università di Camerino, sez. Geologia, Via Gentile III da Varano 7, 62032 Camerino (MC), I valeria01.desantis@studenti.unicam.it; [2]Naturhistorisches Museum (NHM), Minerologisch-Petrographische Abteilung, Burgring 7, 1010 Vienna, AT; [3]Università di Firenze, MEMA, Via G. Capponi 3R, 50121 Firenze, I; [6]Dipartimento di Fisica e Geologia, Università di Perugia, Via Pascoli, 06123 Perugia, I.

Introduction: This study has been devoted to the mineralogical, petrographical, and micro-chemical study of three historical meteorites: Alfianello, Monte Milone, and Siena. We chose to focus on three historical Italian falls, all ordinary chondrites, because they have been scarcely studied in the past, especially for possible shock features.

Samples and methods: The three meteorites have been kindly provided by the Museo di Storia Naturale of the University of Florence. A thin section containing, among others fragments, these three meteorites has been first examined by optical microscopy and, then, used for FE-SEM (University of Perugia) investigation, FE-EPMA analysis (NHM Vienna), and EBSD (University of Florence). A Preliminary Raman investigation has been performed for the Alfianello meteorite at the University of Camerino. Operation conditions for the FE-SEM were working distance of 7.3 mm and accelerating voltage of 15 keV, while with the EPMA analyses were made at high vacuum with an acceleration voltage of 15 KeV. Points were chosen with a spot size of 2.0 μm for olivine and pyroxene crystals and of 6.0 μm for plagioclase crystals (defocused modus). We measured with the EPMA olivine, pyroxene and plagioclase grains in the Alfianello and Monte Milone and kamacite, taenite and troilite in the Alfianello, Monte Milone and Siena. For the Siena meteorite, silicates have been analysed by FE-SEM due to lack of time at the EPMA.

Results: Optical observations, as well as chemical analyses, allowed a quantitative basis for the reclassification of the three meteorites. The Monte Milone meteorite was confirmed to be an L5, in agreement with the official classification made by Maras et al. (1979) [1]. The Alfianello meteorite resulted from chemical analyses an L6, as it was officially classified (Levi-Donati, 1971, and Fioretti et al., 2013) [2, 3]. The Siena meteorite is an LL breccia with petrologic type ranging from 3 to 6, in agreement with early literature (Kurat, 1969) [4]. New observations allowed the identification of shocked phases in some investigated meteorites. In detail, in the Alfianello sample, parallel lamellae of ringwoodite have been found in an olivine matrix. This very rare texture has been only reported in a highly shocked meteorites (i.e. the Sixiangkou L5 meteorite, see Chen et al., 2004, Chen et al., 2006 and Chen et al., 2007) [5-7]. The Alfianello sample will be studied in the next future by electron back-scattered diffraction (EBSD) in order to obtain detailed information on the textural relationships between ringwoodite lamellae and olivine matrix.

References:

[1] Maras A., Levi-Donati G. R., Sighinolfi G. P., (1979), Studies of Italian meteorites: mineralogy, texture and chemistry of Monte Milone, Macerata, shower, *Meteoritics*, vol. 14, 482. [2] Levi-Donati G. R., (1971), Petrological features of shock metamorphism in chondrites: Alfianello, *Meteoritics*, vol. 6, 225-235. [3] Fioretti A. M., Agostini L., Domeneghetti M. C., Molin G., (2013), Studio petrografico– mineralogico delle meteoriti Alfianello e Trenzano cadute nella provincia di Brescia nella seconda metà del 1800, *Natura Bresciana*, vol. 38, 17-24. [4] Kurat G., Fredriksson K., Nelen J., (1969), Der Meteorit von Siena, *Geochimica et Cosmochimica Acta*, vol. 33, 765-773. [5] Chen M., El Goresy A., Gillet P., (2004), Ringwoodite lamellae in olivine: Clues to olivine– ringwoodite phase transition mechanisms in shocked meteorites and subducting slabs, *PNAS*, vol. 101, 15033-15037. [6] Chen M., Li H., El Goresy A., Liu J., Xie X., (2006), Fracture-related intracrystalline transformation of olivine to ringwoodite in the shocked Sixiangkou meteorite, *Meteoritics & Planetary Science*, vol. 41, 731-737. [7] Chen M., Chen J., Xie X., Xu J., (2007), A microstructural investigation of natural lamellar ringwoodite in olivine of the shocked Sixiangkou chondrite, *Earth and Planetary Science Letters*, vol. 264, 277-283.

FIRST FIND OF RINGWOODITE IN THE ALFIANELLO L6 ORDINARY CHONDRITE.

L. Carone[1], V. De Santis[1], L. Pittarello[2], G. Pratesi[3], A. Di Michele[4], G. Giuli[1], [1]Università di Camerino, sez. Geologia, Via Gentile III da Varano 7, 62032 Camerino (MC), I laura.carone@unicam.it; [2]Naturhistorisches Museum (NHM), Minerologisch-Petrographische Abteilung, Burgring 7, 1010 Vienna, AT; [3]Università di Firenze, MEMA, Via G. Capponi 3R, 50121 Firenze, I; [4]Dipartimento di Fisica e Geologia, Università di Perugia, Via Pascoli, 06123 Perugia, I.

Introduction: Ordinary chondrites (OCs) are the most abundant (>80%) group of meteorites recovered on Earth and also among the most primitive materials in the solar system [1, 2]. They are composed of an assemblage of chondrules (60-80 vol.%) and fine grained matrix [3].

Subjected to collisional processes on small bodies, OCs have suffered variable degrees of shock metamorphism [2]. Olivine, pyroxene and plagioclase that underwent to shock pressure might be transformed into high pressure polymorphs, such as ringwoodite (spinel structure), majorite (hollandite structure) and jadeite, respectively [4], or contain other evidence of shock metamorphism, e.g., planar deformation features, shock darkening, amorphization, etc.

According to the shock classification proposed by [2] and updated by [5], six stages of progressive shock metamorphism were defined: from unshocked (S1), characterised by a sharp optical extinction of olivine, to very strongly shocked (S6), with solid-state recrystallisation and melting.

The Alfianello (Brescia, Italy) meteorite is an L6 ordinary chondrite fallen on February 16, 1883. Petrological investigation performed by [6] indicated that it mostly consists of olivine and low Ca pyroxene, while plagioclase, merrillite and apatite occur in minor amounts [7]. Other accessory phases include chromite and ilmenite [6], nickel-iron alloys and sulphides [8]. Plagioclase is commonly transformed into maskelynite and rarely occurs as birefringent crystals [7]. According to the shock classification proposed by [2], the deformation features observed in the investigated sample from the Alfianello meteorite indicate high shock, equivalent to S5.

Experimental: The sample studied here is a petrographic thin section of a fragment 7 x 10 mm in size displaying no fusion crust from the Alfianello chondrite and kindly provided by the Museo di Storia Naturale of the University of Florence.

The investigated sample has been examined with a variety of analytical techniques: optical microscopy, Field Emission Scanning Electron Microscopy (FE-SEM), Electron MicroProbe Analysis (EMPA) and Raman spectroscopy, with the aim of further characterising shock effects and confirm the classification of this meteorites.

Results: We report the first documented occurrence of ringwoodite in the Alfianello meteorite. This high pressure polymorph occurs as rim of an olivine grain, or surrounded by olivine, or as network of planar lamellae, likely oriented along crystallographic planes within olivine. The latter occurrence has been only rarely reported in the literature, e.g., in the Sixiangkou L6 chondrite, [9], in Tenham L6 chondrite, [10] and in Yamato 791384 L6 chondrite, [11].

Further studies: As the occurrence of ringwoodite in lamellae has been only reported for a few ordinary chondrites, all L6, we are planning further studies by transmission electron microscopy (TEM), to determine the mutual orientation of the ringwoodite lamellae and the host olivine and to constrain the formation process.

References: [1] Hutchison R. (2007) *Cambridge Planetary Science, 2,* 506. [2] Stöffler D. et al. (1991) *GCA, 55,* 3845-3867. [3] Florin G. et al. (2020) *GCA, 269,* 270-291. [4] Rubin A. E. (2003) *GCA, 67,* 2695-2709. [5] Stöffler D. et al. (2018) *Meteorit Planet Sci, 53,* 5-49. [6] Levi-Donati G. R. (1971) *Meteoritics, 6,* 225-235. [7] Fioretti A. M. et al. (2013) *Ann. Mus. Civ. Sc. Nat., Brescia 38,* 17-24. [8] Levi-Donati G. R. (1955) *Atti e Mem. Della Accad. Di Scien. Lett ed Arti di Modena V,* 3-16. [9] Chen M. et al. (2004) *PNAS, 101,* 15033-15037. [10] Xie Z. and Sharp T. G. (2007) *Earth & Planet. Sci. Lett 254,* 433-445. [11] Miyahara M. et al. (2010) *Earth & Planet. Sci. Lett, 295,* 321-327.

PRELIMINARY CHARACTERIZATION OF TWO RANTILA FALL FRAGMENTS. A. I. Landi[1], C. Carli[2], F. Capaccioni[3] and G. Pratesi[4], [1] annairene.landi@unitn.it, Università degli Studi di Trento, Via Sommarive, 14 - 38123 Trento - Italy [2] cristian.carli@inaf.it, INAF-IAPS Via del Fosso del Cavaliere, 100 Tor Vergata 00133 - Roma - Italy, [3] fabrizio.capaccioni@inaf.it, INAF-IAPS Via del Fosso del Cavaliere, 100 Tor Vergata 00133 - Roma – Italy, [4] giovanni.pratesi@unifi.it, Dipartimento di Scienze della Terra, Università degli Studi di Firenze, Via G. La Pira, 4 – 50121 Firenze - Italy

Introduction: Rantila is the provisional name for the fall products, for a total recovered mass of about 6 kg, of a meteorite shower occurred on August 17, 2022 in Rantila, Gujarat, India.

This fall is not yet officially recognized and classified, therefore the main purpose of this study is to define its mineralogy and petrology through the investigation of two fragments (about 1.3 x 1 x 0.5 cm) showing different mineral assemblages and textures.

Methods and Data: Mineralogical and petrological characterization was conducted by means of scanning electron microscope (SEM), for the acquisition of BSE (Back Scattered Electrons) and EDS (Energy Dispersive Spectroscopy) maps, and electron microprobe (EPMA) for the quantitative analysis of the elemental composition of each detected phase.

Sample 1 is brecciated and consists mostly of enstatite, with a nearly FeO-free composition ($En_{98.4}Wo_{0.9}Fs_{0.7}$), which is present both as phenocrysts of different sizes, up to 5 mm in length, and as matrix in the brecciated veins. Almost pure forsterite ($Fa_{0.6}$) is quite abundant (about 30% of the investigated surface) occuring in the brecciated veins and as phenocrysts up to millimetric size. Diopside is a minor constituent of the sample and it is present as phenocrysts up to 500 μm in length ($En_{56.3}Wo_{43.4}Fs_{0.3}$), sometimes showing enstatite exsolution lamellae, and as inclusion of micrometric size in enstatite ($En_{56.9}Wo_{42.7}Fs_{0.4}$). Only one plagioclase ($An_{16.3}$) grain of 500 μm in length was detected. Fe oxides are an accessory phase occurring as micrometric inclusions in enstatite phenocrysts. Other accessory phases are sulfides, which occur as isolated troilite ($Fe_{0.99}Cr_{0.01}S_{1.00}$) grains of about 50 μm in size and as a millimetric aggregate composed by troilite ($Fe_{0.99}Cr_{0.01}S_{1.00}$) and minor Cr-Fe phase ($Fe_{0.96}Cr_{1.96}Mn_{0.04}S_{4.00}$). Two 100-μm kamacite (Fe 91.93 wt%; Ni 7.07 wt%; Co 0.64 wt%; Si 0.27 wt%) grains were detected.

Sample 2 is also brecciated and it presents a dark glassy portion on one side. The sample consists of diopside, glass, plagioclase and accessory sulfides. Only one millimetric grain of enstatite ($En_{98.9}Wo_{1.0}Fs_{0.1}$) was detected and forsterite is not present. Glass (SiO_2 70-74 wt%; TiO_2 0.1-0.4 wt%; Al_2O_3 15-16 wt%; CaO 0.1-0.3 wt%; Na_2O 8-9 wt%; K_2O 0.5-1.0 wt%) is the main constituent of the sample and appears dark in colour and heavily fractured, with diopside inclusions as grains up to 500 μm ($En_{58.1}Wo_{41.8}Fs_{0.1}$) and as crystals with elongated shape ($En_{54.8}Wo_{45.2}$). Diopside ($En_{59.2}Wo_{40.6}Fs_{0.2}$) phenocryst (5 x 3 mm) has an inclusion of glass with the above reported composition and plagioclase ($Ab_{95.0}Or_{4.4}An_{0.6}$). Isolated sulfide grains (100-500 μm) are alabandite with high Fe content (up to 15.32 wt%) and minor Mg (up to 1.75 wt%).

The preliminary information here reported reveal interesting characteristics of the two investigated fragments: the main features of the identified phases and the highly reduced nature are typical of aubrites [1], although some typical minor phases, e.g. oldhamite [2] and roedderite [3], were not detected. Moreover, sample 2 shows a modal composition strongly different from sample 1 and completely unusual for the aubrites being composed mostly of glass, with peculiar textural and chemical features, and with enstatite as minor phase.

Finally, this meteorite shows one of the strongest fluorescence among all known meteorites.

Future work: In order to obtain a more complete characterization of the two fragments, further investigations are ongoing. Electron backscatter diffraction (EBSD) technique will be applied to solve the ambiguity in the identification of some phases, e.g. the two polymorphs $FeCr_2S_4$ daubréelite and zolenskyite [4] and to better understand the relationship between crystalline and amorphous phases in the melt.

Further investigations will be conducted also on more fragments of Rantila fall and with additional analytical techniques to obtain a complete characterization of the meteorite and infer information about the parent body.

References: [1] Keil K. (2010) *Chem. Erde*, 70, 295-317. [2] Wheelock M. M. et al. (1994) *Geochim. Cosmochim. Acta*, 58, 449-458. [3] Lorenz C.A. et al. (2020) *Meteorit. Planet. Sci.*, 55, 2670-2702. [4] C. Ma & Rubin A. E. (2022) *Am. Min.*, 107, 1030-1033.
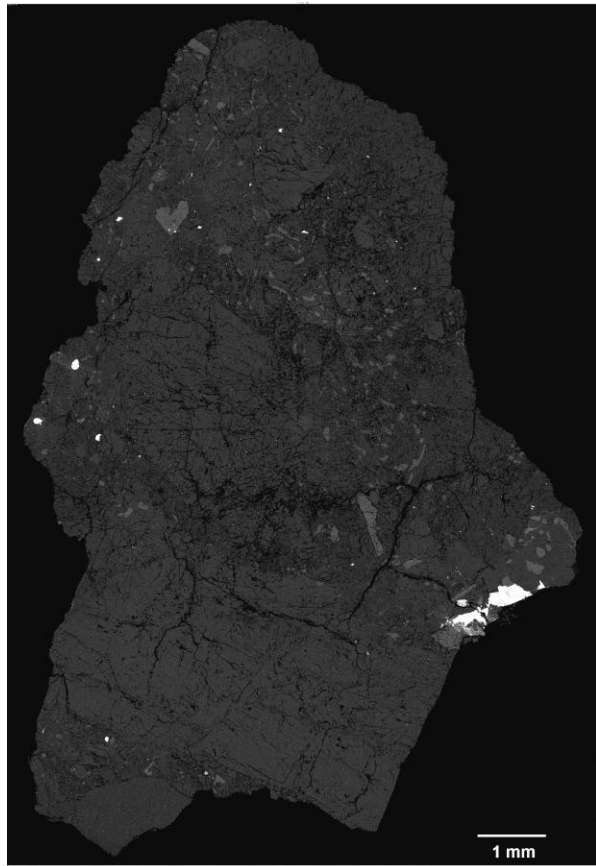
Fig.1. BSE map of sample 1. It is mostly composed of enstatite. Forsterite crystals (e.g. in the upper right border) are represented with slightly darker gray, same as the brecciated veins which are composed mostly of forsterite. Light gray grains are diopside and white colored objects are sulfides, Fe-Ni metals and Fe oxides.
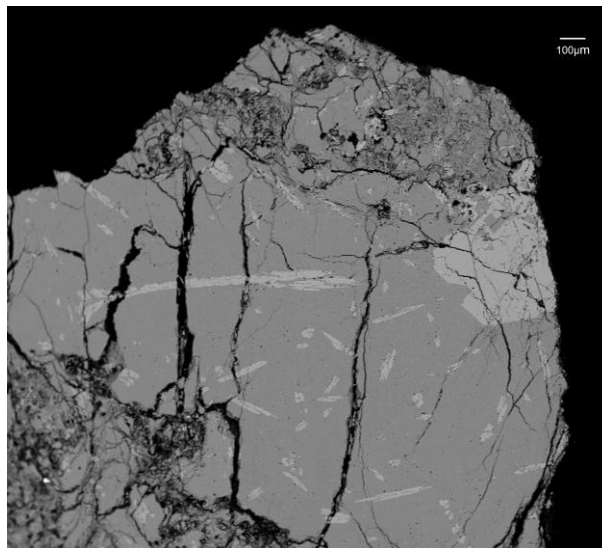
Fig.2. BSE image of glass (dark gray) with diopside inclusions (light gray) in sample 2.

ALTERATION FRONTS IN RECKLING PEAK 17085 CM CARBONACEOUS CHONDRITE: AN INVESTIGATION OF THE AQUEOUS ALTERATION PROCESS IN THE CMs PARENT ASTEROID.

A. Musolino[1,2], L. Folco[2,3], M.D. Suttle[4]. [1]CEREGE, Aix-Marseille Université, Technopôle de l'Arbois-Méditerranée, BP80, 13545 Aix-en-Provence (musolino@cerege.fr). [2]Dipartimento di Scienze della Terra, Università di Pisa, Via S. Maria, 53, 56126 Pisa, Italia (luigi.folco@unipi.it). [3]Centro per l'Integrazione della Strumentazione scientifica dell'Università di Pisa (CISUP), Pisa, Italia. [4]School of Physical Sciences, The Open University, Walton Hall, Milton Keynes, MK7 6AA UK (martin.suttle@open.ac.uk)

Introduction: How the process of aqueous alteration occurred in carbonaceous chondrites' parent bodies is still poorly understood. The CM2 carbonaceous chondrite Reckling Peak (RKP) 17085 from Antarctica is a fresh meteorite whose matrix preserves a network of the so-called 'alteration fronts' – snapshots of an ongoing aqueous alteration process. Alteration fronts, described for the first and only time by Hanowski & Brearley [1], have been also observed in hydrothermal alteration experiments of chondrites [2]. Being collected in Antarctica, RKP 17085 is very well preserved (just minor evidence of terrestrial alteration can be detected): a fact that makes this meteorite an ideal sample for the investigation of this primary geological process.

Materials and methods: Reckling Peak 17085 is a CM carbonaceous chondrite of petrologic type 2, collected in the Reckling Moraine icefield, Antarctica, during the PNRA expedition in 2017 (https://meteoant.dst.unipi.it/index.php). Two polished thin sections of RKP 17085 were loaned from the Museo Nazionale dell'Antartide in Siena, Italy. Once coated with carbon, the two sections were studied by microanalytical Field Emission Gun Scanning Electron Microscopy (FEG-SEM-EDS) at the Dipartimento di Scienze della Terra and Centro per la Integrazione della Strumentazione dell'Università di Pisa (CISUP), Italy. Microanalysis work allowed the characterisation of the meteorite, with the acquisition of high spatial resolution backscattered electron (BSE) images, semi-quantitative chemical analyses, and X-ray maps.

Results and discussion: RKP 17085 is mainly composed of a fine-grained matrix with fibrous/platy minerals (likely phyllosilicates). The matrix is characterized by the presence of brighter 'alteration fronts' (visible in BSD). The alteration fronts (i) have a thickness of ~10-40 μm, (ii) do not intersect the fusion crust (they thus pre-date atmospheric entry), (iii) can form closed areas in the matrix, both including or intersecting other components (chondrules, mineral fragments, calcium–aluminium-rich inclusions), (iv) inside the areas included by fronts the matrix is less porous, but there are no variations in the FeO content in phyllosilicates (in contrast to the 'aureoles' described by Hanowski & Brearley [1]: Fe-enriched areas delimited by fronts).

Like the matrix, the fronts are made of phyllosilicates (but they are too fine-grained for individual phases to be resolved using EDS analysis). Nevertheless, using X-ray maps, it has been observed enrichment in Fe compared to the surrounding matrix, and at the same time, there is no evidence of Fe-oxides/hydroxides.
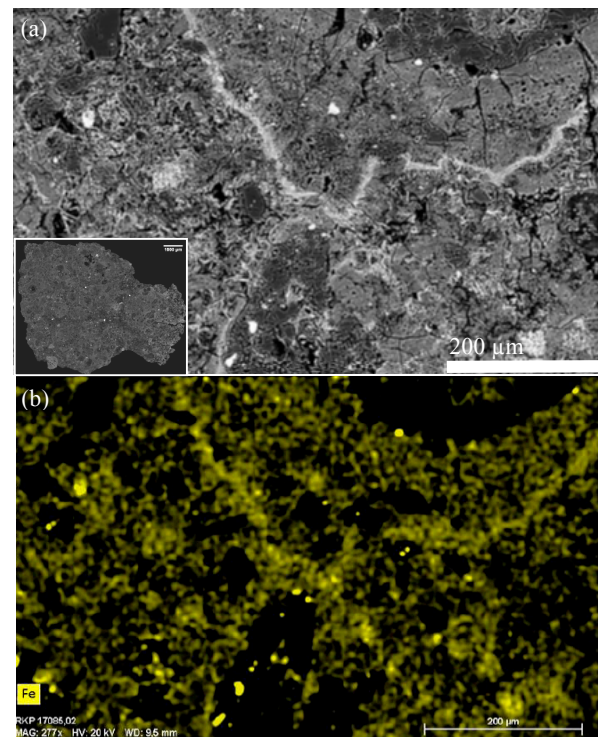
Figure 1 – (a) Area of RKP 17085 with alteration front (brighter band on the top right). Bottom left: BSE image of the thin section of RKP 17085. (b) X-ray map of the area shown above for the element Fe (yellow). The alteration fronts are enriched in Fe compared to the surrounding matrix.

Alteration fronts can be considered as preferred pathways for the circulation of fluids in the parent body. The closed geometry and distribution of the fronts suggest that the fluid responsible for the alteration was already inside the chondritic body, likely in the form of microscopic ice masses. In this scenario, the fluid expanded in a radial way, possibly in re-

sponse to a heating event. The formation of reaction fronts (and aureoles) may occur in particular conditions (e.g. of porosity, amount of fluids, the extent of the alteration), and having RKP 17085 still part of its primary mineralogy and being not intensively altered, fronts could be related to the first stages of alteration [3].

Conclusion: Aqueous alteration fronts are key features for investigating pathways for fluid/element mobilization on CM hydrous/icy parent asteroids. RKP 17085, a fresh CM2 with alteration fronts, has the potential to provide new clues on this geologic process and its products. Further analyses (e.g. IR/Raman Spectroscopy, FIB, TEM) will be carried out on this same meteorite to better constrain the conditions of their formation, their mineralogy, and their role in the alteration of primitive hydrated asteroids.

References: [1] Hanowski, N. P. & Brearley, A. J., 2000. Iron-rich aureoles in the CM carbonaceous chondrites, Murray, Murchison and Allan Hills 81002: Evidence for in situ aqueous alteration. *Meteoritics and Planetary Science,* 35(6), pp. 1291-1308. [2] Suttle M. et al. 2022. Alteration conditions on the CM and CV parent bodies – Insights from hydrothermal experiments with the CO chondrite Kainsaz. *Geochimica et Cosmochimica Acta,* 318, pp. 83-111. [3] Musolino, A. 2021. Exploring the Variability of Primitive Materials and Processes in the Early Solar System: Characterisation of Four Chondritic Meteorites. Published Masters' thesis, University of Pisa.

GEOCHEMICAL CHARACTERISATION AND CR ISOTOPE COMPOSITION OF LIBYAN DESERT GLASSES AND ORDINARY CHONDRITES: PRELIMINARY DATA.

X. Shehaj[1,2], M. Casalini[1*], S. Tommasini[1], R. Avanzinelli[1], G. Pratesi[1], [1] DST - Dipartimento di Scienze della Terra, Università degli Studi di Firenze, via Giorgio La Pira 4, 50121 Firenze (*corresponding: martina.casalini@unifi.it), [2] INAF-IAPS – Istituto Nazionale di Astrofisica – Istituto di Astrofisica e Planetologia Spaziali, Tor Vergata via Fosso del Cavaliere 100, 00133 Roma.

Chromium stable isotopes can be used in a wide range of applications in cosmochemistry, particularly those related to early solar system processes [1]. Meteorites, together with return mission samples, represent unique materials to directly investigate Solar System bodies. Cr isotope systematic represents a powerful geochemical tool to investigate meteorite characteristics and to eventually discriminate between the terrestrial vs. extra-terrestrial contribution on the composition of the fall materials [2].

Cr isotope ratios (^{53}Cr/^{52}Cr and ^{54}Cr/^{52}Cr) can discriminate different meteorite types by the presence of the heterogeneously distributed ^{54}Cr nucleosynthetic anomalies at similar ^{53}Cr excess. Terrestrial rocks, on the other hand, are not expected to show any variation in Cr isotope ratios.

Compared to other tracers (such as Os isotopes and PGE abundance), this systematic has the big advantage of being able not only to identify the presence of extra-terrestrial component in impactites, but also to provide information about the type of the impactor [2].

In order to establish the setup for the analysis of this specific systematic, we present the preliminary compositional data of Cr isotopes and high-precision trace elements on six ordinary chondrites, which are classified, but not yet fully characterised for their geochemical features, used to test the reproducibility of the analytical method. The newly developed method yielded good results with Cr isotope compositions consistent with literature data reported for each class of analysed meteorite [1, 3, 4].

We further tested the applicability of the method, on Libyan Desert Glasses (LDG), an enigmatic type of natural silicate glasses, which occur in well-defined geographic area in the western part of the Great Sand Sea (between Egypt and Libya, North Africa). These materials have gained the attention of many researchers through the last century (early 1930s) but, despite the large number of published studies (>80) committed to this argument, their origin (terrestrial vs. extra-terrestrial) is still debated. The hypothesis that links their origin to meteoritic impacts seems is based on the lack of correlation between their geochemical compositions and that of the local sand or sandstone analysed from various locations in the common region of recovery. On the other hand, there are some differences with respect to classical impact glasses (i.e., the occurrence of peculiar high-T mineral phases or the presence of an impact crater). According to several authors the strongest indication for the presence of a meteoritic component could be retained in the dark streaks of layers showed by some glass samples.

With the aim of shed light on the debated origin of these materials one samples of LDG was analysed along with the meteorite samples. Here we present the preliminary data on its trace element composition and Cr isotope composition.

The analysed LDG sample shows ^{54}Cr/^{52}Cr isotope ratio slightly higher, but within error, of terrestrial values, but also similar to that of specific classes of meteorites (i.e., EH, EL, Aubrites). The trace elements composition of LDG shows ratios between compatible elements (Cr/Ni vs. Co/Ni) that lies in between terrestrial and meteoritic values, whilst incompatible trace elements are indistinguishable from terrestrial materials. In our sample the Cr content is rather low (about 60 ppm) and thus likely reflects a small contribution of extraterrestrial metrial not enough to significantly modify the Cr isotopic composition of the sample.

References: [1] Qin L. and Wang X. (2017) *Rev. Miner. Geochem. 82,* 379-414. [2] Koeberl C. (2003) *Treatise on Geochemistry*, 739-791. A. B. and Author C. D. (1997) *JGR, 90,* 1151–1154. [2] Author E. F. et al. (1997) *Meteoritics & Planet. Sci., 32,* A74. [3] Trinquier A. et al. (2008) *J. An. At. Spec., 23,* 1565-1574. [4] Pedersen S. G. et al. (2019) Meteorit. Planet. Sci., 54, 1215-1227.

New Impact Crater Catalogue Of The Moon Based On The Deep Learning Approach. R. La Grassa[1], E. Martellato[1], G. Cremonese[1], I. Gallo[2], C. Re[1], [1]INAF (Osservatorio Astronomico di Padova, Italy, riccardo.lagrassa@inaf.it), [2]University of Insubria (Varese, Italy).

Introduction: Crater detection offers a great scientific contribution in analysing the geological and morphologies processes of the planetary surfaces and plays a key role in potential future landing sites.

Release a global Moon craters catalogue represents a hard challenge due to the remarkable amount of craters and, considering the low spatial resolution of the global mapping, classical methods lack their performance in the recognition tasks.

Furthermore, small craters are harder to recognize also by human experts and the need to have a sophisticated detection algorithm becomes mandatory.

To address these problems, we use the deep learning model "YOLOLens5x" and the super-resolution to improve impact crater detection.

In this work, we introduce and release the first most complete catalogue by Artificial intelligence (AI), useful to community research to analyze the geological/physical properties linked by its impact craters.

Methodology: The model used is composed of the two main sub-networks, Generator and YOLOv5, which make up a single model that we refer to as *YOLOLens*.

Given x as input, the Generator g(x)=x̃ is a function responsible to approximate the source x into output x̃.

Our proposed Generator creates super-resolution (SR) images starting to a refinement learned networks that are responsible for the refinement process of the input at low resolution (RLNet).

This RLNet is composed of Residual in Residual Dense Blocks to extract local features from previous blocks preserving the residual local information.

The SR output is then used by an object detection model (YOLO) in an end-to-end model where the final error computed will be backpropagated over the unique model designed.

The object detection layers will be responsible for the craters detection tasks using SR generated images useful to recognize small craters of the lunar site observed.

Pre-Processing and Post-Processing: The main workflow is to create a full Moon grid composed of location areas without overlaps taken by the global Lunar mosaic using the cylindrical projection. Due to the distortion effect near the Pole regions and the worst performances obtained by the model in reliably detecting craters in these regions, we change the cylindrical into the orthographic projection in order to avoid dilatation as much as possible.

For each tile orthoprojected, we keep the cylindrical coordinates expressed in longitude and latitude and the distortion coefficient converted in pixels system reference.

The new Moon grid is used for crater detection by YOLOLens and to provide a global counting.

Finally, each predicted crater location given from the pixels reference will be converted using the cylindrical window coordinated provided for each tile and they will be normalized considering the distortion coefficient due to the orthoprojection operation.

All coordinates output in the final lunar catalogue are reported as cylindrical projections in the longitude range [-180, +180] and latitude range [-90, +90].

In Fig.2 we show the global lunar map extracted by YOLOLens.

Results: YOLOLens achieves better performances than other baselines, reporting YOLOLens5x recall of 0.872 against 0.819 of the best model (ELCD [1]) used as benchmark, proving the validity of the model used to retrieve more craters than the Robbins catalogue [2], with respect to the capability analyzed by other baselines.

As result, the extracted craters counted by YOLOLens achieve 3,050,679 craters, where most of the features are in the diameter range of [0.6-1.6] km as showed in Fig.1 (green bars).
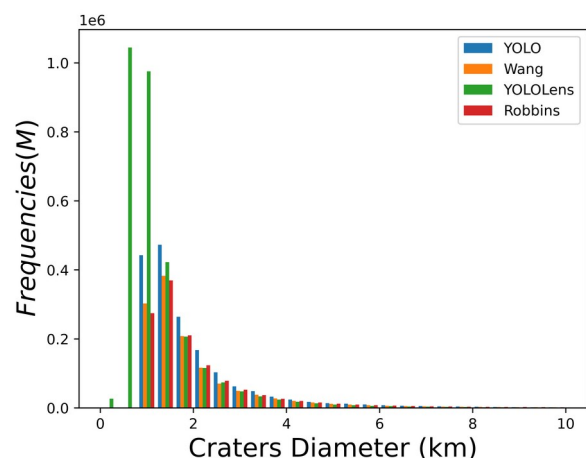
Figure 1: Histogram of the Lunar catalogues.
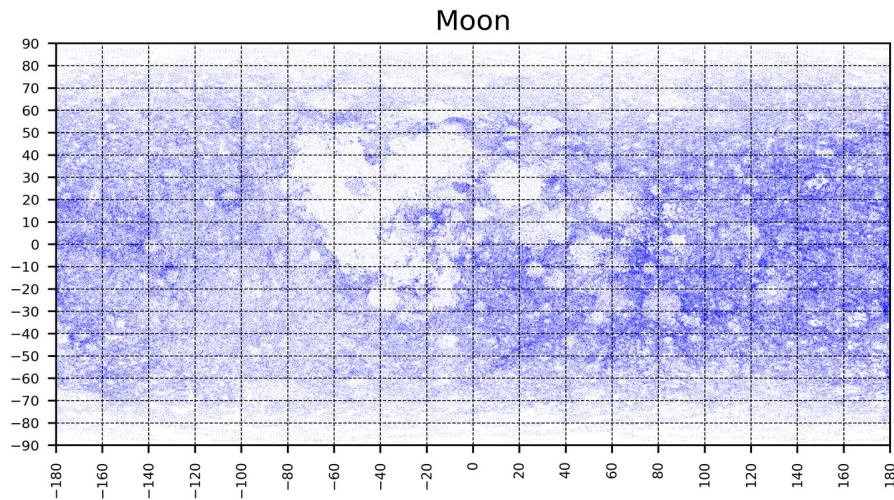
Figure 2: Lunar Map of the detected impact craters

Wang [3] and Robbins [2] catalogues are very similar in the resulting distributions and in counting frequencies (orange and red bars), more precisely Wang catalogue contains 1,319,373 craters and Robbins achieves 1,296,796. The YOLOv5 baseline contains 1,813,424 a higher number of craters in the size range greater than 2 km.

YOLOLens demonstrates a better capability to retrieve small craters due to the super-resolution methodology.

Conclusions: In this work, a new catalogue of Lunar craters entirely created by AI model is released.

It contains >3M impact craters extracted by YOLOLens and almost 2M predicted by YOLO baseline, both in ranges up to 20 km.

The challenge for future work is to improve YOLOLens model and use it as a pre-trained model to create and finalize a new catalogue of other planetary surfaces such as Mercury.

References:
[1] L. Fan, J. Yuan, K. Zha, and X. Wang. Elcd: Efficient lunar crater detection based on attention mechanisms and multiscale feature fusion networks from digital elevation models. Remote Sensing, 2022.
[2] S. J. Robbins. A new global database of lunar impact craters 1–2 km: 1. crater locations and sizes, comparisons with published databases, and global analysis. Journal of Geophysical Research: Planets, 124(4):871–892, 2019.
[3] Y. Wang, B. Wu, H. Xue, X. Li, and J. Ma. An improved global catalog of lunar impact craters with 3d morphometric information and updates on global crater analysis. Journal of Geophysical Research: Planets.

Martian surface photometry with TGO/CaSSIS: current results and future perspectives

G. Munaretto[1], S. Doutè[2], L. Tornabene[3], G. Cremonese[1], M. Pajola[1], A. Lucchetti[1], S. Bertoli[1], E. Martellato[1], P. Borin[1], N. Thomas[4]

[1]INAF, Osservatorio Astronomico di Padova, Vicolo dell'Osservatorio
[2]Universite Grenoble Alpes, CNRS, Institut de Planetologie et d'Astrophysique de Grenoble (IPAG), France
[3]Inst. Earth & Space Exploration, Earth Sci., Western University, London, Canada
[4]Physikalisches Institut Universitat Bern, Switzerland

Introduction: Imaging of Mars with mid to high resolution cameras provide monochrome and multi-band datasets that can be used to investigate the composition, the origin and formation mechanism of Martian surface features. In particular, surface photometry derived from the Colour and surface Imaging System (CaSSIS, [1]) and High Resolution Imaging Science Experiment (HiRISE, [2]) dataset has been performed to constrain the origin and formation mechanisms of Recurring Slope Lineae (RSL, [2]), i.e. low-albedo, yearly-recurrent streaks [3,4].

Images retrieved by such instruments record the flux received by the planet in I/F (i.e., relative reflectance) units, which also incorporates two contributions that must be taken into account and corrected before to any photometric analysis. One contribution is the surface topographic shading (i.e., sun-lit areas are brighter than those in the shade). In order to remove it, either ratios of fluxes from areas with the same illumination and observation conditions are considered (but they may not be available), as was done in [4], or a topographic correction should be performed [5]. The second contribution is the scattering due to dust and aerosol particles in the Martian atmosphere. Such contribution may be removed to a first order by subtracting the I/F of the darkest shadowed pixel from the image [4]. However, this method has a low accuracy, which is not enough to perform quantitative, high-quality, absolute photometric analysis. As a consequence, accurate atmospheric corrections based on the optical and radiative transfer properties of the martian atmosphere need to be applied.

In this work, we will show our current efforts to produce topographically and atmospherically corrected CaSSIS images. In particular, the adopted technique is applied to RSL and will be used to analyze coordinated CaSSIS and HiRISE observations acquired to study the diurnal activity of selected Martian surface features.

Datasets: We first consider the CaSSIS image of the Columbia Hills in Gusev Crater, the investigation area of the Spirit rover. We choose this location because it is well characterized in literature [6,7,8] and also has rover photometric measurements that can be used to validate our methodology.

The topography of the site is given by a 5 m/px CTX-derived DTM, which is used to evaluate the local incidence and emission angle at each pixel of the image. The *photomet* task within the USGS ISIS software is used to ingest the CaSSIS image, apply the atmospheric correction, and normalize each pixel of the image to the same illumination and observation conditions (i.e., perform the topographic correction). In particular, the atmosphere is modeled following the formalism in [9]. Multiple surface photometric functions, either empirical or derived from CRISM observations [7,8] are tested. The final corrected image is then compared with photometric measurements taken by the Spirit rover convolved within the CaSSIS photometric system. In particular, we consider the photometric models derived from the "El-dorado" dunes Spirit observations [6] (Fig 1A, 1B) to simulate what would be observed by CaSSIS and compare it with our atmospherically corrected observations.

Results: We report in Fig. 1A the location of the Columbia Hills and the "El-Dorado" dunes, as well as our atmospherically corrected spectra of this region, and simulated spectra from the Spirit-derived photometric models. We can see a general agreement between all the models, even though those derived from CRISM EPF observations are able to better match the Spirit-derived spectra.

Conclusions: We validated the preliminary atmospheric corrections on CaSSIS images of the Columbia Hills region. A suite of models has been tested, all providing satisfying results, even though those derived from CRISM EPF observations of the site provided an improved correction. Such methodology will be applied to several RSL observations by CaSSIS to better analyze these features and improve their understanding. In particular, the absolute photometry of selected RSL sites and sandy deposits in their proximity will be compared in different locations. This will allow us to test two recently proposed models and understand wether RSL are aeolian sand deposits themselves, or if they are purely aeolian dust removed features. In addition, we will apply this methodology to process coordinated CaSSIS and HiRISE observations of RSL and

other surface features, allowing us to characterize diurnal reflectance variations and have insights on their formation mechanism. Preliminary results will be presented at the conference.
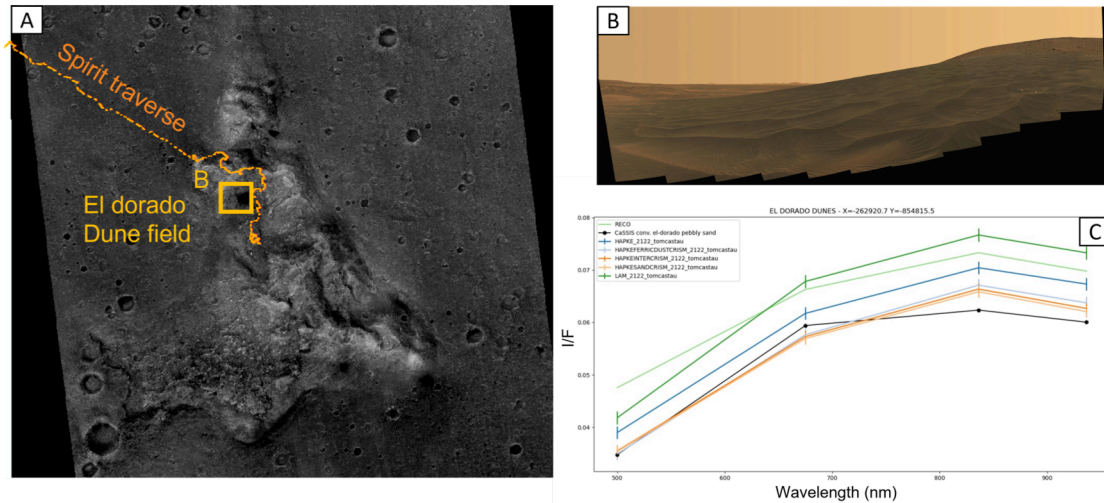
Figure 1. A) CTX image of the Columbia hills, showing the Spirit rover traverse and the location of the "El Dorado" dune field (panel B). C. Comparison between Lambert, Hapke and CRISM-derived atmospheric corrections (coloured lines) and with the I/F predicted from Spirit-derived photometric models (black profile).

Figure 2. A) CaSSIS colour composite showing one of the selected RSL sites. B) Closeup of the region where RSL in association with a sand deposits are identified.

References:
[1] Thomas et al. (2017) Space Sci. Rev. 212 (3–4), 1897–1944;[2] A. S. McEwen et al. (2007), JGR:Planets, [3] A. S. McEwen et al. (2011), Science (6043), 740–743 [4] Munaretto et al. (2020), PSS 187, (2020), 104947 [5] Munaretto, et al. (2021) PSS, 200,105198. [6] Johnson et al., 2015, Icarus, 248,25-71. [7] Fernando et al., (2013), JGR:Planets, 118, 3, 534-559 [8] Fernando et al., (2015), Icarus, 253, 271-295 [9] Tomasko, M. G. et al., (1999)Journal of Geophysical Research, Volume 104, Issue E4, p. 8987-9008

DIELECTRIC PROPERTIES OF SODIUM CHLORIDE DOPED ICE FOR THE CHARACTERIZATION OF EUROPA'S ICE SHELL *Alessandro Brin[1], Sebastian Emanuel Lauro[1], Barbara Cosciotti[1], Elisabetta Mattei[1], Elena Pettinelli[1]*

[1]Mathematics and Physics Dept., Roma Tre University

Introduction: Europa is the Jupiter icy moon target of two different future space missions, Europa Clipper [1] and JUICE [2], in search for liquid water and potential habitable worlds. Since cold ice is relatively transparent to radio waves, these two missions will employ radar sounders to probe the ice shell of the satellite. It has been hypothesized that the impurities in the ice of Europa's crust may have two different origins: exogenic, from impactors or implantation by Io's plasma torus [3], and endogenic, by accretion phenomena at the ice-ocean interface [4]. For the latter, spectra obtained using the Hubble Space Telescope revealed the presence of sodium chloride on its surface [5]. The two radars have been designed for the detection of the ocean beneath the ice crust and the possible upwelling of liquid material at shallow depths. An intensive laboratory activity is required to perform dielectric characterization of ices similar to those speculated for the Europa's crust, in order to estimate the radars signal attenuation and penetration depth, and the dielectric contrasts between ice and brines. Therefore, in this preliminary work we studied the complex permittivity of saline ice samples having different NaCl concentrations, as a function of frequency, temperature and brine volume fraction.

Methodology and ice samples preparation: All the measurements were carried out by means of an Agilent precision LCR meter HP4284A operating in the frequency range $20\,Hz - 1\,MHz$ and coupled to a parallel plate capacitive cell filled with the NaCl solutions. The equivalent circuit of the cell can be schematized by a capacitor, which represents the polarizability of the material, in parallel to a resistor, which takes into account the electric losses of the investigated material [6]. The instrument measures two quantities: the capacitance $C(\nu)$, related to the polarizability of the material, and the loss tangent $tan\delta(\nu)$ which accounts for the electric losses. Therefore, the complex permittivity $\varepsilon(\nu) = \varepsilon'(\nu) - i\varepsilon''(\nu)$ can be estimated from these quantities using two equations:

$$\varepsilon'(\nu) = \frac{C(\nu)}{C_0}$$

$$\varepsilon''(\nu) = \frac{C(\nu)}{C_0} tan\delta(\nu)$$

where C_0 is the capacitance of the empty cell.

The brine volume fraction f_b as a function of temperature has been retrieved through the following equation, obtained by generalizing the formula showed in [7]:

$$f_b(T) = \frac{\left(C_{eq}\rho_b\right)^{-1}}{\left(C_{eq}\rho_b\right)^{-1} - \left(C_{eq}\rho_i\right)^{-1} + (C_0\rho_i)^{-1}}$$

where C_{eq} is the equilibrium NaCl concentration as a function of temperature given by the sodium chloride phase diagram (see Fig.1), ρ_b is the brines density, ρ_i is the density of the ice and C_0 the initial concentration dissolved in the initial solution.
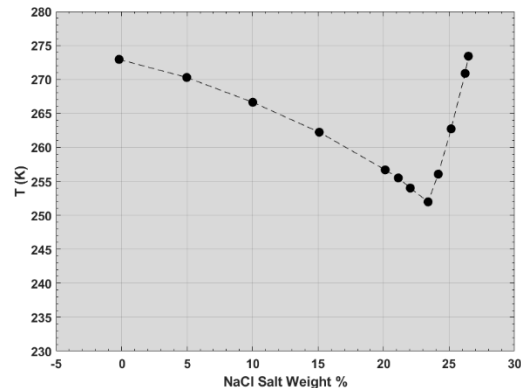
Fig. 1. Phase Diagram of sodium chloride solutions.

We prepared five different ice samples: 1) pure ice, 2) 0.1 mM, 3) 10 mM, 4) 171 mM and 5) 1 M NaCl doped ice, using an ACS Angelantoni climatic chamber in the temperature range $197 - 290\,K$. All the samples were formed directly in the measuring cell, inside the climatic chamber, using bidistilled water (obtained with the Simplicity® UV water purification system); the doped samples were prepared using the sodium chloride provided by the SIGMA-ALDRICH, weighing it on a Gibertini E 50 S/3 scale and mixing it in the water by means of a Bibby B212 hotplate stirrer.

Results: For brevity we reported only the spectra of the complex permittivity of 10 mM and 171 mM doped ice samples in Fig. 2 and 3 for five different temperatures, ranging from 230 K to 270 K. For the 171 mM sample it is evident that above the eutectic temperature of sodium chloride ($T_e = 252\,K$) the behavior of the spectrum is affected by the presence of brine water, with an abrupt increase of both real and imaginary part of permittivity.
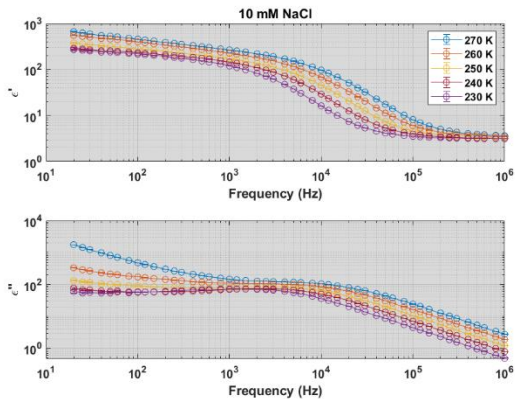
Fig. 2. Real and imaginary part of permittivity of the 10 mM NaCl doped ice sample.
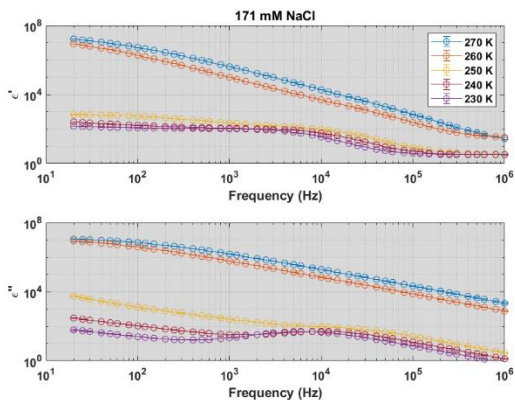
Fig. 3. Real and imaginary part of permittivity of the 171 mM NaCl doped ice sample.

We then fitted the retrieved complex permittivity in temperature with a Markov chain Monte Carlo inversion algorithm assuming a Jonscher model [8]: we have obtained in this way the relaxation frequency ν_{rel} as a function of temperature. The relaxation frequencies of the 10 mM sample were compared to those obtained in [7] for the same salt concentration (see fig. 4): our results are in good agreement with [7], thus confirming the goodness of our experimental procedure.

The preliminary results show an increase in attenuation around the eutectic temperature, particularly pronounced for high concentrated solution, suggesting that the complex permittivity is strongly dependent on brine volume fraction f_b.
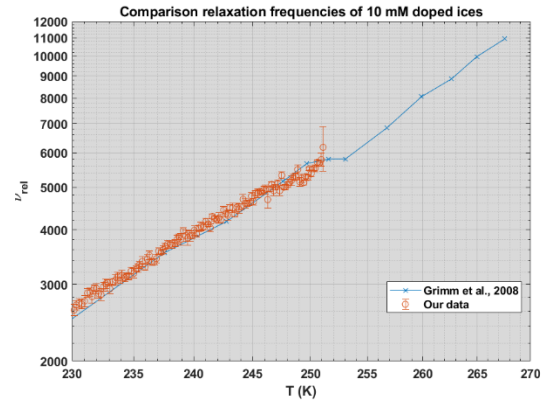
Fig. 4. Relaxation frequencies comparison between our fitting results and those shown in [7]

References: [1] Howell, S., & Pappalardo, R. (2020). Nature Communications, 11(1), 1311 [2] Grasset, O. et al. (2013). Planetary and Space Science, 78, 1-21 [3] Ligier, N. et al. (2016). The Astronomical Journal, 151(6), 163 [4] Wolfenbarger, N. et al. (2022). Journal of Geophysical Research. Planets, 127(9) [5] Trumbo, S. et al. (2019). Science Advances, 5(6), Eaaw7123 [6] Pettinelli, E. et al. (2005). Journal of Geophysical Research, 110(E4), E04013-N/a [7] Grimm, R. et al. (2008). The Journal of Physical Chemistry. B, 112(48), 15382-15390. [8] Jonscher, A. (1999). Dielectric relaxation in solids. Journal of Physics. D, Applied Physics, 32(14), R57-R70.

UNVEALING THE CHEMISTRY OF NITRILES IN TITAN'S ATMOSPHERE: THE REACTION OF EXCITED ATOMIC NITROGEN, N(^{2}D), WITH CYANOACETYLENE (HC$_3$N), ACRYLONITRILE (C$_2$H$_3$CN) AND ACETONITRILE (CH$_3$CN)

L. Mancini[1]*, M. Rosi[2], D. Skouteris[3], G. Vanuzzo[1], G. Pannacci[1], P. Liang[1], P. Casavecchia[1] and N. Balucani[1]

[1]Dipartimento di Chimica, Biologia e Biotecnologie, Università degli Studi di Perugia, 06123 Perugia, Italy;
[2]Dipartimento di Ingegneria Civile e Ambientale, Università degli Studi di Perugia, 06125 Perugia, Italy;
[3]Master-Tec srl, 06128 Perugia, Italy;
*luca.mancini2@studenti.unipg.it

.

Introduction: The study of planets or moons of the Solar System (and beyond) can be of great help in understanding the initial chemical evolution of Earth and the prebiotic chemistry that ultimately lead to the emergence of life. In the Solar System, one of the best candidates for this purpose is Titan, the largest moon of Saturn, which possesses a thick atmosphere mainly composed by molecular nitrogen (like the terrestrial one). Interesting data about Titan and its unique atmosphere became available via ground based observations (including very recent ones by the Atacama Large Millimeter/submillimeter Array, ALMA[1]) and exploratory missions, including the Pioneer 11 and two Voyager missions and, much later, the Cassini-Huygens mission. The main component of the atmosphere of Titan is molecular nitrogen (N$_2$), accounting for more than 94% of the total composition, with the remaining few percent being represented by methane (the second most abundant species) and more complex organic species in trace amounts [2]. Among them, nitriles (such as CH$_3$CN, C$_2$H$_3$CN and HC$_3$N) clearly indicates the involvement of nitrogen in the organic chemistry of Titan. Considering the high stability of the N$_2$ molecule, one of the initial steps for the chemistry of N-bearing molecules is the production of some forms of active nitrogen, including N atoms and ions (such as N$^+$, N^{2+}, N$_2^+$, and N$_2^{+2}$), formed through several process, including electron impact ionization/dissociation, extreme ultraviolet (EUV) photolysis, dissociative photoionization, and cosmic ray induced dissociation [3-5]. The reactions of atomic nitrogen, in its first electronically excited state, N(^{2}D), which represents the most reactive state, with different organic substrates are considered key processes for the formation of species holding a novel C−N bond, thus implying that N(^{2}D) reactions with hydrocarbons have a significant role in the chemistry of Titan's atmosphere. Among the nitriles detected on Titan's atmosphere, cyanoacetilene (HC$_3$N) is on of the most abundant, with a mole fraction of $3.2 \pm 0.7 \times 10^{-5}$ in the thermosphere [6,7]. Acetonitrile (CH$_3$CN) has been detected for the first time in Titan's atmosphere in 1993[8] through the IRAM telescope. The analysis of the vertical distribution[9] revealed a similar mixing ratio of acetonitrile and cyanoacetylene (equal to $\sim 4 \times 10^{-8}$ at 450 km). The first suggestion of the presence of acrylonitrile (C$_2$H$_3$CN) in the atmosphere of Titan came from the detection of the CH$_2$CHCNH$^+$ cation through the Cassini mission [6,10-12]. The ALMA detection [1] of the rotational lines of neutral C$_2$H$_3$CN in the frequency range of 230 to 232 GHz gave the final proof for the presence of acrylonitrile on Titan.

In the present contribution, we report a theoretical and experimental investigation of the reactions of atomic nitrogen, in its first electronically excited state N(^{2}D) with cyanoacetylene and acrylonitrile. Theoretical results on the reaction N(^{2}D) + CH$_3$CN will also be reported. More specifically, on the theoretical side, we have characterized the potential energy surface (PES) through optimization of the most stable stationary points and harmonic vibrational frequencies calculations at the DFT level, using the B3LYP[13,14] functional in conjunction with the correlation consistent valence-polarized set aug-cc-pVTZ[15-17]. The assignment of the identified transition states was performed through intrinsic reaction coordinate (IRC) calculations [18,19]. Subsequently, the energy of all the identified stationary points was calculated using the more accurate coupled cluster CCSD(T) theory[20-22], with the same basis set aug-cc-pVTZ. In the case of particularly meaningful stationary points (such as entrance barriers for bimolecular association processes), more accurate calculations have been performed at the CCSD(T) level corrected with a Density Fitted (DF) MP2 extrapolation to the complete basis set (CBS) and with corrections for core electrons excitations, using Martin's two parameter scheme [23]. Afterwards, using the PES stationary points, we have performed statistical (Rice−Ramsperger−Kassel−Marcus, RRKM) calculations in order to derive the product branching fractions (BFs) at different temperature, including the temperature relevant for Titan's atmosphere.

In the case of the reaction $N(^2D)$ + HC_3N and $N(^2D)$ + C_2H_3CN, the theoretical results so obtained have been used to assist the interpretation of crossed molecular beam (CMB) experiments [24] and characterize the overall reaction micromechanism. Experiments on the $N(^2D)+CH_3CN$ reaction are also planned. By combining experimental and theoretical results, we have established that the reactions with unsaturated nitriles proceed through the barrierless addition of $N(^2D)$ to the π-bond of acrylonitrile and cyanoacetylene, followed by the formation of cyclic and linear intermediates. Further isomerization processes can lead to the formation of different products, mainly related to H-displacement channel, together with the possible formation of other species including HCN and CN. Instead, in the case of the reaction with the saturated CH_3CN, the dominant approach is insertion into one of the C-H bonds. In all cases, the main reaction products are characterized by an additional nitrogen atoms in their structure.

In addition, and somewhat surprisingly, the attack of the $N(^2D)$ atom to the CN group is also feasible. This represents a peculiar observation because, in most cases, the cyano group is considered as a spectator group, that is, it is not directly involved in the reaction because of its high stability and strong triple bond. However, nitrogen atoms in the first electronically excited state possess a very high energy content and the chemical attack on the CN group becomes feasible. The N-attack on CN can lead ultimately to the formation of molecular nitrogen, in very exothermic product channels.

Nevertheless, our calculations revealed the presence of an entrance barrier for the attack of $N(^2D)$ to the CN group. In the case of the $N(^2D)+C_2H_3CN$ reaction, the addition to the lone pair of the N atom is characterized by a very small barrier (located at +0.3 kJ/mol at the CCSD(T) level of theory). A bridge attack to the triple bond is characterized by a submerged transition state located 5 kJ/mol below the reactants, implying the presence of an initial van der Waals adduct that we were not able to localize. In the case of the $N(^2D)$ + HC_3N reaction, a submerged barrier, located 7 kJ/mol below the energy of the reactants, was identified for the bridge attack to the CN triple bond. In both cases the addition of atomic nitrogen to the π-bond of the partner molecules appears to be much more competitive than the attack to the CN group, due to the presence of transition states at an energy close to that of the reactants, which certainly reduces the reactive flux. In the case of the $N(^2D)$ + CH_3CN reaction, preliminary results shows the presence of a submerged barrier for the attack of the $N(^2D)$ atom to the CN group. Also in this case, the preferential approach is represented by

the insertion of atomic nitrogen into one of the C-H bonds, leading to different product channels, mainly related to H-displacement processes. However, this new reaction path can become significant at high temperatures.

The theoretical predictions for the case of $N(^2D)$ + HC_3N and C_2H_3CN are in line with the experimental data on the H-displacement channels leading to the formation of a variety of possible isomeric products. No experimental evidence for the N_2 forming channel was obtained. In conclusion, the title reactions lead mainly to the formation of cyclic and linear products containing an additional C−N bond. Since aerosols surrounding Titan are made by organic macromolecules very rich in nitrogen, the title reactions can give a contribution towards their formation.

References:

[1] Palmer M. Y. et al. (2017) *Sci. Adv.,* 3.[2] Vuitton V. et al. (2014) *Cambridge Planetary Science; Cambridge University Press*, 224-284.[3] Dutruit O. et al. (2013) *Astrophys. J. Suppl. Ser. 204, 20.*[4] chang Y. et al. (2019) *J. Phys. Chem. A,* 123, 2289-2300.[5] Lavvas P. et al. (2011) *Icarus, 213*, 223-251. [6] Cui J. et al. (2009) *Icarus, 200*, 581. [7] Cordiner M. A. et al. (2018) *Astrophys. J. Lett., 859*, L15.[8]Bézard B. et al. (1993) *Bull. Am. Astron. Soc.*, 25, 1100. [9] MArten A. et al (2002) *Icarus*, 158, 532-544. [10] Vuitton V. et al. (2007) *Icarus, 191*, 722-742. [11] Magee B. A. et al. (2009) *Planet. Space Sci., 57*, 1895-1916. [12] Bézard B. et al. (2009) *Cambridge Planetary Science; Cambridge University Press, 158-189*. [13] Becke A. D. (1993) *J. Chem. Phys.,* 98, 1372-1377. [14] Stephens P. J et al. (1994) *J. Phys. Chem.,* 98, 11623−11627 . [15] Dunning T. H. (1989) *J. Chem. Phys.,* 90, 1007-1023. [16] Woon D. E. et al. (1993) *J. Chem. Phys.,*98, 1358-1371. [17] Kendall R. A. et al. (1992) *J. Chem. Phys.,* 96, 6796-6806. [18] Gonzalez C. et al. (1990) *J. Phys. Chem.,* 94, 5523-5527. [10] Gonzalez C. et al. (1989) *J. Chem. Phys.,* 90, 2154-2161. [20] Bartlett R. J (1981) *Annu. Rev. Phys. Chem.,* 32, 359-401. [21] Raghavachari K. et al. (1989) *Chem. Phys. Lett.,* 157, 479-483. [22] Olsen J. et al. (1996) *J. Chem. Phys.,* 104, 8007-8015. [23] Martin J. M. et al. (1996) *Chem. Phys. Lett.,* 259, 669-678. [24] Casavecchia P. et al. (2015) *Int. Rev. Phys. Chem.,* 34, 161-204.

AEOLIAN LANDFORMS IN THE EXOMARS LANDING SITE, A REGIONAL PERSPECTIVE. S. Silvestro[1,2], D.A. Vaz[3], M. Chojnacki[4], A. Pacifici[5], D.C.A. Silva[3], A. Botteon[5], D. Tirsch[6], F. Salese[7], C.I. Popa[1], M. Pajola[8], G. Franzese[1], G. Mongelluzzo[1], F. Cozzolino[1], C. Porto[1], F. Esposito[1]. [1]INAF, Osservatorio Astronomico di Capodimonte, Napoli, Italy (simone.silvestro@inaf.it). [2]SETI Institute, Mountain View, CA, USA. [3]CITEUC, University of Coimbra, Portugal. [4]Planetary Science Institute, Lakewood, CO, USA. [5]IRSPS, Università G. d'Annunzio, Chieti-Pescara, Italy, [6]Institute of Planetary Res., DLR, Berlin, Germany. [7]Centro de Astrobiología, CSIC-INTA, Madrid. [8]INAF, Osservatorio Astronomico di Padova, Italy.

Introduction: The ExoMars mission is set to land in Oxia Planum (18.2° N; 24.3° W) to search for signs of past or present life on Mars [1, 2]. Dust devil tracks, aeolian megaripples or transverse aeolian ridges (TARs) and erosive wind-features named periodic bedrock ridges (PBRs) have been described in and around the landing site suggesting that the wind action had, and still has, a key role in shaping the surface [3, 4]. Here we push our investigation further by looking for other aeolian features in the landing area and, to put these observations into an appropriate atmospheric context, we analyze aeolian features in McLaughlin and Oyama, two impact craters located ~200 km and ~400 km NE from the landing area respectively (Fig. 1a).
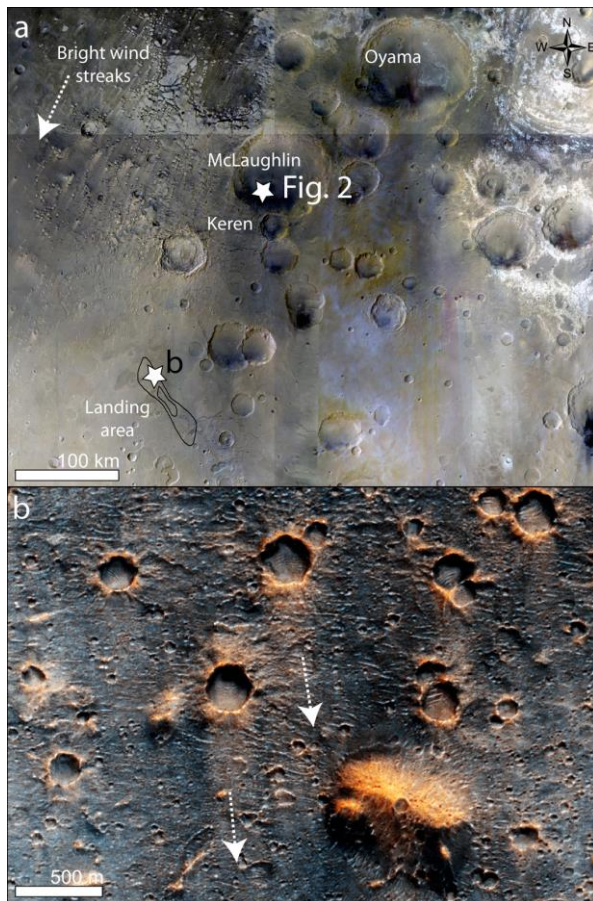
Fig. 1: a) Study area, note the bright-toned streaks indicating the regional winds (HRSC color mosaics). **b)** Wind streaks in the landing area (CaSSIS RGB image MY35_007623_019_0).

Methods: The landing area and its surrounding were analyzed with HRSC, CaSSIS, CTX and HiRISE images in a GIS environment. Dune movement was tracked on orthorectified HiRISE time-series in McLaughlin and Oyama craters and sediment fluxes were computed using the method of [5].

Results: Previous work has highlighted the presence of a complex aeolian pattern in the landing area formed by differently oriented PBRs and TARs [3, 4]. Modern wind directions were deduced from dust devil track orientations, indicating winds blowing from the W-WNW or E-ESE [4]. Thanks to the careful analysis of CaSSIS and HiRISE images, here we report the presence of bright- and dark-toned aeolian streaks indicating winds originating from the NNW-NNE (Fig. 1) and from the E-ESE. Wind streaks having similar orientations are visible outside the landing ellipse suggesting a regional nature for these flows. *McLaughlin and Oyama.* McLaughlin is a 92-km-large crater with a depth of 2.2 km. Like the landing area, its floor shows fan deposits and an enrichment in clay minerals [6, 7]. Here we highlight another important similarity, the presence of the same PBRs/TARs complex pattern reported in Oxia. TARs show dark banding on their SE slopes which can be due to aeolian sorting of loose sands of different granulometry and/or composition and suggesting different formative winds than previously suggested (Fig. 2) [3].

A field of high-flux barchans [8] is accumulated on the crater's southern floor over the ejecta of Keren crater [6, 7]. The ejecta deposit represents a roughness element that is controlling the accumulation of the dunes in this area (Fig. 3a). Previous flux estimations computed on a 2008-2016 image couple [8] are refined here using a co-registration algorithm, which computes the bedrock apparent displacements and corrects the location of the advancing slipfaces. Dune flux (median=3.1 m^2 yr^{-1}) is strongly controlled by the local topography like other areas on Mars [9, 10] (Fig. 3a, b). Dune morphology and migration direction are consistent with the wind streaks visible in the area (Figs. 1 and 3a). Even in Oyama, a 100-km large (~2 km-deep) impact crater (Fig. 1a), we found evidence for a set of regularly spaced E-W trending PBRs underlying a field of scattered barchans.

Dunes migrated toward the South in a 2013-2019 time-range with a flux (median=3 m^2 yr^{-1}) similar to McLaughlin.

Discussion: By identifying PBRs and TARs outside the landing area, we show that winds that formed these features in Oxia Planum were common across the region. This indicates that the wind that eroded the PBRs was not localized, but rather part of a persistent regional wind regime and that even the wind directional change that leaded to the accumulation of TARs was regional in nature.

Dune migration orientations and fluxes in McLaughlin and Oyama, together with the presence of southerly-oriented wind streaks, indicate that even present day winds in the landing area are blowing regionally. A preliminary analysis of Global Circulation Model (GCM) output from the Mars Global Digital Dune Database (MGD³) [11] show that these winds are predicted to blow in northern autumn, between L_S 235° and 258°. A close inspection of the complex PBR/TAR pattern by the ESA Rosalind Franklin rover, will shed light on PBR formation mechanism [12, 13], TARs formative winds and Martian climatic changes [3, 14, 15].

Fig. 2: Dark bands due to aeolian sorting over a dune slope at Great Sand Dunes, Colorado (USA). Dark bands reported over TARs in Oxia might have a similar origin. Photo by the author.

References: [1] Vago J. et al. (2017). *Astrobiology, 17*(6–7), 471–510. [2] Quantin et al. (2021), *Astrobiology*, 21, 3. [3] Silvestro S. et al. (2021), *GRL, 48,* 4. [4] Favaro E. et al. (2021), *JGR, 126,* 4, e2020JE006723. [5] Urso A. et al. (2018). *JGR, 123,* 353–368. [6] Michalski J.R. et al. (2013), *Nat. Geo., 6*, 2. [7] Michalski J.R. et al. (2019), *JGR. 124,* 2. [8] Silvestro S. et al. (2020), *JGR, 125,* e2020JE006446. [9] Vaz D.A. et al. (2017), *Aeol. Res. 26,* 101-116. [10] Chojnacki M. et al. (2018), *JGR, 123,* 2, 468-488. [11] Hayward R. et al. (2007), *JGR, 112,* E11, 1-17. [12] Montgomery D.R. et al. (2012), *JGR, 117,* E03005. [13] Hugenholtz C.H. et al. (2015), *Aeol. Res., 18,* 135–144. [14] Golombek M. et al. (2010), *JGR, 115(E7)*, 1-34. [15] Fenton L.K. et al., (2018), *JGR, 123(4)*, 1–15.
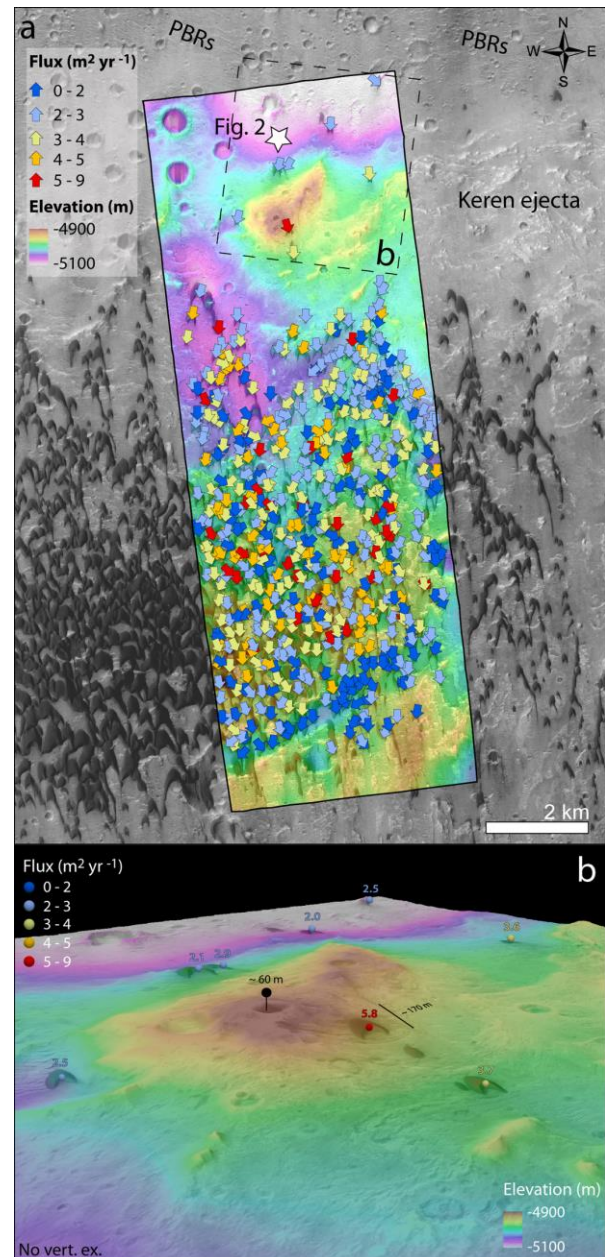
Fig. 3: a) Dune migration in McLaughlin crater. **b)** Note the varying flux for the dunes upwind and downwind the ~ 60 m topographic high (HiRISE ESP_045312_2020_RED in transparency over DTM DTEEC_036859_2020_036569_2020_A01).

UBIQUITY OF LANDSLIDES IN THE SOLAR SYSTEM

M. T. Brunetti[1] and S. Peruccacci[1]
[1]Consiglio Nazionale delle Ricerche–Istituto di Ricerca per la Protezione Idrogeologica, Via della Madonna Alta 126, 06128 Perugia (Italy). E-mail address: maria.teresa.brunetti@irpi.cnr.it.

Introduction: Landslides are mass movements of rocks, soil or debris that occur under the influence of gravity. In the extraterrestrial environment, these structures were first observed in a lunar crater, but mass movements affect almost all solid bodies, including planets, moons, asteroids and comets.

Rock and icy surfaces in Solar System bodies are modified by various processes, such as tectonics, volcanism, impact cratering, weathering, and erosion. They act to a greater or lesser extent depending on the complexity of the body, which is mainly a function of its size [1]. In general, surface processes overlap and interact with each other and may predispose slopes to landslides or may themselves act as triggers for landslides.

As on Earth, landslides observed on solid bodies of the Solar System are classified according to the mechanism of mass displacement and the material involved, that may be rock or soil (or both) mixed with water or ice. Types of movement are falling, toppling, sliding, spreading, or sliding, and a combination of them. The variability of landslide characteristics is reflected in their size (e.g., area, volume, fall height, length), which can vary by orders of magnitude.

By comparing mass movements observed on various bodies in the Solar System, it is possible to analyze the effects of specific body characteristics, such as surface gravity, atmospheric pressure (if present) or the presence of water (in different physical states) on the initiation and propagation of landslides. This can be of great importance in view of manned and unmanned missions involving landings.

The following is a brief review of landslides observed in the extraterrestrial environment, grouped by solid body type.

Terrestrial planets: On the Moon, mass movements were first studied using photographs from the Apollo 10 mission [2]. Improved spatial resolution of the images collected by the Lunar Orbiter program made it possible to recognize gullies on the lunar surface [3]. Gullies were also investigated using data from Chandrayaan-1 and Lunar Reconnaissance Orbiter (LRO) [4]. A systematic classification of lunar mass movements was proposed later using LRO images [5]. An inventory of large rock slides in lunar craters was compiled using the same high-resolution images [6]. Data from LRO together with data from the SELENE-Kaguya probe enabled to study granular avalanches on

the Moon [7]. LRO data were also used by several authors to analyze boulder tracks [8–10].

On Mars, the giant landslides of the Valles Marineris (VM) canyon system were first observed by the Mariner 9 probe [11] and shortly thereafter by the Viking orbiters [12]. The study of Martian landslides began with some pioneering work that analyzed the morphology, rupture mechanism, geology, and age of the sites and compared the landslides with those on Earth. [13,14]. The geometric characteristics of landslides in VM were analyzed using images acquired by the Mars Global Surveyor and a classification of the failures was proposed, based on the morphological characteristics of the landslide deposits [15]. Using data from the Mars Reconnaissance Orbiter (MRO) and adopting the same classification used for terrestrial landslides, a comprehensive geomorphological inventory of the western part of the VM was compiled [16]. A global inventory of landslides on the planet, including the flanks and caldera of the 24-km-high Mons Olympus was obtained few years later [17]. Several authors have studied rock falls and the trajectories of boulders on the surface of Mars (e.g., [18], [19]).

On Venus, rock collapses, rock and/or block landslides, rock avalanches, debris avalanches and possibly debris flows in tectonic features around the equatorial region were observed by analyzing radar images of the surface obtained by the Magellan probe [20].

On the airless Mercury, large rock slides in impact craters were identified and mapped using images from the MESSENGER spacecraft [6].

Planetary moons: In the late nineties, the Galileo probe captured images of landslides on the icy Galilean satellites of Jupiter, Europa, Ganymede, and Callisto [21]. In particular, Callistan lobate deposits were found to be morphologically similar to rapidly emplaced dry-rock avalanches on Earth [22].

Among the moons of Mars widespread mass movements of regolith have been observed in the craters of Phobos thanks to images acquired by MGS and the Viking orbiter [23].

Long-runout landslides were captured by the Cassini mission on Saturn's moons Iapetus and Rhea [24] and by the New Horizons mission on Charon, the Pluto largest moon [25].

Dwarf planets: Landslides on Ceres exhibit a wide range of morphologies: among these, three main flow-like mass movement features have been identified

[26]. High-resolution images collected by the Dawn probe revealed many mass movements, which were classified into three morphological classes: slumps, slides, and flow-like movements [27].

Asteroids: Slides and slumps in craters of asteroid Mathilde were recognized in the late 1990s, by analysing images taken by Near Earth Asteroid Rendezvous (NEAR) Shoemaker probe [28].

The NEAR Shoemaker probe detected active regolith on the surface of Eros, which was modified and redistributed by gravity-driven gradient processes. The most evident landforms indicative of landslide-like movements were observed along the slopes of the largest craters [29].

Significant surface structures (craters, lineaments, landslides, escarpments, and boulders) were revealed by the Rosetta probe during the Lutetia flyby. Notably, there was clear resurfacing through landslides at many locations on the asteroid, including the North Pole [30].

Using Dawn data, three different sets of mass wasting features: (1) slump blocks, (2) spur-and-gully morphologies and (3) landslides in craters were identified in northern rim of the giant Rheasilvia basin [31].

Sliding processes are the main mass movements on Vesta, due to the numerous steep slopes and the presence of a very thick layer of regolith [27].

Comets: The surface of comets has an irregular shape due to the periodic sublimation of ice that occurs when the comet passes close to the Sun. Several rock/ice avalanches resulting from the collapse of steep cliffs were detected by the Rosetta mission on comet Churyumov-Gerasimenko (67P) matching pictures of the surface captured before and after the comet proximity to the Sun [32].

Conclusions: This brief review shows that landslides are ubiquitous in the Solar System. Their presence demonstrates the continuous dynamic evolution of the surfaces of solid bodies. Mass movements are one of the most interesting geologic features because by exposing fresh material they also allow us to study the subsurface composition of extraterrestrial bodies.

References

[1] Melosh H. J. (2011) *Planetary surface processes*, 13 CUP. [2] Pike R. J. (1970) *NASA Spec. Publ.*, 232, 14. [3] Bart G. D. (2007) *Icarus*, 187(2), 417–421. [4] Senthil Kumar P. et al. (2013) *J Geophys Res Planets*, 118(2), 206–223. [5] Xiao Z. et al. (2013) *Earth Planet Sci Lett*, 376, 1–11. [6] Brunetti M. T. et al. (2015) *Icarus*, 260, 289–300. [7] Kokelaar B. P. (2017) *J Geophys Res Planets*, 122(9), 1893-1925. [8] Senthil Kumar P. et al. (2019) *Geophys Res Lett,* 46(14), 7972–7981. [9] Ruj T. et al. (2022) *Icarus*, 377, 114904. [10] Bickel V. T. (2020) *IEEE J Sel Top Appl Earth Obs Remote Sens*, 13, 2831–2841. [11] Sharp R. P. (1973) *J Geophys Res 1896-1977*, 78(20), 4063–4072. [12] Blasius K. R. (1977) *J Geophys Res 1896-1977*, 82(28), 4067–4091. [13] Lucchitta B. K. (1979) *J Geophys Res Solid Earth*, 84(B14), 8097–8113. [14] McEwen A. S. (1989) *Geology*, 17(12), 1111–1114. [15] Quantin C. et al. (2004) *Planet Space Sci*, 52(11), 1011–1022. [16] Brunetti M. T. et al. (2014) *Earth Planet Sci Lett*, 405, 156–168. [17] Crosta G. B. et al. (2018) *Earth Space Sci*, 5(4), 89–119. [18] Roberts G. P. et al. (2012) *J Geophys Res Planets*, 117(E2). [19] Tesson P.-A. et al. (2020) *Icarus*, 342, 113503. [20] Malin M. C. (1992) *J Geophys Res Planets*, 97(E10), 16337–16352. [21] Moore J. M. et al. (1999) *Icarus*, 140(2), 294–312. [22] Chuang F. C. and Greeley R. (2000) *J Geophys Res Planets*, 105(E8), 20227–20244. [23] Shingareva T. V. and Kuzmin R. O. (2001) *Sol Syst Res*, 35(6), 431–443. [24] Singer K. N. et al. (2016) *Nat Geosci*, 5(8), 574–578. [25] Beddingfield C. B. et al. (2020) *Icarus*, 335, 113383. [26] Schmidt B. E. et al. (2017) *Nat Geosci*, 10(5), 338-343. [27] Parekh R. et al. (2021) *J Geophys Res Planets*, 126(3). [28] Thomas P. C. et al. (1999) *Icarus*, 140 (1) 17–27. [29] Chapman C. R. et al. (2002) *Icarus*, 155(1), 104–118. [30] Marchi S. et al. (2012) *Planet Space Sci*, 66(1), 87–95. [31] Krohn K. et al. (2014) *Icarus*, 244, 120–132. [32] Lucchetti A. et al. (2019) *Geophys Res Lett*, 46(24), 14336–14346.

GEOLOGICAL MAPPING AND PRELIMINARY SPECTRAL ANALYSIS OF MARE INGENII BASIN.

G. Tognon[1], G. Salari[2], F. Zambon[2], L. Giacomini[2], J-Ph. Combe[3], M. Massironi[1,4], F. Tosi[2], R. Pozzobon[1], G. Rinaldi[2], S. Fonte[2], [1]Dipartimento di Geoscienze, Università degli Studi di Padova, Via Gradenigo 6, 35131 Padova, Italy, [2]Istituto Nazionale di Astrofisica (INAF), Istituto di Astrofisica e Planetologia Spaziali (IAPS), Via del Fosso del Cavaliere 100, 00133 Roma, Italy, [3]Planetary Science Institute (PSI), 1700 East Fort Lowell, Suite 106 Tucson, AZ, [4]Centro di Ateneo di Studi e Attività Spaziali (CISAS), Università degli Studi di Padova, Via Venezia 15, 35131 Padova, Italy.

Introduction: The Ingenii basin is a Pre-Nectarian impact structure [1] of about 330 km in diameter located on the NE portion of the South Pole Aitken basin. In its interior, the basin presents one of the few basaltic maria occurring on the lunar far side. Mare Ingenii, which only partially covers the floor of the basin, was generated from two adjacent younger craters, Thompson and Thompson M, lying within the Ingenii basin.

In stark contrast with the dark color of the basalt, there are high albedo twisting morphologies indicating a swirl, a lunar feature related to crustal magnetic anomalies whose origin is still debated [2, 3, 4]. Yet another interesting feature within Mare Ingenii is represented by its pit [5, 6, 7], a ~130 m in diameter steep-walled hole located inside Thompson M, which allows a glimpse of the different layers of regolith and basalts constituting the mare and of the boulders lying at the feet of the pit. Moreover, in terms of exploration, pits represent natural shelters against the space environment and thus constitute ideal sites for building human settlements and investigating the lunar volcanic history and evolution, especially through robocrane missions [8].

Here, we present a geological and compositional analysis of the Ingenii basin. A detailed geological mapping has been carried out and followed by a preliminary spectral analysis of the most representative areas of the basin.

Data and methods: The geologic mapping of the Ingenii basin was produced based on the Lunar Reconnaissance Orbiter Wide Angle Camera global mosaic [9] together with elevation data from the Lunar Orbiter Laser Altimeter and Kaguya Terrain Camera merged Digital Elevation Model [10]. A first integration with compositional information, in particular for the basaltic infilling, was performed on the basis of the Clementine UVVIS Warped Color Ratio mosaic (Red: 750/415 nm; Green: 750/1000 nm; Blue: 415/750 nm) [11] which allows a preliminary compositional discrimination of the different materials.

A preliminary mineralogical characterization was done with the Chandrayaan-1/Moon Mineralogy Mapper [12] by processing the calibrated and photometrically corrected data [13, 14, 15]. For distinguishing representative areas with similar spectral characteristics, we identified several Regions Of Interest (ROIs) based on reflectance and other spectral parameters such as absorption band centers, absorption band depths, and spectral slopes. We selected 29 ROIs and we divided them as dark maria regions (showing a homogeneous and smooth aspect with low albedo), swirl regions (showing a heterogenous aspect and high albedo), intermediate albedo regions, and isolated small craters (presenting bright materials).

We then analyzed the main spectral parameters (i.e. band centers, band depths, reflectance at 0.58 µm, global spectral slope, band area ratio, FeO and TiO_2 abundance, Clementine-like color mosaic) to better identify the spectral variability across Mare Ingenii.

Results: Compositional information derived from the Clementine UVVIS Color Ratio mosaic allowed to identify different flooding events characterized by different compositions (e.g. lower and higher TiO_2 content) and superimposed by the bright albedo deposits of the swirl.

The four types of ROIs, each correlated with distinct geologic units, display specific spectral properties that clearly highlight a lithology dominated by pyroxenes phases. A comparison of the continuum-removed reflectance spectra highlights different ranges of absorption for each unit, with the bright materials of the small craters showing the largest band depth values, consistent with optically fresh or relatively less weathered materials, and the smallest band centers values (BCI= 0.92-0.94 µm; BCII= 1.91-1.98 µm). Conversely, dark materials of the mare exhibit larger variability in band depths but have band centers shifted towards longer wavelengths, characteristic of more Ca-rich pyroxenes. Swirl and intermediate regions have a spectroscopic behavior that falls in between bright and dark terrain units.

Conclusions: A first compositional analysis for the Ingenii basin emphasizes the presence of distinct regions characterized by different spectral properties and well correlated with geologic units. In particular, the dark maria, swirl and intermediate regions seem to be characterized by a more pigeonitic to augitic composition with respect to the Ca-free pyroxene abundance of the isolated small craters regions. Further analyses will help in better understanding the mineralogical and

compositional variability within Ingenii and its importance in terms of future exploration.

References: [1] Wilhelms D. (1987) US Geol. Surv. Prof. Pap., 1348. [2] Pinet P.C. et al. (2000) JGR, 105, 9457-9475. [3] Hood L.L. et al. (2001) JGR, 106, 27825-27839. [4] Garrick-Bethell I. et al. (2011) Icarus, 212, 408-492. [5] Haruyama J. et al. (2009) Geophys. Res. Lett., 36, L21206. [6] Martellato E. et al. (2013) Planet. and Sp. Sci., 86, 33-44. [7] Wagner R.V. and Robinson M.S. (2021) LII LPSC, Abstract #2548. [8] Miaja P.F. et al. (2022) Acta Astronautica, 192, 30-46. [9] Robinson M.S. et al. (2010) Space Sci. Rev., 150, 81–124. [10] Barker M.K. et al. (2016) Icarus, 273, 346-355. [11] Lucey P.G. et al. (2000) JGR, 105, 20377-20386. [12] Pieters C.M. et al. (2009) Current Science, 96, 500-505. [13] Boardman J.W. et al. (2011) JGR, 116, 1-15. [14] Clark R.N. et al. (2011) JGR, 116, E00G16. [15] Besse S. et al. (2013) Icarus, 222, 229-242.

POSSIBLE VOLCANIC ORIGIN FOR "MOUNDS" OF THE HYPANIS FAN SYSTEM, MARS: MAGMATIC vs SEDIMENTARY. A. Caramanico[1,2], G. Komatsu[1], M. Pondrelli[1], L. Marinangeli[2], A.C. Tangari[2] [1]IRSPS, Università d'Annunzio, Pescara, Italy, agnese.caramanico@alumni.unich.it [2]DiSPuTer, Università d'Annunzio, Chieti, Italy.

Introduction: Mars is one of the most studied planets in our solar system, although at present day many uncertainties remain about its geological history and evolution through time. One of these is the presence of sedimentary volcanism manifestation on the surface: the level of knowledge and remote sensing dataset we have today are not sufficient to prove, without any doubt, if such a phenomenon happened on Mars. Moreover, the problem of equifinality (different geological processes produce similar landforms [1]) made the research even more complicated. Being able to confirm the presence of sedimentary volcanism would be extremely important: it can help understanding the processes of sedimentation, water saturation, fluid and gas movement in the crust [2], and also probing the subterranean environmental conditions of Mars, more suitable for life or biological activity than the hostile surface. Furthermore, detailed remote sensing study for identification of "potential" sedimentary volcanism features is a necessary step in order to make a proper selection of promising future landing sites [3, 4].

This work can be considered as a geological investigation on the area of Hypanis fan system in the western Chryse Planitia (Figure 2), with the purpose to give useful insight about origins of hundreds of meters to kilometers wide mounds (Figure 1) discovered there. The first step is to focus on collecting available data and making objective observations regarding the geology of the zone, then the second step is interpretation and formulation of hypotheses that fit with the geological context using the multiple hypotheses approach. The aim is to analyze the possible sedimentary volcanism genesis of the Hypanis mounds, from remote sensing observations to the building of plausible hypotheses, in order to achieve interesting considerations about an area potentially important from both geological and astrobiological points of view. Equifinality's issue is taken into serious account, as a guidance on how to investigate and approach the scientific problem: there are many possibilities, crucial in terms of reasonable comparisons, which could form the base of discussion regarding the mound formation. Indeed, two main hypotheses prevail over the others: sedimentary and magmatic/phreatomagmatic volcanism. Due to the poor high-resolution and spectral data coverage of the zone, we suggest that further studies should be performed. Dataset improvements would be required for better understanding the nature of mounds and give a more solid base of the interpretation.
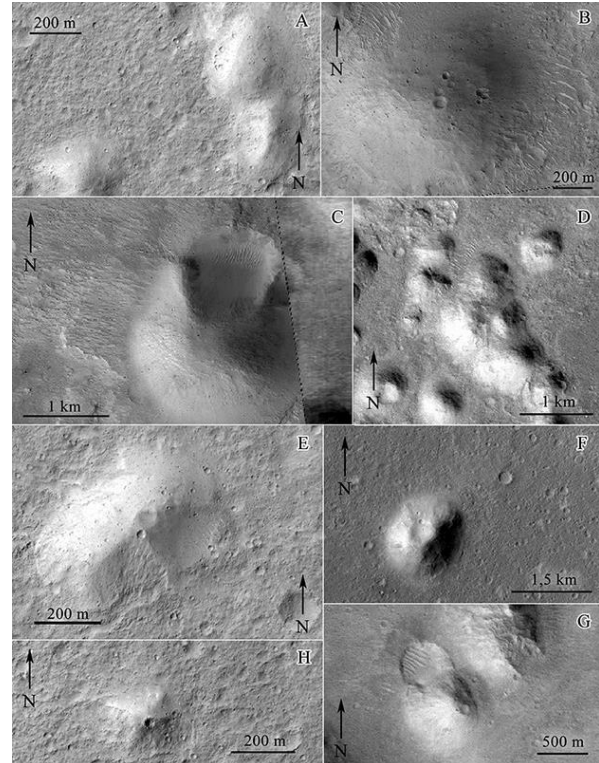
Figure 1 – examples of different kind of mounds found in the study area (A, B, E, H from CTX dataset, C, D, F, G from HiRISE dataset)

Satellite digital dataset: During the research, several satellite data at different space resolution were used starting from the large scale then moving to more detailed scales. The HRSC dataset (average resolution about 50 m/pixel) from the MEX (Mars Express) mission represents the base for building the geological map of the area and the identification of mounds around Hypanis sedimentary body. THEMIS (Thermal Emission Imaging System) nighttime infrared dataset (100 m/px) from ODY (Mars Odyssey) mission is also used to better constraint the units possibly related to grain size and/or compositional differences. Then, a combination of HiRISE DTMs (Digital Terrain Models) (~1 m/pixel) obtained thanks to MRO (Mars Reconnaissance Orbiter) mission and CTX images (5,59 m/pixel) is useful for better understanding the stratigraphic relationships between units.

Due to the complexity of the area, a space/space diagram obtained from a cropped portion of MOLA (Mars Orbiter Laser Altimeter) (463 m/pixel) dataset is
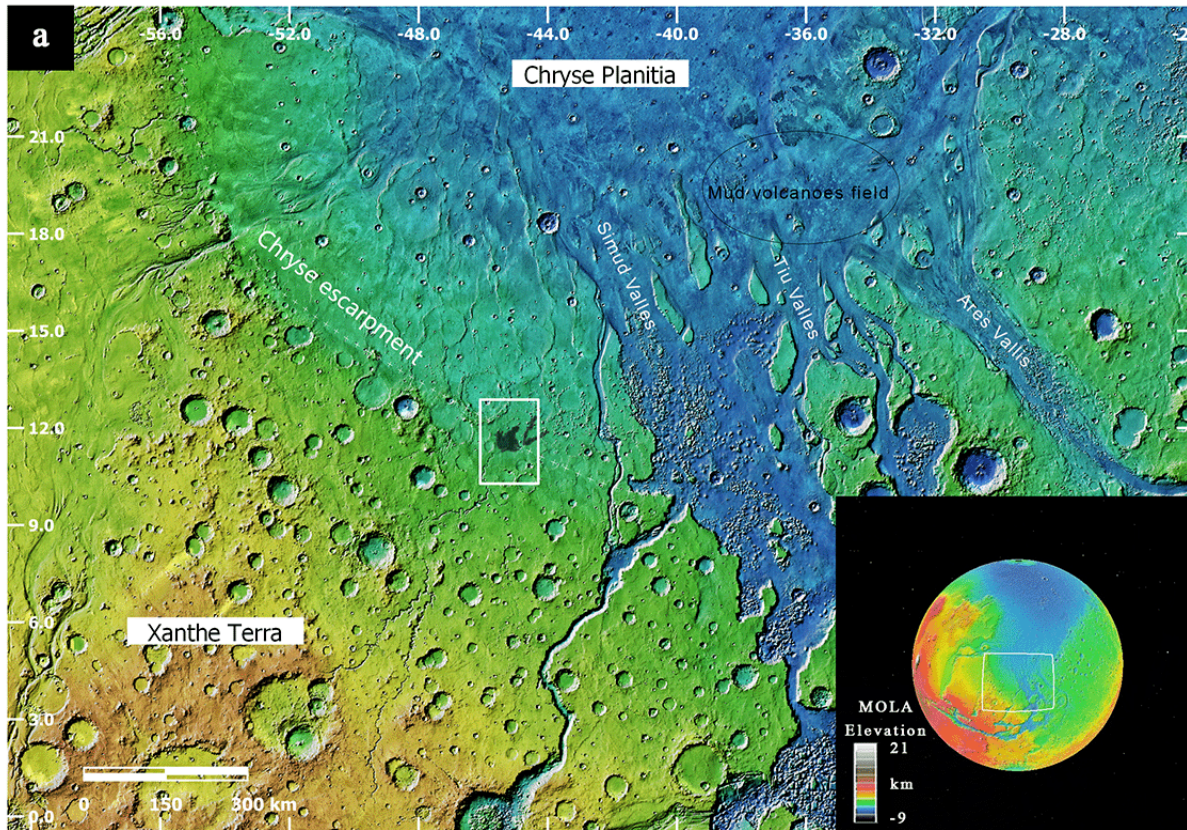
Figure 2 – MOLA+THEMIS IR blend image showing Chryse Planitia and the highlands of Xanthe Terra (a), with the geographic location of the study area (the white rectangle, the shape of the fan body is marked in black); in the circle above, a possible field of mud volcanoes (*Komatsu et al. 2016*)

produced, showing the relative altimetric positions of units and giving an idea of regional topography.

All the dataset used in this work are obtained using the Mars Orbital Data Explorer on the PDS Geoscience Node (*https://ode.rsl.wustl.edu/mars/indexMap Search.aspx*) and PILOT USGS interface for the research of CTX stereopairs (*https://pilot.wr.usgs.gov/ #navigation*). All data have been integrated into the QGIS platform (ver. 3.16) and co-registered in the geographic coordinate system for Mars in an equirectangular projection (Mars_Equi Sphere, central meridian 0). The mapping process was performed on the HRSC image using the tool "Mappy" of QGIS, at a scale of 1:35.000, while the restitution scale is 1:114.000 on the equirectangular projection.

References: [1] Komatsu G. (2007) Rivers in the Solar System: Water is not the only fluid flow on planetary bodies. *Geography Compass, 1/3,* 480-502. [2] Komatsu G. et al. (2014) *Astrobiological Potential of Mud Volcanism on Mars. #1085, Lunar and Planet. Sci. Conf. 45th.* [3] Komatsu G. et al. (2016) *Small edifice features in Chryse Planitia, Mars: Assessment of a mud volcano hypothesis. Icarus 268,* 56-75. [4] Komatsu G., *Brož P.* (2021) *Southern Chryse Planitia on Mars as a potential landing site: investigation of hypothesized sedimentary volcanism. #1164, Lunar and Planet. Sci. Conf. 52th.*

On the nature of the Dark Resistant Unit (DRU) in the Oxia Planum area, Mars

M. Formisano[1], F.Altieri[1], A. Frigeri[1], M.C. De Sanctis[1], C. Federico[1], G. Magni[1], E. Ammannito[2], S. De Angelis[1], M. Ferrari[1]
[1]INAF-IAPS, Via del Fosso del Cavaliere 100, Rome (Italy) (email: michelangelo.formisano@inaf.it)
[2]Italian Space Agency (ASI), Rome (Italy)

Introduction: Oxia Planum is the landing site for the European Rosalind Franklin (RF) rover planned to land on Mars in the next decade, with the main target of searching for traces of (present and/or past) life on Mars [1]. The landing site is located at a latitude of 18°N at the margin of Chryse Planitia basin. The major characteristic of the area is that it is geologically old and with evidences of a paleo-environment where water played a key role [2] and led to the formation of clay-bearing terrains [3,4]. Oxia Planum's thermal state is a matter of debate since in the literature, we find several estimates of the thermal inertia. The aim of this work is to characterize from a thermophysical point of view the Dark Resistant Unit (DRU) characterizing the Germania Lacus region [5] in Oxia Planum, providing new insights to constrain the nature of the material which compose this unit.

Numerical Modeling: Planetary surface temperature is governed by the energy balance (e.g. [4]):

$$S_c\,(1-a)\,cos(z) + Q_{SH} = -K\vec{n}\cdot\vec{\nabla}T + \varepsilon\sigma T^4,$$

where S_c is the solar constant, a the albedo, z the incidence angle, Q_{sh} is the self-heating term, K the thermal conductivity, T the temperature, ε the emissivity and σ the Stefan-Boltzmann constant. The illumination conditions are calculated accordingly [6]: in addition to the direct sunlight, we included the self-heating effect between the facets of the mesh covering our domain of integration (see Fig.1).
The selected domain of integration is a portion of Oxia Planum, 2 km x 0.6 km, with a mean average height of 50 m. This region, since is not completely flat but is characterized by the small craters, allows us to quantify the effect of the self-heating.
We characterized the DRU with the typical parameters of the basalt, assuming a porosity-dependent thermal conductivity. As an additional case, we also tested a composition made of pebbles. The numerical model developed here represents a follow-up of the work recently published in [7].

Results: In Fig. 2 we report, for example, the surface temperature maps for the case characterized by a composition made of pebbles and τ = 0.1, at selected times during the Martian day.
In this scenario, surface temperature ranges from 190 K to 250 K. Temperature oscillations are wide since the "low" thermal inertia that characterizes this composition, i.e. about 500 TIU. On the contrary, in case of a basalt composition, the thermal inertia is greater than 1000 TIU and the temperature variability range is very small (about 20 K).
In some ridges of the craters the temperature is higher than the other regions, due the contribution of the self-heating effect.
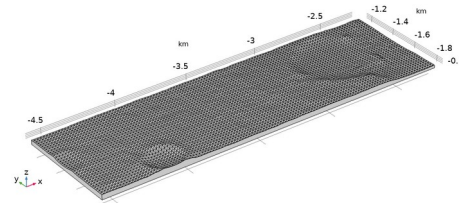
Fig. 1 *Domain of integration of this work: a portion (2 km x 0.6 km) of Oxia Planum.*
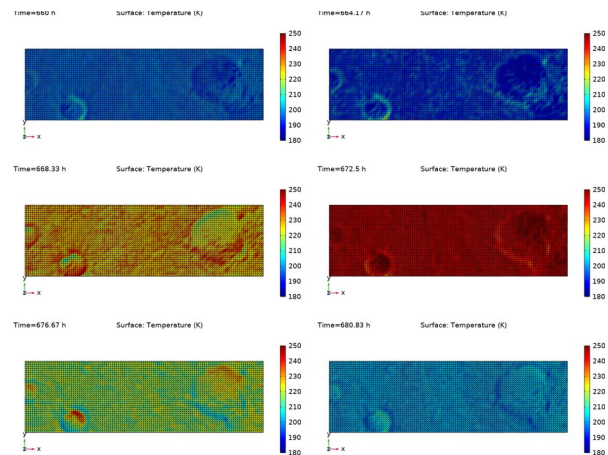
Fig. 2 *Example of surface temperature maps for the pebbles composition and τ=0.1, at selected times during the Martian day.*

Conclusions: By comparing the thermal inertia of the two scenarios developed in this work – basalt and pebbles composition – with the values provided by the Thermal Emission Imaging System (THEMIS) [8], we believe that the pebbles composition is the most likely scenario. In this case, the surface temperatures range from 190 K to 250 K, in case of optical depth = 0.1. These simulations could help to constrain the nature of the dark resistant unit when temperature data of the selected area will be available. Moreover, the methodology here described can be applied to other Mars' sites of interest, providing surface temperature distribution and interior temperature profiles.

References: Vago J.L. et al. (2017), Astrobiology vol.17, pp 471-510.; [2] Quantin-Nataf, C. et al. (2021), Astrobiology, vol.21, n.3; [3] Brossier J. et al. (2022), Icarus, 386,6; [4] Mandon L. et al. (2021), Astrobiology, Vol.21, n.4; [5] Fawdon P. et al. (2021), Journal of Maps, Vol.17,2; [6] Formisano, M. et al. (2018), MNRAS, 458, 695; [7] Formisano M., (2021), Advance in Astronomy,Article ID 9924571; [8] Gary-Bicas C.E. (2021), JGR, Vol.126, 2.

TERRESTRIAL AND MARTIAN PALEO-HYDROLOGIC ENVIRONMENTS: SYSTEMATIC COMPARISON BY MEANS OF PRISMA AND CRISM HYPERSPECTRAL DATA.

A. Zinzi[1,2], V. Camplone[1,2,3,4], E. Ammannito[1], G. Sindoni[1], F. Zucca[4], G. Polenta[1,2]
[1]Space Science Data Center (angelo.zinzi@ssdc.asi.it), [2]Agenzia Spaziale Italiana, [3]INAF-OAR, [4]Università di Pavia

Introduction: The mineralogical characterization of paleo-hydrologic environments on Mars are mainly performed using hyperspectral data acquired by orbiting instruments, looking for spectral signatures of hydrated minerals.

However this approach could be biased by the fact that on Earth this task is usually performed by in-situ analysis, with a very different spatial resolution, making thus not straightforward the comparison among Earth and Mars.

ASI PRISMA (PRecursore IperSpettrale della Missione Applicativa) mission has hyperspectral characteristics very similar to those of NASA CRISM: spatial and spectral resolutions are almost identical, as also the spectral range [1].

Therefore a comparison between data acquired over similar environments on Earth by PRISMA and on Mars by CRISM could constitute the "missing link" facilitating their geological comparison.

PRISMA dataset: PRISMA data are available by completing the registration to the ASI PRISMA portal (https://prisma.asi.it) and different levels of data are available:

- L1: Top-of-Atmosphere spectral radiance;
- L2B: At-Surface radiance
- L2C: At-Surface reflectance
- L2D: At-Surface geocoded reflectance

For this study we mainly used the L2D: the data are made available in a common HDF5 format and, in order to better exploit the dataset features, we developed a Python package able to perform several dedicated tasks.

This software, named ssdcPRISMAreader.py, allows to: a) visualize the RGB image of the PRISMA observation; b) plot the spectrum of a single pixel inside the PRISMA observation; c) select and save an average spectrum from a Region-Of-Interest (ROI) selected by the user.

Making PRISMA data directly comparable to CRISM ones: Apart from selecting PRISMA observation acquired over regions of potential interest for this kind of analysis, up to now one of the main tasks of our work has been constituted by processing PRISMA spectra in order to compare them with CRISM calibrated ones, since these latter are available already photometrically corrected for taking into account the topography and with the removal of atmospheric contribution.

As we already stated, PRISMA L2D data have already passed the atmospheric correction pipeline, but, differently from the CRISM ones, they are not photometrically corrected, in particular no high-resolution topography has been used for this task.

In order to apply this fundamental correction, we followed the work by [2], making it possible to use only astronomical parameters to computer vectors from the Sun to the Earth, and expanding this approach to compute also vectors from S/C to the Earth.

In particular, naming observer's coordinates (latitude and longitude) as (φ_0, λ_0) and subsolar point's coordinates (φ_s, λ_s), Zhang and colleagues found that the x-, y- and z-components of the unit vector S pointing from the observer to the center of the Sun are defined as follows:

$$S_x = \cos \varphi_s \sin (\lambda_s - \lambda_0)$$
$$S_y = \cos \varphi_0 \sin \varphi_s - \sin \varphi_0 \cos \varphi_s \cos (\lambda_s - \lambda_0)$$
$$S_z = \sin \varphi_0 \sin \varphi_s - \cos \varphi_0 \cos \varphi_s \cos (\lambda_s - \lambda_0)$$

By using the S/C coordinates instead of solar ones, we expanded this approach also to compute the unit vector pointing from the observer to the center of the S/C.

These unit vectors, together with an adequate resolution DTM (e.g., ASTER), are then used to compute incidence and emission angles, needed for an accurate photometric correction. In the ssdcPRISMAreader package two different photometric correction methods have been included: Lambert and Lommel-Seeliger.

Selection of Earth environments: Once this preliminar work has been finalized, we started looking for PRISMA observations of interest, i.e. acquired on environments with a geological history similar to those of paleohydrological studies on Mars (for example, Jezero Crater).

In particular, we looked for areas observed by PRISMA already characterized by previous studies from a mineralogical point of view.

The first region selected is that of the Gobi Valley area in central Mongolia. This region is unique on Earth because the subarctic climate area is directly in contact with the semi-arid climate area [3] and for this reason represents a suitable Martian analogue for our study.

The Gobi is characterized by the presence of a certain number of endorheic basins, the outflow of the

basins formed a series of deltaic deposits, and it is precisely in these deposits that we intend to concentrate our analyses.

First results: The ROIs that we have decided to analyze in this first phase of work concern the lacustrine deposits around the endorheic basins shown in Figure 1.

In these areas, hydrated minerals (e.g. phyllosilicates) have been identified [3] with in situ geological investigations and by means of the X-ray diffraction (XRD) technique: we therefore expect to find the same materials with the analysis of the spectra acquired from the PRISMA data.
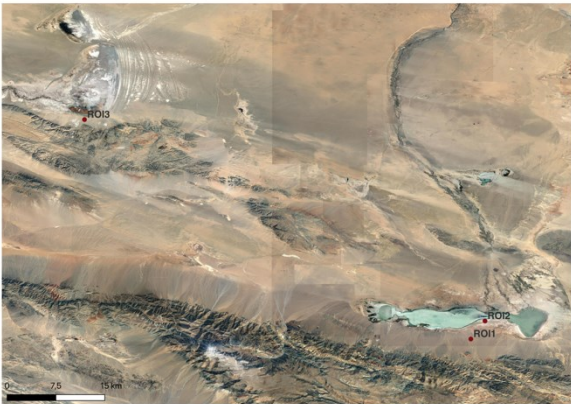
Figure 1: On overview of the Gobi desert area first analyzed in this study. (lat 45° 0'25.42"N; lon 99°59'43.04"E)

The chosen ROIs are located within the Gobi Lake Valley in central Mongolia. The area corresponds to a depression of tectonic origin between the Khangai and Altai Gobi mountains.

These ROIs represent two different source systems: the Khangai Mountains and the Upper Gobi Mountains, which because of their different lithological types (metamorphic basement in the former setting and sedimentary rocks and aeolian deposits in the latter) likely underlie the major differences in the lithology of the sampled sediment [3]. Other elements that contribute to sediment differentiation are related to transport and intensity of alteration related to sediment persistence in water. This determines that at first analysis of the detected spectra, on one side the albite and quartz component is dominant, while on the other, there is an abundance of secondary minerals such as calcite.

Prior to analyze the spectra, we selected only spectral regions in which PRISMA data are adequately accurated (cnf. Fig. 2 in [1]).

A very preliminar analysis of spectra acquired over different ROIs inside PRISMA observations show pe-

culiarities likely due to the mineralogical composition and geological characteristics (Figure 2).
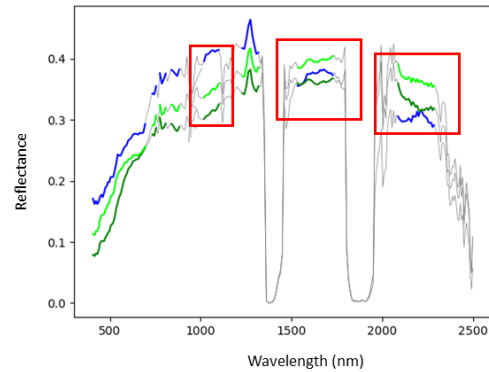
Figure 2: Spectra of ROIs acquired over Gobi Desert: in the red boxes regions of clear spectral differences are highlighted.

Future works: In the future we plan a series of different steps, starting from the identification of spectral signatures of minerals of interest in the PRISMA spectra, up to the direct comparison of PRISMA and CRISM data, even by enlarging the PRISMA dataset of interest to other terrestrial sites.

References: [1] Caporusso G. et al. (2020) *doi: 10.1109/IGARSS39084.2020.9323301*. [2] Zhang T. et al. (2021) *doi:10.1016/j.renene.2021.03.047*. [3] Sekine Y. et al (2020) *doi:10.3390/min10090792*.

A grid of climate models for the Noachian Mars using EOS-ESTM

P. Simonetti[1], L. Biasiotti[1,2], E. Bisesi[1,3], S. Ivanovski[1], M. Maris[1,4], S. Monai[1], G. Murante[1,3,4], L. Silva[1,4] and G. Vladilo[1], [1]INAF/OATs-Trieste, [2]University of Trieste, [3]CNR/IGG-Pisa, [4]IFPU-Trieste

Introduction: Despite its many differences with respect to the Earth, Mars is still the most Earth-like planet in our Solar System and therefore is the prime candidate for planetary habitability studies. For this reason, traces of life are being actively searched for and sometimes invoked to explain poorly understood seasonal variabilities in its atmospheric composition (see e.g. [1]).

Mars' features, combined with the relative ease of reaching it by using robotic probes, has made it the target of a large number of interplanetary missions and half of all the landings outside the Earth-Moon system. This in turn has given us a large amount of in-situ data about martian geology and atmosphere, and allows us to tentatively reconstruct the past history of the planet.

Especially striking are the chemical and morphological alterations left on the martian surface by the presence of liquid water for extended (at least 10^5 - 10^7 yr) periods of time during the first Gyrs after the planet formation [2,3]. Reconciling this fact with the predicted low energy output of the Sun during the same age [4] is a longstanding endeavor in the scientific community known as the Faint Young Sun (FYS) paradox.

Proposed solutions to the FYS paradox can be generally summarized in two large groups. The first one focuses on the search of an atmospheric mix capable to warm the surface up to the point of sustaining an hydrological cycle. Early calculations tested the viability of a thick CO_2-H_2O atmosphere, which is both insufficient to achieve the goal [5] and possibly difficult to reconcile with observational data ([6,7], but see also [8]). More recent ones took into consideration the greenhouse effect produced by other gases such as SO_2 [9,10] or H_2 and CH_4 [11,12,13], but in all cases there are lingering issues with the availability and atmospheric persistence of these gases (see e.g. [14]). The role of infrared backscattering from CO_2 clouds has also been investigated [15], but later calculations cast doubts on its effectiveness [16]. The second group focuses on transient warming solutions to the FYS paradox, such as asteroid impacts [17,18], volcanic eruptions [19] or the destabilization of CH_4 clathrates due to chaotic obliquity changes [20]. None of them, however, are free of issues. The post-impact rainfall pattern predicted by more modern models mismatches observations [21]; photochemically driven formation of highly reflective sulfate aerosols from volcanic SO_2 and H_2S may have cooled, rather than warmed, the

planet [22]; it is highly uncertain if CH_4 can be produced and stored in sufficient quantities in the martian environment in the first place [23].

The Early Mars climate has been investigated by using both 1D Radiative-Convective Equilibrium Models (RCEMs), which basically derive the average planetary energy balance from radiative transfer along a single atmospheric column, and 3D General Circulation Models (GCMs) that resolve the full motion of the atmosphere. RCEMs do not include most or all the climate feedbacks but allow for the rapid exploration of the planetary parameter space. Some of them have been coupled with other codes to investigate mechanisms such as the atmospheric photochemistry [24], the carbonate-silicate cycle [25] or ecological interactions [26]. GCMs are instead computationally expensive, and have been employed to study specific scenarios in greater detail, and especially the hydrological cycle (e.g. [27,28]).

Here, we make the case for the employment of latitudinal Energy Balance Models (EBMs) coupled with flexible atmospheric radiative transfer codes such as EOS-ESTM [29] as better tools than RCEMs to make wide parameter space explorations. Latitudinal EBMs can capture the simplest and strongest climate feedbacks such as the ice-albedo feedback while retaining the high computational efficiency of RCEMs. While this approach is not entirely new [30], it is still niche. At variance with them, we explore several different atmospheric compositions on a grid of possible planetary obliquities and eccentricies, as derived by [31].

Model description: For this study we employ the coupled EOS and ESTM codes. ESTM [32] is a seasonal-latitudinal EBM with enhanced prescriptions for meridional heat transport. Ice and H_2O cloud cover fractions and their effect on the planetary energy balance are included in via simple parametric relations. EOS [33] is a line-by-line atmospheric radiative transfer code derived from HELIOS [34,35] and HELIOS-K [36]. EOS can take as input any molecular line list from popular repositories such as HITRAN [37] and ExoMol [38], which makes it very flexible and easy to keep up-to-date with the latest data. We also include the effects of collision-induced absorption (CIA) for all the binary combinations of CO_2, N_2, H_2O.

The procedure that we adopt can be summarized as follows. First, we generate a set of lookup tables for several different atmospheric compositions and surface

pressures using EOS. Second, we feed them into ESTM to derive seasonal-latitudinal surface temperature maps of the Early Mars for a grid of obliquity and eccentricity values.

As a result, we plan to identify what combinations of atmospheric and planetary parameters can sustain a partially deglaciated Mars under the insolation conditions found in the early part of the history of the Solar System. Preliminary results and implications for future developments of this investigation will be presented .

References: [1] Webster C. et al. (2015) *Science*, 347, 415. [2] Hoke M. et al. (2011) *E&PSL*, 312, 1. [3] Balme M. et al. (2020) *JGRe*, 125, 5. [4] Gough D. (1981) *SoPhys*, 74, 21. [5] Kasting J. (1991) *Icarus*, 94, 1. [6] Lammer H. et al. (2013) *SSRev*, 174, 113. [7] Edwards C. & Ehlmann B. (2015) *Geology*, 43, 863. [8] Bultel B. et al. (2019) *JGRe*, 124, 4. [9] Halevy I. et al. (2007) *Science*, 318, 1903. [10] Mischna M. et al. (2013) *JGRe*, 118, 560. [11] Ramirez R. (2014) *NatGeo*, 7, 59. [12] Wordsworth R. et al. (2017) *GeoRL*, 44, 665. [13] Ramirez R. et al. (2017) *Icarus*, 297, 71. [14] Wordsworth R. et al. (2016) *AREPS*, 44, 381. [15] Forget F. & Pierrehumbert R. (1997) *Science*, 278, 1273. [16] Kitzmann D. (2017) *A&A*, 600, A111. [17] Segura T. et al. (2002) *Science*, 298, 1977. [18] Segura T. et al. (2008) *JGRe*, 113, E11007. [19] Halevy I. & Head J. (1014) *NatGeo*, 7, 12. [20] Kite E. et al. (2017) *NatGeo*, 10, 737. [21] Turbet M. et al. (2020) *Icarus*, 335, 113419. [22] Kerber L. et al. (2015) *Icarus*, 261, 133. [23] Ramirez R. (2018), *NatGeo*, 11, 230. [24] Batalha N. et al. (2015) *Icarus*, 258, 337. [25] Batalha N. et al. (2016) *E&PSL*, 455, 7. [26] Sauterey B. et al. (2022) *NatAs*, 6, 1263. [27] Wordsworth R. et al. (2015) *JGRe*, 120, 1201. [28] Kamada A. et al. (2020) *Icarus*, 338, 113567. [29] Biasiotti L. et al. (2022) *MNRAS*, 514, 5105. [30] Hayworth B. et al. (2020) *Icarus*, 345, 113770. [31] Laskar J. et al. (2004) *Icarus*, 170, 343. [32] Vladilo G. et al. (2015) *ApJ*, 804, 50. [33] Simonetti P. et al. (2022), *ApJ*, 925, 105. [34] Malik M. et al. (2017) *AJ*, 153, 56. [35] Malik M. et al. (2019), *AJ*, 157, 170. [36] Grimm S. et al. (2021), *ApJS*, 253, 30. [37] Gordon I. et al. (2022), *JQSRT*, 277, 107949. [38] Tennyson J. et al. (2020), *JQSRT*, 255, 107228.

MESSENGER Grand Finale at Mercury: surface age and property characterization. E. Martellato[1], R. Luther[2], J. Benkhoff[3], V. Da Deppo[4], C. Casini[1,4,5], P. Palumbo[6,7], A. Rotundi[6,7], A. Slemer[8] and G. Cremonese[1], [1]INAF−Astronomical Observatory of Padua, vic. Osservatorio 5, 35122 Padova, Italy (elena.martellato@inaf.it), [2]Museum für Naturkunde, Leibniz Institute for Evolution and Biodiversity Science, Invalidenstr. 43, 10115 Berlin, Germany, [3]ESA/ESTEC-SRE-S, Keplerlaan 1, 2201 AZ Noordwijk, The Netherlands, [4]IFN−CNR, via Trasea 7, 35131 Padova, Italy, [5]Centre of Studies and Activities for Space "G. Colombo", University of Padua, via Venezia 15, 35131 Padova, Italy, [6]Department of Sciences & Technologies, University of Naples "Parthenope", Centro Direzionale Isola C4, 80143 Napoli, Italy, [7]INAF−Institute for Space Astrophysics and Planetology, via Fosso del Cavaliere 100, 00133 Roma, Italy, [8]Officina Stellare S.p.A., via della Tecnica 87/89, 36030 Sarcedo (VI), Italy.

Introduction: Impact craters are key geological features to investigate the surface and interior of planetary bodies [1]. The statistical analysis of the crater population on planetary surfaces allows age determination of geological events (e.g., lava emplacements [2]), or of structures (e.g., craters or basins [3, 4], sinuous rilles [5], scarps [6]).

At the same time, the specific morphology of an impact structure can provide information on the layering and material properties of the near-surface stratigraphy. Indeed, the final shape of craters depends on the initial energy [7], but also on the target properties, including changes in density, strength, water content, porosity, and composition (e.g., [8]). Along with naturally formed impact structures, there is a number of artificial craters, produced either by a metallic module while the main spacecraft observes the process and the impact products, or by the spacecraft itself crushing at the end of its operative life.

The goal of this work is to (i) infer via crater counting the age of the region of such a crush, and to (ii) model the collision of the NASA MESSENGER spacecraft in 2015 on the Hermean surface. The numerical modelling of this artificial crater is carried out by testing several target scenarios, which will provide an initial indication whether the MESSENGER crater could be observed by SIMBIO-SYS, the imaging system onboard the ESA BepiColombo mission [9]. The overall output of this study will provide a better understanding of the Hermean near-surface.

Methods: The impact location is within the Suisei Planitia (Fig. 1), located north-east of Caloris basin [10]. We did the following analysis:

(i) Age determination. We performed geological characterization of the region around the expected impact point (54.4°N, 149.9°W), and performed crater counting in ArcGIS environment.

(ii) Crater modelling. Numerical models have been carried out with the iSALE shock physics code [11, 12, 13, 14], which is well tested against laboratory experiments and other hydrocodes (e.g., [15]).

We approximated the MESSENGER spacecraft as an aluminum cylinder impacting at ~4 km/s, testing the impact angle values of 30°, 45°, and 90°. The surface was modelled as two-layer target, composed of a regolith layer (described by the basalt ANEOS and the Drucker-Prager model), on top of an underlying basaltic crust (described by an intact and damaged yield envelope). The thickness of the upper regolith layer was varied from 0 (one layer) up to 20 m. Several strength and inner friction values have been tested. A porosity of 40% and 10% was set for the regolith layer and basaltic crust, respectively. The temperature is set to a constant value of 440 K, while no thermal gradient was implemented within the target, which is 100 m thick.
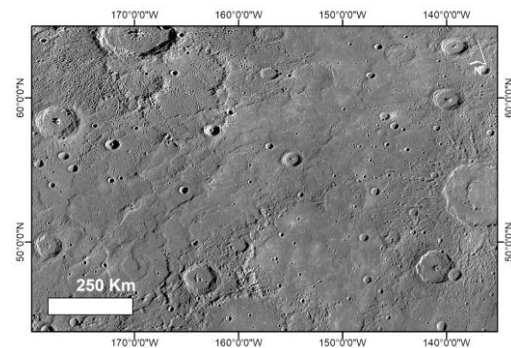
Fig. 1. Image of Suisei Planitia, a smooth plain in the northern hemisphere of Mercury.

Results: The first surface age analysis suggests a young age for Suisei Planitia, due to the relatively low number of craters.

The numerical modelling highlights a very different output when the collision occurs in a competent or weaker targets. In Fig. 2, we compare the formation of the MESSENGER crater in a pure basaltic target (first row), and when considering also an upper regolith layer (second to fourth rows). We find that craters forming in competent rock surfaces are <10 m wide, and about 1 m deep. In two-layer targets with a thin upper regolith layer (1 to 2 m), craters display a flat floor morphology, where the flat bottom occurs in correspondence of the transition between the rheologies governing the two layers. Craters can be as much as ~20 m wide, and 2 m deep. In the case of thick regolith

layers (>5 m), craters develop entirely in the upper layer, and thus their final shape depends on the regolith properties. The diameter is about 20 m, and they can be as deep as 4 m.
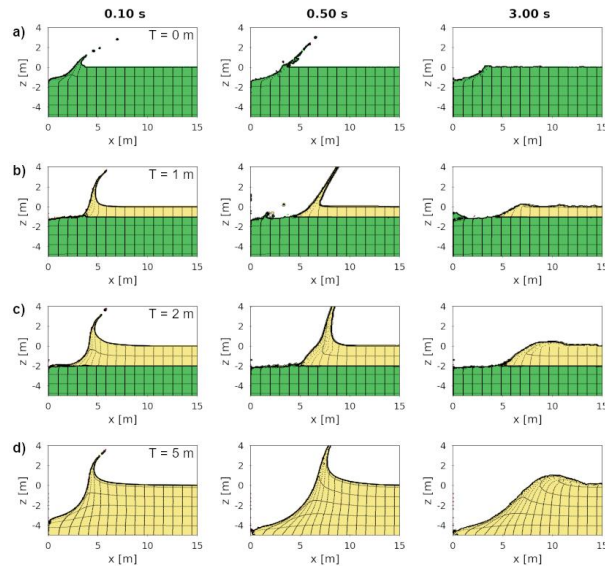
Fig. 2. Comparison of time series models, with a regolith thickness from 0 m (one-single layer model, first row) up to 5 m (two-layer models, second to fourth rows). The colour map refers to the three different materials used: fuchsia for the spacecraft/projectile, green for the basaltic crust, and pale yellow for the regolith.

Discussion and Conclusion: We present the results of the systematic analysis of an aluminum cylinder, with the same mass of the MESSENGER spacecraft, impacting on one- and two-layered targets. The investigation is focused on testing the effects of the target properties (material parameters and layering) on the final crater morphometry. Depending on the model setup, we find a crater diameter ranging from 5 to 20 m, and a crater depth from 1 to 4 m.

Since the crater is generally small (D<20 m), we need to verify whether the MESSENGER crater might be observed by the Spectrometer and Imagers for MPO BepiColombo Integrated Observatory SYStem (SIMBIO-SYS) [9]. It is a suite of three independent channels onboard the ESA BepiColombo mission [16], and precisely: (i) a high resolution imaging channel (HRIC) that will provide images at a spatial resolution of 5 m/pixel at the periherm, (ii) a VIS–NIR spectrometer (VIHI) that will provide the mineralogical global mapping of Mercury's surface in the spectral range 400–2200 nm, with a spectral sampling of 6.25 nm, and a spatial resolution of 400 m/pixel at the periherm during the Global Mapping, and allowing local spectra at 100 m/pixel, and (iii) a stereo imaging channel

(STC) that will provide panchromatic 3D global mapping and colour imaging of selected regions of the Hermean surface, with a spatial resolution lower than 110 m.

Given the instrument performances and the results obtained from the numerical modelling, the MESSENGER crater might be only observed by the high-resolution channel, in the case that the near-surface stratigraphy of the Suisei Planitia is made of a thick layer of regolith. Such a scenario can be likely on Mercury. According to [17], the regolith layer forming in the Hermean smooth plains might be as thick as 25−40 m, while it may increase to values of 40−100 m in the heavily cratered terrains.

The impact area is on Suisei Planitia, whose suggested young age follows the general age trend of the northern smooth plains, for which an emplacement after the late heavy bombardment was advanced [18]. This leads to an expected regolith layer thickness of up to 40 m.

The analysis and modelling of the ejecta distribution might provide an additional support to derive information about the MESSENGER impact point.

References: [1] Melosh H.J. (1989) Impact Cratering: a geological process, Oxford Univ. [2] Hiesinger H. et al. (2000) *JGR, 105(E12)*, 12,239−29,275. [3] Hiesinger H. et al. (2012) *JGR, 117*, E00H10. [4] Fassett C.I. et al. (2012) *JGR, 117*, E00H06. [5] Hurwitz D.M. et al. (2013) *PSS, 79−80*, 1−38. [6] van der Bogert C.H. (2018) *Icarus, 306*, 225−242. [7] Collins G.S. et al. (2012) *Elements, 8*, 25–30. [8] Cintala M.J. et al. (1977) *Proc. Lunar Planet. Sci., 8*, 3409–3425. [9] Cremonese G. et al. (2020) *Space Sci. Rev. 216*, 75. [10] Guzzetta L. et al. (2018) *Mercury: Current and Future Science of the Innermost Planet*, Abstract #6107. [11] Collins G.S. et al. (2016) iSALE-Dellen manual, *figshare*. [12] Amsden A.A. et al. (1980) *Los Alamos Nat Lab Rep* LA−8095, 101 pp. [13] Collins G.S. et al. (2004) *Meteorit. Planet Sci., 39*, 217-231. [14] Wünnemann K. et al. (2006) *Icarus, 180*, 514-527. [15] Pierazzo E. et al. (2008) *Meteorit. Planet. Sci., 43*, 1917-1938. [16] Benkhoff J. et al. (2021) *Space Sci. Rev., 217*, 90. [17] Kreslavsky M.A. and Head J.W. (2015) *LPS XLVI*, Abstract #1246. [18] Denevi et al. (2013) *JGR, 118*, 891−907.

GEOLOGICAL AND STRUCTURAL MAPPING OF THE MICHELANGELO (H-12) QUADRANGLE OF MERCURY: PRELIMINARY RESULTS

S. Buoninfante[1,2], V. Galluzzi[2], L. Ferranti[1,2], M. Milano[1], P. Palumbo[3,2].
[1]University of Naples Federico II, Department of Earth, Environment and Resources Sciences, Naples, Italy (salvatore.buoninfante@inaf.it), [2] Istituto di Astrofisica e Planetologia Spaziali (IAPS), INAF, Rome, Italy, [3]Dipartimento di Scienze e Tecnologie, Università degli Studi di Napoli "Parthenope", Naples, Italy

Introduction: The Michelangelo quadrangle of Mercury (H-12) encompasses the area between latitudes 22.5°S-65°S and longitudes 180°E-270°E. This quadrangle covers almost 6% of the planet's surface with a total area of almost 7 million km^2. The first geological map of the H-12 quadrangle was produced by [1] at 1:5M scale using Mariner 10 data. They identified and mapped five classes of craters and four main plain units. Here, we present preliminary results of a geological study of the quadrangle, derived from the photointerpretation of the MErcury Surface, Space ENvironment, GEochemistry, and Ranging (MESSENGER) Mercury Dual Imaging System (MDIS) imagery. Geologic contacts and linear features were drawn at a mapping scale between 1:300,000 and 1:600,000. The present study is a contribution to the 1:3M geological map series, planned to identify targets to be observed at high resolution during the ESA-JAXA BepiColombo mission [2]. Further purpose of this work is the mapping of tectonic structures at the south-western boundary of the high-Mg region to verify possible links between faults location and the areal distribution of this geochemical terrain, as observed in other quadrangles [3]. We provide an updated structural framework of the area and a new model explaining the reactivation process of the large basins, as also observed in [4], and evaluate the close relationship of thrusts with volcanic vents as shown in [5].

Geological mapping: We mapped tectonic structures and geological contacts using the MDIS derived basemaps, with an average resolution of 166 m/pixel. We use the map-projected Basemap reduced Data Record (BDR), the map-projected Low-incidence Angle (LOI) basemap, the map-projected High-Incidence angle basemap from the East (HIE) and the map-projected High-Incidence angle basemap from the West (HIW). Moreover, we use the USGS global Digital Elevation Model (DEM) to better distinguish morphological features, and the Color and Enhanced color basemaps to identify surface features (faculae, hollows, dark deposits, bright deposits, crater chains). Linear features are subdivided into large craters (crater rim diameter > 20 km), small craters (5 km < crater rim diameter < 20 km), subdued or buried craters, certain or uncertain thrusts, certain or uncertain faults, wrinkle ridges and irregular pits. Geological contacts, mapped as certain or approximate, delimit the geological units grouped into three classes of crater materials (c1-c3) based on degradation degree, and plains (smooth, intermediate and intercrater plains), consistently with other mapped quadrangles [2].

Results: We identified two main regional thrust systems with NW-SE trend and tectonic structures arranged both radially and concentrically with respect to large old basins (Fig. 1). Clear examples of such tectonic structures in the Michelangelo quadrangle can be provided by the Beethoven basin (20.8°S–236.1°E) or by the Vincente-Yakovlev basin (52.6°S–197.9°E). The reactivation structures are the result of previous impact-related normal faults that were reactivated due to the compressive tectonic regime deriving from the global contraction. As previously observed, some tectonic structures in the Victoria quadrangle (H-02) are spatially correlated with the edges of the high-Mg region [3]. Similarly, in the Michelangelo quadrangle the NW-SE system largely borders the southwestern edge of the high-Mg region, although the accuracy of XRS data at these latitudes is much lower than the accuracy of data acquired in the Northern hemisphere. We also show that the volcanic vents on Mercury are often found along lobate scarps, such as in the Sayat-Nova crater, or in soft-linkage zones between thrust segments, such as at the b2 basin rim. As observed on Earth, curvilinear fault surfaces like those characterizing lobate scarps or, even better, the linkage areas between fault arrays represent weakness zones acting as preferential pathways for magma uprising.

Conclusions and future work: The geological mapping of the H-12 quadrangle is nearly complete, and the observed structural framework reveals scenarios not different from those observed in other quadrangles of the planet [e.g., 3]. The presence of old impact basins highly influenced the alignment of faults and the interaction of fault systems helped subsurface volatiles and magma to reach the surface. Further investigations are ongoing on this quadrangle to better frame its tectonic evolution.

Figure 1. Linear features of the Michelangelo quadrangle (H-12) in Lambert Conformal Conic projection. Blue lines indicate NW-SE fault trend; purple lines indicate NE-SW fault trend; green lines indicate N-S trend; yellow lines indicate reactivated faults bordering the basins. Red circles enclose the NW-SE fault systems identified in the Michelangelo quadrangle.

References:
[1] Spudis P. D. and Prosser J. G., (1984). *U.S. Geological Survey*, IMAP 1659.
[2] Galluzzi et al. (2021). *LPI Contrib., 2610.*
[3] Galluzzi et al. (2019). *J. Geophys. Res., 124(10),* 2543-2562.
[4] Fegan E. R. et al., (2017). *Icarus, 288,* 226-234.
[5] Thomas R. J. et al., (2014). *J. Geophys. Res., 119,* 2239-2254

GEOLOGICAL STUDIES WITH MATISSE: a Mercury surface study case

V. Camplone[1], A. Zinzi[2], M. Massironi[3], A.P. Rossi[4], F. Zucca[5] [1] Asi-Ssdc/Inaf-Oar (veronica.camplone@ssdc.asi.it), [2] Asi-Ssdc/Asi, [3] Geosciences Department Of The University Of Padua [4] Constructor University [5] University of Pavia.

Introduction The analysis of the surface of planetary bodies is a fundamental field of Space Exploration, with past, current, and future missions devoted to increase our knowledge of the Solar System bodies.

The wide range of data resulting from these missions, if appropriately incorporated into specific platforms, can support and enhance the analysis of the geology/surface geomorphology of planetary bodies.

. For this purpose, as part of the WP Solar System Exploration (SSE) in SSDC, MATISSE (Multi-purpose Advanced Tool for the Instruments of the Solar System Exploration) was developed in recent years [1].

The software is currently at its version 2.0, available at *https://tools.ssdc.asi.it/Matisse*.

MATISSE currently ingests both public and proprietary data from 5 missions (NASA Dawn, ESA Mars Express, NASA Mars Reconnaissance Orbiter, NASA MESSENGER, ESA Venus Express), 5 targets (1 Ceres, 4 Vesta, Mars, Mercury and Venus) and 7 instruments (VIR VIS, VIR IR, MARSIS, CRISM, MDIS-NAC, VIRTIS VIS, VIRTIS IR). However, it is worthy to note that its modular structure easily allows it to integrate a wider range of instruments and targets from past, present and future missions. In addition, as of this version, MATISSE is now able to accommodate geological mapping products.

Methodology: We started studying the geological maps that created on the basis of the PLANMAP (https://planmap.eu) and GMAP/EPN2024 (https://www.europlanet-gmap.eu) projects. Currently in our tool there are the geological units of some areas of Mars [2], Mercury and the geological map of Ceres [3]. For example, the geological map of the Hokusai quadrangle (Figure 1) [4] on Mercury has been added into the MATISSE tool.

First we uploaded each geological units on Quantum Geographic Information System (GIS) software (http://qgis.org). We extracted individual polygons and we converted them into "Multipolygon" geometries using Python.

In this way it was possible to load the geometries of the units into the MATISSE database, based on the DBMS PostgreSQL, with its plugin PostGIS, especially designed for geospatial applications. Among the MATISSE capabilities there is the possibility to select the geological units to be analyzed regardless of the dataset that the user selected.

The case of Mercury: Figure 2 shows the initial screen of the MATISSE tool for the Mercury target.

It is possible to select the Mission (e.g. MESSENGER), the Instrument (MDIS-NAC) and the Geological Unit of interest (e.g. Smooth Crater Floor): In this way the user can visualize the lithology on both spectrometric and visible data.
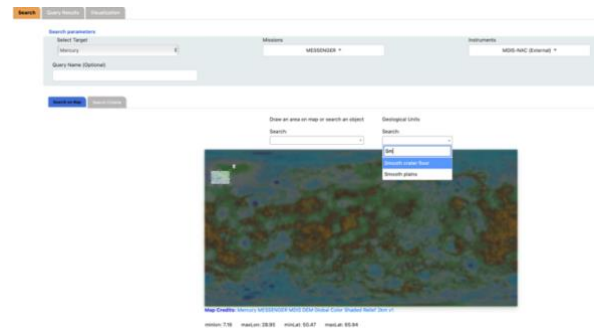
When the query is completed, results are shown as a table of observations (Figure 3), together with relevant geospatial information.

Once the observation of interest is selected, a second query appears. At the end of the query, the selected area will be displayed on the dataset we have chosen, in this case on the MDIS-NAC /MESSENGER instrument (Figure 3).
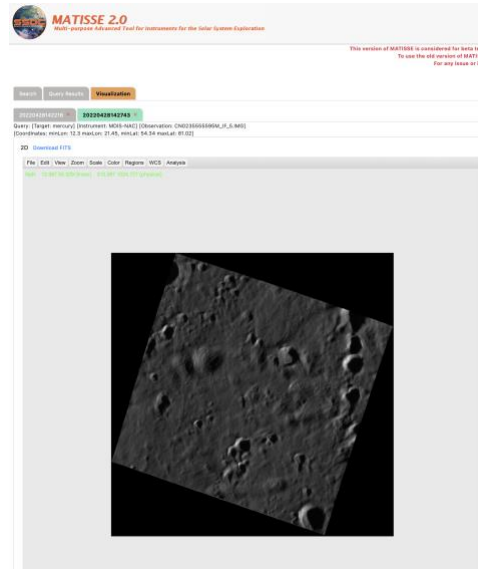
Discussion: Analyzing a first scientific case we show in this preliminary work how the functions (the selection of geological units) added in the MATISSE tool (version 2.0) can support and expand the geological research of a planetary surface.

For what regards Mercury's surface, it is possible to analyze in detail and compare the different textures of the mapped geological units on different regions of the planet. For example, with MATISSE it will be possible to study the different types of ejecta flows mapped on the surface of Mercury and compare their different textures and colors. MATISSE also allows users to analyze data directly online, without any need to download them.

Xiao and Komatsu [5], using the MESSENGER camera data obtained during the orbital mission, found craters with ejecta flows and central pits. Thanks to these multi-observations we could compare the ejecta flows, and explain the factors that influenced their formation on Mercury surface [6].

Conclusions: The correct distinction of the different geological units on a planetary surface allows planetologists to address their geological evolution and age in order to provide the right analysis tool for the selection of scientifically important areas for analysis.

Therefore MATISSE will allow an accurate analysis of the different geological units using a single instrument. In collaboration with the PlanMap and GMAP/EPN2024 teams, we are currently working to include other geological units identified on the surface of Mercury to be ready for in depth analyses when the **BepiColombo** mission will deliver much more data of the planet.

Furthermore we are planning to include also the Moon and its geological maps in MATISSE being particularly relevant t for robotic and human missions of the next years and decade.

References:

[1] Zinzi A. et al. (2016) Astron. Comput., 15, 16-28.
[2] Pondrelli M. et al. (2010) Earth and Planetary Science Letters, 304, 511-519
[3] Williams, D.A., et al. (2019) Final Dawn LAMO-based global geologic map of Ceres. 50th Lunar Planet. Sci. Conf., Abstract #1252, Lunar and Planetary Institute, Houston;
[4] J. .Wright et al., (2019), Journal of Maps. VOL 15, NO 2,509-520;
[5] Z. Xiao et al., (2013), Impact craters with ejecta flows and central pits on Mercury. Planetary andSpaceScience82–83 (2013)62–78;
[6] A. Blance et al., (2022) A global Survey of Mercury for Ejecta Flows: Investigating their Origins, Prevalence, and Significance. Vol. 16, EPSC2022-728, 2022;

Landing site characterization of Marius Hills pit (Moon): a feasibility evaluation for the ESA Lunar Caves CDF study.

Riccardo Pozzobon[1] ,Francesco Sauro[2], Angelo Pio Rossi [3], Maurizio Pajola [4], Matteo Massironi[1] and the DAEDALUS and ESA Lunar Caves CDF teams

1) Dipartimento di Geoscienze, Università degli Studi di Padova (riccardo.pozzobon@unipd.it)
2) Directorate of Human and Robotics Exploration, European Space Agency
3) Constructor University Bremen
4) INAF-Osservatorio Astronomico di Padova

Introduction: A significant push in the technology development and mission study feasibility for human and robotic exploration of the surface and subsurface of the Moon has raised over the past few years among the scientific community and space agencies. Because of the recent successful implementation of the first phase of NASA Artemis program of taking humans back to the Moon and and the concurrent development of ESA EL3 (European Large Lunar Lander), new steps in this direction are being taken. In all cases, it is clear that the development of new technology to safely land and navigate in harsh and unknown environments goes in parallel and is strongly tied with new landing sites detailed characterization.

In particular, in 2020 ESA issued a call for ideas through its its Open Space Innovation Platform in the SysNova Lunar Caves system studies framework. The target was to design a mission for the exploration of the lunar subsurface ,by accessing a lava tube from a collapse of its roof called "skylight". A specific location was targeted for such mission study, being the so-called MHH (Marius Hills Hole, discovered in the past decade [1]. We hereby present a landing site characterization in support to the proposed DAEDALUS [2] robotic mission for skylight nd underground void mapping and characterization, evaluated in a Concurrent Design Facility study of ESA.

Rationale of the study: The exploration of the Marius Hills lava tube is tied to the possibility to land, rove and approach safely to the MHH skylight. If this is not properly addressed and the terrain not characterized, no exploration mission would be possible. The design of the hardware and payload itself is influenced by the terrain morphology and properties. Therefore, it is mandatory to characterize in high detail the terrains surrounding the skylight both in terms of hazard and safety. Ideally, in order to reach an access point as close as possible to the MHH, the landing site and surrounding terrain should present reasonably low slopes, be obstacle-free with a relatively low boulder presence, and the regolith on the surface should be able to sustain inertial platforms with a relevant mass. In addition, the location should guarantee an easy approach to the pit up to a location where the Daedalus sphere will be deployed. Therefore, in order to

characterize the feasibility of landing, approach and deployment of the Daedalus sphere several aspects of the terrains surrounding the pit must be investigated taking into account several morphometric parameters:

- flat surface over steep overhanging pit margins, with a general slope safety margin of 15°;
  hazard free landing area (low crater density, low slopes less than 10°, relatively boulder-free);
- hazard-free or low-hazard trafficability from landing ellipse to the pit;
- safest closest approach point to the pit.

Geologic context: Marius Hills one of the largest volcanic regions on the Moon, recently interpreted as a shield volcanic complex [2] and is located in the Oceanus Procellarum on the lunar near side. It is characterized by the presence of a large number of small cones set on a ~300 km shield. In addition, on its flaks very large rilles are present, among which the largest are maned rille A and B (Besse et al., 2011, Spudis et al, 2013). The MHH is a nearly circular hole of ~65 m in diameter, located at 303.3°E, 14.2°N roughly in the middle section of the so-called "rille A" in correspondence of a ~90° change of direction. The first discovery was achieved via SELENE-Kaguya Terrain Camera images [1] whose first depth estimate was of ~80m [3].

Data and methods: The landing site was characterized on a bundle-adjusted LROC NAC stereo DEM (~4 meters of resolution), further denoised and refined with the shape from shading technique and co-registered with the LOLA laser altimeter point data for absolute altitude reference. This allowed us to retrieve the highest possible detail in the topography and detect small features at highest possible terrain resolution.

Trafficability hazard characterization: The terrain was analyzed with several morphometric algorithms. Automatic quantitative crater detection was performed using the multi-scale TPI (Topographic Position Index [4]). General slope, convexities and concavities of the terrain were also extracted along with boulder presence mapped on original LROC images at 0.5 m/pixel resolution.

In summary, the following hazards were assessed:

- *Crater density:* Of all craters we identified, some of appear not hazardous (very shallow, a few decimeters per meter in diameter, with low to negligible slopes);
- *Slopes:* slopes thresholds were extracted following the Burrough and McDonnell (1998) technique, and they represent the major trafficability constraint on the area. Based on both HERACLES [6], MSL Curiosity/Perseverance and Exomars rover constraints [7] we selected a maximum slope safety threshold to be <15°. A safety margin in slope threshold was set at <10°
- *Craters' depths:* craters shallower than 1 m and with inner slopes <15° were considered safe.
- *Boulder abundance:* less than 50 boulders are present in the whole area and none imply any relevant hazard.

The final result is a hazard map (see fig. 1) with safe areas, low hazard and no-go areas.

Skylight floor characterization: Since the objective of the ESA call for ideas and subsequent Concurrent Design Facility system study is the deployment of a robotic device inside the lunar cave for vertical and horizontal exploration, we attempted to also characterize the cave floor to assess trafficability, which directly impacts on the system design. Boulder mapping was performed on the MHH floor using high-incidence sunlight (~12°) LRO/LROC-NAC image (M155607349RE) with a spatial scale of 0.42 m/pixel. Boulder abundance and density maps were produced in order to locate the best deployment option for robotic device deployment (see fig. 2), which resulted in the NW pit floor sector.

Discussion: The MHH surroundings show a high safety regarding landing and trafficability hazards. The area is not affected by relevant obstacles such as boulders nor relevant slopes. The landing itself should be sufficiently safe in terms of engineering constraints: the slopes are <10° in most of the area and the no-go zones are limited to few impact craters and depressions apart from the skylight itself and secondarily by the inner edge of the Marius Hills Rille A. The MHH floor is characterized by a pile of large boulders and regolith, but the orthwestern portion should be sufficiently safe to deploy a robotic device with chances of navigation and mapping.
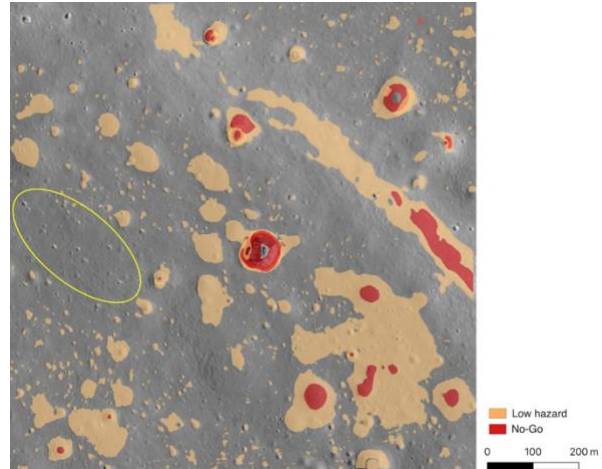
Figure 1: Hazard map of the MHH and its surroundings. The MHH is located at the center of the image, whereas the safest landing area is marked in yellow. Low hazard and no-go areas are marked in orange and yellow respectively.
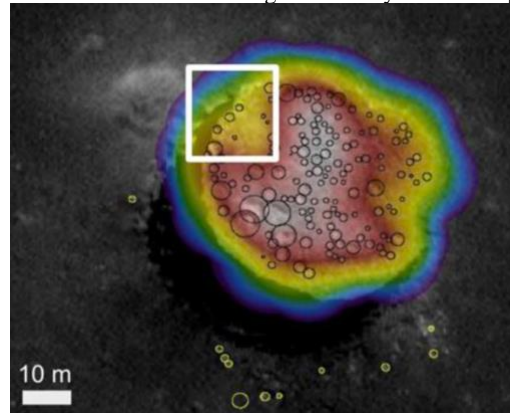
Figure 2: LROC NAC image (M155607349RE, 0.42 m/pixel) with visible boulders on the floor mapped with circles an abundance density map.

References:
[1] Haruyama et al., 2009, Possible lunar lava tube skylight observed by SELENE cameras. Geo- physical Research Letters, 36(21), 2009. ISSN 1944-8007.
[2] D. Borrmann, A. Nüchter and the DAEDALUS team. Lunar Caves Exploration with the Daedalus Spherical Robot. In 52nd Lunar and Planetary Science Conference (LPSC 2021), 2021
[3] Robinson, M. S., et al.,. «Confirmation of Sublunarean Voids and Thin Layering in Mare Deposits». Planetary and Space Science 69, n. 1 (1 agosto 2012): 18–27.
[4]Pozzobon., R., et al., (2019) Fluids mobilization in Arabia Terra , Mars : Depth of pressurized reservoir from mounds self-similar clustering., Icarus 321, 1-22
[6]Landgraf, M, William Carey, V Hipkin, J Carpenter, e H Hiesinger. «HERACLES – Exploring the Moon in an International Context», s.d., 4.
[7] Pajola, M., et al., 2017. Boulder Abundances and Size-Frequency Distributions on Oxia Planum-Mars: Scientific Implications for the 2020 ESA ExoMars Rover». Icarus 296 73–90.

THE PLANETARY MAPPING AND GIS LABORATORY AT IAPS INAF Alessandro Frigeri[1], Andrea Apuzzo[1] Gabriele Vizzini[1], Linda Morgissi. [1]Istituto Nazionale di Astrofisica - INAF, Istituto di Astrofisica e Planetologia Spaziali – IAPS, Rome - Italy (e-mail: Alessandro.Frigeri@inaf.it)

Introduction: The laboratory for planetary mapping and Geographic Information System (GIS) at INAF-IAPS was established in 2019 from a call for proposals to support IAPS laboratories. Unlike the other facilities of INAF which are mainly focused on physics experiments and instrument setup, this laboratory is devoted to the field of planetary mapping for the exploration of the bodies of the Solar System. The concept of the laboratory has developed in the last decade throughout the increasing use and need of digital cartographic and photogrammetric techniques to support of the scientific and technical activities of missions to the Solar System, and to analyze geospatial data. Moreover, the introduction of GIS-ready data products in the planetary data archives [1] as for example the NASA Planetary Data System (PDS, [2]) or the ESA's Planetary Science Archive (PSA, [3]), requires not only adequate software tools but also building experience and knowledge on how to handle these dataset and formats.

Main aspects: The laboratory focuses on three main aspects: cartography, photogrammetry, and Geographic Information System (GIS).

Geologic and geoscientific mapping consists in the development of original thematic maps based on quantitative or interpretative computations and observations based on pre-existing dataset. New interpretative maps can be developed in the laboratory using specialized software and hardware. The correct cartographic representation is guaranteed by the most up-to-date specialized software which guarantees reprojection of data among different coordinate reference system (Figure 1). Photogrammetric processing includes remote sensing processing, and stereogrammetry. Remote sensing geometric processing is mainly done with the Integrated Software for Imagers and Spectrometers (ISIS, [5]) Free Open-Source Software (FOSS) developed by USGS Astrogeology Science Center. With stereogrammetry techniques we produce digital terrain models at various scale by processing imagery frames of the same scene taken from different points of view. from remote sensing and outcrop scale imagery (see Figure 2).

Geographic Information System (GIS), initially developed for environmental analyses on Earth, have started to be used and adapted for planetary data in the last 15 years [6] and their use for geospatial processing and geostatisics is now part of the scientific work. The workstations at the laboratory are maintained with the
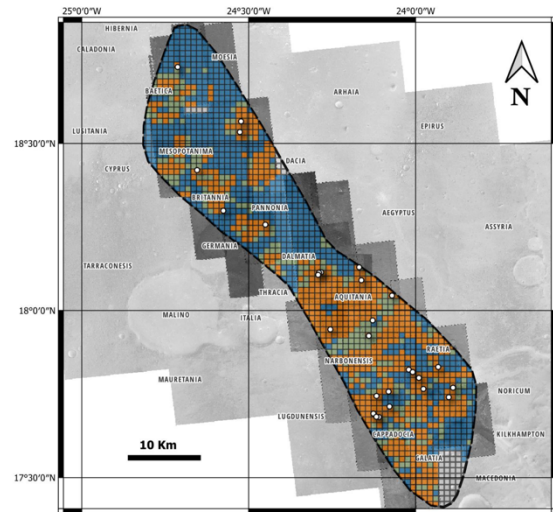
Figure 1: an example of interpretative mapping developed in a GIS environment in the laboratory: the map of fractured terrains interpreted from NASA/MRO HiRISE and CTX basemaps over the landing ellipse of Rosalind Franklin rover of the ESA ExoMars program [4].

most up-to-date desktop GIS, tools, and suites to spatially to spatially process data delivered by orbital and landed planetary missions.

The structure of the laboratory: Since its original proposal and design in 2019, the laboratory was taught to be both a physical and a virtual working place. The physical space is located at IAPS in Rome, in a dedicated room where specialized geospatial hardware and software is available. The virtual space is represented by a web site (http://gislab.iaps.inaf.it) and network-based services to promote international standards for the interoperability of planetary geospatial data over computer networks. Software developments and experimental codes and scripts are managed at the GitHub collaborative platform at https://github.com/GISlab-IAPS where users can download codes and scripts and contribute by submitting improvements or notes about issues and need for enhancements of functionalities.

Ongoing activities: The laboratory is currently supporting research activities for mission to Mars, mainly with the ExoMars program's Ma_MISS [8], to the Moon with the Lunar Gravitational Wave Antenna (LGWA, [9]) and ESA/PROSPECT [10], as well offering geomorphologic and geologic context for field work campaigns on terrestrial analogs of planetary environments [11].
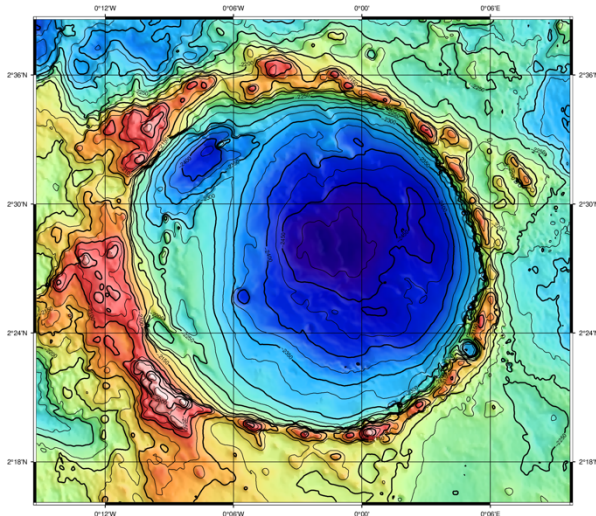
Figure 2: The Digital Terrain Model (DTM) of Nikumi crater on Mars [6] produced from archived images of the NASA Mars Reconnaissance Orbiter (MRO) Context Camera (CTX) using the Ames Stereo Pipeline software (ASP, [7]).

Besides these mission-specific activities, the laboratory supports software developments and tests of experimental codes as well as community efforts at the European scale as the Europlanet / GMAP project [12] and promoting training of students. In 2023, plans include continuing existing collaborations on planetary mapping, supporting interns in their theses works and promoting data interoperability and FOSS.

References: [1] Gaddis L. and Hare T. (2019) Planetary Data Workshop, Abstract #7045. [2] Renfrow J. T. et al. (1986) Bull. Am. Astron. Soc. [3] Arivset C. et al. (2007) ADASS XVI. [4] Apuzzo A. et al. (2023) PSS submitted. [5] Gaddis et al. (2015) LPSC Abstract #1846 [6] Hare, T.M., et al., (2009), LPSC XL Abstract #2538. [6] Baschetti B. et al. (2023) Adv. Space Res., under review. [7] Beyer R.A. et al. (2018) ESS 5. [8] De Sanctis et al. (2023) this conference [9] Harms J. et al. (2021) Astrophys. J. 910 [10] Heather, D. et al. (2022) EPSC Abstract #533 [11] Ferrari, M. et al. (2022) EPSC Abstract #153 [12] Nass, A. et al. (2021) EPSC Abstract #383

GEOLOGICAL MAPPING OF SEDIMENTARY SEQUENCES OF IMPACT CRATERS IN ARABIA TERRA: A TEST SITE FOR STANDARDIZED PLANETARY MAPS.

M. Pondrelli[1], I. Di Pietro[2], A.C. Tangari[3], M. Pantaloni[4], L. Marinangeli[3], G. Schmidt[5], F. Salese[6], S. Silvestro[7], A. G. Fairén[6], E. Luzzi[8], M. Massironi[9], R. Pozzobon[9], A. Nass[10], A.P. Rossi[8], [1]IRSPS, Università G. d'Annunzio, viale Pindaro 42, 65127, Pescara, Italy monica.pondrelli@unich.it , [2]Agenzia Spaziale Italiana, Roma, Italy ilaria.dipietro@asi.it , [3]Laboratorio di Telerilevamento e Planetologia, Dip. di Scienze Psicologiche, della Salute e del Territorio (DISPUTer), Università G. d'Annunzio, Via Vestini 31, 66013, Chieti, Italy lucia.marinangeli@unich.it , [4]Servizio Geologico d'Italia, ISPRA, via V. Brancati 48, 00144, Rome, Italy marco.pantaloni@isprambiente.it , [5]GeoQuTe Lab, Roma Tre University, Rome, Italy, [6]Centro de Astrobiologia CSIC-INTA, Madrid, Spain, [7]Istituto Nazionale di Astrofisica (INAF), Napoli, Italy, [8]Department of Physics and Earth Sciences, Jacobs University Bremen, Campus Ring 1, 28759, Bremen, Germany, [9]Department of Geosciences, University of Padova, Via Gradenigo 6, 3131, Padova, Italy, [10]DLR, Institute of Planetary Research, Rutherfordstrasse 2, 12489 Berlin, Germany,

Introduction: Sedimentary sequences are among the most appealing deposits present on Mars due to their implication in reconstructing the past climatic conditions and potentiality to preserve fossil life. The availability of different types of data at different resolutions and the ingestion in GIS environment, provide an impressive suite of tools to develop planetary geological maps.

These datasets allow the realization of thematic maps with an approach somewhat akin to the relatively 'objective' geological map approach well-known on Earth. For Mars the data coverage is extremely large and with high-resolution in correspondence of small areas (e.g., basins) making the mapping process easier and more significant. This is generally true for most of the sedimentary systems on Mars. Such an approach would allow to distinguish the deposits characterized on the base of their objectively defined characters (i.e., tone, texture, absence/presence of sedimentary structure, compositional hints) from the genetic interpretation provided by the morphological characters. A clear distinction between descriptive and interpretative units is specifically envisaged when geomorphological interpretation is particularly controversial. Stratigraphy represents another concept that needs to be included within map information. Unlike on Earth, sedimentary (and not only) systems preserve their morphological assemblages down to the deep stratigraphic record, making the recognition of unconformities and stratigraphic relations a pre-requisite to a correct interpretation of Martian units.

In the framework of the GMAP (Geologic MApping of Planetary bodies) project, herein we present an attempt to include all these different but complementary information combined in the same cartographic product taking advantage of GIS-based tools. Moreover, we aim at testing, where possible, the Earth-born symbols designed for the Geological Map of Italy [1,2] as an attempt to make the 'language' of geological maps as uniform as possible.

Study site: Our work was focused on the southern portion of Arabia Terra (Figure 1) where several impact craters show internal layered sequences [3]. The study area is represented by the set of three craters shown in Figure 2.
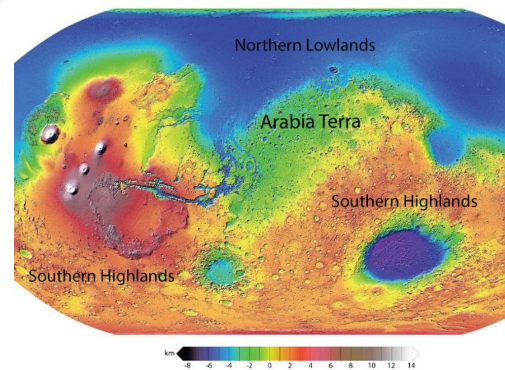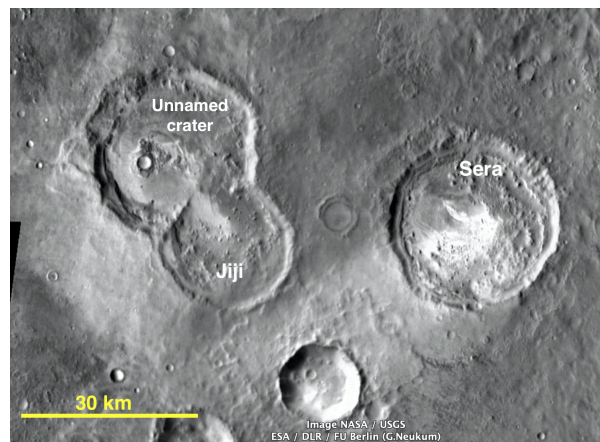

Figure 1 - Arabia Terra location.

Figure 2 - Image of the study area in south-western Arabia Terra focused on the Sera, Jiji and an unnamed crater.

Mapping approaches: We realized a geological map (Figure 3) including i) a polygon shapefile with the units described using the as objective as possible characters, ii) a linear shapefile to define the nature of the stratigraphic boundaries, and iii) a linear shapefile with tectonic features and interpretative

geomorphological structure. Although geology is an interpretative science, this organization allows to focus, simultaneously but separately, on the description, on the stratigraphic relations (emphasizing the missing time) with different hierarchy, and on the genetic interpretation, respectively. The genetic interpretation in turn is constrained by the reconstruction of the vertical and lateral relationships among the units that allow to interpret the genesis of a specific landform in the framework of a context of associated landforms (i.e., landscape).
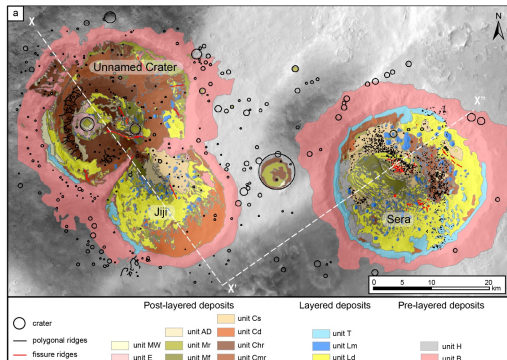
Figure 3 - Geological map of the studied area with the distinction between the three main sequence: pre-layered, layered and post-layered units. Modified from [4]

The purpose of this approach is to introduce a concept that addresses the 'objective' description of the units with all the available dataset that in turn might favor the reproducibility of these observations in different areas/settings. As an example (Fig. 4), the Layered Light Toned Deposits were described as light toned, moderately rough, layered and associated with flat or very low-dipping terrains at CTX scale. Whereas they show a bedsets thickness of few meters and they are disrupted in a post-depositional meter-scale polygonal pattern at the HiRISE scale. This unit onlaps the older 'Substratum' and is covered in disconformity by the Dark-toned layered deposits or by the mantling unit.
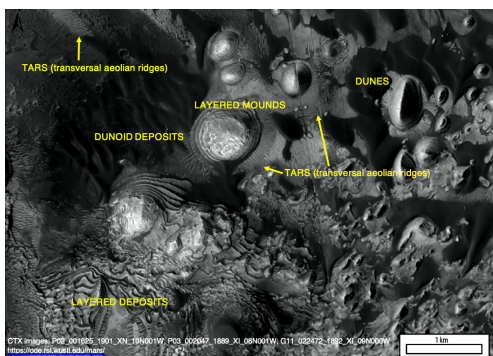
Figure 4 - CTX-based perspective view of the sedimentary deposits filling Sera crater.

The stratigraphic reconstructions allowed to identify a succession of depositional events separated by unconformities which are expressed by space-space and space-time reconstructions.

The next step will include the CRISM hyperspectral data in the unit definition. An example of the capability of the spectral images to discriminate different compositions is shown in Figure 5 where surface material with different mafic minerals content can be distinguished.
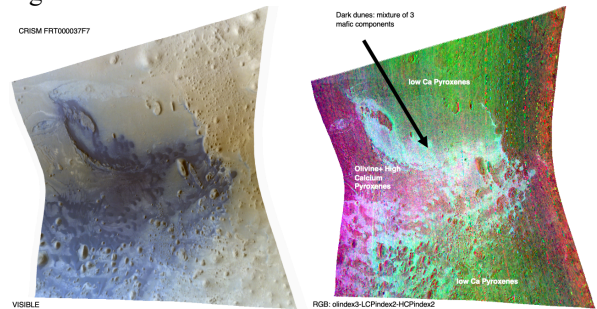
Figure 5 – CRISM hyperspectral RGB combination in real (left) and false (right) color using indexes for the identification of different mafic minerals.

The problem of the different resolution among the images and the limited coverage of the spectral data will have to be addressed in order to organize a consistent legend.

Finally, we plan to identify a set of graphical symbols describing the surface features, locating potential limits in current GIS symbology implementation. The aim is to develop a 'language' as uniform as possible between Earth and Planetary geological-geomorphological maps.

References: [1] ISPRA (2009) *Carta Geologica d'Italia. Guida alla rappresentazione cartografica. Modifiche e integrazioni ai Quaderni 2/1996 e 6/1997,* pp 166. [2] ISPRA (2018) *Carta Geomorfologica d'Italia. Guida alla rappresentazione cartografica. Modifiche e integrazioni al Quaderno 4/1994,* pp 95. [3] Schmidt et al. (2021) *JGR*, 126. [4] Di Pietro et al., *JGR*, submitted.

CLAY-RICH DEPOSITS IN OXIA PLANUM AND NORTH XANTHE TERRA: AN UPDATED OVERVIEW OF THE INFRARED DATA IN CONTEXT WITH EXOMARS ROVER MISSION.

J. Brossier*, F. Altieri, M.C. De Sanctis, A. Frigeri, M. Ferrari, S. De Angelis, A. Apuzzo, and the Ma_MISS team. IAPS – INAF, Rome, Italy (jeremy.brossier@inaf.it).

Introduction – ExoMars rover mission is expected to deliver the "*Rosalind Franklin*" rover to explore Oxia Planum, a region straddling between Arabia Terra and Chryse Planitia (335.5E, 18.2N). Oxia Planum shows evidences of a long-lived aqueous activity [1–4], where near-infrared data reveal widespread outcrops of recently exhumed clay-rich deposits (Figure 1). Exo-Mars rover will explore these outcrops to search for signs of past or present life on the planet, as biosignatures might be preserved in the sedimentary rocks [5]. Meanwhile, we also focus on clay-bearing outcrops detected in north Xanthe Terra (313E, 13N) [6], a region that has already been proposed for several rover missions (Figure 1). Clays detected at Oxia Planum and north Xanthe Terra are among those found all over circum-Chryse Planitia [7], a flat lowland region and bottom end of many outflow channels.
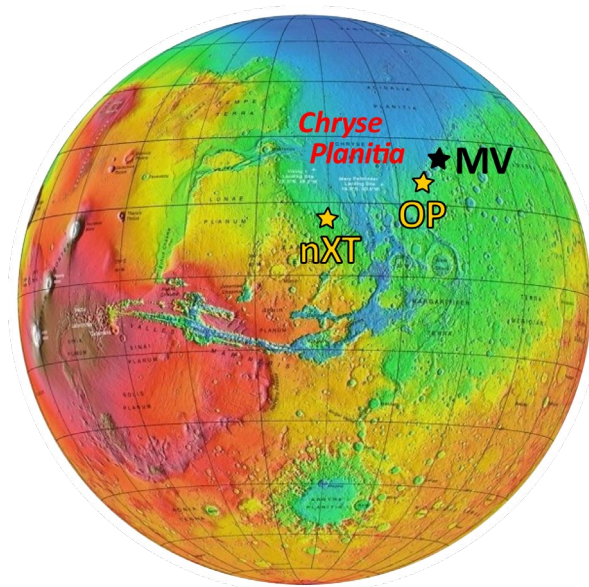
Figure 1 – MOLA global topographic map with key regions around circum-Chryse Planitia: Oxia Planum (OP), north Xanthe Terra (nXT), and Mawrth Vallis (MV).

Both sites are thought to be closely comparable owing to their geologic units and relative stratigraphy. Like in Oxia Planum, several morphological features indicate a fluvio-deltaic and lacustrine history in north Xanthe Terra [8–10], particularly the Sabrina and Hypanis valley systems. Despite a possible detection of Fe,Mg-rich clays at the fan deltas, no detailed spectral survey has been done in the entire area. An in-depth analysis of these outcrops is essential to better determine possible mineral phase(s) and search for changes in the clay mineralogy related to differences in formation and weathering conditions. We examine near-infrared data, notably the absorptions centered in the 1.0–2.6 µm spectral range, to better constrain the clay mineralogy.

Data & Methods – Spectral signatures of the clay outcrops are extracted from data collected by the CRISM instrument [11], having spatial resolutions from 20 to 40 m·px^{-1} and a spectral resolution of 6.6 nm. We used several CRISM cubes acquired in the infrared spectral range (1–4 µm), targeting the two regions. They are first processed with the CAT ENVI toolkit for atmospheric and photometric corrections. Corrected cubes are then denoised to reduce noise and residual atmospheric contributions, and finally enhance mineralogical absorptions in the "*ratioed*" spectrum. We define our regions of interest (ROIs) to delineate the clays. For doing that, we calculate band depths at 1.9 and 2.3 µm [12] to select pixels with strong absorptions and map the ROIs for each cube.

Results – We retrieve the band centers for all pixels composing the ROIs within the three absorptions of interest (1.4, 2.3, and 2.4 µm), after continuum removal to emphasize the absorptions. The band centers do not strongly vary for the three absorptions, with average values being 1.410, 2.305 and 2.397 µm, respectively. Overall, these values are quite similar in Oxia Planum and north Xanthe Terra [4,6].

Discussion – CRISM cubes reveal several absorptions in the 1.1–2.6 µm range. Paired absorptions near 1.4 and 1.9 µm are common to hydrated minerals, while an absorption near 2.3 µm indicates a (Fe,Mg)-OH vibration. Clays in Oxia Planum and Xanthe Terra are consistent with Fe,Mg-rich clays, combining absorptions at 1.41, 1.92, 2.30–2.31 µm and weaker overtones near 2.39–2.40 µm. Martian Fe,Mg-rich clays generally show spectral variability in these absorptions, from Fe-rich (e.g., nontronites, hisingerites) to Mg-rich (e.g., saponites, hectorites) compositional phases. For instance, nontronites display typical absorptions near 2.28–2.29 µm and at 2.40 µm, while saponites have absorptions near 2.31–2.32 µm and at 2.39 µm. Nevertheless, intermediate band centers obtained for the mapped outcrops rather correlate with either Fe-rich saponites or vermiculites (associated with hydrobiotite) (Figure 2). Band centers within these absorptions vary
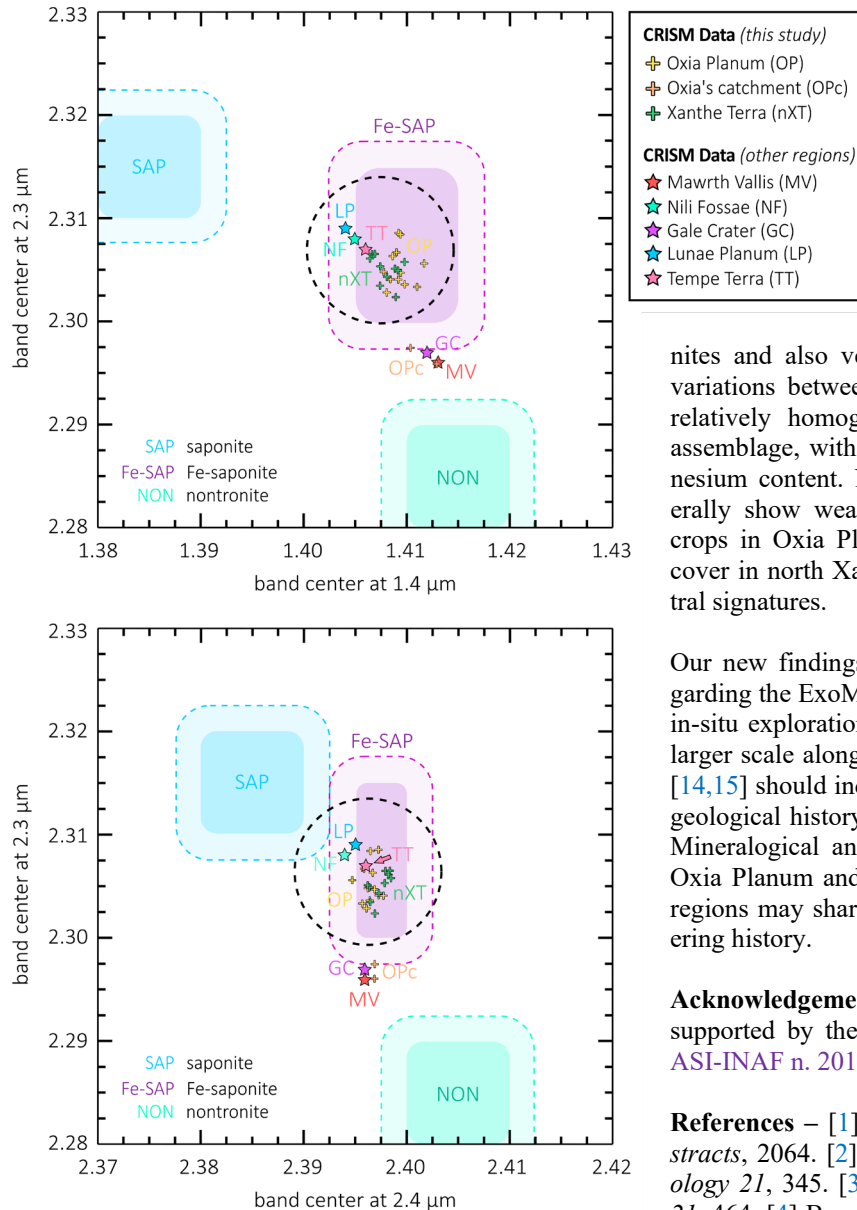
doing that, we reported the exact positions of the 1.4, 2.3 and 2.4 µm absorption bands, and searched for possible variations in these band centers. Furthermore, we also mapped the "*clearest*" exposures of clays in the two regions, in context with the morphology and topography. In both regions, the clays are consistent with Fe-bearing saponites and also vermiculites. We only observe subtle variations between the targeted outcrops, implying a relatively homogeneous distribution of the mineral assemblage, with very little changes in iron and magnesium content. Nonetheless, Xanthe's outcrops generally show weaker signatures relative to most outcrops in Oxia Planum, likely due to significant dust cover in north Xanthe Terra attenuating the clay spectral signatures.

Our new findings allow for further investigations regarding the ExoMars rover mission and eventual future in-situ explorations. Additional geologic analyses at a larger scale along the circum-Chryse Planitia province [14,15] should indubitably provide new insights on the geological history and stratigraphy of the two regions. Mineralogical and morphological similarities seen in Oxia Planum and north Xanthe Terra imply that both regions may share a common depositional and weathering history.

References – [1] Carter et al. (2016) *47th LPSC Abstracts*, 2064. [2] Quantin-Nataf et al. (2021) *Astrobiology 21*, 345. [3] Mandon et al. (2021) *Astrobiology 21*, 464. [4] Brossier et al. (2022) *Icarus 386*, 115114. [5] Vago et al. (2017) *Astrobiology 17*, 471. [6] Brossier et al. (under review) *PSJ*. [7] Carter et al. (2015) *10th EPSC Abstracts*, 661. [8] Fawdon et al. (2018) *EPSL 500*, 225. [9] Adler et al. (2019) *Icarus 319*, 885. [10] Adler et al. (2022) *JGR 127*, e2021JE006994. [11] Murchie et al. (2007) *JGR 112*, E05S03. [12] Viviano-Beck et al. (2014) *JGR 119*, 1403. [13] Michalski et al. (2015). *EPSL 427*, 1403. [14] Frueh et al. (2022) *53rd LPSC Abstracts*, 1877. [15] Hauber et al. (2021) *52nd LPSC Abstracts*, 2057.

Figure 2 – Scatterplots of 2.3 µm vs 1.4 µm band centers for the clay-rich outcrops seen in Oxia Planum and north Xanthe Terra, compared with values retrieved elsewhere on Mars (Mawrth Vallis, Nili Fossae and Gale crater), as well as some candidate minerals.

very little throughout the two regions. Exact positions therein depend on the relative abundance of iron and magnesium in the clay structure, and also the oxidation state of iron [13].

Conclusions – In this study, we report a detailed analysis of the clay-bearing outcrops found in Oxia Planum and north Xanthe Terra, in order to compare them with terrestrial analogs and other regions on Mars [4,6]. By

Improvement of the MARSIS On-Board SW, on the Mars Express Mission. Preliminary scientific results on Phobos and Mars.

A. Cicchetti[1], C. Nenna[1], M. Cartacci[1], R. Noschese[1], R. Orosei[2]

[1] Istituto di Astrofisica e Planetologia Spaziali, Istituto Nazionale di Astrofisica, Rome, Italy
[2] Istituto di Radioastronomia, Istituto Nazionale di Astrofisica, Bologna, Italy

Introduction

The Mars Advanced Radar for Subsurface and Ionosphere Sounding (MARSIS) is a powerful instrument for subsurface remote sensing of the Mars planet. Since the beginning of operations, about fifteen year ago, many successful observations have been carried out, in particular for the study of Mars South and North Polar Layered Deposits (PLD).

At this point of this fruitful mission, having acquired a good knowledge of the Mars environment, it was decided to improve the instrument science performances, mitigating some instrument technical limitations, that were required at the beginning of the mission, but which were proven to be excessive and, above all, limiting.

The new on-board Software is now operative on the instrument and almost fully commissioned. Recently, it allowed to see beneath the surfaces of Mars and its moon Phobos in more detail than ever before.

Upgrade description

The new on-board SW includes a series of upgrades that improve signal reception and on-board data processing, to increase the amount and quality of science data sent to Earth.

Two new Operative Modes have been added to the ones already in use. The first one is **SSM**, it is related exclusively to the observation of Mars. It is similar to the existing main dual-channel subsurface mode SS3. The processing for the first operative channel will remain unchanged, while, on the second one, a dedicated new processing algorithms, have been developed in order to extract, from the received echoes just the samples containing with a relevant science information and discarding the remaining ones, that contain only noise.

The new second operative mode **SSP**, is designed mainly to optimize the observation of Phobos, however it can also be used on Mars, over small science targets of particular interest. Thanks to SSP, it is now possible to collect a large segment of raw unprocessed data, about 134 seconds, compared to the previous nominal segment of 24 seconds; SSP will also optimize adaptively the Receiver Gain during the flyby, thereby improving the dynamic range of the receiving channel used for recording the raw Science Data.

At the same time, data rate on the SC OBDH bus, will be strongly reduced, allowing MARSIS, PFS and SPICAM to operate simultaneously. This software upgrade is a major change, practically transforming MARSIS in a brand new instrument on board Mars Express, almost 20 years after its launch.

Improved Phobos Observations

The latest Phobos flyby (23/September/2022) offered the opportunity to test the performance of the MARIS SW upgrade.

The MARSIS instrument was originally designed to observe exclusively Mars. As a result, it was designed for use at the typical distance between the spacecraft and the planet's surface – more than 250 km.

The new SW upgrade allows MARSIS to be used at much closer distances (the minimum detectable range is now set at 40km). During this flyby, we used MARSIS to study Phobos from as close as 82 km. Being so close to Phobos allows to study its structure in more detail and identify important features that could not be detected from further away.

Thanks to the predicted Mars Express orbit geometry, in the next years [2023 : 2025], MARSIS will be able to observe Phobos even closer, at distances below 50km, providing new opportunities to study this unique celestial body, and contributing to solving the mystery surrounding Phobos' origin.
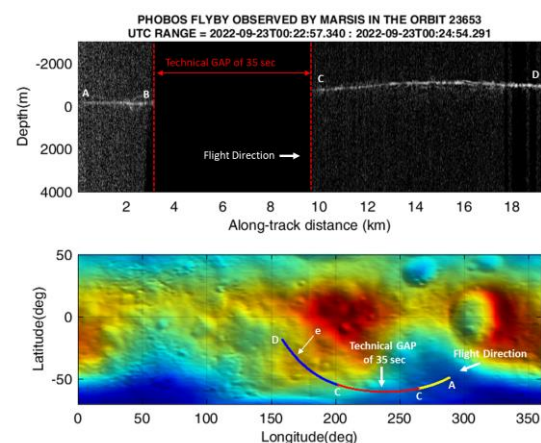

Fig. 1: Phobos observed by MARSIS with its new operative mode SSP

Figure 1 shows the 'radargram' acquired by MARSIS during the flyby. A radargram reveals the echoes produced when the radar signal emitted by MARSIS bounces off something and returns to the instrument. The brighter the signal, the more powerful the echo.

The continuous bright line shows the echo from the moon's surface. The lower reflections are either 'clutter' caused by features on the moon's surface, or, more interestingly, signs of possible structural features below the surface.

Section A-B was recorded using the older configuration of the MARSIS software. The new configuration was prepared during the 'technical gap' and successfully used for the very first time from C-D.

The bottom panel shows the path of the observation, across the Phobos surface.

Simulation of the Phobos flyby

This Phobos flyby was also important, due to the presence of weak secondary echoes which could have been generated by discontinuities in the subsurface (cavities, layers of different materials, etc.) or by surface lateral clutter.

Isolating the echoes reflected by off-nadir surface, that could arrive at the radar antenna at the same time as subsurface nadir echoes and comparing them with the simulated echoes, from the surface return using Digital Terrain Model, it is possible to solve this ambiguity.

Figure 2 shows the comparison between the simulation results, with the real data acquired by the radar. The comparison is made difficult by the low power level of the echoes, often comparable with the noise power of the receiver, the study is still on-going.
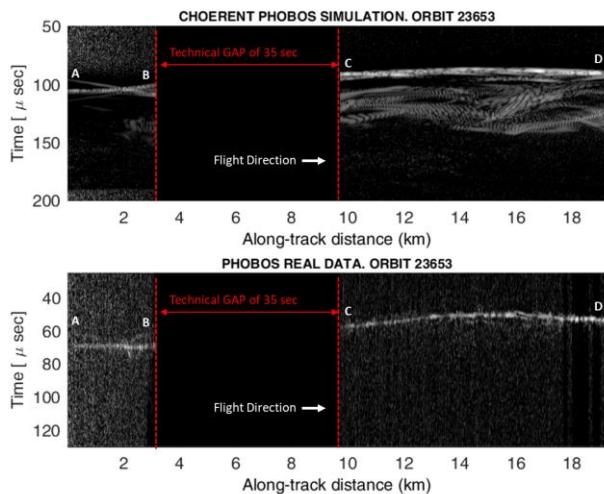
Fig. 2: Phobos Comparison between Simulated and Real Data

Improved Mars Observation in SSP mode

Several observations have been planned, on Mars areas of high scientific interest and when the spacecraft was on the night side of Mars, to minimize ionospheric distorsion of the signals. Figure 3 shows an example of a MARSIS radargram collected with the new Science Operative Mode (SSP), in the orbit 22795 (geen path across the surface). Figure 3 also shows an old fly-by on the same area, in the orbit 21886 (white path across the surface); the improvement with the new SW is evident.
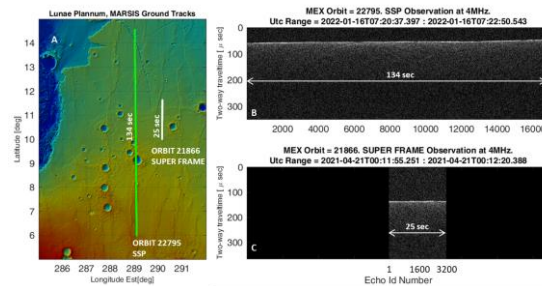
Fig. 3: Mars Data Comparison

References

[1] Safaeinili, A. et al (2007) First International Conference on the Exploration of Phobos and Deimos, LPI Contribution No. 1.

[2] Plettemeier, Dirk; Hahnel, Ronny; Hegler, Sebastian; Safaeinili, Ali; Plaut, Jeff; Gaskell, Bob; Orosei, Roberto; Cicchetti, Andrea; Picardi, Giovanni, Numerical computation of radar echoes measured by MARSIS during Phobos flybys, Radar Conference, 2009 IEEE , vol., no., pp.1-6, 4-8 May 2009.

[3] Cicchetti, A., Cartacci, M., Gim, Y. et al., 2011. MARSIS: Latest Phobos Flyby. Data Processing Results and Advanced Radar Configuration Design. EPSC-DPS Joint Meeting 2011 497.

[4]. A. Cicchetti, et al., Observations of Phobos by the Mars Express radar MARSIS: Description of the detection techniques and preliminary results. Adv. Space Res. 60, 2289-2302 (2017).

[5]. Orosei, R. et al. Radar evidence of subglacial liquid water on Mars. Science 361, 490–493 (2018).

EOLO MEGARIPPLE ARCHIVE: MAPPING THE RECENT AEOLIAN DEPOSITS TO SUPPORT THE LUMINESCENCE INVESTIGATION ON MARS
L. Marinangeli[1] , M.Pondrelli[1], S. Silvestro[2], I. Di Pietro[3,1], A. Caramanico[1], A.C. Tangari[1] and the IN-TIME team, [1]Università G.d'Annunzio – Ud'A, Chieti-Pescara lucia.marinangeli@unich.it, [2]INAF-OACN Napoli simone.silvestro@inaf.it, [3]Agenzia Spaziale Italiana, Roma ilaria.dipietro@asi.it .

The IN TIME project: The *In Situ Instrument for Mars and Earth dating application* (IN-TIME; https://intime-project.eu/) project addresses the technological and economic viability of a leading-edge instrument for dating of Mars' surface based on the luminescence techique. The project is funded under the European Union H2020-MSCA-RISE-2018 research programme (G.A. n. 823934) and involve a consortium of seven European organizations and industries from Italy, Spain and Cyprus coordinated by ALMA Sistemi Srl and University of Texas as associated US partner.

Dating of recent (< 1 Million years) events on Mars using crater counting is difficult due to the uncertainties in the idenfication of fresh craters, but the chronology of these events are needed to better constraint the development of future human missions.

Luminescence is an ability of minerals to emit light after being excites with various kinds of energy.

It is commonly used to estimate the burial age of sediments by determining how long ago the mineral grains were last exposed to daylight. Many minerals are capable of luminescing in the dark when appropriately irradiated and stimulated. For dating purposes, however, quartz and feldspar are the dosimeters that have received the most focus. Attempts have also been made to use zircon and calcite but these are not commonly used for dating because of a number of drawbacks.

Thus, the application of luminescence for dating rock samples on Mars has the following two main constraints:

1. It may measure burial age and thus date processes, not older than <0.5-1 My;
2. It requires quartz or k-feldspar as mineralogical components in the sample.
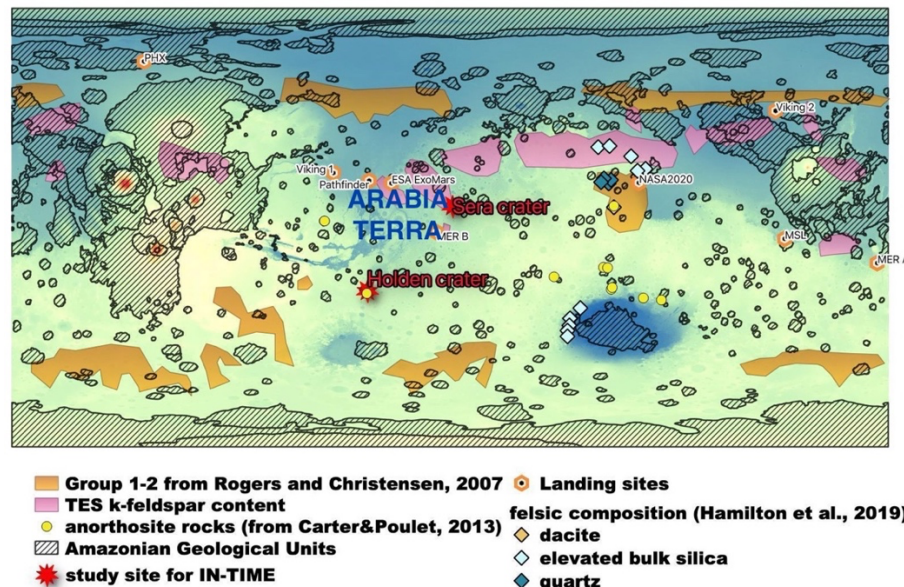
Figure 1 – Summary of information to refine scientific case of luminescence investigation on Mars. Group 1-2 correspond to the more silica-rich surface identified by TES and THEMIS data. (MOLA topography as base map)

The distribution of Quartz and Feldspar minerals on Mars is not well constrained due to the lack of detailed information from remote observations and very limited in situ analysis. Furthermore, remote sensing acquisition may be significantly affected by atmospheric conditions which may prevent the correct identification of minerals/chemical species from averaged spectra.

The volcanic sequence of Syrtis Major appears to be enriched of crystalline silica though it is laterally in contact with the olivine-rich layers of Nili Fossae [1,2]. Other exposures of potential felsic minerals have been

lately interpreted as a combination of amorphous silica and quartz likely due to hydrothermal alteration of the basaltic bedrock. However, it should be noted that mineralogical analysis from rovers returned an unexpected presence of felsic minerals: Curiosity found alkali-rich float rocks in Gale crater, (mugearites) and coarse-grained alkali feldspar–bearing lithologies, while Spirit rover also encountered alkaline volcanic rocks (plagioclase-rich relative to pyroxene and olivine in Gusev crater [3,4].

The UdA's group in collaboration with INAF-OACN has been carrying out a geological mapping activity to identify potential areas to fullfill the applicability of in situ luminescence measurements on Mars. We focus our search for sites of interest for luminescence investigation on the intriguing region of Arabia-Margaritifer Terra (Figure 1) where large occurrences of recent sedimentary deposits have been observed and hold evidence of a more sialic bedrock as well as sedimentary deposits.

The geological approach: The selection of potential sites for the luminescence investigation on Mars, requires a detailed knowledge of the in situ characteristics in terms of stratigraphy and composition.

Combining different types of compositional maps, including the distribution of the Amazonian geological units and the sites where more felsic composition has been observed so far, we identified a few sites in the Arabia-Margaritifer region and Syrtis Major to be studied in more details to provide a realistic context for luminescence dating on Mars.

Arabia Terra (Figure 1) is an equatorial region on Mars which shows an interesting interaction between water-related and aeolian deposits. The sedimentary sequence includes the sulfates deposits firstly identified in Meridiani Planum (Opportunity rover landing site) and a large number of fluvio-deltaic including paleo-lakes[5]. The aeolian features and deposits are widely present and show different phases of activation [6]. Our work is focused in the identification of the megaripple complex patterns which has been proved to record "recent" climatic changes on Mars [6,7]. Dunes/megaripples have the potential (and they do) to form stratigraphic successions and different superposed generations of aeolian landforms reflecting different wind regimes [8].

Furthermore, the global distribution which may reflect changes of atmospheric conditions at large scale, possibly similar to the Polar Layered Deposits, and thus can be considered a potential tool to correlate successions in different parts of the planet.

The EOLO megaripple database: Our work to build the database consists to identify sites with different generations of megaripples at HiRISE scale (25-32 cm/pixel). We have currently analyzed almost one thousand of HiRISE images and identified ~600 regions of interest with 120 sites where megaripple are reworked (Figure 2).

We plan to continue the analysis of the Arabia Terra area and then move to quadrangles at different latitudes to compare the patterns and morphology of these peculiar features and check where such reworing patterns might suggest recent (late Amazonian) climatic changes.

References: [1] Bandfield et el. (2006) *GRL*, 33, L06203. [2] Sautter et al. (2016) *Lithos*, 254–255, 36–52. [3] Cousin et al. (2017) *Icarus*, 288, 265–283. [4] Udry et al. (2018) *JGR*, 123(6), 1525–1540. [5] Squyres et al. (2006) *JGR*, 111, 1-19. [6] Golombek et al. (2010) *JGR*, 115, 1-34. [7] Fenton et al. (2015) *Aeolian Research*, 16, 75-99. [8] Kocurek and Ewing, (2005) *Geomorphology*, 72, 1-4.
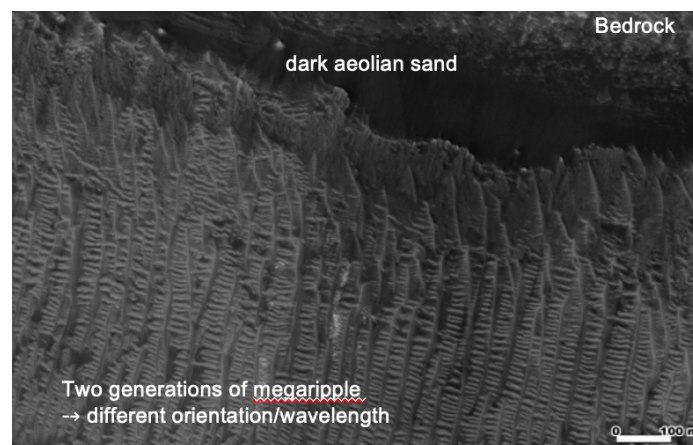

Figure 2. A typical pattern of reworked megaripples with two main trends, E-W and N-S. A more recent episodes of aeolian deposition is represented by the dark sand overlyiong the bright-toned megaripples.

THE SURFACE OF MERCURY INVESTIGATED BY MEANS OF PRINCIPAL COMPONENT ANALYSIS ON MASCS/MESSENGER DATA. A. Galiano[1], F. Capaccioni[1], G. Filacchione[1], C. Carli[1], [1]INAF-IAPS Istituto di Astrofisica e Planetologia Spaziali, Rome, Italy (anna.galiano@inaf.it).

Introduction: The surface of Mercury hosts several spectral units mainly identifiable for differences in reflectance and spectral slope [1,2,3,4]. The major terrains identified on Mercury are the smooth plains, Intermediate Terrain (IT), and Low-Reflectance Material (LRM). The smooth plains probably formed through effusive volcanism [3], the IT are heavily cratered terrains [3], the LRM is supposed to be the early graphite-bearing crust exposed by impacts [5]. Minor colour units on the planet include hollows [6], pyroclastic deposits, fresh crater ejecta, and Red Material (RM) [1]. Hollows are shallow depressions with a flat floor and an irregular shape [6,7], whose formation is probably linked to the loss of a volatile component in the parent material [8]. Pyroclastic deposits are the product of explosive volcanism on Mercury [9,10]. Fresh crater ejecta and RM are found in association with rims, ejecta, and rays of impact craters [11]

The units were first observed with the application of Principal Component Analysis (PCA) on photometrically corrected MDIS (Mercury Dual Imaging System [12]) images, acquired during the first two flybys of NASA/MESSENGER spacecraft, and combining the second principal component, the first principal component and the 430/1000 nm ratio in the red-green-blue image [3]. The hermean units are characterized by a positive spectral slope in the MDIS spectral range (395-1040 nm), but the units are described as "red" or "blue" if the slope is more or less steep, respectively than the average terrain.

Smooth plains are subdivided into High-reflectance Red Plains (HRP), Intermediate Plains (IP) and Low-reflectance Blue Plains (LBP). HRP is the brightest and reddest of the smooth plains; IT and IP are spectrally similar to the average terrain; LBP is spectrally intermediate between IP/IT and LRM, the darkest and bluest unit on Mercury [3]. Hollows are among the brightest geological units on Mercury and show a relatively flat VIS slope [4]. Pyroclastic deposits are usually characterized by a central pit (the vent of explosion) surrounded by a spectrally bright and red terrain (facula) [9,10]. Fresh crater ejecta are supposed to be compositionally similar to the surface layers and their high reflectance and shallow spectral slope are probably ascribed to a minor space weathering alteration [1]. The RM (spectrally bright and with a red spectral slope) is, on the contrary, probably compositionally different from the rest of the surface, being excavated from deeper layers as a consequence of impacts [11,13].

The surface of Mercury was also investigated by means of photometrically corrected MASCS data, by estimating the reflectance at 575 nm, the spectral slope in the VIS-to-IR range (410/750 nm ratio) and the spectral slope in the UV-to-VIS range (310/390 nm ratio). By placing these spectral parameters in the red, green and blue channels, a colour composite image of Mercury was obtained thank to which the surface was divided into four units: average (including plains), dark blue (LRM and LBP), red (pyroclastic deposits and HRP), and bright (hollows and fresh ejecta) units [14]. A PCA was also applied on MASCS data acquired during the first two MESSENGER flybys and not corrected for viewing geometry [15].

In this work, we characterized the surface of Mercury by applying the PCA on photometrically-corrected and quality-filtered MASCS data acquired during the MESSENGER orbital phases.

MASCS data: We used data acquired by VIRS (Visible and Infrared Spectrograph), the point spectrometer of the MASCS instrument, which collected reflectance spectra of the surface of Mercury in the Visible (VIS, 300-1050 nm) and Near-Infrared (NIR, 850-1450 nm) range, with a spectral sampling of 5 nm/band [16]. In particular, the PCA was applied on photometrically-corrected and high-quality VIRS data [17], i.e. acquired during the phase orbits, with a footprint length lower than 25 km and a footprint length/width ratio less than 10, with optimal observing angles (incidence and emission angles < 65°) and with VIS detector temperature lower than 30°C.

The Principal Component Analysis: The PCA was applied on high-quality VIRS data in the 300-800 nm range, using 21 spectral channels. The PC1 accounts for 98.72% of the total variance of the dataset, whereas the PC2 and PC3 contain respectively 0.95% and 0.17% of the dataset variability. The PC4 to PC21 cover together about 0.15% of the variance: these components contain negligible information and are strongly influenced by noise.

Results: We combined the PC1, PC2 and PC3 maps in the red, green, and blue channels respectively, obtaining the "RGB-PCA" image. The colour composite image allows for distinguishing the major terrains described above. In addition, among the minor terrains, hollows and fresh ejecta can be discriminated by pyroclastic deposits and Red Material.

The RGB-PCA image separates the pyroclastic deposits with a spectrally distinct facula from the deposits with a minor spectral contrast: in particular, faculae with high reflectance and strong spectral slope have a reddish tone in the RGB-PCA image, whereas a magenta/purple colour is associated to the faculae with lower reflectance and less steep spectral slope. Thus, in the PC2 vs. PC3 scatterplot [**Fig.1**], the spectrally distinct faculae (red diamonds) show lower PC2 and PC3 values than the faculae with a lower reflectance and spectral slope (violet diamonds).
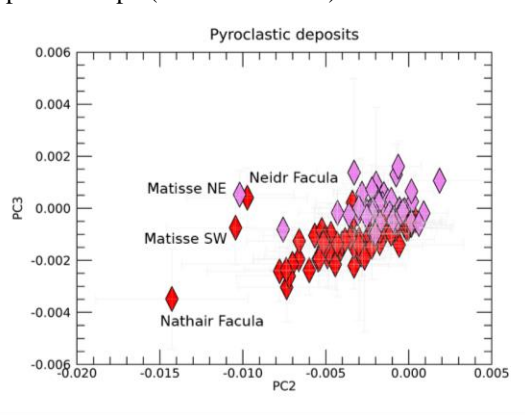
Fig1. PC2 vs. PC3 scatterplot for spectrally distinct faculae (red diamonds) and for faculae with a minor spectral contrast with respect to the surrounding terrain (violet diamonds).

The density plot of PC1 vs. PC2 shows a bimodal trend, with two clusters that separate from the main one (centred at PC2 value of 0.00). We explored the density plot by subdividing it into three clusters [**Fig.2**]: Cluster A (blue rectangle, corresponding to PC2>0.005), Cluster B (red rectangle, PC2<-0.005) and Cluster C (green rectangle, -0.005<PC2<0.005).
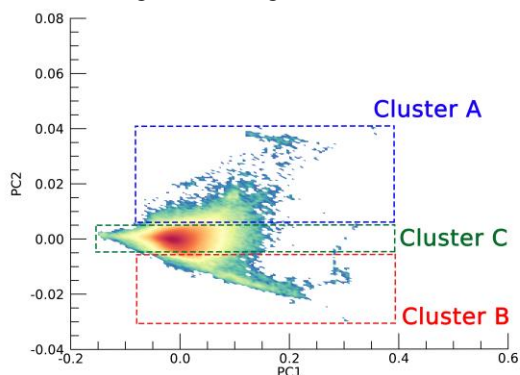
Fig2. PC1 vs PC2 density plot. Blue, red and green boxes define, respectively, Cluster A, Cluster B, and Cluster C.

From a preliminary analysis of the mean spectra of these clusters, we observe a progressive reddening in the VIS range (500-800 nm) from Cluster A to Cluster C to Cluster B.

The spatial location of Cluster A identifies areas with a lower spectral slope, i.e. fresh ejecta, hollows, LRM and LBP.

Cluster B includes units with a redder spectral slope, i.e. pyroclastic deposits, RM, HRP and IT.

Cluster C was investigated by estimating the mean value of PC1 (0.002), and the corresponding standard deviation (SD=0.023). Starting from the mean value and moving in steps of 1SD, we defined several classes, characterized by progressively higher values of PC1, reflectance and the UV slope (estimated in the 300-400 nm range), whereas the VIS slope assumes progressively minor values. Areas of Cluster C with relatively high reflectance and low VIS slope are coincident with the wall of craters and with the wall of some explosive vents.

References: [1] Robinson, M.S. et al. (2008), *Science 321*, 66. [2] Murchie, S.L. et al. (2008), *Science 321*, 73. [3] Denevi, B. et al. (2009), *Science 324*, 613. [4] Blewett, D.T. et al. (2009), *EPSL 285*, 272-282. [5] Peplowski, P.N. et al. (2016), *Nat. Geosci.9*, 273-276. [6] Blewett, D.T. et al. (2011), *Science 333*, 1856-1859. [7] Vaughan, W.M. et al. (2012), *LPSC XLIII*, Abstract #1187. [8] Blewett, D.T. et al. (2013), *J. Geophys. Res.:Planets 118*, 1013-1032 [9] Head, J.W. et al. (2008), *Science 321*, 69-72 [10] Goudge, T.A. et al. (2014), *J. Geophys. Res.: Planets 119*, 635-658. [11] Ernst, C.M. et al. (2010), *LPSC XL*, Abstract #1900. [12] Hawkins, S.E. et al. (2007), *Space Sci. Rev. 131*, 247-338. [13] Stöffler, D. et al. (1975), *J. Geophys. Res. 80*, 4062-4077. [14] Izenberg, N.R. et al. (2014), *Icarus 228*, 364-374. [15] D'Amore, M. et al. (2011), *LPSC XLII*, Abstract #1608. [16] McClintock, W.E. and Lankton, M.R. (2007), *Space Sci. Rev. 131*, 481-521. [17] Galiano, A. et al. (2022), *Icarus 388*, 115233.

STRUCTURAL ANALYSIS OF THE DISCOVERY QUADRANGLE (H-11), MERCURY.

A. Sepe[1], L. Ferranti[1,2], V. Galluzzi[2], and P. Palumbo[3,2]

[1]Dipartimento di Scienze della Terra, dell'Ambiente e delle Risorse, Università degli Studi di Napoli "Federico II", Naples, Italy (antonio.sepe3@studenti.unina.it)

[2]INAF, Istituto di Astrofisica e Planetologia Spaziali (IAPS), Rome, Italy

[3]Dipartimento di Scienze e Tecnologie, Università degli Studi di Napoli "Parthenope", Naples, Italy

Introduction: Mercury's quadrangle "Discovery" (H-11) is located at southern mid-latitudes (22.5°S−65°S and 270°E−360°E) in a heavily cratered region roughly antipodal to the Caloris Basin [1]. It is named after the NE−SW trending Discovery Rupes, one of the longest and highest lobate scarps on the planet (600 km in length and 2 km high), which seems to exhibit a right-lateral strike-slip component of displacement [2]. The quadrangle includes also a probable impact basin recognized in previous studies named Andal−Coleridge [3][4] or Bramante−Schubert [5], surrounded by a one- to five-ring system.

Since the only geomorphological map of the quadrangle dates to the time of the Mariner 10 (M10) mission [1], we aim to produce a high-resolution structural map of the quadrangle that will contribute to the 1:3M quadrangle geological map series which are being prepared for the BepiColombo mission [6].

Data and methods: We have produced a high-resolution structural map of the quadrangle (Fig. 1) by using MESSENGER/MDIS basemaps and the digital elevation model (DEM) of [7], following the methods and symbology adopted in [6]. The structural analysis of the quadrangle was carried out by mapping tectonic structures and plotting their azimuths in rose diagrams to recognize preferential trends at the regional scale. By following the observation of [5] that the Discovery, Adventure and Resolution Rupes occur along an arc more than 1000 km long, we investigated the structural relationships among the three scarps plus another scarp (here named Discovery-2) that seems to be the westward continuation of the Discovery Rupes (Discovery-1) by making a total of 38 profiles across the four scarps and measuring their height (H). This method assumes that the scarp height represents the throw of the fault. Indeed, the effects of exogenous erosion — which on Earth are usually significant and tend to quickly reduce the morphological expression of the throw— on Mercury are limited to impact cratering that, although relatively intense, is localized. Finally, by following the methods used in [8] and [9], we identify the transient crater of the (probable) Andal−Coleridge or Bramante−Schubert Basin and define its multi-ring structure.

Map and trend of structural features: The structural map in Figure 1 shows more than 400 segments of contractional structures (lobate scarps, high-relief ridges and wrinkle ridges) that appear to be arranged in a circular pattern, approximately at the center of the quadrangle, with two NW−SE and NE−SW-trending linear systems.

The rose diagrams show a NW−SE preferential trend of the structures and two less prominent ~N−S and NE−SW trends.

The mapped structures appear to be arranged around an area of crustal thinning, identified in the crustal thickness map [10], that roughly coincides with a broad topographic low approximately centered in the Schubert crater (43°S, 54°W).

Analysis of the Discovery, Adventure and Resolution Rupes: The scarp height (H) was measured on each profile and then plotted as a function of the position of each profile on the fault trace, which corresponds to the fault length (L). The diagram shows that the four scarps are characterized by several peaks, each of which represents a fully formed fault segment.

From the analysis of the H−L diagram, we found that the four structures analyzed represent segments of two different scarps, the Discovery Rupes and the Adventure−Resolution Rupes (with Discovery-2 being the western tip of the Discovery Rupes), which appear to be kinematically linked, since the cumulative throw falls approximately in the center of the system, consistent with typical fault growth patterns [11].

Multi-ring structure of large impact basins: The roughly circular pattern and strongly arcuate trend of the mapped structures could indicate the presence of the ancient Andal−Coleridge or Bramante−Schubert multi-ring basin. The area of crustal thinning identified from the crustal thickness map could represent the transient crater of the basin [9]. Although there exist scaling laws to calculate the diameter of lunar transient craters [9], there are none for Mercury. Approximating the crustal thinning area to a circumference, we estimate a transient crater with a diameter of ~500 km, partially consistent with the scaling law proposed by [9] for a weak lunar lithosphere. We used the approach proposed by [8] to define the position and the number of the rings, considering the Discovery Rupes as a segment of the so-called "topographic rim" [12]. In this way, we recognized a system of four concentric rings tangent to the main scarps of the quadrangle (Astrolabe

Rupes, Mirni Rupes and Discovery Rupes). The Adventure−Resolution Rupes is not concentric to the basin here proposed but appears to be concentric to another area of crustal thinning close to the Rabelais crater (60°S, 62°W), probably another impact basin.

Conclusions and future work: A complex structural picture emerges from the present work. The concentricity of the structures to a topographic low and an area of crustal thinning suggests the presence of an ancient multi-ring basin, so the mapped structures could be the morphological evidence of one or more rings surrounding the basin. The Discovery Rupes appears to be concentric to the Andal−Coleridge basin, while the Adventure−Resolution Rupes is concentric to another, smaller impact basin. This means that the two scarps formed as a result of two distinct local-scale processes, i.e., impacts, and were reactivated by Mercury's global contraction as a linked fault system.

The lack of N−S trending structures and their concentric pattern could be due to the presence of the Andal−Coleridge or Bramante−Schubert multi-ring basin, which could have defined mechanical discontinuities in the crust, influencing the localization and orientation of thrusts that would have represented preferential weak zones along which the global contraction of Mercury acted.

We aim at improving the structural map of the quadrangle to better define the diameter and center of the transient crater by finding or developing an *ad hoc* scaling law, and at further investigating the fault reactivation and deformative evolution of the basin.

Figure 1 Structural map of the "Discovery" (H-11) quadrangle of Mercury in LCC projection. The blue circle represents the transient crater rim inferred from the crustal thickness map while the red circles represent the rings of the basin inferred from the analysis of the structural map and the DEM.

References: [1] Trask and Dzurisin (1984). USGS, IMAP 1658. [2] Massironi et al. (2014). *Geological Society, London, Special Publications,* 401(1), 269-290. [3] Spudis and Strobell (1984). Lunar and Planetary Science Conference, 814-815. [4] Fassett et al. (2012). *Journal of Geophysical Research: Planets*, 117(E12). [5] Watters et al. (2001). *Planetary and Space Science*, 49(14-15), 1523-1530. [6] Galluzzi et al. (2019). *Journal of Geophysical Research: Planets*, 124(10), 2543-2562. [7] Becker et al. (2016). *47th Annual Lunar and Planetary Science Conference*, p. 2959. [8] Spudis and Guest (1988). In: *Mercury*, 118-164. [9] Potter et al. (2012). *Geophysical Research Letters*, 39(18). [10] Genova et al. (2019). *Geophysical Research Letters*, 3625-3633. [11] Kim and Sanderson (2005). *Earth-Science Reviews*, 68(3-4), 317-334. [12] Pike (1988). In: *Mercury*, 165-273.

SEGMENTATION ANALYSIS OF SELECTED LOBATE SCARPS ON MERCURY

L. Ferranti[1, 2], V. Galluzzi[2], A. Sepe[1], F. Menna[1], M. Annunziata[1], and P. Palumbo[3,2]
[1]Dipartimento di Scienze della Terra, dell'Ambiente e delle Risorse, Università degli Studi di Napoli "Federico II", Naples, Italy (luigi.ferranti@unina.it)
[2]INAF, Istituto di Astrofisica e Planetologia Spaziali (IAPS), Rome, Italy
[3]Dipartimento di Scienze e Tecnologie, Università degli Studi di Napoli "Parthenope", Naples, Italy

Introduction: Interaction and linkage of individual fault segments during the growth of major faults is a well established mechanism in the Earth crust, e.g., [1][2]. To our knowledge, however, this mechanism was never studied on other solid planets. In this contribution, we show results of displacement and length distribution analysis along the trace of major fault systems in the Victoria (H-02) and Discovery (H-11) quadrangles that allow to test hypothesis of fault segmentation.

Fault segmentaton and growth through segments linkage: Terrestrial faults are composed of fault segments at all scales as a consequence of crustal heterogeneity and strain evolution during their growth. As a population of segments that are broadly aligned along-strike grow, they interfere and can join to form a single and much longer fault, i.e., fault linkage [1][2]. Adjoining fault segments are said to be soft- or hard-linked as long as they are or are not in direct physical contact, respectively. The connection zones between two fault segments is called a relay structure.

Recognition of segment linkage is based on mapping the trace of segments first, and then by analysing the vertical displacement pattern along the fault trace. Single crustal faults tend to show a maximum throw in their central part, gradually decreasing toward the tips, generating a bell-shape or elliptical throw profile. Upon linkage between individual segments, there will be a throw minimum at the relay structures. The total displacement curve along the fault will therefore show as many maxima as the number of fault segments that are linked, with the maxima positioned at the centre of individual segments. As the fault accumulates displacement, the throw profile will approach that of an individual fault with a single, central maximum. However, the existence of previous segments is still evidenced by saddles and peaks that have not been totally erased, prompting recognition of fault linkage.

Victoria-Endeavour-Antoniadi Fault System – Length-frequency distribution: The Victoria Rupes-Endeavour Rupes-Antoniadi Dorsum (VEA) fault system stretches about NNW-SSE across the whole H-02 quadrangle, forming one of the longest (~4500 km) lobate scarp alignments on the planet [3][4].

A detailed mapping of the VEA performed by [4] showed that it is segmented into three distinct sectors, namely the Victoria Rupes (VEA-VR), Endeavour Rupes (VEA-ER) and Antoniadi Dorsum (VEA-AD). These individual arrays are distinguished based on systematic changes in fault trends and in width of the fault zone, and on the local occurrence of volcanic vents that help define segment boundaries. Kinematic analysis indicates the fault system is composed by predominat thrust faults and accompanying oblique ramps [4].

Based on the previous mapping results [4], we analyzed the length-frequency distribution of individual fault segments within the three arrays. Using different length bins (10, 15, 20, 30 km) for sampling the fault frequency, we found the most satisfactory results for bins between 15-30 km. Figure 1 shows the length-frequency distribution plot for the whole VEA system using the 20 km bin, and clearly documents that the number of segments is inversely proportional to their length.
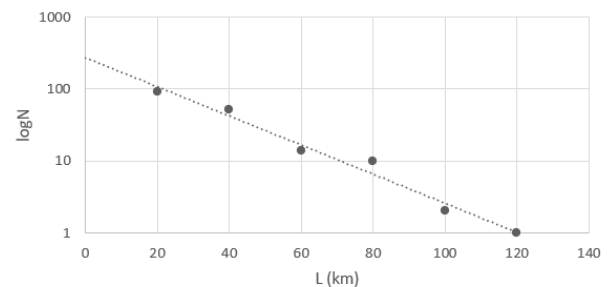

Figure 1 Length-frequency distribution for the VEA array, 20 km bin.

Victoria-Endeavour-Antoniadi Fault System: – Fault linkage mechanisms: We tested the distribution of fault segments defined by structural mapping through the analysis of displacement profiles along the three fault arrays of the VEA system. We estimated vertical displacements along the three arrays by measuring the height of the lobate scarp along 22 profiles crossing the arrays.

Our method is based upon the assumption that the topographic scarp represents an accurate proxy of the fault throw. While on Earth erosive processes tend to

quickly reduce the morphological expression of fault throw, the same process can be neglected on Mercury including the point-effective meteoric cratering. We designed the length of profiles to minimize the effects of local topographic irregularities (e. g., crater rims and ejecta) and to retrieve the regional slope offset by faults. In addition, in cases where more than a single scarp was present, we considered the cumulative height of the *n* number of individual scarps.

Figure 2 shows that each of the fault arrays has a maximum displacement in the central part of the fault trace, gradually decreasing toward the tips. Whereas the VEA-VR array has a broader, elliptical shape, the VEA-ER and VEA-AD arrays resembles the more traditional bell-shape profile.

Figure 2 Vertical displacement profile for the Victoria Rupes, the Endeavour Rupes and the Antoniadi Dorsum fault arrays.

The observation that the height of the scarp has a minimum value at profile 15 could mean that the limit between the VEA-ER and VEA-AD arrays should be placed more to north than what defined by mapping, in correspondence with profile 15. This would place the maximum scarp height of profile 18 at a central position in the array, in agreement with the theoretical model of maximum throw in the central part. A similar consideration can apply to VEA-ER, which in the new formulation would have the maximum in the central part (profiles 11-13).

The findings of three distinct elliptic or bell-shaped curves documents that the three lobate scarps grow as individual faults before linking into a longer fault system. Similarly, the presence of a cumulative slope of limited height at the terminations between the systems (e.g. profiles 8-9, 15) is compatible with the presence of segment boundaries.

The VEA-VR, VEA-ER and VEA-AD are in turn made up of individual fault segments that were linked at an early stage of growth of the fault system. This is suggested by minor culminations withn each curve (e. g., profiles 18-21 for VEA-AD, profiles 11-13 for VEA-ER, Figure 2). Whereas these minor segments are likely hard-linked, the main arrays and particularly VEA-VR and VEA-AD are probably soft-linked (e. g., [2]).

The overall trend of the displacement profile exhibits a progressive northward decrease of scarp height. This observation suggests that VEA-AD, which has the maximum cumulatve height in the array, has developed before the others, and that the system has grown from south to north. In this hypothesis a possible continuation of the entire system should be searched in the Kuiper (H-6) quadrangle south of Victoria quadrangle.

Discovery-Adventure-Resolution Rupes Faults:
Fault segmentation and linkage have been studied for the NE-SW trending, right-transpressive Discovery, Adventure and Resolution Rupes (DAR) lobate scarps as well (see [5] for a detailed analysis). Analysis of scarp height on 38 pofiles across these faults shows that the ~550 km long Discovery Rupes grow linking two different faults, each composed of several segments and sub-segments. The Adventure and Resolution Rupes in turn forms a ~500 km long linked system that trends en-echelon with the Discovery Rupes. Given the large separation, the Adventure-Resolution and the Discovery Rupes are not physically linked. However, the cumulative displacement of the two lobate scarps shows a central maximum coniststent with a soft-linked kinematica connection between the two fault systems.

Discussion and Conclusions:
The length-frequency distribution analysis carried on the VEA fault system nicely illustrates that the number of segments is inversely proportional to their length, in perfect agreement with the studies conducted on the terrestrial faults (e. g., [6]).

Analysis of fault scarp heights along the trace of the VEA and DAR systems shows elliptical or bell-shaped displacement profiles for individual fault arrays and segments, resembling the geometry established for terrestrial faults. The throw maxima are located in the center of the faults and the minima at their boundaries, suggesting fault growth through segment linkage.

The above findings suggest that faults have geometric similraties during growth and that their geometrical evolution does not depend on the geodynamic context (plate tectonics, global contraction, tidal despinning).

References: [1] Cartwright et al. (1995). *Journal of Structural Geology*, 17(9), 1319–1326. [2] Kim and Sanderson (2005). *Earth-Science Reviews*, 68(3-4), 317-334. [3] Byrne et al. (2014). *Nature Geoscience*, 7(4), 301-307. [4] Galluzzi et al. (2019). *Journal of Geophysical Research: Planets*, 124(10), 2543-2562. [5] Sepe et al., this meeting. [6] Wallace (1990). *U.S. Geolgical Survey Professional Paper* 1515, 3-12.

LICIACUBE ACTIVITIES AT ASI-SSDC: PROCESSING, CALIBRATION, ARCHIVING AND ANALYSIS OF images.

A. Zinzi[1,2], V. Della Corte[3], R. Espiritu[4], O. Barnouin[4], E. Dotto[5], M. Amoroso[1], I. Bertini[6,3], J.R. Brucato[7], A. Capannolo[8], S. Caporali[7], M. Ceresoli[8], G. Cremonese[9], M. Dall'Ora[10], J.D.P. Deshapriya[5], I. Gai[11], L. Gomez Casajus[11], E. Gramigna[11], P. Hasselmann[5], S. Ieva[5], G. Impresario[1], S.L. Ivanovski[12], R. Lasagni Manghi[11], M. Lavagna[8], M. Lombardo[11], A. Lucchetti[9], E. Mazzotta Epifani[5], D. Modenini[10], M. Pajola[9], P. Palumbo[3,6], D. Perna[5], S. Pirrotta[1], G. Poggiali[7], A. Rossi[13], P. Tortora[11], F. Tusberti[9], M. Zannoni[11], G. Zanotti[8].

[1]Agenzia Spaziale Italiana, Roma, Italy (angelo.zinzi@ssdc.asi.it), [2]Space Science Data Center-ASI, Roma, Italy, [3]INAF Istituto di Astrofisica e Planetologia Spaziali, Roma, Italy, [4]Johns Hopkins Applied Physics Lab, Laurel, MD, USA, [5]INAF Osservatorio Astronomico di Roma, Monte Porzio Catone (Roma), Italy, [6]Università degli Studi di Napoli "Parthenope", Napoli, Italy, [7]INAF Osservatorio Astrofisico di Arcetri, Firenze, Italy, [8]Politecnico di Milano, Italy, [9]INAF Osservatorio Astronomico di Padova, Italy, [10]INAF Osservatorio Astronomico di Capodimonte, Napoli, Italy, [11]Università di Bologna, Bologna, Italy, [12]INAF Osservatorio Astronomico di Trieste, Italy, [13]CNR Istituto di Fisica Applicata "Nello Carrara", Sesto Fiorentino (Firenze), Italy

Introduction: LICIACube is an ASI mission part of the NASA DART first Planetary Defense mission, constituted by a 6U cubesat developed and assembled by Argotec and whose scientific team is led by INAF.

Launched on November 24th 2021 it started its autonomous mission on September 11th 2022, so that it has been able, after 2 orbital maneuvers to acquire images with its two cameras LEIA and LUKE in the close vicinities of the Dimorphos-Didymos system, soon before and after the DART impact on Dimorphos [1].

SOC Data Management: In order to adequately share data acquired over the course of the mission, the Space Science Data Center of the Italian Space Agency (ASI-SSDC) hosted and managed the Scientific Operations Center (SOC) [2].

Here, images sent to Earth from the spacecraft through DSN antennas and MCC (Mission Control Center) located at Argotec premises in Turin are converted to standard FITS files: the first step is the conversion of raw-from-telemetry data to raw FITS and then, using an algorithm developed by the LICIACube scientific team and hosted at LICIACube SOC, images are radiometrically calibrated and included in a FITS file.

The FITS file format, together with the archive designed, have been previously defined in collaboration with APL and PDS, so that all the LICIACube archive will be readily compliant to the PDS4 standard, in order to be used as a PDS bundle.

The entire process has been thought to be automatic, so that, as soon a new image is made available by the MCC, it is processed and shared with all the DART-LICIACube team through the SOC webpage (with access restricted to the team members).

As the archive is designed to be compliant to PDS4 standard, it is also straightforward to include it in the SSDC MATISSE webtool. This tool will be used to search for images basing upon geographical and geometrical constraints and, more relevant, to be viewed directly on the 3D shape model of tha targets, thus facilitating its scientific understanding.

Conclusions: As the whole flow worked in the correct way, it is hence demonstrated the ability of ASI and SSDC to manage the SOC of a planetary exploration mission, making use of well-established standard for data exchange.

This will make it possible to expand the activities of SSDC in the future, by managing more and more datasets of operational missions, and making use of its tools for advanced data analysis.

References: [1] Dotto E. et al. (2023) *Nature, In Preparation*. [2] Zinzi A. et al. (2022) *doi: 10.3847/PSJ/ac6509*.

VISIBLE SPECTROSCOPIC SURVEY OF NEAR EARTH OBJECTS FROM THE ASIAGO OBSERVATORY IN THE FRAMEWORK OF THE NEOROCKS PROJECT

Monica Lazzarin[1], Fiorangela La Forgia[1], Elisa Frattin[1], Andrea Farina[1], Paolo Ochner[1] and the NEOROCKS Team*

[1]University of Padova, Physics and Astronomy Department, 35122, Padova, 00390498278232, monica.lazzarin@unipd.it

Introduction: We present an update of our ongoing spectroscopic survey of Near Earth Objects (NEOs), performed with the Asiago Telescopes. The program is part of the EU-funmded NEO Rapid Observation, Characterization and Key Simulations (NEOROCKS) project, focused on the acquisition and analysis of data on new discovered small size objects.

The importance of NEOs is widely recognized as they can help to investigate the origin and evolution of the Solar System, in particular also the origin of life and water on Earth, they are possible future mining resources, but they are also possible threatening objects to our planet. This is particularly true for the Potentially Hazardous Asteroids, a subgroup of NEOs characterized by orbits that can make close approaches to the Earth and large enough to cause significant regional damage in the event of an impact.

So, it is particularly important and urgent to know in detail their dynamical, physical, and compositional properties in order also to have more information to establish mitigation strategies.

Our observations are performed with the 1.22m Galileo Telescope equipped with a Boller & Chivens and the 1.80m Copernico Telescope equipped with AFOSC (Asiago Faint Object Spectrograph and Camera), located at the Asiago Observatory, Italy, covering a spectral range between 0.4 - 1 micron. The observation of PHAs is particularly challenging because of their typical faintness and their high rate of velocity.

Nevertheless, since the beginning of the project, January 2020, we have observed about 70 NEOs of which about 28 PHAs. Some of them are newly discovered, with a size range from 30m to about 900m. Most of them have an unknown taxonomic classification or not a clear one yet. We perform the taxonomic classification through a comparison with spectral types from Bus-Binzel Taxonomy (2002) and with laboratory meteorites spectra from Relab database. Up to now we have found different types of asteroids, spanning from carbonaceous C to silicate S, and also some rare types as O or B. Some objects (eg, 1988 OR2 and Didymos) have been observed during their rotational periods, allowing the study of their surface variegation. In particular we are performing a systematic follow up of the PHA Didymos since the impact of the DART spacecraft on 26th September 2022 on its moon Dimorphos, with spectroscopic observations started in October 2022 as soon as the object was observable in the north hemisphere and that we will carry on until it remains visible, spring 2023. We will present the results of the observational campaign obtained so far.

A DATABASE FOR THE THERMAL ANALYSIS OF THE COMET 67P

E. Rognini[1,2], A. Zinzi[1,3], F. Tosi[4]

[1]ASI Space Science Data Center (SSDC), Via del Politecnico, 00133 Rome, Italy (edoardo.rognini@ssdc.asi.it)

[2]INAF-OAR Osservatorio Astronomico di Roma, Via Frascati 33, 00078, Monte Porzio Catone (RM), Italy

[3]Agenzia Spaziale Italiana (ASI), Via del Politecnico snc, 00133, Rome, Italy (angelo.zinzi@ssdc.asi.it)

[4]INAF-IAPS Istituto di Astrofisica e Planetologia Spaziali, Via del Fosso del Cavaliere 100, 00133 Rome, Italy (federico.tosi@inaf.it)

Introduction: The ESA mission Rosetta was the first to enter orbit around a comet, namely 67P/Churyumov-Gerasimenko, and to deploy a lander to its surface. In this work we aim at designing a database of thermal observations provided by the VIRTIS-M instrument onboard the Rosetta orbiter [1], with the goal of making it easier to analyze thermal data [2] and compare them with temperature values predicted by thermophysical models. This can ultimately disentangle diurnal and seasonal effects for various morphological regions.

Methods: We load VIRTIS-derived temperature data on a SQL database. These data are accessible and processable through proper SQL queries, making it possible to perform a systematic analysis for any given location of the comet nucleus covered by VIRTIS data. The shape model (in SPICE format) is "CSHP_DV_130_01_LORES_OBJ.bds" [3], made up of 104k triangular plates ("facets").

Preliminary results: We can visualize a subset of data proving the potential of our SQL database of thermal observations. Very first preliminary results are shown in Fig. 1.

Future Work: The comparison between observed and predicted temperature values in principle could constrain thermophysical models not only for a small portion of the surface [2] but also for much larger areas of the comet nucleus, allowing a link with morphological and geological processes. The use of a SQL database will allow a series of systematic comparisons that will prove crucial for future studies following up the work presented in [2].
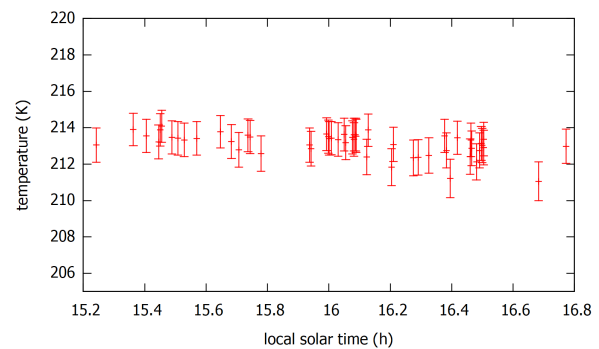
Figure 1: Example of temperature trend for a selected set of points. Every point refers to a VIRTIS pixel, that covers several facets of the shape model; the local solar time is an average value between different facets.

References:

[1] Coradini, A., et al. (2007), *Space Science Reviews*, 128, 529-559

[2] Tosi, F., et al. (2019), *Nature Astronomy*, 3, 649–658

[3] Beth A., et al., (2017), in European Planetary Science Congress. pp EPSC2017–516, 634

NEOROCKS: the EU H2020 programme for NEO Rapid Observation, Characterization, and Key Simulations.

E. Dotto[1], M. Banaszkiewicz[2], S. Banchi[3], M.A. Barucci[4], F. Bernardi[5], M. Birlan[6], B. Carry[7], A. Cellino[8], S. Ieva[1], J. De Leon[9], M. Lazzarin[10], E. Mazzotta Epifani[1], A. Mediavilla[11], D. Perna[1], E. Perozzi[12], V. Petropoulou[1], P. Pravec[13], C. Snodgrass[14], C. Teodorescu[15] and the NEOROCKS team*

[1]INAF – Osservatorio Astronomico di Roma, I (elisabetta.dotto@inaf.it); [2]NEOSPACE sp. z o.o., PL; [3]Resolvo s.r.l., I; [4]LESIA – Observatoire de Paris, F; [5]Space Dynamics Services s.r.l., I; [6]IMCCE – Observatoire de Paris, F; [7]Observatoire de la Côte d'Azur, F; [8]INAF – Osservatorio Astrofisico di Torino, I; [9]Instituto de Astrofisica de Canarias, S; [10]Università di Padova, I; [11]DEIMOS Space, S; [12]ASI-Agenzia Spaziale Italiana, I; [13]Astronomicky Ustav AV CR, CZ; [14]University of Edinburgh, UK; [15]DEIMOS Space s.r.l., RO

Introduction: "NEOROCKS - The NEO Rapid Observation, Characterization and Key Simulations project" is an EU project funded in the framework of the Horizon 2020 - Work Programme 2018-2020 Leadership in Enabling and Industrial Technologies – Space.

The NEOROCKS project: The project started on January 2020 and will end on June 2023. It has proposed a radically new approach to address the challenges posed by the NEO investigation for planetary defence: the dynamical and physical characterizations - two domains usually kept separate – were carried out in strict connection and the scientific/observational activity devoted to physical characterization has been driven by the theoretical work on orbital dynamics.

The NEOROCKS Ambitions: The activity has been organized and carried out in order to address the following ambitions:
— Ambition 1: Networking large aperture telescopes
— Ambition 2: Advancing NEO physical properties modelling and simulations
— Ambition 3: Improving the orbit determination process Ambition 4: Addressing the imminent impactors monitoring
— Ambition 5: Establishing a NEO physical properties data centre
— Ambition 6: Fostering international cooperation for follow-up observations
— Ambition 7: Raise the public awareness on NEO and impact hazard

The NEOROCKS Results and legacy: An overview of the activities we carried out, the results we oobtained and the legacy that NEOROCKS leaves to the Planetary Defence community will be presented and discussed.

*NEOROCKS Team: S. Anghel, A. Bertolucci, F. Calderini, F. Colas, A. Del Vigna, A. Dell'Oro, A. Di Cecco, L. Dimare, I. Di Pietro, P. Fatka, S. Fornasier, E. Frattin, P. Frosini, M. Fulchignoni, R. Gabryszewski, M. Giardino, A. Giunta, T. Hromakina, J. Huntingford, J.P. Kotlarz, F. La Forgia, J. Licandro, H. Medeiros, F. Merlin, J. Nomen Torres, F. Pina, G. Polenta, M. Popescu, A. Rozek, P. Scheirich, A. Sergeyev, A. Sonka, G.B. Valsecchi, P. Wajer, A. Zinzi.

FUTURE PERSPECTIVES OF THE NEO PHYSICAL PROPERTIES DATABASE BY THE NEOROCKS EU PROJECT. I. Di Pietro[1], E. Perozzi[1], A. Mediavilla[2], E. Dotto[3], A. Zinzi[1,4], M. Giardino[1,4], A. Giunta[1] and the NEOROCKS team*. [1] ASI-Agenzia Spaziale Italiana, I (ilaria.dipietro@asi.it), [2] DEIMOS Space, S, [3] INAF – Osservatorio Astronomico di Roma, I, [4] SSDC – Space Science Data Center, ASI, I

Introduction: The EU funded NEOROCKS (Near-Earth Objects Rapid Observation, Characterization and Key Simulations) project aims to improve knowledge on physical characterization of Near Earth Objects (NEOs) for planetary defense. Astronomical observations (and the related modelling to derive their dynamical and physical properties) can support a pragmatic planetary defense approach, i.e. providing operational loops and information systems to protect us and our ground infrastructures from potential threats. The increasing NEO discovery rate, dominated by small-size objects, represents the major challenge for planetary defense. In particular, "imminent impactors", with short warning times, are a major threat. In this light, NEOROCKS proposes an advanced approach, focused on data dissemination and aimed to optimize observational activities, enhancing modelling and simulation tasks, fostering international coordination, and thus boosting results to global level and exploiting results in order to speed-up response times. The project looks at working in synergy with other initiatives undertaken at European and international level (i.e., NEO Segment of the ESA SSA (European Space Agency Space Situational Awareness) programme and the UN Office for Outer Space Affairs (UNOOSA)).

Due to the lack of a unique database for all different data products resulting from physical characterization of NEO observations, the deployment of a NEO physical properties database is one of the main outcomes of the EU funded NEOROCKS project. A permanent infrastructure devoted to space-data management will guarantee the necessary maintenance and evolution of the NEOROCKS technical portal beyond the nominal lifetime of the project.

Database: A data model has been designed following the well-defined IVOA (International Virtual Observatory Alliance) standards. It has been envised the ability to store, maintain, give access and be regularly updated at all different levels of processing, from raw data to final products, in order to be compliant with existing virtual observatory (VO) services. The NEOROCKS database is integrated within the project Technical Web Portal and available to the only consortium partners to date. The final goal is to permanently guarantee the access and the necessary maintenance to the NEOROCKS technical portal and database beyond the end of the project, thus granting the continuation of the project approach and the update of its results.

This will be achieved through partnership with the Space Science Data Centre (SSDC), a facility of the Italian Space Agency (ASI) (https://www.ssdc.asi.it), which is equipped with necessary HW/SW environment. The long standing experience in hosting data produced by several astronomical missions makes ASI-SSDC the proper facility to take up the role of mantaining and disseminating data and tools developed within the NEOROCKS project [1]. Over the years, this data center has acquired, managed, processed and distributed space mission data following FAIR (Findable, Accessible, Interoperable, Reusable) principles [2], i.e. using international standards which assure both the long-

term archive preservation and the interoperability with other data centers.The NEOROCKS project will greatly benedift of the opportunity to perpetuate the results obtained by the project by the migration of the data and of the tools developed to the ASI-SSDC.

Future perspectives: The final goal is to provide the scientific community – involved in Near-Earth Objects physical characterization – with an enduring repository and on-line tools, able to support and maximize the scientific exploitation (and return) of data, and to optimize follow-up observations. The possibility of having a reference repository of NEO physical properties data from raw images to final products – hosted by an exsiting well established astronomical data centre (ASI-SSDC) – will ensure that the efforts carried out during the project will remain publicly available to the international astronomical community and further enhanced in the future. The access to external users will be provided after the forthcoming migration of both portal and database within the Space Science Data Center. The relocation at ASI-SSDC will extend not only the maintenance and the operability of the database, beyond the duration of the NEOROCKS project, but it also will meet one of the major goals of the EU Horizon 2020 Programme. Finally, a permanent facility paves the way toward an international cooperation on NEO physical characterization, maximizing the experience gained during the project at a global level and, hence, providing roadmaps of the next steps.

References: [1] Zinzi, Angelo, et al. (2021) *LPI Contributions* 2549 (2021): 7032. [2] Wilkinson, Mark D., et al. (2016) *Scientific data,* 3.1: 1-9.

SEARCH AND STUDY FOR METEORITES ANALOGUES TO DIDYMOS IN PREPARATION TO THE MILANI/HERA INVESTIGATION.

*G. Massa[1,2], E. Palomba[2], A. Longobardo[2], F. Dirri[2], M. Angrisani[1,2], C. Gisellu[1,2], T. Kohout[3,4].

[1]University of Rome "Sapienza"
[2]INAF Istituto di Astrofisica e Planetologia Spaziali, via Fosso del Cavaliere, 00133 Rome, Italy
[3]Department of Geosciences and Geography, University of Helsinki, Finland
[4]Institute of Geology of the Czech Academy of Sciences, Czech Republic
*email: giuseppe.massa@inaf.it.

Introduction: The Hera mission is under development in the Space Safety Program of the European Space Agency (ESA). The mission will follow the Double Asteroid Redirection Test (DART) mission [1] and its launch is planned in October 2024. Hera will arrive near the binary system (Didymos and its moon Dimorphos) around late December 2026. Its objectives are to investigate the subsurface and interior properties, and to measure in great detail the outcome of the kinetic impactor mission DART on the Dimorphos asteroid, thus providing extremely valuable information for asteroid impact threat mitigation, mining, and science purposes [2]. Hera will carry two CubeSats, i.e., Milani and Juventas, that will be deployed in the close proximity of the Didymos system. Milani is a CubeSat developed by Tyvak International srl, and its scientific objectives are:

- To map the global composition of the Didymos and Dimorphos asteroids;
- To characterize the surface of the Didymos and Dimorphos asteroids;
- To characterize dust clouds around the Didymos and Dimorphos asteroids.

These goals will be achieved thanks to Milani payloads, including the VISTA and ASPECT instruments. VISTA (Volatile In-Situ Thermogravimetre Analyser) is a micro-thermogravimeter devoted at detecting the presence of dust particles smaller than 10-20 μm, at characterizing volatiles (e.g., water) and light organics (e.g., carboxylic acids with low carbon chain) by using Thermo-Gravimetric Analysis (TGA) cycles and at monitoring the molecular contamination in support of other instruments on-board cubesat or satellites [3,4,5]. ASPECT (Asteroid Spectral Imager) is a miniaturized hyperspectral imager extending from the visible up to shortwave infrared (SWIR) wavelengths. The Asteroid Spectral Imager takes 2D snapshots at a given wavelength. When multiple snapshots are combined, a spectral datacube is formed, where the wavelength bands are separated in the time domain [6].

Scientific Objectives: In this work we will show our studies in support of the future Milani investigation of Didymos asteroids. We started with the selection of meteorites analogue to the Didymos and Dimorphos system, that in future will be processed and then analyzed by means of spectroscopy and TGA techniques. The purpose of this work is to predict and support the interpretation of the scientific results that will be obtained from Milani.

Methods: We defined a procedure to identify the best Didymos analogues by using the Didymos spectrum taken by [7] and the RELAB and PSF meteorites spectra databases.

Didymos was found to be probably an Sq-type asteroid [8], so it is compositionally linked to the ordinary chondrites meteorites. Therefore, we selected all the spectra of about 300 ordinary chondrites from the RELAB and PSF databases.

Since the band center is not affected by space weathering [9], we did not have to take into account the differences in space weathering between the meteorites and Didymos, this is why we used this spectral parameter to identify the analogues. We calculated the band center of the pyroxenes at 0.9-1 μm in each ordinary chondrite spectrum and compared it with that retrieved in the Didymos spectrum [7] (Figure 1). The band center was calculated as the location of the reflectance minimum inside the band after the continuum removal [10]. Then, we selected the ordinary chondrites spectra whose band center is consistent with Didymos within the uncertainties (from 0.95 to 1.01 μm).
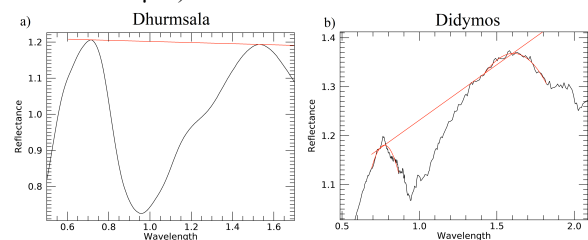

Figure 1: *a) An ordinary chondrite spectrum from RELAB database, in red is plotted the 0.9 μm band continuum; b) Didymos spectrum smoothed over a boxcar of 11, in red are plotted the continuum and the polynomial fit of the shoulders.*

Since other spectral parameters are affected by space weathering, we defined an upper/lower limit according to their behavior with respect to the space weathering in order to add other constraints in addition to the band center. [11,12] showed that space weather-

ing can decrease the values of band depths and can be the cause of a spectral reddening. Thus, we calculated on Didymos spectra the 0.9 μm band depth (0.11), that we used as a lower limit, and the continuum slope (0.225), that we used as an upper limit. Then, we calculated the band depth [13] at 0.9 μm and the continuum slope, defined as the slope of the line tangent to the maxima of the 0.9 μm band shoulders, of the ordinary chondrites spectra and selected only those compatible with the limits set by Didymos spectra.

Finally, we have selected around 60 ordinary chondrites that are candidates to be analogues to Didymos asteroid. In Figure 2 we have the histogram of the ordinary chondrites sub-type [14] that we selected with the constraints described above (on band center, band depth and slope), it shows that the H ordinary chondrites seem to be outliers in this selection while the most probable sub-type is the L one.
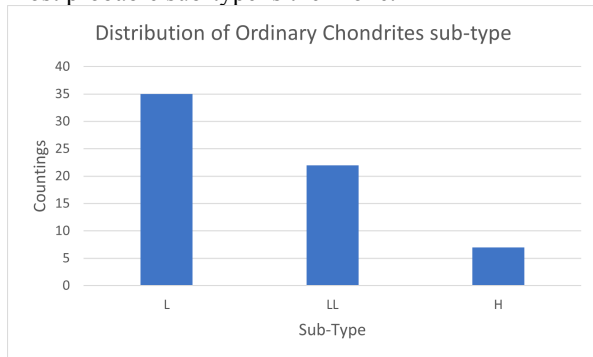
Figure 2: *Distribution of Ordinary Chondrites sub-type.*

Future perspectives: The future perspectives of this work are:

- Improve our selection using other constraints;
- Acquire spectra and perform TGA cycles of the chosen analogues;
- Reproduce space weathering with laboratory techniques (e.g., Ion irradiation, Laser bombardment) on the analogues in order to simulate the weathering that occurred on the surface of Didymos;
- Acquire spectra and perform TGA cycles of the treated analogues and compare them with previously obtained data.

References

[1] P. Michel and al., "European component of the AIDA mission to a binary asteroid: Characterization and interpretation of the impact of the DART mission.," *Advances in Space Research 62.8,* pp. 2261-2272, 2018.

[2] P. Michel and al., "The ESA Hera mission: detailed characterization of the DART impact outcome and of the binary asteroid (65803) Didymos.," 2022.

[3] F. Dirri and al., "A review of quartz crystal microbalances for space applications.," pp. 48-75, 2019.

[4] D. Scaccabarozzi and al., "Thermo-mechanical design and testing of a microbalance for space applications.," pp. 2386-2397, 2014.

[5] E. Palomba and al., "Volatile in-Situ Thermogravimeter Analyser (VISTA) payload developed for MILANI cubesat for HERA Space Mission.," 2022.

[6] T. Kohout and al., "Feasibility of asteroid exploration using CubeSats—ASPECT case study.," pp. 2239-2244, 2018.

[7] J. De León and al., "Observations, compositional, and physical characterization of near-Earth and Mars-crosser asteroids from a spectroscopic survey.," 2010.

[8] A. F. Cheng and al., "AIDA DART asteroid deflection test: Planetary defense and," pp. 104-115, 2018.

[9] Y. Ueda and al., "Changes of Band I Center and Band II/Band I Area Ratio in reflectance spectra of olivine-pyroxene mixtures due to the space weathering and grain size effects.," 2002.

[10] A. Longobardo and al., "Photometric behavior of spectral parameters in Vesta dark and bright," pp. 20-35, 2014.

[11] C. Lantz and al., "Evidence for the effects of space weathering spectral signatures on low albedo asteroids.," 2013.

[12] R. Brunetto and G. Strazzulla, "Elastic collisions in ion irradiation experiments: A mechanism for space weathering of silicates.," *Icarus 179.1,* pp. 265-273, 2005.

[13] R. N. Clark and T. L. Roush, "Reflectance spectroscopy: Quantitative analysis techniques for remote sensing applications.," pp. 6329-6340, 1984.

[14] H. Y. McSween Jr, M. E. Bennett III and E. Jarosewich, "The mineralogy of ordinary chondrites and implications for asteroid spectrophotometry.," pp. 107-116, 1991.

Laboratory investigation of icy surface analogs of some Solar System objects. A. Migliorini[1], Z. Kanuchova[2], S. Ioppolo[3], G. Strazzulla[4], [1]Institute for Space Astrophysics and Planetology, INAF, Italy, [2]Astronomical Institute, Slovakia, [3]Aarhus University, Denmark, [4]Catania Observatory, INAF, Italy

Introduction: Ultraviolet-visible (UV–Vis) spectroscopy has been extensively used to study ices in the Solar System. In 1995, ground-based observations revealed two features centered at 577.3 and 627.5 nm that were attributed to solid O_2 in Ganymede's trailing hemisphere [1]. The same features were identified on Europa and Callisto in later after [2]. The observed features are recognized to be the result of a double electronic transition of two adjacent O_2 molecules [3, 4], although the presence and mantaince of molecular oxygen in icy surfaces like those of the Galilean satellites are still debated. Our purpose is to provide new insight on the characterization of molecular oxygen at low temperatures (20 to 40 K) to further constrain the nature of the observed features on the Galilean satellites.

The proposed measurements allow building a background for the future interepretation of data acquired with the MAJIS instrument [5] on board the ESA JUICE mission.

Laboratory measurements: In 2019 we obtained spectra of pure O_2 ice layers and its mixtures with H_2O, N_2 and CO_2 in the vis range using the AU-UV beam line of the ISA ASTRID2 ring storage, at the University of Aarhus. It can accommodate a large variety of end-station experimental setups to measure photoabsorption spectra in the 115-700 nm range by using two gratings [6, 7]. For the present measurements in the UV–Vis, we used the low energy grating (LEG) with spectra acquired in transmission-absorption mode over the wavelength range of 310–670 nm at 0.2 nm steps. The apparatus for this experiment is a custom-made Portable Astrochemistry Chamber (PAC), a high vacuum (HV) system with a base pressure of 10^{-9} mbar, described in [8, 9]. Ice samples were prepared by deposition of the materials (pure O_2 and its mixtures $H_2O:O_2$, $N_2:O_2$, and $CO_2:O_2$) on the MgF_2 substrate window cooled down to 20 K. Gas mixtures were made in a dedicated pre-chamber and admitted into the main chamber by an all-metal needle valve. The ratios of the mixing gases were determined via partial pressures measured by means of a mass-independent capacitance manometer prior to deposition. Direct deposition was carried-out at normal incidence with respect to the substrate through a 6 mm diameter tube extending inside the main chamber.

Results: We obtained spectra of pure O_2 at 20K, 30K, 35K and 40K, as well as O_2 1:1, 1:2, 1:10 mix-

tures with H_2O, CO_2 and N_2 deposited at 20K and heated to 30 K and 35 K [10].

In the pure O_2 spectra, the two O_2 bands at 577.3 and 627.5 nm, due to oscillations of adjacent O_2 molecules, can be seen, while for temperatures higher than 35 K the bands disappear because of O_2 sublimation, as shown in Figure 1. We reported slight changes in the band shape and position with temperature, in agreement with [3], as well as differences in the relative intensities of the two bands.
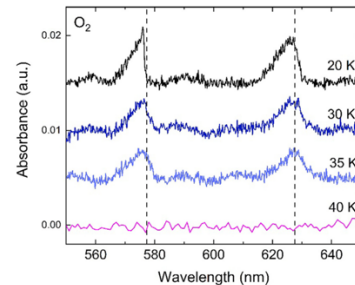

Figure 1. UV-VIS spectra of pure O_2 at different temperatures. The (0,0) and (1,0) bands are clearly visible at 577 nm and 627 nm, respectively, for temperatures lower than 40K.

In the mixtures, we observed that the spectral profile, shape, relative intensities, and peak position of the two O_2 bands vary as a function of the mixing ratios, ice composition, and temperature.

These measurement were compared to high resolution ground-based observations of Ganymede in the visible obtained at the Telescopio Nazionale Galileo. In this sectrum, the O_2 (1,0) transition at 577.3 nm is well visible, while the (0,0) one is less recognizable and hence it was not taken into account. Through a comparison with the pure O_2 spectra, we were able to confirm that the observed O_2 bands are likely a combination of the different ice forms, following [3]. This finding is in agreement with the idea that O_2 might be trapped in a cold subsurface layer within the Ganymede's icy surface [11].

The mixtures we considered in our measurements allowed to improve the fit of the telescopic spectrum of Ganymede, with an overall better agreement of the observational band peak positions in the case of mix-

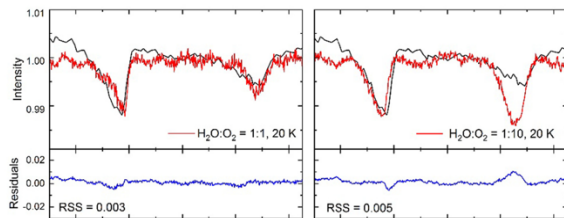tures where O_2 is the dominant species (1:10 proportion).

Figure 2. Comparison between the Ganymede's spectrum (in black) and the $H_2O:O_2$ mixtures (in red). The (1,0) band is quite satisfactorily reproduced in both cases, although a better agreement is obtained when O_2 is the dominant species.

Further measurements of O_2 and mixtures with different compounds are foreseen in 2023 to further constrain the nature of the observed O_2 bands in the icy surfaces of the Galilean satellites and other objects of the Solar System.

References:

[1] Spencer et al. 1995, J. Geophys. Res. 100 (E9), 19049-19056.

[2] Spencer and Calvin, 2002, ApJ 124 (6), 3400-3403.

[3] Landau et al. 1962, Astrochim. Acta 18 (1), 1-19.

[4] Mason et al. 2006, Faraday Discuss. 133, 311-329.

[5] Piccioni et al. 2019, IEEE 5th International Workshop on Metrology for AeroSpace (MetroAeroSpace).

[6] Eden et al., 2006, Chem. Phys. 323, 313-333.

[7] Palmer et al., 2015, J. Chem. Phys. 142 (13), 134302.

[8] Ioppolo et al. 2020, A&A 641, A154.

[9] Ioppolo et al. 2021, A&A 646, A172.

[10] Migliorini et al. 2022, Icarus 383, 115074.

[11] Vidal et al. 1997, Science 276, 1839-1842.

Visible and Near-Infrared Spectroscopy of Mars Analogues in support of the ESA's ExoMars Rover Mission.

S. Filomeno[1,2], S. De Angelis[1], F. Altieri[1], M. C. De Sanctis[1], M. Ferrari[1], E. Ammannito[3], A. Frigeri[1], E. La Francesca[1], M. Formisano[1], L. Rossi[1], and the Ma_MISS team, [1]Institute for Space Astrophysics and Planetology, IAPS-INAF, Via Fosso del Cavaliere, 100, 00133, Rome, Italy, [2]La Sapienza University, Rome, Italy, [3]Italian Space Agency, ASI, Via del Politecnico snc, 00133, Rome, Italy (simone.filomeno@uniroma1.it, simone.filomeno@live.com)

Introduction: Mars is a primary destination to search for signs of life in our solar system, and this search has driven the most recent missions to the red planet, including ExoMars . To support the ExoMars Rosalind Franklin Rover [1], properly exploiting the data that will be acquired by the Ma_MISS (Mars Multispectral Imager for Subsurface Studies) spectrometer [2,3], here we investigate the behaviour of laboratory spectra collected in the visible and near infrared range at different temperatures and pressures on Martian analogues.

Instrumental Setup: Data used in this work are reflectance spectra acquired in the VNIR range (0.35–2.5 μm) on five Martian analogue minerals exploiting the ASD Fieldspec-4, a commercial spectrometer in use at IAPS/C-Lab and equipped with an environmental cell allowing us to expose the samples to different ambient conditions. For illuminating the samples and collecting reflected light from the sample, the spectrometer is coupled respectively with a Quartz-Tungsten-Halogen light source whose light is directed through an optical fibre and with an optical fibre bundle carrying the signal to the spectrometer. High vacuum, down to $P = 10^{-7}$ mbar, is obtained through a primary diaphragm pump and a secondary turbomolecular pump. The powder sample to be measured is placed horizontally within a stainless-steel cup, below which a ceramic heater allows increasing the temperature up to 673 K [4,5].

Data Acquisition: The used samples are Illite (IMt2), mixed-layer Illite-Smectite (ISCz1), Beidellite (Beid), Nontronite (NAu1) and (NAu2), initially studied at room pressure and temperature. For further analysis, the pressure inside the cell was progressively reduced from 10^3 to around 10^{-4} mbar to explore the spectral behaviour at different pressures. During this operation the spectrometer was set to acquire the spectra at a fixed frequency and with an optimised exposure time of 100ms (which guarantees the acquisition to be at constant pressure conditions). After reaching the minimum pressure, the sample's temperature was increased at steps of 50K to allow the evaporation of the most strongly bound water molecules to the mineral lattice. Since the sample cup is in direct contact with the heater and the sample thermalization occurs in a few minutes, we can assume a sample temperature accuracy <5 K with respect to the value measured by the thermocouple [4].

In *Fig.1 (Top)* there are shown all the spectra acquired for the ISCz1 sample at room temperature and varying the pressure zoomed on the absorption bands of interest. A change in the strength of the hydration features is clearly visible.

Data Analysis: The acquired spectra were calibrated by dividing the data with the Spectralon spectrum (~99% reflectance) after having subtracted the background signal from both. These background data were acquired through an acquisition with the illumination source occulted.
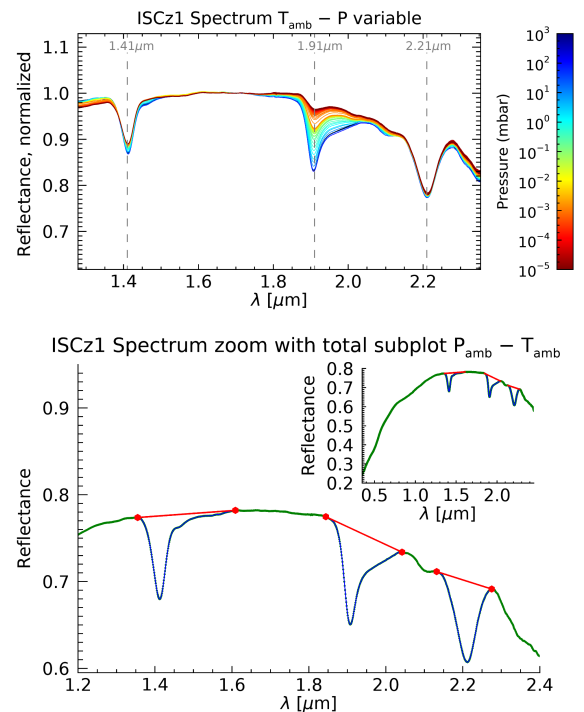

Fig.1: (Top) ISCz1 Spectrum at P_{amb} and T_{amb} ; (Bottom) ISCz1 Spectrum at T_{amb} and with P variable zoomed in the bands with the straight-line continuum superimposed in red and the hydration bands highlighted in blue. Their edges are indicated with a red point. It is also present a subplot of the total spectrum.

Aim of this work is to investigate and characterise the spectral behaviour of the studied samples at different pressure and temperature. For this purpose, we focus on the study of the OH and H_2O bands around 1.4, 1.9 and 2.2 μm for the different mineral samples through the evaluation of the trend of several spectral indices (Band Depth, Band Centre position, FWHM, …) with

pressure and their relation. Before extracting these indices the continuum removal was executed. It is based on the use of a 'slope evaluation algorithm' developed for an iterative identification of the band edges (shifting with pressure variation) to identify the best one for each band shoulder. Then, the continuum was delineated as a first order polynomial passing between the band edges. The result of this method is shown in *Fig.1 (Bottom)* for the ISCz1 sample at P_{amb} and T_{amb}. The continuum was removed by dividing the measured reflectance with the estimated continuum [6]. The spectral indices were estimated from the values of the band centres which were derived by fitting a second order polynomial on the neighbourhood of the band minimum of interest (after continuum removal) [7].

Discussion: The results deriving from the analysis are useful to understand if mineral de-hydration and its behaviour with pressure influence the band minimum position and band depth, so how much it can contribute to an accurate mineral identification. Evaluating the band centre differences between the values at Earth pressure (P_{Earth}) and at Mars pressure (P_{Mars}), notable trends are not observed for most of the samples. Some minerals exhibit significant shifts for the band centres at pressures lower than P_{Mars} suggesting that this kind of analysis can be also very useful for bodies with more extreme surface pressures (near the vacuum) like asteroids. In *Fig.2* it is possible to observe the shift of the NAu2 band centre through the various pressures for the 2.3μm band.
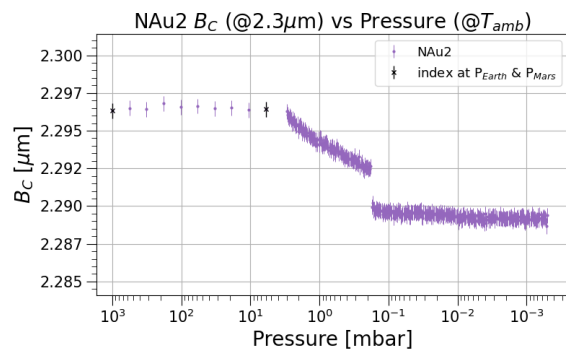
Fig.2: NAu2 band centres at 2.3μm vs. P. With a black 'x' marker the values at PEarth=1bar and at PMars=6mbar are reported.

Laboratory band centres at P_{Mars} were also compared with data from Oxia Planum, where clay minerals were identified by the Mars Reconnaissance Orbiter's Compact Reconnaissance Imaging Spectrometer for Mars (MRO-CRISM). In this way, it was observed the compatibility of the laboratory nontronites with the minerals detected in the Oxia's Catchment Area, according with the results of Brossier J. [8]. The band depth parameter results to show a greater variation, with the pressure decrease, than the band centre. The results suggest that, for each analogue mineral and absorption band, the variation of intensity is not negligible. In fact, passing from P_{Earth} to P_{Mars}, it varies from 6% to 46% mainly for the 1.4μm and 1.9μm H_2O absorption bands. Consequently a further analysis has to be carried out on this index.

Future Work: Among the next steps there would be the improvement of the algorithm for continuum identification and removal to extend the study to other families of minerals. Since the analysed bands are a convolution of multiple absorption, it would be possible to recognise all the absorptions implementing after the continuum removal a gaussian deconvolution process for a more rigorous study. An important improvement would be the clear definition of area boundaries in the scatterplots of the band centres for some mineral groups. This could be done by characterising many different samples of the same family having slightly different compositions. The study of samples acquired at different pressure and temperature conditions, in order to reproduce the conditions of different planetary surfaces (and the martian pressure at 6 mbar), represents a novelty in this field. For a better reproduction of the martian environment to which its minerals are exposed, it would be also necessary to reproduce its temperature and simulate its atmospheric content (95% CO2). This could be possible by employing a new environmental cell which is still under development.

References:
[1] Vago J.L. et al. (2017) *ASTROBIOLOGY* Volume 17, Numbers 6 and 7, 471-510.
[2] De Sanctis, M.C., et al. (2022), *Planetary Science Journal*, 3, 6, id.142, 15 pp.
[3] De Sanctis M.C. et al. (2017) *ASTROBIOLOGY*, Volume 17, Numbers 6 and 7, 612-620.
[4] De Angelis S. et al*.,* (2018) *REVIEW OF SCIENTIFIC INSTRUMENTS*, 89, 103107.
[5] De Angelis S. (2017), *Planetary and Space Science,* 144, 1–15.
[6] Milliken, R. E. (2006), Ph.D. thesis, Brown University, Rhode Island.
[7] De Angelis S. et al. (2015), *Planetary and Space Science*, 117, 329.
[8] Brossier, J. et al. (2022), *Icarus*, 386, 115114.

REFLECTANCE SPECTRA OF MASCAGNITE AND SALAMMONIAC MINERALS BY VARYING VIEWING GEOMETRY.

M. Fastelli[1], B. Schmitt[2], P. Beck[2], O. Poch[2], A. Zucchini[1] ,F. Frondini[1] and P. Comodi[1]
[1] Department of Physics and Geology, University of Perugia, I-06123, Perugia, Italy [2] Univ. Grenoble Alpes, CNRS, IPAG, 38000 Grenoble, France. (maximiliano.fastelli@gmail.com)

Introduction: The reflectance spectra of minerals in the near and mid infrared regions have diagnostic absorption features that are essential to understanding planetary formation and evolution [1]. Mineral spectral bands are closely linked to the different configurations of atoms and molecules inside the crystal structure, but they can vary in terms of position and shape also as a function of physical parameters [2]

Regarding the viewing geometry, the reflectance spectra collected by spacecraft missions are bidirectional in the most part, that is, the incidence of the sun light has a specific angle and thus the reflected light from the surface has itself a proper emergence direction [3]. Furthermore, with the creation of increasingly high-performance spectral cameras, the effect of surface roughness and observation geometry can be also considered.

The surface reflectance spectra of many Solar System bodies, such as Mercury, Uranus' moons and asteroids, is affected by observation geometries [4-6]. With regard to icy bodies, chaos terrain on Europa's surface, that represents resurfacing process, can be identified for incidence angles $> 70°$ [7]. On Pluto's surface, changing the viewing geometry generates significant spectral changes in the N_2, CO and CH_4 absorption bands [8]. On the dwarf planet Ceres a negative slope in the 0.5-2.5 µm spectral region has been observed in the fresh impact craters and is related to possible change in physical properties and composition [9].

In this work the Bidirectional Reflectance Distribution Function (BRDF) spectra of salammoniac NH_4Cl and mascagnite $(NH_4)_2SO_4$ minerals were collected to investigate how the observations geometries can influence the NH_4^+ signature. These samples might represent the two most important NH_4^+ minerals on icy bodies surfaces . In addition, these data will be used for future interpretation of reflectance spectra of Pluto's surface as well as on other planetary bodies such as icy satellites, asteroids, Kuiper Belt Objects (KBOs) and comets.

Results:
Two selected mascagnite-$(NH_4)_2SO_4$ and salammoniac-NH_4Cl samples were checked and characterized using X-ray powder diffraction (XRPD) technique. The reflectance spectra analysed in this study were collected using the custom-made bidirectional reflectance spectro-goniometers SHINE (SpectropHotometer with variable INcidence and Emergence) (at the Cold Surface Spectroscopy facility (CSS) of the IPAG laboratory (https://cold-spectro.sshade.eu).

BRDF spectra are collected in the 1 - 4.5 µm range considering a set of 3 incidence (i) angles ($i = 0°$; 30°; 60°) and 9 emergence (e) angles between -70° and 70° at room temperature. The NH_4^+ overtone and combinations bands located at ~ 1.09, 1.32, 1.62, 2.04, 2.2 and 3.05 µm are experimentally investigated.

The band positions remain essentially unchanged with varying incident and emergence angles. On the other hands, bands' area and depth show the highest variability for $i \geq 30°$ and e greater than ±40°. These bands' parameters evidence a dual behaviour: (i) for spectral features located below 2 µm there is an increase at low emergence angles and for incidence angles close to nadir; while (ii) spectral characteristics over 2 µm increase according to the angle of incidence. We observe an important dependence of the band depth and area on incidence angle, up to 30°, compared to moderate variation with emergence angles. Furthermore, the ~ 3 µm feature desaturate and becomes more defined at ± 70° emergence angles. A general trend of spectral blue shift with change in observation geometry is observed.

Discussions:
Mascagnite and salammoniac represent two of the most accredited ammonium-bearing minerals presumed on the surface of either small bodies such as comets and/or asteroids [10] or icy bodies such as Pluto and its moons [11].

In general, the relative change in reflectance values is already evident for small emergence angle variations ($e = \pm 20°$). For $e \geq 40°$, the spectral variation becomes significant and much more appreciable. At geometric configurations with i = 60° and $e \geq 40°$ we can notice that the reflectance spectra of the inclined geometries tend to diverge from the one measured in nadir geometry.

The results obtained in this work show that observation geometry can have a strong impact on band parameters, such as depth and area, in both ammonium bearing minerals, in terms of shape of NH_4^+ absoption features. Both incidence and emergence angles affect absorption bands and slopes.

Conclusions:
The collected reflectance spectra are affected by the change in observation geometries. We notice that

divergence from near-nadir measurements becomes significant for $e \geq 40°$. Characteristic NH_4^+ features are located at ~1.06, 1.3, 1.56 and 2.02, 2.2 and 3.0 μm. Depth and area parameters of these features display a dual behaviour: (i) for absorption bands located below 2 μm and for incidence angles close to nadir and low emergence angles, the parameter values tend to increase, conversely, for high emergence angles, the values tend to decrease; (ii) spectral features over 2 μm generally increase with different trends depending on the angle of incidence. The greatest increase occurs for $i = 60°$.

NH_4^+ – minerals identification has a strong impact on understanding their thermal evolution and the constructions of geophysical internal models providing information on oceans/brines compositions, possible explanations of geological phenomena, like cryovolcanism, and implications for biological activity.

The laboratory spectra reported here add information on the band dependence on viewing geometries of two selected ammonium bearig minerals and should aid the remote data interpretation from *New Horizons* LEISA and *Dawn*-VIR spectrometers.

Acknowledgments:

References:

[1] Mustard, J. F., & Glotch, T. D. (2019). *Remote Compositional Analysis: Techniques for Understanding Spectroscopy, Mineralogy, and Geochemistry of Planetary Surfaces*, 21-41. [2] Beck, P. et al. (2012). *Icarus, 218(1)*, 364-377. [3] Pommerol, A., and Schmitt, B. (2008). *JGR: Planets,* 113(E12). [4] Warell, J., and Bergfors, C. (2008). *Planet. Space Sci., 56(15)*, 1939-1948. [5] Nelson, R. M. et al. (1987). *JGR: Space Physics, 92(A13)*, 14905-14910. [6] Magrin, S. et al. (2012). *Planet. Space Sci., 66(1),* 43-53. [7] Neish, C. D. et al. (2012). *Icarus, 221(1)*, 72-79. [8] Cruikshank, D. P. et al. (2015). *Icarus, 246*, 82-92. [9] Stephan, K. et al. (2017). *Geophys. Res. Lett. 44(4)*, 1660-1668. [10] Poch, O. (2020). *Science, 367(6483)*, eaaw7462. [11] Cook, J.C. et al. (2018). *Icarus 315*, 30–45

Using the DAVIS laboratory setup to simulate and test Ma_MISS surveys on rock samples.

L. Rossi[1], S. De Angelis[1], M. Ferrari[1], E. La Francesca[1], M. C. De Sanctis[1], A. Frigeri[1], M. Formisano[1], F. Altieri[1], J. Brossier[1], E. Ammannito[2], S. Pirrotta[2], R. Mugnuolo[2].
[1]Istituto di Astrofisica e Planetologia Spaziali IAPS-INAF, Via Fosso del Cavaliere 100, 00133 Rome, Italy (lorenzo.rossi@inaf.it), [2]Italian Space Agency, ASI, Via del Politecnico snc, 00133 Rome, Italy.

Introduction: DAVIS, the new laboratory model of Ma_MISS, will soon be used to perform complete surveys inside rock samples. This will allow the test of various survey strategies and will support the optimization of Ma_MISS acquisition sequences.

The Ma_MISS instrument: Ma_MISS (Mars Multispectral Imager for Subsurface Studies) is the miniaturized VNIR spectrometer embedded in the drill system of the Rosalind Franklin rover [1, 2]. Ma_MISS will perform spectral reflectance measurements inside holes bored into the surface of Mars up to a depth of 2 m. It will characterize the mineralogy and stratigraphy of the borehole walls and will allow the in-situ study of the subsurface environment, before sample extraction and analysis. Taking advantage of the drill tool rotation and vertical translation (which can be finely controlled), Ma_MISS can acquire reflectance spectra at many different locations inside a borehole, to build up a sort of hyperspectral image of its walls and map the local stratigraphy.

Ma_MISS survey optimization: Ma_MISS can survey the borehole walls in many different ways, depending on what sequence of spectral acquisitions and drill movements is commanded. An acquisition sequence mainly determines the spatial sampling and the total number of acquisitions to perform. The main tradeoff to be made is between a finer spatial sampling, the completeness of the survey, and the amount of resources needed to perform it (e.g. time, data volume, power). To maximize the science return while limiting the required survey time, the acquisition sequences need to be tested and optimized. To this end, we will soon start to test complete Ma_MISS surveys on rock samples with DAVIS, trying various survey sequences and assessing their performance. Different survey strategies might be better suited for different kinds of soil: for each survey, the definition of the optimal acquisition sequence will also need to be based on the expected local stratigraphy and granulometry. Thus, it will also be important to experiment with various kinds of samples to gain a better understanding of what works best in each condition.

The DAVIS laboratory setup: The Drill for Analogues and Visible Infrared Spectrometer (DAVIS) is the new laboratory model of Ma_MISS. Its goal is to
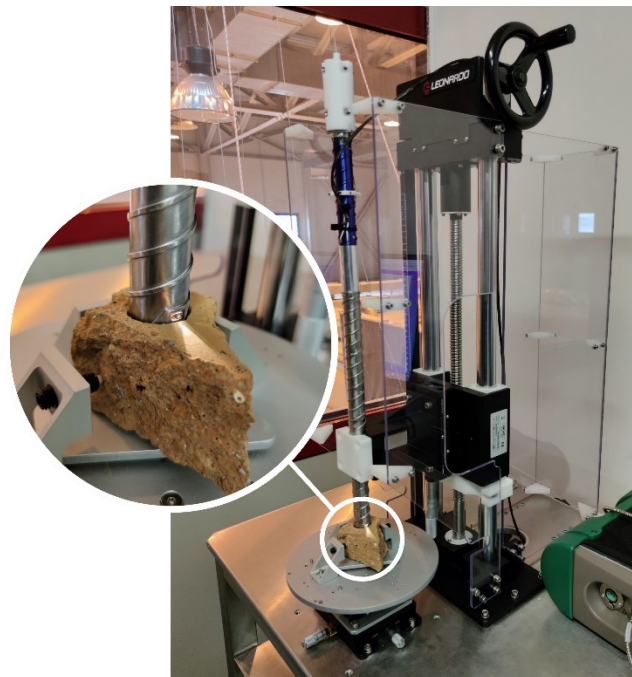

Figure 1: DAVIS-LD

Figure 2: DAVIS-MOT.

drill holes in Martian analogues and other rock samples and to perform spectral reflectance measurements inside them. The DAVIS laboratory setup is made up of two standalone instruments: the Laboratory Drill (DAVIS-LD) and the Ma_MISS Optical Tool (DAVIS-MOT).

DAVIS-LD: The Laboratory Drill, shown in Figure 1, is a manually actuated drill system, with a drill tip that is a replica of the flight model one [3]. It is mainly used to prepare samples for later DAVIS-MOT analysis, boring holes through them. The drill motor control unit can also provide some telemetry data such as rotational speed and current drawn while drilling. This data can provide useful insights into the mechanical properties of the sample being drilled.

DAVIS-MOT: The Ma_MISS Optical Tool (Figure 2) reproduces the Ma_MISS optical system [4]. It features a replica of the flight model drill tip which includes a complete Ma_MISS optical head, together with its sapphire window, light source, illumination fiber bundle, and signal fiber. The signal fiber is then coupled to two commercial spectrometers for data acquisition. The drill tool is fixed to a sliding stage that allows its vertical translation, while the sample holder is mounted on a rotation stage. These positioning stages were originally manually actuated, and this limited the number of acquisitions we could get on a sample, preventing the test of complete Ma_MISS survey sequences. We are currently upgrading the setup with motorized stages so that the acquisition process can be automated. This will allow us to perform complete surveys of rock samples, with a large number of individual spectral acquisitions. Therefore, it will also provide an extended database of reference measurements. This laboratory setup will also be used to characterize the reflectance of samples with a curved geometry. With respect to flat rock slabs, these samples are more representative of the conditions Ma_MISS will face during the operative phase of the mission on Mars.

DAVIS as a tool to test survey strategies: Up to now, the DAVIS setup has been used to perform spectral reflectance measurements on several samples, both in the form of drilled rock samples and slabs. This allowed us to test the performance of the instrument and also provided useful data to be used for the generation of simulated Ma_MISS surveys. Once its automation upgrade is complete, it will also be used to execute and test Ma_MISS acquisition sequences to perform complete surveys inside rock samples. The acquired data will be studied and visualized to derive the composition of the sample and try to reconstruct its stratigraphy. Various survey sequences will be tried on the samples, to assess and compare their performance.

Ma_MISS survey simulation tool validation: Data acquired with DAVIS will also be useful to improve and validate the software tools we are developing to simulate and visualize Ma_MISS data. As an example, we recently developed a simple software tool to generate simulated Ma_MISS spectral acquisition. The simulated data is produced starting from a few measured spectra, a geometrical definition of the stratigraphy and the Ma_MISS acquisition sequence to be simulated [5, 6]. An example of a visualization of a simulated Ma_MISS survey is shown in Figure 3. Comparing the generated products with real data acquired with the DAVIS setup will be instrumental in improving and extending the simulation tool.

References: [1] De Sanctis M.C. et al. (2017): Astrobiology, 17, 6-7.
[2] De Sanctis M.C. et al. (2022): Planet. Sci. J. 3 142
[3] Rossi L. et al. (2022): LPSC 53, Abstract #1353.
[4] De Angelis S. et al. (2022) LPSC 53, Abstract #1796
[5] Ferrari M. et al. (2022): LPSC 53, Abstract #1339
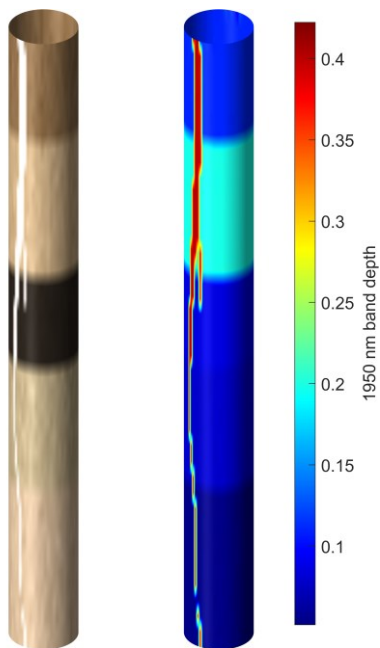[6] Rossi L. et al. (2022): EPSC 2022, Abstract #391

Figure 3: Example of simulated Ma_MISS data visualization. Left: RGB color derived from spectrum. Right: 1.95 μm band depth.

STEREO VALIDATION ACTIVITIES FOR THE NEW STEREO HYPERSPECTRAL PUSHBROOM CAMERA: HYPSOS.
Cristina Re,[1] Chiara Doria[2], Livio Agostini[2], Igor Dorgnach[2], Emanuele Desirò[2], Riccardo La Grassa[1], Luigi Lessio[1], Gabriele Cremonese[1], Andrea Meneguzzo[2], Giampiero Naletto[3], Massimiliano Tordi[4], [1]INAF (Osservatorio Astronomico di Padova, Padova, Italy, cristina.re@inaf.it), [2] Center of Studies and Activities for Space (CISAS), Padova, Italy, [3]University of Padova, Department of Physics and Astronomy "Galileo Galilei", Padova, Italy, [4]Eie Group Mestre (VE), Italy.

Introduction: Nowadays, one of the main objectives of a space mission dealing with the observation of a solid body is to obtain the three-dimensional reconstruction of the observed surface. The Digital Terrain Model includes the three-dimensional spatial characteristics of the framed region and it is the result of complex procedures starting from at least two images of the same region acquired from different points of view.

HYPSOS, HYPerspectral Stereo Observing System [1], is an instrument that will employ a new technology able to give simultaneously both 3D spatial and spectral information of the observed features. With the spectral and the spatial information, we can create a representation of the surface linked with the hyperspectral information emitted and diffused by the objects on the surface in 3D space. Thus, we name the resulting data product as Hyperspectral Digital Terrain Model (HDTM). The benefit of capturing 3D and hyperspectral information at the same time, with the same technology (instrument), without co-registration problems, is very promising and challenging.

Before a new camera system can be used, it should be characterized to ensure the validity of the resulting data products. Of course, an important step for the use of the stereo camera is the camera modelling.

In this context, a proper stereo validation procedure has been conceived in laboratory to demonstrate the capabilities of HYPSOS to reconstruct a 3D surface; this procedure is based on the previous experience made with the stereo camera of BepiColombo [2].

The described results can be used to formulate a complete methodology for stereo information extraction from a set of two images acquired with a hyperspectral pushbroom technology as HYPSOS.

The HYPSOS prototype: HYPSOS optical prototype that has been realized in laboratory during the past years. Light from two different directions, with an inclination of $\pm 20°$ with the respect to the optical axis is collected by a couple of flat mirrors. The two beams of light pass through two 45° tilted Schmidt-Pechan prisms (SPP), which provide a 90° rotation of the FoV; in this way both lights path have in common the same optical elements after the SPP. Then, light passes through a Three Mirrors Anastigmatic (TMA) telescope and is folded by a flat mirror. Finally, the light passes through the entrance slit of an imaging spectrometer composed by four lenses and a reflection grating, and a bidimensional detector collects the two separated spectra.

In order to carry on the photogrammetric activities before the complete assembly of the optical prototype, a commercial camera has been used to simulate the HYPSOS acquisition on the Experimental Setup.

Stereo Validation procedures: To illustrate the stereo validation method, we start with presenting the Laboratory Setup equipment used in the experiment. Then, the calibration method is described summarizing the modelling of linear push broom cameras and finally the photogrammetric steps for deriving the 3D reconstruction are explained together with the first metrics for the correspondent accuracy definition.

Experimental Setup. To perform on the optical bench in laboratory the Stereo Validation of HYPSOS, we use a Stereo Validation Setup (SVS) whose main components are: one rotational stage (devoted to reproduce the stereo angle of HYPSOS), a linear stage to select the channel, a translator that allows the acquisition in push-broom mode, a collimator lens (achromatic doublet with nominal focal length of 1010 mm), an illumination source (halogen lamp) and a biplanar calibration gauge of 4×4 cm^2 (chessboard). The specifically designed reference gauge provides a high number of easily detectable reference points; based on that, the components of the projection matrix M can be estimated.

Pushbroom camera model and projection matrix estimation. The adopted geometric calibration technique follows the method introduced by Gupta and Hartley [3] that under some assumptions, allows to greatly simplify the computational steps usually involved in the pushbroom model calibration.

This description of a linear pushbroom sensor contains the interior and exterior camera parameters with the compact representation by a projection matrix (M) that allows to apply the camera model likewise a pinhole camera model. While the pinhole model encodes a perspective projection in both horizontal and vertical (u, and v) pixel axes centered at the focal point, the pushbroom model encodes a perspective transformation only along the v direction. The u direction encodes an orthographic projection.

In the method implemented in a Python code, the 3D coordinates of the bi-planar calibration gauge have been imported once accurately measured with a laser

scanning system. The corresponding image coordinates, instead, have been extracted with a corner finder method of the Camera Calibration Toolbox which is included in the OpenCV libraries [4] from the stereo images acquired with the experimental setup.

The resulting calibration model has been assessed by the reprojection error (Fig. 1), where the residuals (image coordinates – projected object coordinates) $r_i = x_i - M X_i$ reach standard deviation values of 0.063 px along x and 0.0426 px along y.
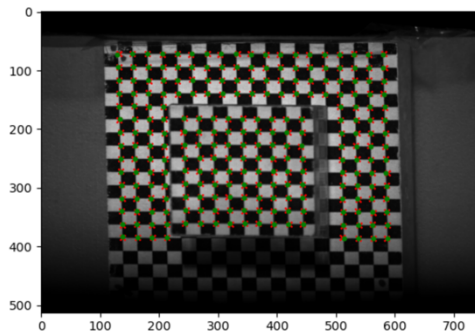
Fig.1: In red the corners of the chessboard extracted with cornerfinder; in green the 3D coordinates reprojected using the estimated projection matrix.

Photogrammetric Process for 3D extraction information. In the first phase, a set of match points (i.e., pixels in the two views that correspond to the same point in the real world, also referred to as tie points) between the two images are established by means of the 3DPD software [5,6]. The disparity maps refined by Least Square Matching method have been then triangulated in a second phase. With the information about the cameras known by the calibration process with the gauge and defined in the correspondent projection matrices M1 (for the image acquired with inclination of 20°) and M2 (for the image acquired with inclination of -20°), one can analyze the disparity and derive the 3-D coordinates in the form of a sparse point cloud as in Fig.2.
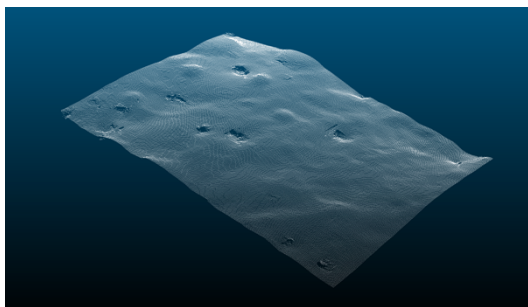
Fig. 2: Point cloud extracted from the photogrammetric process of the stereo images.

In order to quantify the accuracy of the 3D reconstruction, the point cloud has been aligned with a high resolution laser scanner acquisition (20 μm precision) used as reference. The statistics of the discrepancies between the two models are 0.135 mm in terms of Standard Deviation and considering the projection of the pixel on the target of 0.093 mm, the results obtained are quite promising and lead to consider that the new innovative concept of HYPSOS will be able to accurately reconstruct the target surface.

Next Steps: When the complete opto-mechanic system of HYPSOS will be ready for stereo spectral acquisitions the tools for deriving the HDTM will be able to generate spatial 3D information in the form of point cloud or gridded DTM and the spectral information will be exported in the form of coregistered orthophoto for each spectral band, with the same projection and pixel size of the DTM.

Conclusions: The stereo validation procedures performed in laboratory permit to confirm the complete methodology for the stereo hyperspectral reconstruction of a surface with the HYPSOS system. With the spectral and the spatial information we will create a representation of the surface in 3D space linked with hyperspectral information emitted and reflected by the surface itself. The quality of the spectral information will depend on both the band and the pixel position. Looking at the HDTM we could look at the surface properties of each pixel for each spectral band, providing to the scientific community an extremely powerful dataset for the planetary exploration.

References:
[1]Naletto et al (2022) SPIE Proc., ICSO Conference
[2] C. Re, et al., (2017) Planetary and Space Science 136, 1-14
[3] R. Gupta and R. Hartley (1997) *IEEE Trans. Pattern Anal. Mach. Intell. 19 (9), 963–975*
[4] C. Harris, M. Stephens (1998), *Proceedings of 4th Alvey Vision Conference. Manchester, UK,* pp. 147–151
[5] E. Simioni et. al. (2021) *Planetary and space science 198, 105165*
[6] C. Re, et al., (2022) *Planetary and space science 219, 105515*

Dust detector on-board Milani CubeSat: VISTA FM calibration and instrument main goals in the framework of Hera Mission. C. Gisellu[1,2], F. Dirri[1], E. Palomba[1], A. Longobardo[1], E. Nardi[2], E. Zampetti[3], D. Scaccabarozzi[4], B. Saggin[4], M. Angrisani[1,2], G. Massa[1,2]

[1]INAF-IAPS, Via del Fosso del Cavaliere, 100, 00133, Rome (chiara.gisellu@inaf.it); [2]Università di Roma Sapienza, Piazzale Aldo Moro 5, Rome, Italy; [3]CNR-IIA, Via Salaria km. 29.300, 00016, Montelibretti, Rome, Italy; [4]Politecnico di Milano, Polo Territoriale di Lecco, Via G. Previati 1c, Lecco, Italy.

Introduction: Hera is a planetary defence mission under development at the European Space Agency (ESA), due to launch in October 2024. Hera's main goals are the investigation of the Didymos binary system and the evaluation of the outcome of NASA DART (Double Asteroid Redirection Test) mission kinetic impactor test, which occurred in September 2022 [1]. HERA will carry two CubeSats, i.e., Milani and Juventas, that will be deployed in the close proximity of the Didymos system. Juventas, developed by Gomspace, is devoted to the geophysical characterization of Dimorphos. VISTA dust detector and ASPECT visible and near-infrared imaging spectrometer are the two scientific payloads on-board Milani, which is developed by Tyvak International.

VISTA is developed by an Italian Consortium composed of three Research Institutes: INAF-IAPS, CNR-IIA and Politecnico di Milano. The calibration and functionality tests of VISTA FM are presented, as well as the performance tests of VISTA EQM to detect and characterize sub-micron particles by deposition rates and Thermo-Gravimetric Analysis (TGA).

VISTA working principle: The instrument core is a PCM (Piezoelectric Crystal Microbalance), which is a widely used sensor for monitoring molecular contamination in space [2] and characterizing the dust composition processes in different planetary environments [3]. The frequency variations directly depends on the deposited sample mass on the crystal surface, according to Sauerbrey equation [4].

The sensor head consist of: 1) two AT-cut quartz crystals mounted in a sandwich-like configuration; 2) a Thermal Control System (TCS), composed of two integrated heaters and a Thermo-Electric Cooler (TEC); 3) a Proximity Electronics (PE). Thanks to the TCS, VISTA is capable of performing Thermo-Gravimetric Analysis, which is a technique widely used to perform thermal cycles in order to detect volatile compounds by using deposition/sublimation and absorption/desorption rates [5]. VISTA can also monitor particles lower than 10-20 µm.

VISTA for Hera Mission: Three different models are manufactured and tested: VISTA Engineering Qualification Model (EQM), shown in Figure 1, Flight Model (FM) and Flight Spare (FS).
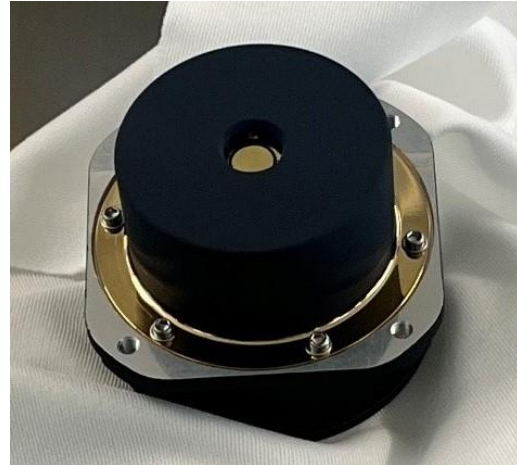

Figure 1. VISTA EQM developed for ESA Hera mission.

VISTA instrument is composed of a sensor head, while the in-flight operations are managed by Milani On Board Computer (OBS) including Telecommands for TCS and PE.

Currently, VISTA EQM and FM successfully passed respectively the qualification and the acceptance test campaigns and are delivered to the prime contractor for integration on the CubeSat and further testing activities.

After Milani deployment from Hera main spacecraft, VISTA will accomplish the following scientific goals: 1) detect the presence of dust particles smaller than 10 µm (residual dust particles from the impact and suspended dust in the binary system or coming from dust levitation process); 2) characterization of volatiles (e.g., water) and organics (e.g., low carbon chain compounds) by TGA cycles (the desorption/sublimation rates and temperatures are used to characterize volatiles and organics) [6][7]; 3) molecular contamination monitoring in support to other instruments (e.g. ASPECT), coming from outgassing processes on-board Milani (this goal can be achieved during the overall mission duration).

Calibration: The sensor frequency can change not only because of mass deposition/release, but also variation of environmental parameters, such as external temperature. This effect is generally avoided thanks to PCM configuration, i.e. double crystals, even though a frequency difference due to the crystals temperature variations can be expected. Thus, a calibration frequency versus temperature is needed due to slight differences in the crystals curves (f vs T). In order to disentangle frequency variations due to mass deposition and temperature variations, the EQM, FM and FS are calibrated by measuring the frequency as a function of temperature at different set-points.

Contamination monitoring and Thermo-Gravimetric Analysis: VISTA capability to monitor depositions processes, i.e. accumulation on sensor surface and desorption processes is verified by using a miniaturized setup composed by an effusion cell containing an organic compound (COOH based), placed in the Field Of View (FOV) of the sensing crystal and heated up to 100-120°C. The experimental setup is shown in Figure 2.
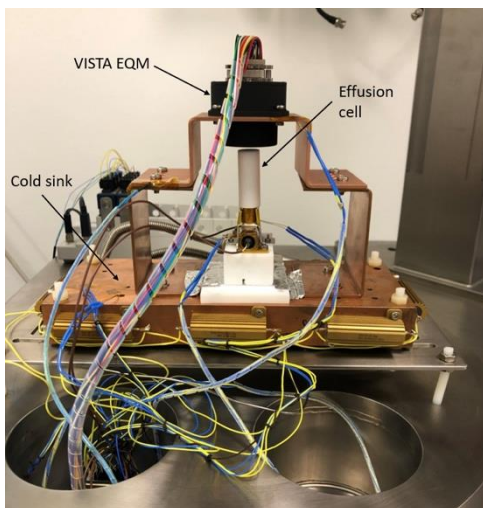
Figure 2. Experimental setup for contamination monitoring.

The sensor is connected with four screws with a copper U shape and in contact with a cold sink set to -10°C to help the molecules condensation on the crystal surface. The frequency is monitored during the tests and the deposited flux can be retrieved at each temperature set point. An example of variation of mass deposited on the sensor during the test is shown in Figure 3.
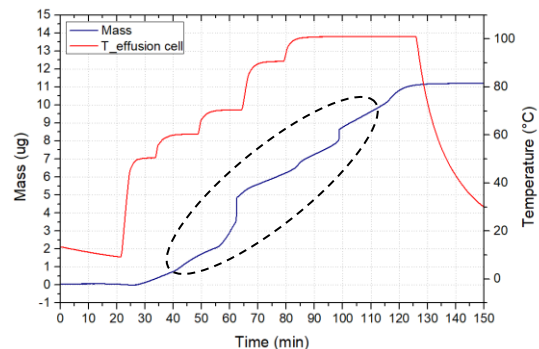
Figure 3. Monitored deposition process (black dotted line) from 50°C to 100°C.

TGA cycles are then performed by heating the crystals by means of the built-in heaters, in order to allow desorption of deposited mass, as depicted in Figure 4.
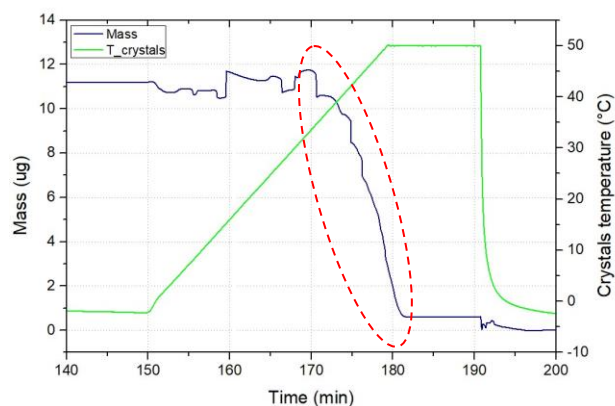

Figure 4. Mass desorption (red dotted line) during TGA cycle, with the crystals heated up to 50°C.

Two methods are used to retrieve the enthalpy of sublimation by using the deposition rates: the Van't Hoff relation [6] or Langmuir relation [7]. By measuring two different deposition rates, k_1 and k_2, at two different close temperatures T_1 and T_2 (e.g. from 30 to 35°C, from 35 to 40°C, etc.), it is possible to obtain the ΔH_{sub} by means of Van't Hoff relation or throughout all the temperature range (e.g. from 30 to 70°C) by using Langmuir relation. The desorption rates obtained from TGA can be used as well to calculate the $\Delta H_{sub,TGA}$ and compare it with the $\Delta H_{sub,deposition}$ result obtained during the deposition process in order to compare the results coming from the two methods.

References: [1] P. Michel et al., 2022 Planet. Sci. J. 3 160; [2] Dirri et al., 2016, AMT 9, 655–668; [3] Palomba E. (2016), OLEB, 46 (2-3); [4] G. Sauerbrey 1959, Z. Phys., 155, 206-222; [5] C.B. Bargeron et al., Proc. SPIE 2261, (1994) ; [6] S.W. Benson et al. 1968; [7] I. Langmuir, 1913.

The PVRG spectral database of lab-made volcanic products on the SSDC infrastucure: a new catalog of reference spectra to characterize volcanic terrains on planetary bodies.

Alessandro Pisello[1], Angelo Zinzi[2], Matteo Bisolfati[1], Massimiliano Porreca[1], and Diego Perugini[1]
[1]Università degli Studi di Perugia, Dipartimento di Fisica e Geologia, Perugia, Italy (alessandro.pisello@unipg.it)
[2]ASI-SSDC/ASI, Roma, Italy

Introduction: Silicate glasses represent a major component in volcanic products, but their spectral characteristics are not always considered when dealing with the interpretation of planetary and asteroidal surfaces and terrains. Space analogues described in spectral libraries are mostly constituted of crystalline materials rather than amorphous products. This happens because of the lack of spectral features of amorphous products, but this kind of blurred/featureless spectra are indeed observed on planetary surfaces, and, moreover, very recent studies have shown how amorphous phases can also deeply influence the spectral response of volcanic terrains [1]. For this reason, we have started an extensive investigation of the spectral response of silicate glasses, which were produced using experimental petrology tools at the Petro-Volcanology Research Group in Perugia (PVRG) covering large range of possible natural chemical compositions, but also comprehending incipient crystallization within glassy phases. We have therefore used different techniques to characterize such analogues: reflectance in the Visible and Near-Infrared (VNIR) [2], again reflectance in the Mid-Infrared Region (Mid-IR) [3] and reflectance and emissivity in the Thermal-Infrared Region (TIR) [4].

We have observed how different spectral techniques allow us to retrieve interesting correlations between change in spectral characteristics and chemical/textural composition. As examples, we have observed promising correlations between spectral slope/albedo and iron content and speciation of the investigated samples in the VNIR [2], but also between silica and alkaline content and spectral shift/shape in the Mid-Infrared Region [3,4]. Moreover, it is observed how evolution of spectral shape in the MIR region carries interpretable and useful information on granulometry of the investigated terrains.

These findings suggest that accounting for glassy phases for the interpretation of planetary volcanic terrains is useful because i) it permits to distinguish which parts of the spectra carry information about crystalline phases and which not, and ii) glasses spectra carry themselves important information (iron, silica and alkaline content) that can be used to classify volcanic rocks and therefore to define geological history of planetary bodies. For these reasons, we want to offer a tool where such dataset can easily be observed and investigated.

The ASI (Italian Space Agency) Space Science Data Center (SSDC) [5] is an infrastructure thought to archive open access data in the field of space sciences for different missions and purposes, and it operates using international standards such as those regarding Planetary Virtual Observatory [6] to maintain and disseminate data applying the FAIR (Findable, Accessible, Interoperable, Reusable) principles. Within SSDC infrastructure, we have created an environment to provide open access to this kind of data by creating a spectral database in which raw spectral data can be found together with the relative peer-reviewed publications in which such data are discussed. Up to now (May 2022) the database is only reacheable through the SSDC pages and with access restricted to people inside the group, but it is already planned to made the catalog completely public in a very near future, not excluding the possibility of making it available as a VO resource in a more advanced phase. Such environment will be explorable in the "Catalogs" list of the SSDC website (https://www.ssdc.asi.it/) under the name Spectral Database for Silicate Glasses with Natural Composition (Fig 3), where it will be possible to visualize, compare, and filter-search spectra, making it a fundamental tool for planetary scientists to account spectra of amorphous phases within their analyses of planetary surfaces.

References: [1] Leight et al., 2022. Remote Sensing of Environment, 273, 112965. [2] Pisello, et al., 2022. Icarus, 374, 114801. [3] Pisello, et al., 2022. Icarus, 388, 115222 [4] Pisello, et al., 2019. Scientific reports, 9(1), 1-13. [5] Zinzi et al., 2018. Advances in Space Research, 62(8), 2306-2316. [6] Erard et al., 2019. arXiv preprint arXiv:1907.06521.

DAEDALUS CAM: AN IMMERSIVE STEREOSCOPIC CAMERA TO EXPLORE LUNAR CAVES

C. Pernechele[1], E. Simioni[1], R. Pozzobon[2], M. Massironi[2], V. Della Corte[3],
M. Landoni[4], B. Saggin[5], D. Scaccabarozzi[5],
on behalf of the Daedalus CAM team

[1]INAF Padova, vicolo Osservatorio 5, I-35122, Padova (claudio.pernechele@inaf.it)
[2]University of Padova, [3]INAF IASP (Roma), [4]INAF Brera (Milano), [5]Polytechnic University (Milano).

Introduction: The possibility to explore the lunar subsurface by accessing lava tubes from skylights has been subject to an ESA's call for ideas in its Open Space Innovation Platform in the SysNova Lunar Caves system studies framework. The aim is to enter and explore the skylight named Marius Hills Hole in Oceanus Procellarum (303.3°E, 14.2°N), which is believed to be an access point to a large underground void. Lava Tubes represent a source of interest for the science community since Kaguya, LRO and GRAIL missions have unequivocally underlined the presence of deep voids below the Lunar surface.

These subsurface voids could be the base for long-term presence in human exploration framework [1] because:

- represent a natural shield from possible impacts of micrometeorites and cosmic rays (here the equivalent radiation is the 0.3% of the surface one).
- are characterized by stable environments with an average temperature of
- might provide access to resources such as possible sources of water

This could change the paradigm of how approach future lunar exploration today and open new doors to Martian exploration.

Mission Summary: In this light a robotic sphere named DAEDALUS (Descent and Exploration in Deep Autonomy of Lava Underground Structures) [2,3] has been proposed and selected for a subsequent ESA CDF (Concurrent Design Facility) in order to descend and map the collapse pit and eventually navigate and map the underground cave.

Since the objective of the mission is the deployment of a robotic sphere able to explore inside the lunar cave both for vertical and horizontal exploration, the goal of the instrument is the characterization of the cave floor and ceiling, also aiming to confirm the preliminary results defined by the NAC images in [2].

For this reason, the DAEDALUS is designed as a sphere and lowered into the pit using a robotic crane [4] system mounted on a dedicated rover (avoiding the sloping area before the void).

While descending the skylight the laser scanner and the panoramic cameras are used to create a 3D point cloud of the shaft. An encoder measuring the tether length gives an initial depth estimate.

In the meantime, thermal, radiation and dust sensors will provide information local environment conditions. When passing the cave ceiling, the lidar system acquires the first 3D point cloud from within the cave allowing for a structural analysis of the cave. The cameras are foreseen to capture a full view of the main void using natural illumination. For this reason, a FPGA-based exposure algorithm able to balance panoramic exposures is under development.

Once touching the ground, the sphere detaches from the tether and navigates through the cave autonomously using the 3D data acquired before for initial navigation planning.
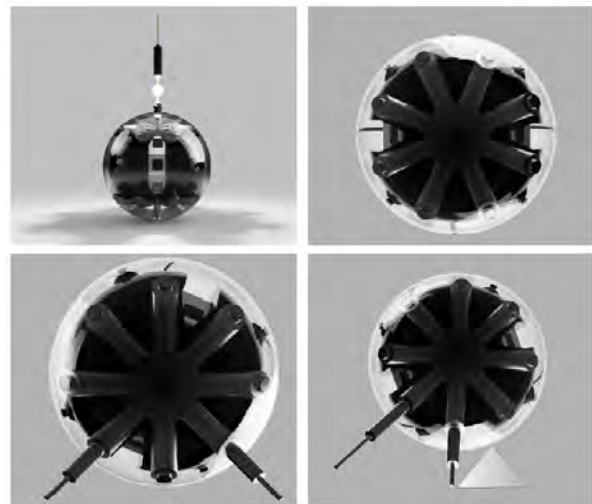

Fig 1: The different modes of the DAEDALUS Sphere. Top-Left: Descending Mode. Top-Right: Rolling Mode. Bottom- Left: Scanning Mode. Bottom-Right: Obstacle Mode.

Payload: The DAEDALUS robot has been designed to be equipped with environmental sensors, laser scanners and an optical instrument (Daedalus CAM) able to provide a 360 view of the vertical and subsurface environment and to retrieve as large amounts of data as possible. This is aimed both to answer scientific questions such as the morphology

and composition of the lava layers outcropping in the vertical walls of the skylight, and to characterize in detail the morphology and assess the trafficability of the cave floor and eventual obstacles or hazards to plan further exploration.

The Daedalus CAM is an optical camera composed of four Bifocal Panoramic Lenses (BPLs) [5] settled in a crossed configuration. A BPL (see top left panel in Fig. 2) is a lens which may record a panoramic field of view (FOV) of 360°x100° and, simultaneously, a round FOV of 20° with higher resolution (frontal field).
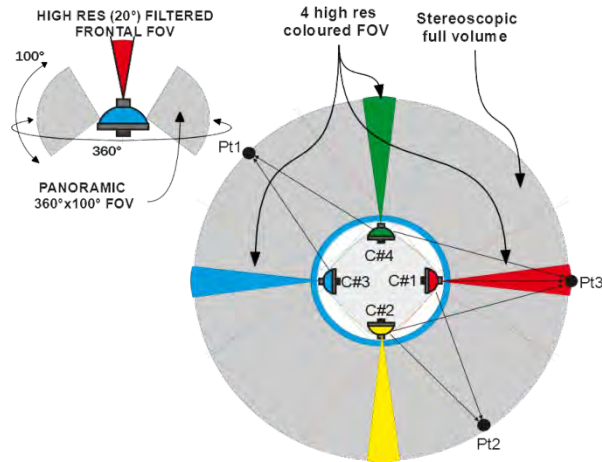
Fig. 2: BPL and Daedalus CAM concept.

A BPL, coupled with a 2k x 2k format image sensor, provides an angular resolution of 0.1°/px (paraxial) in the panoramic field and about 0.03°/px in the frontal field. Placing four of such BPLs, as shown in Fig. 3, the full volume surrounding the Daedalus CAM may be sampled in stereoscopic mode: all the points of the whole space around are viewed by at least two cameras (as ex. Pt1 and Pt2 in Fig. 2). Some areas are seen by three or even four lenses. Some points, such as Pt3 in Fig.2, are seen by two cameras in the panoramic field and, simultaneously, by the frontal (higher resolution) FOV. The panoramic lower resolution fields serve for contextual vision, for SLAM (simultaneous localization and mapping) algorithms in robotic-mode and to avoid possible hazards during the descent. The four colored higher resolution channels operate scientific recognition in four different pass-band filters allowing the monitoring of any rock structure and texture with a detail previously conceivable only by human crew or rover with robotic arms. This can provide an estimate of thermal stress induced micro fracturing as well as to perform a modal analysis of the distribution of clasts/phenocryst within a rock.

Once the descent travel is completed, the Daedalus CAM will provide a full 3D reconstruction of the yet unknown pit walls. Each of the four subsystems (lens+ image sensor) has a volume of 350 cm^3 and a weight of 195 g. The power consumption for the four image sensors is 4 W, working at 12 V.

In order to test the camera functionalities a mockup, shown in Fig. 3, has been manufactured. The cross has a 450 mm linear dimension, to replicate the Daedalus sphere real dimension (465 mm). Images acquisition and analysis are currently undergoing.

Fig. 3: The Daedalus CAM mockup.

DAEDALUS CAM images will be dewarped after downlink. Their geometrical calibration is in development in our laboratory [6].
Part of the team involved has developed, in the past years, the 3DPD [7], a stereo processing chain, capable of producing 3D reconstructions, called Digital Terrain Models (DTM), starting from satellite. These photogrammetric activities are currently applied to the Martian images of CaSSIS and are the starting point for the future processing of the stereo pairs that will be acquired by the STC stereo camera [8] for the BepiColombo mission.

References:

[1] Haruyama *et al.* (2012) (pp 139-163) Springer. [2] Pozzobon *et al*. (2021), 52th LPSC, Abstract #1886). [3] Borrmann *et al*. (2021), 52th LPSC, Abstarct #2073. [4] Miaja et al., (2022), Acta Astronautica [5] Pernechele (2016), *Opt Expr*., 24(5), 5014. [6] Simioni *et al.* (2020), ISPRS. [7] Simioni *et al*. (2021) PSS. [8] Cremonese *et al.,* 2020

Astroinformatic and Digital Planetology Laboratory in INAF. R. Politi[1], A. Aronica[1], S. Fonte[1], S. Ivanaoski[2], J.S. Liu[1], C. Magnagico[1], R. Peron[1], C. Re[3], E Simioni[3], D. Turrini[4], M. Zusi[1].
[1]INAF-IAPS, via fosso del cavaliere 100, I-00133 Rome, Italy (romolo.politi@inaf.it),
[2]INAF-OATS, via G.B. Tiepolo 11, I-34143 Trieste, Italy
[3]INAF-OAPD, vicolo Osservatorio 5, I-35122, Padua, Italy
[4]INAF-OATO, via Osservatorio 20, I-10025, Pino Torinese (To), Italy

Introduction: The LAPD (Astroinformatics and Digital Planetology Laboratory) is a distributed research infrastructure involving several INAF institutes and University Sections and covering multiple research fields in the computational domain. Its main task is to design and develop algorithms for data analysis and simulations. Each code is validated and optimized in strict contact with scientific teams: the final users of the tools. The optimization task takes into account the specific hardware infrastructure used for the production phase, and is the input for the hardware deployment and optimization. In addition, the Laboratory designs, develops and validates the ground segment, the archives, and the dissemination systems for some INAF-led international space missions and payloads. The team supports the deployment of software, hardware, and, last but not least, dissemination of the acquired know-how.

The Laboratory activities are grouped in the following fields:

- Space Missions Ground Segment
- Data Archive
- Simulation of observation
- Numerical simulation
- High Performance and High Throughput Computing
- Robotic and Drones.

Space Mission Ground Segment: this is the historical activity of the laboratory and the first field of joint collaboration of the LAPD members. We work on the two areas of the ground segment, the uplink and the downlink. The uplink consists in the preparation and validation of the instrument command stack that will be sent to the spacecraft (after multiple interactions with the Space Operation Center of the Space Agency). The downlink consists of generating the raw and calibrated data file, starting from the instrument telemetry. An example of downlink pipeline is shown in Figure 1.

For this activity, we are involved in many current and future ESA planetary missions, i.e., BepiColombo, and JUICE, as well as Space observatories like ARIEL. Some examples of the products of this activity can be found in [1] and [2].
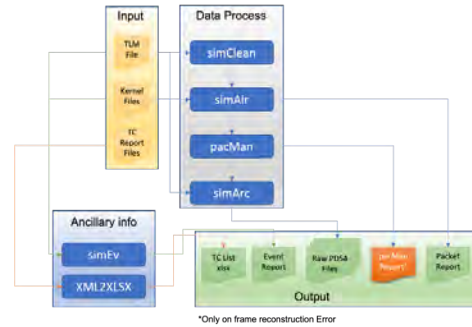

Figure 1: Block diagram of the pipeline developed for BepiColombo SIMBIO-SYS.

Data Archive: This activity is linked to space missions as well. We work on the design of the storage structure, sometimes also from an HW point of view, and the metadata identification for the best description of the experiment results. The managed archive follows the standards for the long-term preservation archives recomended by the planetology community (PDS3 for the heritage archives and PDS4 for the present ones). We also work on the short/medium-term archives using more friendly formats like CDF, netCDF, or relational databases (e.g., PostgreSQL). Recently, we have started to work on not planetological archives (e.g., ARIEL archives) and archives for ground observation with a close collaboration with INAF IA2.

Simulation of Observations: All the Space missions to Solar System Bodies required, in all their phases, the development of tools to simulate acquisitions, verify and optimize the observation strategy, and define the essential parameters for Operations. The LAPD developed the Simulator for Operation of Imaging Missions (SOIM)[3,4], a flexible software tool for simulating such payloads that represents a transversal activity to different research lines favoring the optimization of performances and, with the collaboration of the scientific group, the validation of scientific requirements.
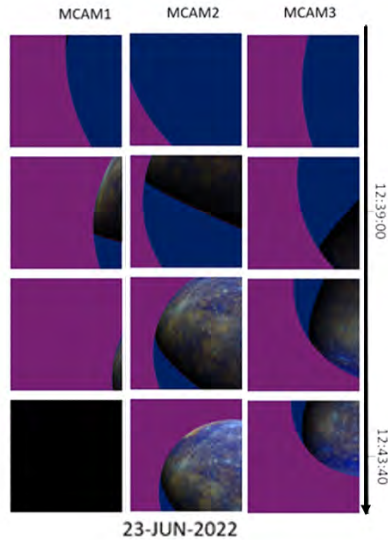
Figure 2: Rendering of the MCAMs at 5-minute intervals in a neighborhood of the C.A of Mercury flyby

This tool is currently used on the ESA BepiColombo mission to plan the Monitoring Cameras (M-CAM) [5] acquisitions during the several flybys in the cruise phase and the SIMBIO-SYS suite observations to the Mercury surface. An example of the output is shown in Figure 2.

Numerical Simulation: LAPD is associated with Arxes, a multidisciplinary INAF research program aiming to answer the fundamental questions of planetary formation and supporting many ground- and space-based national and international projects by developing new methods, theoretical models, and computational tools. The overarching scientific goal of Arxes is to link the compositional characteristics and the architectures of planetary systems to their formation and evolution histories, to shed light on the sources of their differences and similarities. LAPD supports Arxes through code parallelization, development of numerical libraries, multi-language programming and automation scripting, as well as by managing its computational cluster Genesis. Some results of this activity can be found in [6] and [7].

HPC and HTC: while the code developed and distributed by the LAPD is generallyserial, when addressing problems associated with marked computation loads we develop parallel and GPU-accelerated codes, e.g., the Mercury-Arxes n-body code. This activity has allowed us to be part of the National High-Performance, Big Data, and Quantum Computing Center since its creation, and in particular, we are involved in two spokes of the PNRR HPC project (Fundamental

Physics and Space Economy and Astrophysics and Cosmos). In parallel, we are also working on High throughput computing focusing on the archive (re)generation and analysis.

Robotics and Drones: The laboratory developed several projects using drones to explore terrestrial terrains analogous to planetary surfaces. Those projects aim to demonstrate the potentiality of these drones (especially the flying ones) to study efficiently and with high-resolution selected regions of space bodies. As secondary products of those researches, there are some terrestrial applications, e.g., the detection of re-trigger points after fires. This kind of application also requires a particular type of computation called Urgent Computing, fast computing, and prioritized access to HPC infrastructure for emergency computations such as fires or severe weather prediction during matters of immediate concern.

A transversal activity is outreach. The LAPD is involved in several initiatives, e.g., the European Researchers' Night or lectures in schools of different levels. The Laboratory is also working on an outreach project describing the ESA BepiColombo Mission through a virtual reality application usable by modern mobile phones.

The LAPD organizes group periodic seminars on particular technical topics to share the knowledge acquired by individual members on the specific projects they are working on.

References:
[1] R. Politi (2020) INAF Technical Report DOI: http://dx.doi.org/10.20371/INAF/TechRep/38
[2] R. Politi (2020) SCOSpy Software DOI: 0.20371/INAF/SW/2020_00001
[3] A. Slemer (2019) Montly Notices DOI: https://doi.org/10.1093/mnras/stz3060
[4] E. Simioni (2022) INAF Technical Report DOI: https://doi.org/10.20371/INAF/TechRep/202
[5] E. Simioni (2022) INAF Technical Report DOI: https://doi.org/10.20371/INAF/TechRep/125
[6] D. Turrini (2019) Atropysical Journal : DOI: 10.3847/1538-4357/ab18f5
[7] D.Turrini (2021) APJ Doi: 10.3847/1538-4357/abd6e5

MAKING JANUS READY TO LAUNCH: ON GROUND CALIBRATION CAMPAIGN.

L. Agostini[1], C. Tubiana[2], F. Sarti[3], T. Bilotta[3], P. Palumbo[4,2], S. Hviid[5], A. Aboudan[1], S. Mottola[5], A. Dattolo[3], V. Della Corte[2], M. Amoroso[6], A. Colosimo[3], G. Cremonese[7], C. Crews[8], I. Ficai Veltroni[3], A. Galeotti[3], L. F. Livi[3], M. Zusi[2], and the JANUS team. [1]CISAS (Centro di Ateneo di Studi e Attività Spaziali) "G. Colombo" – Università di Padova, Padua, Italy (livio.agostini.1@phd.unipd.it), [2]INAF-IAPS Roma, Istituto di Astrofisica e Planetologia Spaziali di Roma, Rome, Italy; [3]Leonardo SpA, Firenze, Italy; [4]Universita' degli Studi di Napoli "Parthenope", Napoli, Italy; [5]DLR, Berlin, Germany; [6]ASI, Rome, Italy; [7]INAF-OAPD Astronomical Observatory of Padova, Padova, Italy; [8]Center for Electronic Imaging, The Open University, Milton Keynes, UK.

Introduction. JUICE (JUpiter ICy moons Explorer) is the first large mission (L1) of the European Space Agency's (ESA) program Cosmic Vision 2015-2025 having as main objective the investigation of habitable worlds around gas giants, studying Jupiter, its icy Galilean moons Ganymede, Europa and Callisto and their interactions [1]. JUICE is equipped with 10 instruments designed to answer to a broad range of scientific questions. JANUS (Jovis Amorum ac Natorum Undique Scrutator) [2] is the high-resolution optical camera developed considering the great variability of observing conditions, allowing orders-of-magnitude steps ahead in terms of coverage, resolutions and time evolution with respect to what was achieved with previous missions to Jupiter. The instrument scientific objectives are the characterization of icy satellites surfaces (with focus on Ganymede), tectonics, cryovolcanism, craters' morphology, surface composition, Io's volcanism, surface wheatering, exospheres, Jupiter atmosphere and dynamics, plumes, thorus, rings and aurorae and satellites' librations. A science plan is under development to maximize the scientific return of the instrument and the mission itself [3]. To be ready for the science phase, besides the planning, it is required that the instrument is calibrated and is able to provide quantitative data in physical units. In this work we present the on-ground calibration campaign, the performed activities and the expected results.

The JANUS camera. JANUS is structured in three main subsystems: the Main Electronics Unit (MEU), controlling the overall instrument and interfacing the spacecraft, the Proximity Electronic Unit (PEU), managing the low-level detector connection along with the digitization of signal, and the Optical Head Unit (OHU), which includes the telescope, the detector, the filter wheel and the cover [4]. The camera has a nominal focal length of 467 mm, a radiometric F# of 4.5 and a pixel pitch of 7 μm with a fill factor of 100% due to the back-illumination configuration of the detector. The instrument has multi-spectral capabilities thanks to 13 selectable filters, with a global spectral range from the UV to the NIR (340 nm-1080 nm).

On ground calibration campaing. The calibration campaignwas performed in the Leonardo S.p.A. facility (Campi Bisenzio, FI, Italy) in October 2021 and it has been conceived to verify a broad range of aspects of the instrument. The team has performed a quick-look analysis in loco and currently the data analysis is on-going. The results of these activities will be the retrieval of the Key Data Parameters (KDP) required to calibrate the data.

The calibration setup. Figure 1 shows a sketch of the calibration setup.
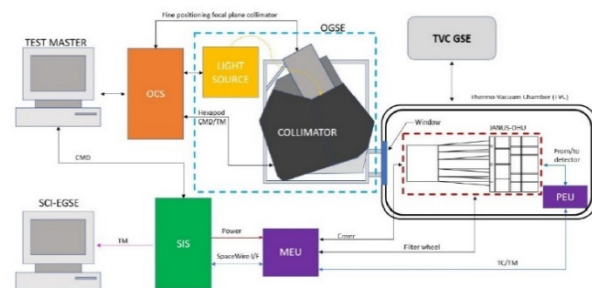

Figure 1: Sketch of the calibration facility with OGSE for collimated beams. For non-collimated beams configuration, the collimator is substituted by an integrating sphere.

The activities are planned in Automatic Test Procedure (ATP) scripts. They are interpreted by the Test Master which sends telecommands to the OGSE (Optical Ground Support Equipment) control (OCS) and to the instrument by means of the Spacecraft Interface Simulator (SIS). The OGSE has two configurations: a "Collimated beams" (CB) and a "Non Collimated beams" (NCB) configuration. The first consists of a custom collimator (already used for the calibration of other instruments, such as HRIC/SIMBIO-SYS on the BepiColombo mission) on a six-degrees of freedom kinematic device (hexapod). Different targets (pinholes, slits, 1951 USAF resolution target…) can be placed on the focal plane of the collimator and their position is fine-tuned thanks to a micrometric motorized stage. These targets are illuminated by a small integrating sphere fed by a monochromator. The zero-order is selected for polychromatic measurements. The Non Collimated beams OGSE is instead an integrating

sphere with a variable shutter aperture useful to produce various levels of radiance.

The OHU along with the PEU are located inside a custom-made thermovacuum chamber (TVC) which is controlled by a dedicated Thermal Ground Support Equipment (TGSE). Thanks to this, the performance of the instrument has been verified at three different setpoints (nominally *HOT, MIDDLE, COLD* operational temperatures).

Calibration measurement strategy: In Table 1 are summarised the different type of measurement performed during the on-ground calibration campaign. Beside the "classic" aspects of an optical instrument (radiometric, geometric and spectral characterization) we also included the characterization of various instrument-related behaviours, such as the distorsion induced by the rolling shutter readout.

Radiometric	
ITF vs radiance	Instrument response at various levels of radiance (fixel integration time). All filters. All temperature setpoints
ITF vs integration time	Instrument response at various levels of integration time (fixed radiance). All filters. All temperature setpoints.
Geometric	
Boresight	Single angular orientation of collimated beam wrt instrument. Variation of the boresight position wrt filter and temperature. HOT and COLD setpoints.
Line of Sight	63 angular orientantion of collimated beam (that is 63 grid points on focal plane). Determination of geometrical properties: focal length, boresight direction, distortion map, IFOV, FOV. All filters. MIDDLE setpoint.
Spectral	
SRF	Monochromatic scan. Evaluation of filter central wavelengths and bandpass. All filters. MIDDLE setpoint.
Performance	
MTF	Slanted edge method, horizontal and vertical directions. Evaluation of MTF. All filters. All temperature setpoints. 3x3 map wrt field of view.
Focus Scan	Evaluation of the best focus positions, scan along OGSE focal axis. Slanted edge method. 5 positions in FOV. Panchromatic filter. All temperature setpoints
USAF	Acquisition of USAF target. Suppotting measurement to slated edge. For F1, 3x3 angular points. Single angular pointing for all filters.
DARK	Evaluation of readout chain and detector performance. Offset, DSNU, dark current rate (up to 100s). All temperature setpoints.
Detector performance	Evaluation of repetition time, image lag, compression, binning and windowing, simulation of rolling shutter
	distortion in flight and investigation of spurious effects.
Straylight	
In field (Ghosts)	Evaluation of the pattern and relative intensities. Source in 3x3 angular positions inside FOV. Combination of various OD filters and integration times.
Near field	Evaluation of the pattern and relative intensitites. Source at the limit of FOV and up to 4°/5°

Table 1: Calibration measurement type and explanation. Acronyms: ITF (Instrument Transfer Function), SRF (Spectral Response Function), MTF (Modulation Transfer Function), IFOV (Instantaneous Field of View), FOV (Field of View), DNSU (Dark Signal Non Uniformity), OD (Optical Density), OGSE (On Ground Support Equipment)

Discussion and Conclusion: During the calibration campaign the acquired amount of data was larger than what will be generated during the entire mission. Currently, almost all of the "classic" aspects of the calibrations have been preliminarily analyzed and compared with specific models of the instrument showing a good agreement with the expectations. The instrument shows a negligible radiometric response variation with temperature (less than 2% in the HOT-COLD range), Within the next year, we foresee to have a radiometric calibration for each pixel (namely ITF, Instrument Transfer Function). The detector's and readout chain performances show a stable behaviour with temperature with a median readout noise of 2.5 DN and a dark current generation < 6 DN in 100 s. The on-ground calibrations have also provided an insight into the real behaviour of JANUS under different stimuli and a solid basis for in-flight calibrations planning and data analysis, in particular for the geometrical calibration. According to [7] the results in terms of MTF are in line with the requirements.

References: [1] Grasset et al., (2013), *PSS,* 78, 1-21. [2] Palumbo et al., (2014), *EGU conference.* [3] Tubiana et al. (2022), Italian National Congress of planetary science. [4] Dalla Corte et al., (2019), 2019 IEEE MetroAeroSpace. [7] Sarti et al. (2022), ICSO 2022.

TRIS: TRansmission and Illumination System.

E. La Francesca[1], M. C. De Sanctis[1], S. De Angelis[1], E. Ammannito[2], M. Ferrari[1], A. Raponi[1]
[1]Institute for Space Astrophysics and Planetology, IAPS-INAF, Via Fosso del Cavaliere, 100, 00133, Rome, Italy,
[2]Italian Space Agency, ASI, Via del Politecnico snc, 00133, Rome, Italy (eliana.lafrancesca@inaf.it).

Introduction: The use of InfraRed spectroscopy in the exploration of the Solar System can provide useful information for the surface characterization of the various rocky bodies, both through remote-sensing and in-situ (landers/rovers) instruments. Gathering up the heritage of Ma_MISS (Mars Multispectral Imager for Subsurface Studies) onboard Rosalind Franklin rover mission [1,2,3], TRIS is a Research and Development (R&D) program to increase the TRL (Technology Readiness Level) of transmissions (optical fibers) and illuminations systems. The main goal is to extend toward the IR spectral range the sensitivity of a Ma_MISS like instrument.

TRIS is currently undergoing a feasibility study at the INAF-IAPS institute of Rome, in the framework of an ASI agreement and with the collaboration of Leonardo. Here we present some preliminary results.

Setup and optical element description: The optical elements under testing within the TRIS program are IR illumination sources and optical fibers.

The IR illumination sources are made of a thin film resistor of diamond-like nanostructured amorphous carbon. The active area is 1.7 mm x 1.7 mm, with an emissivity of 0.8 in the spectral range $1 \div 20$ μm. The operating temperature is adjustable by changing the voltage and amperage values. To find the best solution for our purposes, we studied IR sources coupled with four different optical solutions: one reflectorless source, two with different parabolic optics, and one coupled to an elliptical reflector (see Fig.1, bottom panel).

The optical fibers are characterized by an Indium Fluoride Glass (IFG- InF_3) with core/cladding diameter of 200/260 μm. The numerical aperture is 0.2, external coating is in peek. The transmission wavelength range is 0.3 – 5.5 μm.

Two different set-ups were used to characterize the optical elements of TRIS in the different spectral ranges, with an overlap in the near-infrared range.

In the VIS-NIR, 0.3 to 2.5 μm, the ASD FieldSpec4 spectrophotometer was used: this covers the spectral range thanks to three different detectors (Si photodiode,

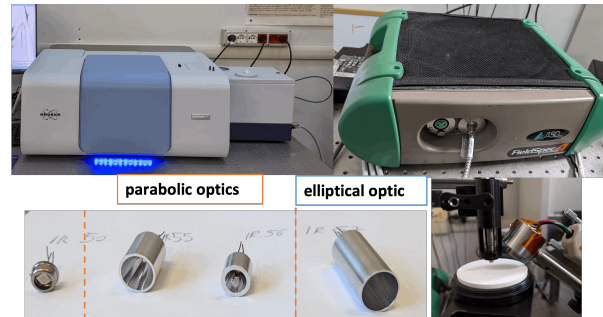0.35-1 μm, and InGaAs, 1-1.8 and 1.8-2.5 μm) with a spectral sampling of 1 nm.

Figure 1:Above are photos of the instrumentation used for qualification tests of the optical components of TRIS in the different wavelength ranges. Top left is the FTIR, top right is the FieldSpec. Below is a photo of the IR sources studied, , with the different reflectors, and a snapshot of the set-up mounted to study the signal in reflectance (over Labsphere spectralon 80%) of the IR50 source (reflectorless).

In the NIR to MID-IR, $1.22 \div 18$ μm, a Bruker's FTIR, INVENIO model, was used (see Fig.1, top panel), the detectors were a DLaTGS (at room temperature) and a liquid nitrogen cooled MCT (Mercury Cadmium Telluride), the resolution was 0.13 nm. To minimize losses due to optical alignment in the characterization of fiber transmission, the FTIR was equipped with a fiber compartment with SMA connectors, while to connect the fiber to FieldSpec a SMA adaptor was used.

Qualifying Test Measurements: In this section we present some results of the initial characterization tests of the optical components. Regarding the optical fibers transmittance measurements, we see substantial agreement in the results obtained in the two ranges (see Fig.2). Measurements in the visible-near infrared were made using a QTH (Quartz Tungsten Halogen) lamp as the source, while in the IR the Bruker internal MIR source, a silicon carbide (SiC) Globar, was used.

The error associated with these measurements is the standard deviation given by consecutive acquisitions upon fibers mounting/dismounting and inversion. The estimated error is about 3 percent.

For clarity, the manufacturer's data were also plotted, we can observe substantial agreement. In the region above 5 microns we observe a higher

transmittance value than that given by the manufacturer, although this region is beyond our intentions
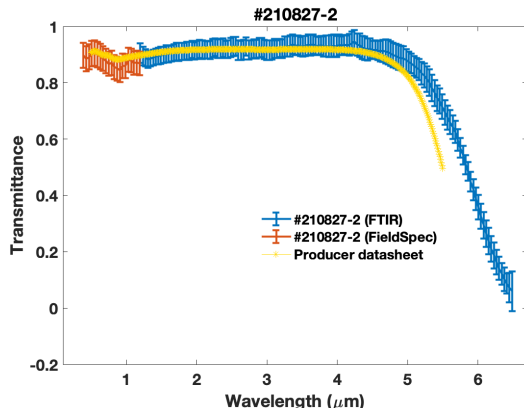

Figure 2: Measured fiber transmission with the two different spectrometers. The associated error is the measured standard deviation. Bottom panel, uncalibrated Radiance of IR source measured with Bruker's FTIR. Producer values are plotted too.

Preliminary characterization measurements of the infrared sources were carried out with both FieldSpec and FTIR. Analysis of the data obtained is on-going.

Future Steps: The investigation and characterization of TRIS prototype performances will continue in the spectral study of the IR sources at wavelengths longer than 2.5 μm, with a full Bruker FTIR calibration. We will also begin the various stress tests, thermal cycling, radiation resistance, and mechanical stresses in order to test the resilience of the optical components of TRIS to the stresses and challenges that the space environment demands.

Conclusions: The feasibility study and implementation of a fiber-optic instrument in the infrared range could be an important tool for the spectral study of planetary surfaces in a range particularly important for both the detection of water, organics and ammonium compounds (detected on minor bodies such as Ceres [4]). Illuminating with fiber optics reduces also the thermal load that could alter environmental conditions and consequently the spectrum of the sample.

References: [1] De Sanctis, M. C., et al. *The Planetary Science Journal* 3.6 (2022): 142. [2] De Sanctis M.C. et al. (2017), *Astrobiology* 17, 6-7, 612-620. [3] Vago J. et al., et al.: (2017) *Astrobiology*, 17, 6-7, 471-510. [4] De Sanctis, M. C., et al. *Nature* 528.7581 (2015): 241-244.

Ma_MISS AND SCIENTIFIC ACTIVITIES IN SUPPORT OF THE EXPLORATION OF THE MARTIAN SURFACE AND SUBSURFACE IN THE NEXT DECADE

Maria Cristina De Sanctis[1] (mariacristina.desanctis@inaf.it), Francesca Altieri[1], Simone De Angelis[1], Marco Ferrari[1], Alessandro Frigeri[1], Sergio Fonte[1], Eleonora Ammanito[2], Jeremy Brossier[1], Marco Giardino[2], Andrea Apuzzo[3], Michelaneglo Formisano[1], Lorenzo Rossi[1] G. Vizzini[3] and Ma_MISS team. [1]Institute for Space Astrophysics and Planetology IAPS, National Institute of Astrophysics, 100 Via del Fosso del Cavaliere, 00133 Rome, Italy. 2 ASI, Agenzia Spaziale Italiana, viale del Politecnico, 00133 Roma, Italy, 3 Univ. Roma 3, Roma, Italy.

Introduction: Mars is a primary destination to search for signs of life in our Solar System and probing the subsurface is a key element in this quest. ExoMars 2022 mission was designed with the aim of searching life into the Martian subsurface, accessing to sequences of buried layers that may host biomarkers. The ExoMars rover mission (in collaboration with ROSCOSMOS) was put on hold at the beginning of 2022 due to the geo-political situation and it is now reconfigured for a departure in 2028, using European technology to land. The rover, called Rosalind Franklin, will remain almost the same as in the 2022 configuration, while the platform will be completely redesigned and built. Accessing the unaltered subsurface has been the innovative approach of the ExoMars mission. Such an approach has been recently adopted also for the new NASA mission concept called MLE (Mars Life Explorer): the design foresees a lander with a drill capable to reach subsurface layers, extracting samples to the be analyzed by a payload very similar to ExoMars' one. Here we will describe the scientific and technological activities to support the Martian exploration, in the context of the rover mission, specifically for the Ma_MISS instrument, as well as in a broader context.

Rosalind Franklin rover: Access to the Martian subsurface is the characterizing element of the ExoMars 2022 rover mission. ExoMars 2022 includes a drill to collect subsurface samples and has a complex payload able to conduct detailed investigations of composition, search for organics, and recognize indicators of past or extant life (fig.1) [1]. The drill is a critical element of the mission which will explore and collect samples down to 2 m of depth . An essential part of the payload is Ma_MISS (Mars Multispectral Imager for Subsurface Studies) experiment hosted by the drill system [2,3]. Ma_MISS is a Visible and Near Infrared (VNIR) miniaturized spectrometer with an optical head inside the drill tip capable of observing the borehole. walls from where the samples are collected. The samples taken by the drill will be successively analyzed by a suite of instruments on the rover, searching for complex organic molecules and indicators of life.

Given the political context, ExoMars has been redesigned for a European only mission and will be launched in 2028. In the next 6 years, many activities

are planned in support of the scientific return of Martian missions, and in particular of Ma_MISS. The workplan is broadly illustrated hereafter.

Optimization of the Ma_MISS performance: Unlike the previous missions, the drill, and Ma_MISS measurements will be the deepest compositional measurements made on Mars. Ma_MISS can detect compositional gradients with depth, changes in type and abundance of minerals, weathering fronts or rinds, and diagenetic veins or nodules, changes in granulometry. The spectral range of Ma_MISS (0.4-2.3 microns) is optimal to detect changes in the occurrence and crystal chemistry of olivines and pyroxenes as well as Fe(II)/Fe(III) in silicates, oxides, and salts, that record different environments. Similarly, we expect to see changes in the hydration state, with uppermost surfaces more desiccated than interiors. We will test different minerals, mixtures, and stratigraphic sequences with our laboratory breadboards, in order to:

- Optimize the acquisitions based on the expected mineralogy and stratigraphy
- Develop a reference database to interpret the collected data
- Relate the spectral data with the mechanical data inferred from the engineered data from Rover subsystems, in particular drill telemetry that can provide information on the mechanical properties of the drilled rocks.

Modelling of the properties Martian surface and subsurface: The investigation of the Martian subsurface requires the knowledge of the thermal properties of the surface and subsurface. Water ice is present only under specific condition of temperature and pressure, thus thermal modelling is an essential part of the subsurface investigation. Moreover, hydration of the minerals should change with depth and local condition (diurnal and seasonal variation). Thermal modelling can be applied not only to Oxia planum (Exomars landing site) but to several other Mars' sites of interest, providing surface temperature distribution and interior temperature profiles.

Data analysis of previous and ongoing missions: The data acquired by past and ongoing missions are ex-

tremely useful for understanding if and where life could have been present on Mars. The landing sites of the most recent rover missions have been selected only after careful evaluation of the "astrobiological potential" of the area, in a process lasting about 5 years for each mission. Such evaluations have been done using the available remote sensing data. However, new data and techniques can be adopted to better understand the geological context of the landing sites, refining our knowledge of the areas from which the samples will be collected. Such a detailed knowledge of the context is absolutely needed to firmly identify any sample as interesting from an "astrobiological" perspective. Moreover, the knowledge of the areas is the base to locate areas on Earth where to observe directly the processes and minerals similar to what we expect on Martian (terrestrial analogues).

Laboratory and fieldwork activities: Terrestrial analogues of the landing sites of in-situ missions are critical to improve our ability to understand the data collected remotely by the rovers. Rosalind Franklin in particular focuses on the exploration of the layers of rock within the first two meters below the ground, which are not exposed and thus not observable from remote sensing instruments. For this reason, studying analogs on Earth is critical to build experience in interpreting the widest possible reasonable shallow subsurface scenarios we may find underneath the landing site [4]. We plan to organize fieldwork focused on studying areas on Earth with a geologic context similar to Oxia Planum on Mars. We are locating the analog field site with the support of the geologic map [5] and orbital spectroscopic observation [6,7]. During fieldwork, we will localize key outcrops where we will observe the stratigraphic context, record in situ spectra, and extract samples to be measured in the laboratory with the DAVIS copy of Ma_MISS [8].

Some examples of activities in the field are the VIS-NIR measurement campaign at Río Tinto [9], the one for the selection of the analogous sample CAP-1 [10] in southern Tuscany and others carried out for structural geological studies.

Conclusions: The delay in the Exomars launch can represent an opportunity to improve our knowledge of the landing site, using remote sensing data and terrestrial analogues. Moreover, the laboratory breadboard is the key element to optimize the scientific return, in terms of acquisition strategy and data analysis of the Martian unaltered subsurface.

References. [1] Vago et al. (2017) *Astrobiology* 17, 471–510. [2] De Sanctis et al. (2017) *Astrobiology* 17(6–7), 612–620. [3] De Sanctis et al. (2022) *PSJ* 3, 142. [4] Ferrari et al. (2023) Astrobiology. [5] Fawdon et al. (2022) *53rd LPSC Abstracts*, p. 2210. [6] Brossier et al. (2022) *Icarus* 386, 115114. [7] Mandon et al. (2021) *Astrobiology* 21, 464–480. [8] De Angelis et al. (2022) 53rd *LPSC*, abs#1796. [9] Ferrari et al. (2022) *EPSC2022-153*. [10] Costa et al. *EPSC2022-165*.

Fig.1 Schematic view of Ma_MISS instruments with the different parts in the rod/tip and on the Drill box
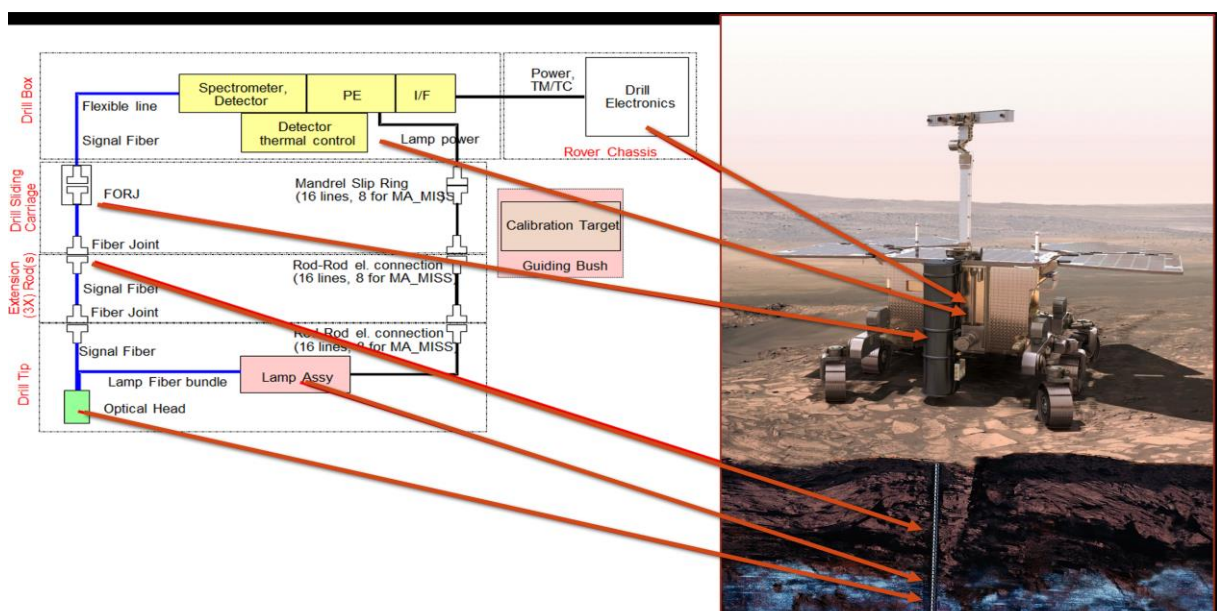
SHARK THE HIGH-CONTRAST IMAGER AND SPECTROGRAPH FOR LBT

D. Mesa[1] and V. D'Orazi[2]

[1] INAF – Osservatorio Astronomico di Padova, Vicolo dell'Osservatorio 5, Padova 35122, Italy
dino.mesa@inaf.it
[2] INAF – Osservatorio Astronomico di Padova, Vicolo dell'Osservatorio 5, Padova 35122, Italy

Introduction: SHARK is the new high-contrast imager and spectrograph for the Large Binocular Telescope (LBT). It will be composed by two different instruments that will be installed on the two different entrance foci of the LBTI (see Figure 1). The first instrument (SHARK-VIS - see Figure 2) will operate at visual wavelengths between 0.4 and 0.9 micron with a field of view of 10x10 arcsec. It will have an angular resolution of 15 mas and it will be able to obtain frames with a rate of 1 KHz. It will be installed at the telescope in 2023. The second instrument (SHARK-NIR . See Figure 3) will operate in the near-infrared in the Y, J and H spectral bands between 0.96 and 1.7 micron. It will exploit the recently updated adaptive optics (AO) system of LBT called SOUL to obtain a Strehel ratio larger than 80% on a total field of view of 18x18 arcsec. It has also a long-slit spectroscopic (LSS) observing mode that will allow to obtain spectra at medium resolution (R up to 700) for known comapnion of nearby stars. This instrument is currently installed at LBT and it is in its commissioning phase. Day-time tests have been performed during last months with encouraging results. Starting from January 2023 on-sky tests and observations will be performed to define and improve the instrument capabilities. The main scientific driver for SHARK is the high-contrast imaging of giant planets at large separations (10 au or more) from nearby (less than 150 pc) and young (few hundreds of Myrs) stars. It will be also possible to investigate the birth environment of planets, the proto-planetary disk when we will observe very young systems (with ages of 10 Myr or less). SHARK will allow to perform also different science topics like the study of stellar jets, of AGN and of evolved stars like AGB and post-AGB objects. Finally, an important topic will be the study of solar system objects with particular importance for the study of small bodies (asteroids and moons). This lasttopic present very promising possibilities given   its similitude of the SHARK.NIR camera with the SPHERE/IRDIS camera that in the past years allowed a number of interesting results in the solar system field.
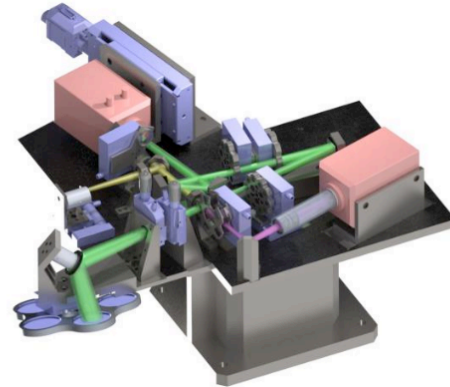

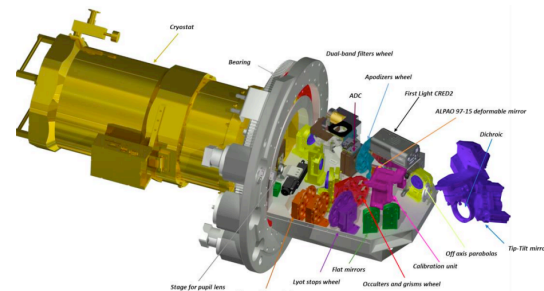Figure 2 - Mechanical design of SHARK-VIS
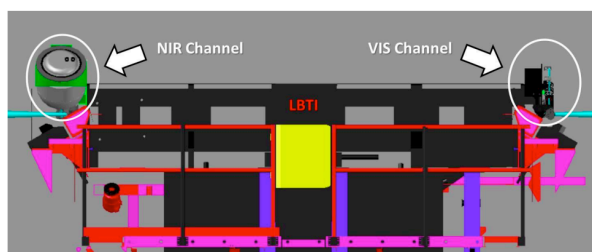

Figure 3 - Mechanical design of SHARK-NIR

Figure 1 - Positions of the two SHARK instruments at the LBT foci.

HYPERVELOCITY IMPACTS ON COMET INTERCEPTOR DUST IMPACT SENSOR AND COUNTER FOR DUST SHIELD AND DETECTION SYSTEM ASSESSMENT.

S. Ferretti[1,2], V. Della Corte[2], A. M. Piccirillo[1,2], I. Bertini[1,2], S. Fiscale[1], A. Longobardo[2], L. Inno[1], A. Rotundi[1,2], E. Ammannito[3] and G. Sindoni[3], [1]Dipartimento di Scienze e Tecnologie, Università degli Studi di Napoli "Parthenope", CDN, IC4, 80143 Naples, Italy, (stefano.ferretti@assegnista.uniparthenope.it), [2]Istituto di Astrofisica e Planetologia Spaziali, Istituto Nazionale di Astrofisica, Via del Fosso del Cavaliere, 100, 00133 Rome, Italy, (vincenzo.dellacorte@inaf.it), [3]Italian Space Agency (ASI), via del Politecnico snc, 00133 Rome, Italy.

Topic: *Instrumentation.*

Introduction: Essential details on the formation and evolution of the early Solar System are encoded in the dust ejected by cometary nuclei. Multiple short-period comets have already been studied in situ [1], but multiple perihelion passages modified their pristine condition. Dynamically new comets (DNCs) remain pristine bodies since they never visited the inner Solar System stationing in the Oort cloud, more than 2000 A.U. from the Sun.

Comet Interceptor (CI) is the first F-class space mission selected by the European Space Agency to study a DNC or an interstellar object passing through the inner Solar System for the first time [2]. The Dust Impact Sensor and Counter (DISC) is an instrument included in the Dust Field and Plasma (DFP) suite, part of the payload dedicated to characterize the dust that CI will observe in the coma of its target. DISC will measure hypervelocity impacts (HVIs) of cometary dust particles 1–400 µm in size at speeds in the range 10–70 km/s, i.e. the speed range of the flyby. It aims to: 1) characterize the dust particles mass distribution in the range 10^{-15}–10^{-8} kg; 2) retrieve information on dust structural properties from impacts duration [3].

DISC design: DISC is a $121\times115.5\times46$ mm^3 aluminum box containing the detection system and its electronics (Fig. 1). The sensing element consists in a $100\times100\times0.5$ mm^3 aluminum plate with three piezoelectric traducers (PZTs) at its corners. Far from the impacted area, the shockwaves induced by HVIs become acoustic Lamb waves that propagate reaching the PZTs. The resonant vibration is processed by two electronic boards, mounted under the sensing plate, returning individual particles momentum.
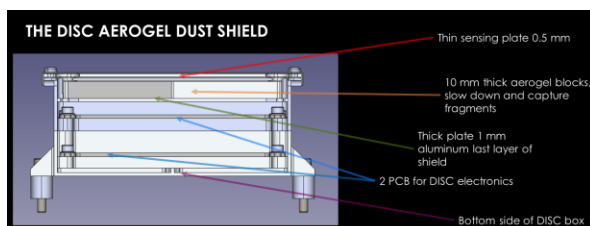

Fig. 1: DISC sectional drawing showing the sensing element, dust shield, and electronics mounting.

DISC electronics and the spacecraft (S/C) surface beneath it need to be shielded from hazardous dust particles possibly perforating the sensing plate. For this aim, we designed a never-used-before dust shield: four 12 mm-thick aerogel blocks inserted in a 1.5 mm-thick aluminum frame are mounted underneath the DISC sensing surface.

DISC impact detection system is derived from the GIADA Impact Sensor subsystem, used onboard Rosetta space probe to measure low-velocity dust impacts [4]. In order to ensure that the measurement concept is suitable for CI, i.e. at HVIs regime, two aspects need to be verified, namely DISC capability to:

- survive the expected coma dust environment;
- measure the momentum of dust particles with 10^{-15}–10^{-8} kg in mass and impacting at speed in the range 10–70 km/s.

Dust shield assessment: To check for the DISC survival in the expected coma dust environment, we tested the dust shield performance using a two-stage Light-Gas Gun (LGG) (Open University, Milton Keynes) shooting mm-sized particles of different materials at speeds around 5 km/s [5,6]. This facility allowed us to test DISC resistance to momenta in the range 10^{-2}–10^{-1} kg·m/s and to energies of the order of 10^2 J. The dust shield proved to survive at impacts with energies of about 200 J released by a 3 mm nylon bead at 5.5 km/s, with failure when impact energies are greater than 400 J. DISC resistance to higher-energy particles will be improved using the aerogel thickness of 2 cm. This thickness was selected comparing the experiment results with experimental ballistic limit equation (BLE) of similar configuration [7]. The performed tests show that with our design the resistance to HVIs, with respect to the limits expressed by BLE, is improved up to 30%.

These experiments showed that DISC is compatible with the foreseen coma dust environment. Integrating a thick aerogel layer in the design will reduce the risk of failure due to the expected hyper speed particles to low enough values even for the S/C more exposed to the dust flux. The S/C beneath DISC unit, in addition, is further protected by DISC lower layers.

DISC performance: DISC will have to measure momenta in the range 10^{-11}–10^{-3} kg·m/s [8]. The LGG facility allows to reach high momentum values by shooting heavy particles. However, the collision dynamics for mm-sized objects of common terrestrial materials is very different from equivalent cometary dust particles, thus a different strategy to simulate the foreseen impact momentum range is needed.

The expected HVI effects can be replicated using the apparatus that we assembled at INAF-IAPS in Roma, that includes a high-power pulsed laser beam (Fig. 2). Indeed, according to the late stage equivalence, laser intensity, beam dimension, and pulse duration can be tuned to match a particle's impact pressure, section, and shock duration, respectively [9]. Laser intensities of 10^9–10^{10} W/cm^2 can generate surface pressures from kbar to Mbar, corresponding to cometary dust particles colliding at 3–6 km/s. Using the Nd:YAG laser (λ = 1064 nm), emitting τ = 6 ns pulses with pulse energy of E_{pulse} = 1.2 J, we can cover a momentum range of 10^{-10}–10^{-5} kg·m/s.

Real dust particle impacts close to CI foreseen HVIs can be performed using a Van der Graaf (VdG) gun, i.e. an electrostatic accelerator that can shoot µm-sized dust particles up to 20 km/s [10]. This facility allows to reproduce momenta of 10^{-9}–10^{-7} kg·m/s, which partly overlap with laser simulated shots momentum range. VdG real impacts will be used to calibrate our high-power laser pulses facility and verify their representativity of cometary dust HVIs.

The expected energy range for dust impacts that will occur during CI flyby is 10^{-7}–10^2 J; the highest values of the range are not simulated by the laser apparatus. However, the wide energy/pulse duration range, with some attenuators and pulse reducers, allows to cover the mJ energy range.

The setup dedicated to laser simulated HVIs is reported in Figure 2. A polarizer attenuator splits the laser beam and allows to tune its power. A couple of mirrors prevents backwards reflections from reaching the laser aperture. A beam expander enlarges the laser beam before entering the vacuum chamber, where it is then focused by a plano-convex lens on the DISC breadboard mounted on a 3-axis translational stage. The vacuum chamber is fundamental to prevent plasma generation in air around the focus.

By properly tuning the laser parameters, this strategy allows to achieve representative simulations of cometary dust HVIs that will occur during the CI flyby. In addition to assessing DISC performance, simulating similar impacts many times provides statistics to calibrate DISC detection system and individual dust particle momentum measurements methodology with great accuracy.
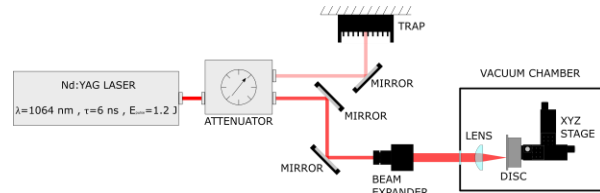

Fig. 2: Optical setup for high-power pulsed laser simulated dust particle hypervelocity impacts.

Summary: DISC dust shield mechanical resistance to cometary dust HVIs was tested by shooting different mm-sized particles at about 5 km/s using a LGG facility. Momenta of 10^{-2}–10^{-1} kg·m/s and energies of the order of 10^2 J were released during collisions. The tests demonstrated that the DISC dust shield can survive impacts with kinetic energy expected during the DNC close encounter and allow the instrument operability and measurement requirements compliance.

A dedicated optical setup was realized and used to extend the tested impact parameters ranges through high-power laser pulses simulations of foreseen CI HVIs. Such experiments play a fundamental role for accurate calibration of the instrument.

References: [1] Keller H. U. and Kührt E. (2020) *Space Sci. Rev., 216(1),* 1–26. [2] Snodgrass C. and Jones G. H. (2019) *Nat. Commun., 10(1),* 1–4. [3] Della Corte V. et al. (2021) *LPSC LII,* Abstract #2332. [4] Esposito F. et al. (2002) *Adv. Space Res., 29(8),* 1159–1163. [5] McDonnell J. A. M. (2006) *Int. J. Impact Eng., 33(1–12),* 410–418. [6] Hibbert R. et al. (2017) *Procedia Eng., 204,* 208–214. [7] Ryan S. et al. (2010) *Hypervelocity Impact Symposium,* (No. JSC-CN-19432). [8] Di Paolo F. et al. (2021) *LPSC LII,* Abstract #1238. [9] Pirri A. N. (1977) *Phys. Fluids, 20(2),* 221–228. [10] Friichtenicht J. F. (1962) *Rev. Sci. Instrum., 33(2),* 209–212.

COMPARISON OF INFRARED SPECTRAL FEATURES FROM PLANETARY SURFACES AND LABORATORY ROCK SAMPLES.

M. Bisolfati[1], A. Pisello[1], M. Porreca[1], A.Zinzi[2,3], D. Perugini[1], [1]Dipartimento di Fisica e Geologia, Università di Perugia (matteo.bisolfati@studenti.unipg.it), [2]Space Science Data Center – ASI, [3]ASI – Agenzia Spaziale Italiana (angelo.zinzi@asi.it).

Introduction: Infrared (IR) remote sensing spectral characterization of planetary surfaces allows us to obtain geochemical information useful to geological mapping and planetary evolution investigation [1–9]. We propose near/mid-infrared (NIR/MIR) [1-14μm] range spectral characterization of volcanic systems by means of comparison between planetary surfaces infrared spectra, measured by probes, and terrestrial analogue rock samples infrared spectra, measured in laboratory. Clustering and categorization machine learning algorithms are utilized to spectral comparison as well as spectral data analysis [10–14].

Martian surface emissivity data was obtained from radiance measurements of Thermal Emission Imaging System (THEMIS) [15] in the wavelength range between 7-15μm in order to investigate 4000km[2] at resolution of 100m of Elysium and Tharsis Mars volcanic regions [16,17].

Regarding Earth data, Crater of the Moon basaltic flow (Snake River, southern Idaho, SRP) [18] surface emissivity data were obtained from Spaceborne Thermal Emission and Reflection Radiometer (ASTER) measurements with 100m spatial resolution in the wavelength range between 8-12μm [19].

Regarding our samples, 11 samples collected to volcanic product of SRP have been already synthesized into glass powdered samples to Petro-Volcanology Research Group laboratory at the Perugia University and measured in reflectance at the temperatures of RT and 750K and emissivity at 450, 600, 750 and 900K to the Planetary Emissivity Laboratory (DLR) [20]. Others samples are being process in order to considering variables that influence NIR and MIR spectral contrast. Our measurement will be published in The Space Science Data Center (SSDC) spectral dataset in collaboration with Italian Space Agency (ASI) [21]. Meanwhile, we have access to more of 20000 thermal infrared spectra of a variety of materials, including minerals, rocks and soils of both the PDS Geosciences Node Spectral Library [typically 0.2-2.5μm] and ASU Thermal Emission Spectroscopy Laboratory Spectral Library [7-50μm] [22,23].

In addition to the clear spectral contrast in thermal infrared response of Earth carbonate system and volcanic products, the same volcanic structures show evident spectral contrast. On Earth a factor of importance in controlling spectral response is the growth of vegetation [24,25]. Therefore, Mars basaltic flow investigation able us to identify spectral contrasts relate only to geochemical properties that can give us information about an age-related change in spectral response.

References: 1.   Bandfield, J. L. A Global View of Martian Surface Compositions from. **287**, 5 (2000).
2.   Cannon, K. M. *et al.* Spectral properties of Martian and other planetary glasses and their detection in remotely sensed data. *Journal of Geophysical Research: Planets* **122**, 249–268 (2017).
3.   Christensen, P. R., Bandfield, J. L., Smith, M. D., Hamilton, V. E. & Clark, R. N. Identification of a basaltic component on the Martian surface from Thermal Emission Spectrometer data. *Journal of Geophysical Research: Planets* **105**, 9609–9621 (2000).
4.   Cooper, B. L., Salisbury, J. W., Killen, R. M. & Potter, A. E. Midinfrared spectral features of rocks and their powders. *Journal of Geophysical Research: Planets* **107**, 1-1-1–17 (2002).
5.   Liu, L., Zhou, J., Jiang, D., Zhuang, D. & Mansaray, L. R. Lithological discrimination of the mafic-ultramafic complex, Huitongshan, Beishan, China: Using ASTER data. *Journal of Earth Science* **25**, 529–536 (2014).
6.   Michalski, J. R., Kraft, M. D., Sharp, T. G., Williams, L. B. & Christensen, P. R. Mineralogical constraints on the high-silica Martian surface component observed by TES. *Icarus* **174**, 161–177 (2005).
7.   Rogers, A. D. & Hamilton, V. E. Compositional provinces of Mars from statistical analyses of TES, GRS, OMEGA and CRISM data. *Journal of Geophysical Research: Planets* **120**, 62–91 (2015).
8.   Salisbury, J. W. & Walter, L. S. Thermal infrared (2.5–13.5 μm) spectroscopic remote sensing of igneous rock types on particulate planetary surfaces. *Journal of Geophysical Research: Solid Earth* **94**, 9192–9202 (1989).
9.   Christensen, P. R. *et al.* Evidence for magmatic evolution and diversity on Mars from infrared observations. *Nature* **436**, 504–509 (2005).
10.   ABD EL WAHED, M., Kamh, S., Ashmawy, M. & Shebl, A. Transpressive structures in the Ghadir Shear Belt, Eastern Desert, Egypt: evidence for partitioning of oblique convergence in the Arabian Nubian Shield during Gondwana Agglutination. *Acta Geologica Sinica   English Edition* **93**, 1614–1646 (2019).

11. Loughlin, W. P. Principal component analysis for alteration mapping. *Photogrammetric Engineering and Remote Sensing* **57**, 1163–1169 (1991).

12. Pournamdari, M., Hashim, M. & Pour, A. B. Spectral transformation of ASTER and Landsat TM bands for lithological mapping of Soghan ophiolite complex, south Iran. *Advances in Space Research* **54**, 694–709 (2014).

13. Tu, T.-M., Su, S.-C., Shyu, H.-C. & Huang, P. S. A new look at IHS-like image fusion methods. *Information fusion* **2**, 177–186 (2001).

14. Yesou, H., Besnus, Y. & Rolet, J. Extraction of spectral information from Landsat TM data and merger with SPOT panchromatic imagery—a contribution to the study of geological structures. *ISPRS journal of photogrammetry and remote sensing* **48**, 23–36 (1993).

15. Christensen, P. R. *et al.* The thermal emission imaging system (THEMIS) for the Mars 2001 Odyssey Mission. *Space Science Reviews* **110**, 85–130 (2004).

16. Horvath, D. G., Moitra, P., Hamilton, C. W., Craddock, R. A. & Andrews-Hanna, J. C. Evidence for geologically recent explosive volcanism in Elysium Planitia, Mars. *Icarus* **365**, 114499 (2021).

17. Hauber, E., Brož, P., Jagert, F., Jodłowski, P. & Platz, T. Very recent and wide spread basaltic volcanism on Mars. *Geophysical Research Letters* **38**, (2011).

18. Kuntz, M. A. *et al.* The Great Rift and the evolution of the Craters of the Moon lava field, Idaho. *Cenozoic Geology of Idaho: Idaho Bureau of Mines and Geology Bulletin* **26**, 423–437 (1982).

19. Hulley, G. C. *et al.* The ASTER Global Emissivity Dataset (ASTER GED): Mapping Earth's emissivity at 100 meter spatial scale. *Geophysical Research Letters* **42**, 7966–7976 (2015).

20. Pisello, A. *et al.* Retrieving magma composition from TIR spectra: implications for terrestrial planets investigations. *Scientific reports* **9**, 1–13 (2019).

21. Zinzi, A., Capria, M. T., Palomba, E., Giommi, P. & Antonelli, L. A. MATISSE: A novel tool to access, visualize and analyse data from planetary exploration missions. *Astronomy and Computing* **15**, 16–28 (2016).

22. Guinness, E. A., Arvidson, R. E. & Slavney, S. The planetary data system geosciences node. *Planetary and space science* **44**, 13–22 (1996).

23. Christensen, P. R. *et al.* A thermal emission spectral library of rock forming minerals. *Journal of Geophysical Research: Planets* **105**, 9735–9739 (2000).

24. Rothery, D. A. & Lefebvre, R. H. The causes of age dependent changes in the spectral response of lavas, Craters of the Moon, Idaho, USA. *International journal of remote sensing* **6**, 1483–1489 (1985).

25. Neinavaz, E., Schlerf, M., Darvishzadeh, R., Gerhards, M. & Skidmore, A. K. Thermal infrared remote sensing of vegetation: Current status and perspectives. *International Journal of Applied Earth Observation and Geoinformation* **102**, 102415 (2021).

FINDING LONG-PERIOD SOLAR SYSTEM OR INTERSTELLAR OBJECTS WITH MACHINE LEARNING IN LSST.

A. Vanzanella[1,2], L.Inno[1,2], T. Daylan[3], I. Bertini[1], M. Fulle[4], A. Rotundi[1,5], S. Fiscale[1], C. Tubiana[5], V. Della Corte[5], E. Mazzotta Epifani[6], E. Ammannito[7], G. Sindoni[7]

[1]Science and Technology Department, Parthenope University of Naples, CDN IC4, 80143, Napoli (I) antonio.vanzanella@studenti.uniparthenope.it, [2]INAF-Osservatorio Astronomico di Capodimonte, Napoli (I), [3]Department of Astrophysical Sciences, Princeton University and Kavli Institute for Astrophysics and Space Research, Massachusetts Institute of Technology (US), [4]INAF-OATs, Trieste (I), [5]INAF-IAPS, Roma (I), [6]INAF-OAR, Rome (I), [7]ASI, Rome (I)

Topic: Small bodies.

Introduction: The Legacy Survey of Space and Time (LSST) of the Vera C. Rubin Observatory will start in 2024 survey the Southern Hemisphere sky for ten years, producing a "movie" of the dynamical universe.

Among the different science drivers, LSST is also built the purpose of obtaining a complete census of all Solar System objects. However, objects that are moving too slowly or are too far away to be detected by existing automatic pipelines would go undetected. To address this problem, we want to build a detection pipeline for these objects using a Machine Learning (ML) approach.

The algorithm we use is splitted in two stages: first, we created an ex-novo dataset to use as a training a test set and then we built the 3-dimensional Convolutional Neural Network responsible for the detection of slow-moving objects in those datasets.

The Datasets: Currently no real LSST data is available, but the Dark Energy Science Collaboration (DESC)[1] created a data preview (DP0) of LSST-like images as realistic as possible. Unfortunately, these images did not contain transients, which forced us to inject simulated objects in the images. The sample that we want to use as input is an ordered sequence of LSST images where we injected the PSF of the simulated object that moves in a consistent manner. The movement of the objects was created starting from the ephemeris computed on Trans-Neptunian objects listed in the JPL database, and matching them with the corresponding image's observation date. The whole process resulted in a 5000 samples of 50 frames each, divided in positive and negative ones.

TIME

Figure 1 – Different images of the same positive samples sorted by time. Same of the physical characteristics are shown above the cutouts.

Without data augmentation		
Training set	Validation set	Test set
~310	~150	~200
With data augmentation		
Training set	Validation set	Test set
~4500	~950	~200

Figure 2 – Number of dataset samples with data augmentation or not.

The ML algorithm: Working on images sequence required to handle a cube of data so we built a 3D-CNN to classify the samples between positive and negative. Each sequence is a single sample; if it contains an injected object, it is a positive sample otherwise it is a negative ones. The CNN uses the convolution to extract the features from data with a grid-like topology. In this case, the features are constrained to a third axis representing time. The information flows through many convolutional block, where different techniques have been applied, ending in a fully connected layer where the actual classification takes place. Different tests have been made trying different training configurations. Besides, different variations in the model architecture have been tested, such as the inclusion of an Long short-term memory (LSTM) cell after each convolutional block.
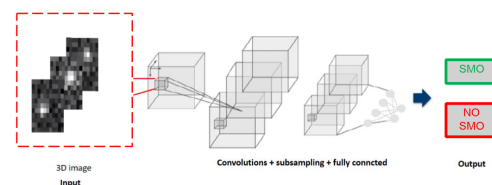
Figure 3 – A simplified version of the 3D Convolutional Neural Network. On the left the animations produced as video, in the middle an abstraction of the many layers and on the right the output.

Results: We made several tests in order to empirically optimize the parameters for the training: regularization and normalization techniques, number of epochs, learning rate, etc. . The best performance was achieved by the 3D-CNN, with 90% of accuracy obtained by using L2-Regularization, while the LSTM fallen short of expectations with an accuracy of 70%.
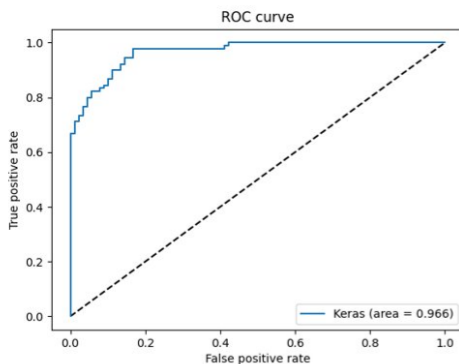
Figure 4 – ROC of 3D-CNN trained for 100 epochs using L2-regularization and without any normalization.

References:
[1] LSST Dark Energy Science Collaboration (LSST DESC), Abolfathi, B., et al. (2021*) The Astrophysical Journal Supplement Series*.

THE AGE OF SATURN'S RINGS: CLUES FROM RING MOON COMPOSITION. M. Ciarniello[1], G. Filacchione[1], P. D. Nicholson[2], M. M. Hedman[3], J. N. Cuzzi[4], M. El Moutamid[5], N. Rambaux[6], O. Mousis[7,8], S. Charnoz[9], A. Hendrix[10], K. Miller[11], K. Baillie[6], P. Estrada[4], H. Waite[10].

[1]INAF-IAPS, via del Fosso del Cavaliere, 100, 00133, Rome, IT (mauro.ciarniello@inaf.it), [2]Astronomy Department, Cornell University, Ithaca, 14853, NewYork, USA, [3]Department of Physics and Astronomy, University of Idaho, Moscow, 83844, ID, USA, [4]Space Sciences Division, NASA Ames Research Center, Moffett Field, 94035, CA, USA, [5]Cornell Center for Astrophysics and Planetary Science, Cornell Universiy, Ithaca NY 14853, USA, [6]IMCCE, Observatoire de Paris, PSL University, CNRS, Sorbonne Université, Paris, 77 Avenue Denfert-Rochereau, Paris, 75014, France, [7]Aix-Marseille Université, CNRS, CNES, Institut Origines, LAM, Marseille, France, [8]Institut universitaire de France (IUF), France, [9]Institut de Physique du Globe de Paris, Université de Paris, 1 Rue Jussieu, Paris, France, [10]Planetary Science Institute, Tucson, AZ, USA, [11]Southwest Research Institute, San Antonio, TX, USA.

Introduction: The determination of Saturn's ring age through formation scenarios has been a major field of investigation since the two Voyager missions [1]. Two different scenarios have been proposed in the past to explain Saturn ring origin: they could be primordial, remnants of the proto-planetary disk [2,3], or alternatively the product of the disruption of either a locally-formed satellite [4,5,6] or an extrinsic interloper [7,8,9] brought within the Roche limit by gas drag or tidal forces. Both scenarios are characterized by a series of constraints which need to be addressed by theoretical and observational perspectives.

The main rings we observe today are evolved objects, both in terms of composition, altered by the meteoritic flux [10] and space weathering coupled with possible self-cleaning mechanisms [3], and from a structurally and dynamical point of view, because of the competing effects of viscous spreading on one side and containment by the orbital resonances induced by regular satellites and nearby ring moons on the other [11].

Ring moons, in particular, likely formed from the recent aggregation of ring particles [12] which successively evolved on orbits placed immediately outside the main ring system.

Moving outwards from the main rings, these objects can be further grouped into:
- inner ring moons: orbiting within (Pan, Daphnis) and in close proximity (Atlas) of the A ring, and straddling the F ring (Prometheus and Pandora);
- coorbital satellites: Janus and Epimetheus, sharing a common "horseshoe" orbit between the F-ring and Mimas, and exchanging position approximately every 4 years;
- ring-embedded moons: associated with the G-ring (Aegeon) or partial rings/arcs (Methone, Anthe and Pallene).

The ring moons preserve to some extent the composition of the ring particles from which were accreted. Thus, investigating their surface composition in comparison to the main rings and the largest Saturn's icy moons, would provide important clues to understand the different processes acting within the Saturn's system. This would help to look back through the evolution of the Saturn's system in general, and, by consequence, of the main rings, in an effort of finally constraining their primordial composition, origin and age.

Ring moon surface composition from UV-VIS-IR photometry and spectroscopy: In this contribution we will review the spectrophotometric properties of the ring moons by exploiting the extensive set of observations provided by the Cassini UVIS [13], ISS [14] and VIMS [15] optical experiment, covering altogether the spectral range from 0.1 to 5.1 µm.

Remote sensing data of the ring moons will be put in the broader context of Saturn's main rings and inner mid-sized icy moons observations, for which extensive compositional analysis has been performed in the last two decades [16, 17, 18].

Like Saturn's main rings and inner mid-sized icy moons, ring moon spectra present the prominent water ice absorption features at 1.5, 2, and 3 µm, in addition to a distinct absorption shortward of 0.55 µm, indicating the presence of non-icy contaminants. In order to further characterize the spectral variability among ring moons, and in comparison to Saturn's main rings and mid-sized icy moons, we employ a suite of spectral indicators computed from VIMS spectra. These are the spectral slopes in the 0.35-0.55 µm and 0.55-0.95 µm wavelength intervals, and the band depth of the 1.5-µm and 2-µm water ice absorption features. This information is complemented with indicators derived from ISS observations, as the GRN/UV3 and IR3/GRN color filter ratios, and albedo-related quantities [19].

We will discuss the correlations among the different spectral indicators and their radial distributions in the Saturn's system in terms of variability of the relative abundances of the non-icy contaminants mixed with water ice, their mixing modality, and regolith grain size. This information will be used to characterize the effect of the different processes in the Saturn's environment (nearby ring contamination [20], meteoritic flux [10], high-energy particles fluxes [19]) affecting the ring moon surfaces.

References:

[1] Goldreich P. and Tremaine S. (1982) *Ann. Rev. Astron. Astrophys.*, 20, 249-283. [2] Pollack J. B. (1975) *Space Sci. Rev.* 18, 3-93. [3] Crida A. et al. (2019) *Nat. Astron.* 3, 967-970. [4] Charnoz S. et al. (2009) in *Saturn after Cassini-Huygens*, Dougherty, Esposito, Krimigis Ed., Springer-Verlag, 537-576. [5] Canup R. M. (2010) *Nature*, 468, 943. [6] Cuk M. et al. (2016) *Astrophys. J.*, 820, id.97, 16 pp. [7] Dones L. (1991) *Icarus,* 92, 194-203. [8] Wisdom J. et al. (2022) *Science*, 377, 1285-1289. [9] Hyodo R. et al. (2017) *Icarus,* 282, 195–213. [10] Cuzzi J. N. and Estrada P. R. (1998) *Icarus*, Volume 132, Issue 1, pp. 1-35. [11] Nicholson P. D. et al. (2018) in M. Tiscareno, C. Murray (Eds.), *Planetary Ring Systems*: *Properties, Structure and Evolution* (Cambridge Planetary Science), pp. 276-307, Cambridge: Cambridge University Press. [12] Charnoz S. et al. (2010) *Nature,* 465 (7299): 752-754. [13] Esposito L. W. et al. (2004) *Space Sci. Rev.* 115 (1-4): 299–361. [14] Porco C. C. et al. (2004) *Space ... al. (20 ... Spa ... chi ... ne ... G. et al. (20 ... Icarus* 220(2):1064–1096. [17] Clark R. N. et al. (2012) *Icarus* 218(2):831–860. [18] Ciarniello M. et al. (2019) *Icarus* 317:242–265. [19] Hedman M. M. et al. (2020). *AJ* 159(4):129. [20] Buratti B. J. et al. (2019) *Science* 364: eaat234.
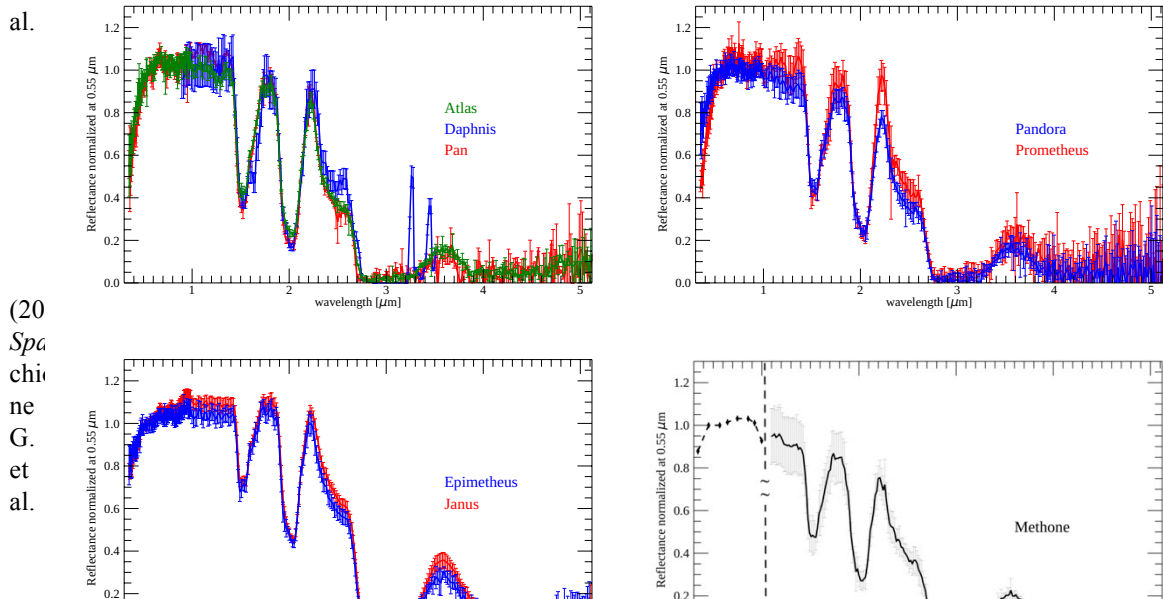
Figure 1. Ring moon full-disk reflectance spectra from available VIMS observation. Methone reflectance at visible wavelengths is derived from ISS observations, while the corresponding IR part of the spectrum, from VIMS observations, has been arbitrarily scaled to match the reflectance around 1 μm.

VIS-MIR SPECTRAL CHARACTERIZATION OF THE NWA 12184 METEORITE AND MODIFICATIONS INDUCED BY SOLAR WIND IRRADIATION EXPERIMENT.

A. Galiano[1], F. Dirri[1], M. Ferrari[1], S. Stefani[1], G. Piccioni[1], M.E. Palumbo[2], C. Scirè Scappuzzo[2], G. Baratta[2], R.G. Urso[2], C. Carli[1], A. Musolino[1,3], G. Filacchione[1], E. Bruschini[1], A. Raponi[1], M. Ciarniello[1], [1]INAF-IAPS Istituto di Astrofisica e Planetologia Spaziali, Rome, Italy (anna.galiano@inaf.it), [2]INAF-OACT, Osservatorio Astrofisico di Catania, Italy, [3]Università di Napoli "Parthenope", DIST, Centro Direzionale Isola C4, I-80143 Naples, Italy.

Introduction: Planetary bodies unprotected by a magnetic field and/or atmosphere are exposed to space weathering processes, such as micro-meteoritic impacts and solar wind irradiation, resulting in an alteration of the spectral properties of surface materials. Under laboratory-controlled conditions, micro-meteoritic impacts can be reproduced through 1064 nm pulsed-laser irradiations carrying an energy density of ~10 J/cm^2 [1], while the solar wind irradiation is mimicked by He$^+$ or Ar$^+$ ion beams with energies of ~1 to hundreds of keV [2,3,4]. After performing ion irradiation bombardments, several authors [2,3] have found that the spectral variations induced by the ion beams on carbonaceous chondrites (CC) depend on the meteorite type. In the VIS-NIR range, dark meteorites show a spectral brightening and bluing after irradiation, due to the carbonization process, while high albedo meteorites become darker and redder as a consequence of the production of nanophase iron particles [3]. In the MIR range, a shift of the Reststrahlen peaks was observed in different CCs samples [2,3].

We planned to observe spectral variations caused by ion irradiation on a CM2 meteorite (sample from Northwest Africa 12184, NWA 12184), to clarify how the spectral properties of minor bodies' surfaces, such as the Near-Earth Asteroid 162173 Ryugu, are affected by space weathering processes.

In this work, spectral characterization of the NWA 12184 was performed at different spatial resolutions in the VIS-MIR range: this allowed us to constrain the mineralogical composition of the matrix and chondrules and characterize the spectral variations caused by the simulation of solar wind. Further characterization was performed by μ-Raman spectroscopy to improve the compositional information concerning the refractory and carbonaceous material thanks to the increase in the spatial resolution achievable with this technique compared to the VIS-IR measurements.

NWA 12184 meteorite: The sample we have procured comes from a meteorite collected in Algeria in 2018 which experienced a low degree of weathering [5]. From the entire sample, measuring 24.5x17.6 mm and with a thickness of 1.9 mm, a small section of interest measuring 14x20 mm was selected for spectral investigation before and after weathering processes, by performing a "dry-cut" with a 600 μm thick blade. The sample shows chondrules with a mean diameter of 0.3 mm, CAIs, and mineral fragments set in a Fe-rich matrix, also composed of Ca-carbonates, sulfides, and phyllosilicates [5].

Spectral acquisitions: The CM2 was analyzed in a wide spectral range from VIS to MIR, at different spatial resolutions thanks to the five complementary laboratory techniques listed below (from T1 to T5).

- T1: Bidirectional reflectance spectra of different areas of CM2 were acquired in the 0.35-2.5 μm spectral interval (VIS-NIR, spectral sampling of 3 nm in VIS and 10-12 nm in NIR) with a Fieldspec-Pro Spectrophotometer mounted on a goniometer. The measurements were performed at standard geometry (i=30°, e=0°) with an illuminated spot of ~6 mm in diameter (one area acquired with the T1 and labelled NWA12184_01 corresponds to the densely dotted circle of *Fig.1, left panel*).
- T2: The FT-IR analysis was performed by using a Fourier transform interferometer (mod. Bruker Vertex 80) operating in the 1.7-15 μm range (NIR-MIR, spectral sampling 4 cm^{-1}) with the MCT detector (i=30°, e=0°). The spectral acquisition of an area of ~5 mm in diameter (dash-dotted ellipse in *Fig.1, left panel*) was executed to have a representative spectrum of the overall meteorite sample.
- T3: In a restricted region where T2 was applied, a grid of 800x800 μm was defined (solid rectangle in *Fig.1, left panel*) and 180 spectra with a spot of 60x60 μm were collected in the 2.5-16.6 μm (MIR, 4 cm^{-1} spectral sampling) using an IR microscope (mod. Bruker Hyperion 3000) connected to the Vertex 80 interferometer.
- T4: The hyperspectral characterization in the VIS range from 0.42 to 0.73 μm (10 nm spectral sampling) was performed by using the breadboard of the fISPEx instrument [6] allowing to measure the reflectance of the entire surface of the sample with a spatial resolution of about 60 μm/px at standard geometry (i=30°, e=0°).
- T5: μ-Raman was performed using a Bruker SENTERRA II spectrometer equipped with an Olympus microscope. The used excitation laser wavelength was 532 nm. Several spectra were collected in the same restricted area of T3 measurements characterizing the composition of chondrules and matrix with a spatial resolution of 30 μm.

Results: The VIS-NIR spectra of the meteorite acquired with T1 show a broad band at about 1.0 µm (*Fig.1, right panel*), suggesting the occurrence of olivine widespread in the meteorite. The VIS-NIR spectrum named NWA121184_01 (blue spectrum) is characterized by an additional absorption band at about 0.9 µm, which could be ascribed to pyroxenes: the corresponding area is shown in *Fig.1 (left panel)* and includes both the matrix and a chondrule of ~1 mm in diameter (Chondule A).

The NIR-MIR spectrum (not shown) of the representative area acquired with T2 shows the Reststrahlen peaks at 11.32 µm and at 11.82 µm: the region, that does not include the Chondrule A, confirms a forsteritic composition (Mg-rich olivine) of the matrix.
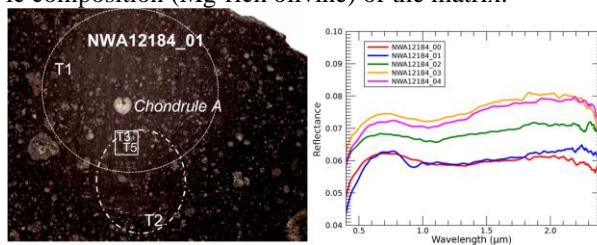
Fig.1. *Left:* Areas acquired with the T1 (densely dotted circle), T2 (dash-dotted ellipse), T3 and T5 (solid rectangle) techniques. The T4 technique was applied to the entire sample. *Right:* VIS-NIR spectra of areas acquired with T1 (the blue spectrum refers to the NWA12184_01 area shown in the *left* panel).

The area of NWA 12184 explored in the 800x800 µm grid (analysed with T3, T4 and T5) includes the matrix and three chondrules, i.e. Chondrule 1 (C1), Chondrule 2 (C2) and Chondrule 2 (C3) (*Fig.2a*) [7]. The MIR (*Fig.2b*) spectra (T3) in the 8-14 µm spectral range suggest a spectral similarity between forsterite and the meteorite sample, for the occurrence of the Reststrahlen peak at 11.42 µm (in the mean spectra of C1 and matrix) and the peak at 11.93 µm (in the mean spectra of chondrules and matrix). In addition, the spectra of C2 and C3 resemble that of the enstatite (Mg-rich orthopyroxene), for the peaks at 9.45, 9.84, 11.6 µm (in the mean spectrum of C2) and a shoulder at 10.8 µm (in the mean spectrum of C3). The MIR spectra in the 2.5-8 µm spectral range (T3) suggest that the meteorite sample contains traces of adsorbed water due to the presence of the bands at 3.0 µm and 6.0 µm. A weak absorption at about 4.0 µm is observed exclusively in the spectra of the chondrules, suggesting the putative presence of carbonates.

VIS spectra of C2 acquired with ƒISPEx (T4, *Fig.2c*) show a higher reflectance and stronger spectral reddening in the 0.4-0.5 µm spectral range with respect to C1, C3 and matrix.

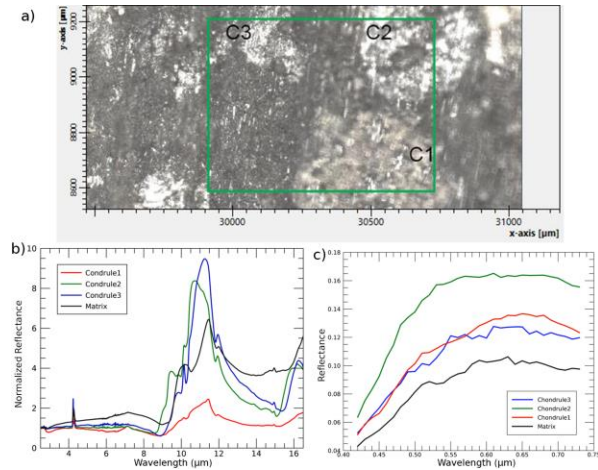**Fig.2.** *(a)* Area of NWA 12184 spectrally investigated with T3, T4 and T5 techniques. NIR-MIR mean spectra acquired with T2 *(b)* and VIS spectra acquired with T4 *(c)* of chondrules and matrix.

The µ-Raman analysis (T5) confirms the results obtained with the T3 highlighting the presence of carbonaceous material in the matrix and a fine intergrow of olivine and pyroxene in C2 and C3.

Solar wind simulation: After spectral characterization, the CM2 meteorite has been exposed to a He^+ flux of 200 keV at INAF-OACT to simulate the effects of the solar wind on airless carbonaceous bodies. We plan to repeat again the spectral measurements after the ion irradiation of the sample in order to observe the spectral variations induced by the ion flux.

References: [1] Brunetto, R. et al. (2005), *Icarus 180*; [2] Brunetto, R. et al. (2018), *P&SS 158*; [3] Lantz, C. et al. (2017), *Icarus 285*; [4] Vernazza, P. et al. (2013), *Icarus 225*; [5] Gattacceca, J. et al. (2020) *Meteoritics & Planet. Sci., 55*; [6] Filacchione, G. et al. (2022), *SPIE 12188*, id.1218809; [7] Galiano, A. et al. (2022), *LPSC LIII*, Abstract #1540.